SIGNATURES OF PLANETS: OBSERVATIONS AND MODELING OF STRUCTURE IN THE ZODIACAL CLOUD AND KUIPER DISK

By

ELIZABETH K. HOLMES

A DISSERTATION PRESENTED TO THE GRADUATE SCHOOL
OF THE UNIVERSITY OF FLORIDA IN PARTIAL FULFILLMENT
OF THE REQUIREMENTS FOR THE DEGREE OF
DOCTOR OF PHILOSOPHY

UNIVERSITY OF FLORIDA

2002

Copyright 2002

by

Elizabeth K. Holmes

This thesis is dedicated to

my grandparents, Josephine and Chester Marshall,

my aunt, Cecilia Marshall,

and Dr. Herbert Zook.

ACKNOWLEDGMENTS

I would like to thank Dr. Stanley Dermott for being my advisor. I would also like to thank Dr. Henry Kandrup, Dr. Elizabeth Lada, and Dr. Bo Gustafson for being on my committee and for all of their useful discussions. I also appreciate the time Dr. David Tanner spent serving as the external member on my committee.

I am grateful to Dr. Harold Butner for introducing me to the wonderful world of observational submillimeter astronomy.

This dissertation was funded in part by a NASA GSRP grant entitled "Detecting Planets in Circumstellar Disks."

I would like to thank my parents, James and Barbara Holmes, for their love and encouragement.

Lastly, I would like to extend my gratitude to all of my friends, especially Joannah Hinz, Elisha Polomski, and Karl Haisch for their friendship and commiseration, Jen Muehlbauer and Alan Pierson for providing me with a refreshing perspective of life outside of astronomy, James Radomski for keeping me sane with his saberlike wit, Veera Boonyasait for the sweetness that lies beneath his laconic shell, Gus Muench for hurling wiffle balls at me when I wasn't looking, Tomas Waldemarsson and Karen Wilson for being the kind people they are, Ily Vass for suffering through being my office mate this final year, Lauren Jones for dragging me to yoga class, and many others for their friendship and support.

TABLE OF CONTENTS

ACKNOWLEDGEMENTS iv

LIST OF TABLES viii

LIST OF FIGURES x

ABSTRACT xix

CHAPTERS

1 INTRODUCTION 1

1.1 Observations 3
1.2 Dynamical Models of Circumstellar Dust Disks 4
1.3 Numerical Integrations 4
1.4 Objective of this Dissertation 5

2 DYNAMICS OF DUST IN CIRCUMSTELLAR DISKS 8

2.1 Forces on a Dust Particle 8
2.1.1 Gravity 9
2.1.2 Radiation Pressure 9
2.1.3 Poynting Robertson Light Drag 10
2.1.4 Solar Wind Corpuscular Drag 12
2.1.5 Lorentz Force 12
2.1.6 Neutral Interstellar Gas Drag 13
2.1.7 Other Processes: The Yarkovsky Effect and Collisions . . 16
2.2 Secular Perturbation Theory 18
2.3 Mean Motion Resonances 24
2.3.1 Physics of Resonance 24
2.3.2 Dynamics of Resonance 24
2.3.3 First Order External Resonances 26

3 WARPED DISKS AND THE OFFSET OF THE ZODIACAL CLOUD 33

3.1 COBE Observations of the Warp in the Zodiacal Cloud 34
3.2 Applications of Secular Perturbation Theory to HR 4796 42
3.2.1 Warp: Variation of Forced Inclination 42
3.3 Heuristic Models of Warped Disks 45
3.3.1 Exo-zodiacal Cloud Model 46
3.3.2 Implications for SIRTF 48
3.4 COBE Observations of the Offset in the Zodiacal Cloud 50

3.5 ISO Observations 52

4 RESONANT STRUCTURE IN THE KUIPER DISK 58

4.1 Introduction 59
4.1.1 Kuiper Belt 60
4.1.2 Planetary Debris Disks 61
4.2 Size-Frequency Distribution of the Kuiper Disk 62
4.3 Resonant Structure: Mean Motion Resonances 73
4.3.1 Source Bodies 76
4.3.2 Analytical Predictions for Trapping 79
4.3.3 Other Resonances 84
4.3.4 Additional Forces 84
4.3.5 Numerical Integrations 86
4.4 Discussion 115

5 SEARCHING THE COBE DATA FOR THE PLUTINO DISK 118

5.1 COBE Observations 120
5.2 Kelsall Zodiacal Cloud Model 123
5.2.1 Kelsall Background Zodiacal Cloud Model 124
5.2.2 Kelsall Dust Band Model 125
5.2.3 Kelsall Circumsolar Ring Model 127
5.2.4 Discussion of Kelsall Models 127
5.3 Dynamical Zodiacal Cloud Models 128
5.3.1 Background Zodiacal Cloud 129
5.3.2 Dynamical Dust Band Model 131
5.3.3 Dynamical Circumsolar Ring Model 138
5.4 Arendt ISM Models 143
5.4.1 Bright Source Blanking and the Faint Source Model (G_S) 144
5.4.2 ISM Model (G_I) 145
5.5 Residuals 147
5.5.1 Subtracting the Kelsall Model 152
5.5.2 Subtracting the Kelsall Model With a Modified Offset . . 156
5.5.3 Subtracting the Reach Model 161
5.5.4 Discussion of Inadequacies of Empirical Models 163
5.5.5 Dynamical Background Zodiacal Cloud Model 168

6 SURVEY OF NEARBY STARS FOR SUB-MILLIMETER EMISSION 179

6.1 Introduction 179
6.2 Observations 180
6.2.1 Selection Criteria 182
6.3 Color Correcting the IRAS Flux Densities 183
6.4 Results 188
6.5 Discussion 189
6.5.1 Dust Mass 191
6.6 Conclusions and Future Work 193

7 CONCLUSIONS 200

7.1 Warp and Offset 200
7.2 Resonant Structure in the Kuiper Disk 201
7.3 Searching the COBE Data for the Plutino Disk 202
7.4 Sub-millimeter Observations 203
7.5 Future Work 204
7.5.1 Plutino Disk 204
7.5.2 Building a Complete Background Zodiacal Cloud Model . 204
7.5.3 Applications to Planetary Debris Disks 205

APPENDIXES

A SIMUL 207

B OPTICAL PROPERTIES OF DUST PARTICLES 209

REFERENCES 211

BIOGRAPHICAL SKETCH 219

LIST OF TABLES

2-1 Laplace coefficients for the β=0 no drag case for several important first order resonances in the Kuiper belt. 27

2-2 Laplace coefficients for the β=0 no drag case for several important second order resonances in the Kuiper belt. 28

3-1 Orientation of the planes of symmetry with respect to the ecliptic. . . 37

3-2 Osculating elements of known and hypothetical perturbers in the HR 4796 system. 44

3-3 ISO observations of the north and south polar brightnesses of the zodiacal cloud. 53

4-1 Location of the 3:2 external mean motion resonance as a function of $\beta = F_{rad}/F_{grav}$ 80

4-2 Critical parameters on 10 and 100 μm diameter dust particles for $e' = 0.05$ and $e' = 0.25$. 83

4-3 Magnitude of various forces on 10 μm ($\beta = 0.04868$) and 100 μm ($\beta = 0.00446$) diameter spheroidal dust particles. 86

4-4 Ratios of the magnitude of the forces on a 10 μm ($\beta = 0.04868$) and 100 μm ($\beta = 0.00446$) dust particle. 87

4-5 A comparison of results for numerical runs for 7 μm diameter particles ($\beta = 0.07104$) originating from 10 km diameter source bodies. 107

4-6 Percentage of particles in the 5:3 resonances for the plu_10km_7mu_250 numerical run. 114

5-1 Relevant parameters for Kelsall zodiacal cloud model. 125

5-2 Values for $R(\lambda)$ for the ISM model. 147
5-3 Parameters for sine curve fits to the 25 μm average polar COBE data and Kelsall background cloud model. 157
6-1 SMTO Source List. 194
6-2 IRAS Fluxes and Upper Limits [Jy]. 195
6-3 SMTO Bolometer Observations 1999-2000. 195

LIST OF FIGURES

2-1 Decomposition of osculating elements into forced and proper elements. 23

2-2 The maximum libration widths in a-e space for the 3:2 external mean motion resonance with Neptune. 31

3-1 COBE DIRBE data showing the warp in the zodiacal cloud in the 25 μm wave band. 38

3-2 Variation of Forced Inclination and Forced Node with respect to semi-major axis for different sized particles. In the asteroid belt, I_{forced} and Ω_{forced} are locked on to Jupiter's inclination and node, respectively. . 39

3-3 The brightness of the north and south ecliptic poles as seen by COBE versus ecliptic longitude of Earth for the 4, 12, 60, and 100 μm wave bands. 41

3-4 Secular perturbation theory variation of I_{forced} with respect to semi-major axis for HR 4796. 43

3-5 Infrared observations of HR 4796. 45

3-6 Characterizing the warp in HR 4796. 46

3-7 Heuristic variations of Ω_{forced} and I_{forced}. 47

3-8 Warped model cloud viewed at 1.35 pc as it would appear in the 70 μm wave band assuming a SIRTF sensitivity limit of 610 μJy. 48

3-9 Warped model as it would appear to SIRTF. 49

3-10 Offset of the zodiacal cloud in the 12 (left) and 25 μm (right) wave bands. 51

3-11 North and south polar brightness curves for the ISO data (top) and COBE data (bottom). 54

3-12 Shifted north and south polar brightness data are shown for the ISO data points (top) and COBE curve (bottom). 55

3-13 Scaled north and south polar brightness data are shown for the ISO data points (top) and COBE curves (bottom). 56

4-1 A plot of the known Kuiper belt objects with data obtained from the Minor Planet Center. 60

4-2 Cumulative surface area for the asteroid belt (assuming a D_o of $\approx$ 201 km, appropriate for a $D_{max} \approx 229$ km) associated with $q = 1.83$, the theoretical collisional equilibrium value of the size-frequency index. . 64

4-3 Cumulative surface area for the asteroid belt (top) assuming a $D_{max} =$ 50 km and $M_{cum} = 0.0003 M_{\oplus}$ for size-frequency indices $q = 1.80, 1.83,$ and 1.86. (bottom) The cumulative surface area for the Kuiper belt assuming a $D_{max} = 2300$ km, the diameter of Pluto, and $M_{cum} = 0.1 M_{\oplus}$ for size-frequency indices $q = 1.80, 1.83,$ and 1.86. 68

4-4 The total brightness in MJy/sr versus cumulative area for the asteroid belt (top) and Kuiper belt (bottom) assuming a cumulative mass of the Kuiper belt of $M_{cum} = 0.1 M_{\oplus}$. The calculated brightness for the Kuiper belt is significantly higher than the upper limits given by Teplitz et al. (1999). 70

4-5 Line of sight (LOS) brightness in MJy/sr versus cumulative area for the asteroid belt (top) and Kuiper belt (bottom) assuming a cumulative mass of the Kuiper belt of $M_{cum} = 0.1 M_{\oplus}$. The calculated brightness for the Kuiper belt is significantly higher than the upper limits given by Teplitz et al. (1999). 71

4-6 Total brightness (top) and LOS brightness (bottom) for the Kuiper belt with the same parameters as in the previous figures except that $M_{cum} = 0.3 M_{\oplus}$. 72
4-7 Model of a Plutino disk. 74
4-8 A Plutino in the 3:2 mean motion resonance with Neptune. 75
4-9 A model of a Kuiper disk from asteroidal particles (with a distribution of eccentricities and inclinations) in the 3:2 mean motion resonance with Neptune with a non zero libration amplitude. 76
4-10 Δa as a function of the the diameter of the parent Plutino from which the dust particles escape. 78
4-11 Eccentricity versus semi-major axis for particle 1 in a RADAU run for the no drag case ($\beta = 0$) including the effects of the gravitational perturbations of seven planets. 89
4-12 Variation of semi-major axis, resonant argument, and eccentricity with time for particle 1 in a RADAU run for the no drag case ($\beta = 0$) including the gravitational effects of seven planets. 90
4-13 Eccentricity versus semi-major axis for particle 10 in a RADAU run for the no drag case ($\beta = 0$) including the gravitational effects of seven planets. 91
4-14 Variation of semi-major axis, resonant argument, and eccentricity with time for particle 10 in a RADAU run for the no drag case ($\beta = 0$) including the gravitational effects of seven planets. 93
4-15 Eccentricity versus semi-major axis for particle 10 in a RADAU run for the $\beta = 0$ case including gravity and the Lorentz force ($U = 5\ V$). 94
4-16 Variation of semi-major axis, resonant argument, and eccentricity with time for particle 10 in a RADAU run for the $\beta = 0$ case including gravity and the Lorentz force ($U = 5\ V$). 95

4-17 Eccentricity versus semi-major axis for particle 10 in a RADAU run for the $\beta = 0$ case including gravity, the Lorentz force ($U = 5\ V$), and the effects of neutral interstellar gas drag ($C_D = 1$). 96
4-18 Variation of semi-major axis, resonant argument, and eccentricity with time for particle 10 in a RADAU run for the $\beta = 0$ case including gravity, the Lorentz force ($U = 5\ V$), and the effects of neutral interstellar gas drag ($C_D = 1$). 97
4-19 Percentage of particles in the 3:2 mean motion resonance with Neptune assuming particles were generated from source body of 0 km in diameter in the 3:2 resonance. 98
4-20 Percentage of particles in the 3:2 mean motion resonance with Neptune assuming particles were generated from source body of 10 km in diameter in the 3:2 resonance. 99
4-21 Percentage of particles in the 3:2 mean motion resonance with Neptune assuming particles were generated from source body of 100 km in diameter in the 3:2 resonance. 100
4-22 Close up of the plot of the percentage of particles in the 3:2 mean motion resonance with Neptune assuming particles were generated from source body of 10 km in diameter in the 3:2 resonance. 101
4-23 Percentage of particles (with $\beta = 0.07104$) in the 3:2, 6:4, 5:3, and 2:1 resonances assuming the particles were generated from a source body of 10 km in diameter in the 3:2 resonance. 102
4-24 Eccentricity versus semi-major axis for particle 1 in a RADAU run including the Lorentz force where $U = 20\ V$. 105
4-25 Variation of semi-major axis, resonant argument, and eccentricity with time for particle 1 in a RADAU run including the Lorentz force where $U = 20\ V$. 106

4-26 Eccentricity versus semi-major axis for a particle trapped in the 5:3 mean motion resonance with Neptune. 108
4-27 Variation of semi-major axis, resonant argument, and eccentricity with time for particle 125 in a RADAU run (for 7 μm diameter particles released from a 10 km source body) including the standard forces. . . 109
4-28 Eccentricity versus semi-major axis for particle 81 in a RADAU run including the standard forces and the Lorentz force where $U = 20\ V$. 110
4-29 Variation of semi-major axis, resonant argument, and eccentricity with time for particle 81 in a RADAU run including the standard forces and the Lorentz force where $U = 20\ V$. 111
4-30 Eccentricity versus semi-major axis for particle 2 in a RADAU run including the standard forces and the Lorentz force where $U = 20\ V$. 112
4-31 Variation of semi-major axis, resonant argument, and eccentricity with time for particle 2 in a RADAU run including the standard forces and the Lorentz force where $U = 20\ V$. 113
4-32 The variation of semi-major axis, resonant argument, and inclination with time for particle 8 in a 5:3 inclination resonance. 115
4-33 The X-Y distribution of orbits for the standard forces case, both Lorentz force cases, and the neutral interstellar gas drag case. 117
5-1 Trailing/leading asymmetry as seen in the COBE data. 121
5-2 COBE DIRBE Weekly Sky Map data in the 60 μm wave band for Week 33 (corresponding to $\lambda_{\oplus} = 287°$). 122
5-3 Kelsall background zodiacal cloud model. 126
5-4 Average polar brightness for the 25 μm COBE DIRBE data vs. the Kelsall background cloud model. 132
5-5 For this dissertation, we construct an Aitoff projection of the total Eos dust band model in the 25 μm wave band. 133

5-6 An Aitoff projection of the total Themis dust band model in the 25 μm wave band. 134
5-7 An Aitoff projection of the total Koronis dust band model in the 25 μm wave band. 135
5-8 An Aitoff projection of the total dust band model in the 25 μm wave band. 136
5-9 A COBE Weekly Skymap type projection of the total dust band model in the 60 μm wave band for Week 33 (corresponding to $\lambda_{\oplus} = 287°$). . 137
5-10 True background zodiacal cloud model for Week 33 in the 25 μm wave band for the original Kelsall background zodiacal cloud model and the dynamical dust band model. 139
5-11 Exo-solar system view of a dynamical model of Earth's resonant ring composed of 12 micron diameter particles as viewed in the 12 μm wave band. 141
5-12 COBE Weekly Skymap type projection of the resonant ring model, constructed with 15 μm diameter particles in the 60 μm wave band for Week 33 (corresponding to $\lambda_{\oplus} = 287°$). 142
5-13 The ISM model in the 60 μm wave band for Week 33 (corresponding to $\lambda_{\oplus} = 287°$). 145
5-14 25 μm COBE DIRBE data in weekly skymap format. 148
5-15 60 μm COBE DIRBE data in weekly skymap format. 150
5-16 [Trailing scans for the 60 μm COBE DIRBE data. 151
5-17 Residuals obtained in the 25 μm wave band by subtracting the Kelsall background cloud model from the COBE data. 153
5-18 Residuals obtained in the 25 μm wave band by subtracting the Kelsall background cloud model and the dynamical dust band model from the COBE data. 154

5-19 [Residuals obtained in the 60 μm wave band for Week 33 by subtracting the Kelsall background cloud model and the dynamical dust band model from the COBE data initial residuals. 155
5-20 Kelsall background cloud model with modified offset. 158
5-21 Residuals from the subtraction of a Kelsall model with a modified offset and the dynamical dust band model for Week 33 in the 60 μm wave band. 159
5-22 Residuals from subtracting the dynamical dust band model and a Kelsall background model with an offset modified to match that of the COBE data in the 25 and 60 μm wave bands. 160
5-23 The Reach background zodiacal cloud model for Week 33 in the 25 μm wave band. 163
5-24 Residuals we obtained in the 25 μm wave band by subtracting the Reach background cloud model, with the offsets set to zero, and the dynamical dust band model from the COBE data. 164
5-25 Residuals obtained in the 25 μm wave band by subtracting the Reach background cloud model, with the offsets set to those used in the Kelsall model, and the dynamical dust band model from the COBE data. 165
5-26 Residuals obtained in the 25 μm wave band by subtracting the Reach background cloud model, with offsets which match the COBE data, and the dynamical dust band model from the COBE data. 166
5-27 The Kelsall background zodiacal cloud model for Week 33 in the 25 μm wave band with an offset that matches that seen in the data. 167
5-28 Values for forced eccentricity for various size particles near the Earth. 169

5-29 True background cloud model for the outer background zodiacal cloud model once the low frequency component of the dust band model has been removed for Week 33 in the 25 μm wave band. 171
5-30 Residuals obtained for Week 33 in the 25 μm wave band by subtracting the outer zodiacal background cloud model and the dynamical dust band model from the COBE data. 172
5-31 Total background zodiacal cloud model for particles 9 μm in diameter in the 25 μm wave band for Week 33. 174
5-32 Residuals obtained for Week 33 in the 25 μm wave band by subtracting the scaled total zodiacal background cloud model and the dynamical dust band model from the COBE data. 175
5-33 Horizontal line cut through the ecliptic of the residuals shown in Figure 5-32. 176
5-34 Residuals from the subtraction of a Kelsall model with a modified offset, the dynamical dust band model, and a model for galactic emission for Week 33 in the 60 μm wave band. 178
6-1 Scan 7548 of HD 131156 at 1300 μm. 184
6-2 The extinction curve and overlay near-IR power law fit. 187
6-3 Blackbody ($\beta = 0$) and graybody ($\beta = 1$ and 2) fits to the star subtracted color corrected IRAS fluxes for (a) HD 165341, (b) HD 185144 (σ Dra), (c) HD 4614 (η Cas A and B), and (d) HD 32923. 196
6-4 Blackbody ($\beta = 0$) and graybody ($\beta = 1$ and 2) fits to the star subtracted color corrected IRAS fluxes for (a) HD 192425 (ρ Aql), (b) HD 82189 (22 UMa), (c) HD 39415, and (d) HD 37357 197
6-5 Blackbody ($\beta = 0$) and graybody ($\beta = 1$ and 2) fits to the star subtracted color corrected IRAS fluxes for β Leo. 198

6-6 Blackbody ($\beta = 0$) and graybody ($\beta = 1$ and 2) fits to the dust component of the color corrected IRAS fluxes and upper limits for HD 131156.199

Abstract of Dissertation Presented to the Graduate School
of the University of Florida in Partial Fulfillment of the
Requirements for the Degree of Doctor of Philosophy

SIGNATURES OF PLANETS: OBSERVATIONS AND MODELING OF STRUCTURE IN THE ZODIACAL CLOUD AND KUIPER DISK

By

Elizabeth K. Holmes

May 2002

Chairman: Dr. Stanley F. Dermott
Major Department: Astronomy

There is a possible connection between structure in evolved circumstellar disks and the presence of planets, our own zodiacal cloud being a proven example. Asymmetries in such a disk could be diagnostic of planets which would be otherwise undetectable. Using COBE DIRBE observations, we link structure in the zodiacal cloud, namely the warp and offset of the cloud, to the presence of planets using secular perturbation theory. In addition, we obtain supplementary ISO observations and determine a scale factor for the data which we apply to calibrate the data to the observed COBE brightness.

A Kuiper dust disk will have a resonant structure, with two concentrations in brightness along the ecliptic longitude arising because 10-15% of the Kuiper belt objects are in the 3:2 mean motion resonance with Neptune. We run numerical integrations of particles originating from source bodies trapped in the 3:2 resonance and we determine what percentage of particles remain in the resonance for a variety

of particle and source body sizes. The dynamical evolution of the particles is followed from source to sink with Poynting-Robertson light drag, solar wind drag, radiation pressure, the Lorentz force, neutral interstellar gas drag, and the effects of planetary gravitational perturbations included.

We then conduct an observational search in the 60 μm COBE data for the Kuiper disk, which is predicted to be, at most, a few percent of the brightness of the zodiacal cloud. By removing emission due to the background zodiacal cloud and the dust bands, we expect to see the trailing/leading signature of Earth's resonant ring. However, when subtracted from the data, we find that none of the empirical background zodiacal cloud models give the residuals predicted by theory. We conclude that a dynamical two-component (both inner and outer) zodiacal cloud model must be created to complete the search.

Lastly, we extend our work outside the solar system and obtain upper limits on the flux around ten Vega-type stars using the Sub-millimeter Telescope Observatory in the 870 μm and 1300 μm wave bands, which will be used to determine the most promising candidates for future observations.

CHAPTER 1
INTRODUCTION

Launched in 1983, the Infrared Astronomical Satellite (IRAS) detected excess far-infrared emission from more than 15% of all nearby main sequence A-K stars, indicating the presence of circumstellar dust clouds (Backman and Paresce 1993, Elachi et al. 1996). Our solar system is believed to have evolved out of a gravitationally collapsed disk of material which coalesced into planetesimals and, over time, planets. The gravitational presence of the massive planet Jupiter increased relative velocities of planetesimals in its vicinity, preventing them from aggregating into planets, and instead forming the asteroid belt. In the outer solar system, beyond the orbit of Neptune, lies the Kuiper belt, home to some of the most primitive objects in the solar system. Located at approximately 30 to 50 AU, it is also the proposed source of short-period comets (Jewitt 1999). The Kuiper belt was formed either because planet formation at that heliocentric distance did not occur due to the low density of planetesimals and the long encounter time scale and/or planetesimals were displaced into the region due to perturbing encounters with Uranus and Neptune (Backman and Paresce 1993).

In the inner solar system, collisions between asteroids supply dust particles to the sun's inner dust disk, the zodiacal cloud. The zodiacal cloud has several different sources of material: asteroidal and cometary particles, interstellar grains to a lesser extent, and possibly dust from the Kuiper belt (Dermott et al. 1994a, Liou et al. 1995, Dermott et al. 1996a, Grogan et al. 1996, and Liou et al. 1996). As Kuiper belt Objects (KBOs) continue to be found, the existence of a Kuiper dust disk having an equilibrium grain population orbiting at 30 to 50 AU has been postulated (Backman

et al. 1995). The circumstellar material detected by IRAS around other stars is most analogous to the Kuiper disk (Backman and Paresce 1993). A Kuiper disk would most likely have a resonant structure, with two concentrations in brightness along the ecliptic longitude. This large scale structure arises because 10-15% of the Kuiper belt objects, the Plutinos, are in the 3:2 mean motion resonance with Neptune (Jewitt 1999, Malhotra 1995).

In either disk component, the orbit of a particle can be described by a set of six osculating elements: the semi-major axis (a), eccentricity (e), inclination (I), longitude of ascending node (Ω), the longitude of pericenter ($\tilde{\omega}$), and the mean longitude (λ). In low-order secular perturbation theory, the classical method used to study the long term orbital evolution of both planets and dust particles in the solar system assuming the eccentricities and inclinations are low, osculating elements are decomposed into **proper elements**, which depend on initial conditions, and **forced elements**, which are imposed on the particle's orbit by the gravitational perturbations of the planets. This theory can be applied even in the presence of drag forces (Dermott et al. 1992, Kortenkamp 1996). Consequently, we can show that the orbits of dust particles in a circumstellar cloud are directly affected by the planets therein. It is possible to extend the preceding argument to other evolved solar systems and theorize that there is a connection between evolved circumstellar disks and the presence of planets and/or planetesimals in the system (Backman and Paresce 1993, Dermott et al. 1999b).

At least three different types of asymmetries can serve to indicate bodies orbiting a star in a disk: 1) a **warp** in the plane of symmetry of the disk due to the variation of the forced inclinations of the particles with respect to their astrocentric distances (Dermott et al. 1999a, Dermott et al. 1999b), 2) an **offset** in the center of symmetry of the disk with respect to the central star due to forced eccentricities of the dust particles (Holmes et al. 1998), and 3) density enhancements in the plane of

the disk due to **resonant trapping** of dust particles (Dermott et al. 1994b, Jayaraman 1995). All three of the above asymmetries have been identified in our own solar system from the analysis of infrared satellite data from IRAS and the Cosmic Background Explorer (COBE). In this dissertation, we study these asymmetries in three different ways: observationally, through the analysis of space craft data from IRAS, COBE, and the Infrared Space Observatory (ISO), theoretically by the construction of dynamical models, and numerically using computer simulations.

1.1 Observations

IRAS was operated in four wave bands: 12, 25, 60, and 100 μm. Though not the focus of this thesis, IRAS data is used as a comparison to the ground-based observational results obtained in Chapter 6. The Diffuse Infrared Background Experiment (DIRBE) on the COBE spacecraft was designed to search for the cosmic infrared background, diffuse infrared radiation originating from outside of the Milky Way galaxy. COBE DIRBE operated for 10 months from December 11, 1989 to September 21, 1990 in 10 photometric wave bands at 1.25, 2.2, 3.5, 4.9, 12, 25, 60, 100, 140, and 240 μm (Hauser et al. 1998). COBE data is the main focus of this thesis and is discussed in Chapter 3, 4, and 5. Launched in 1995, the Infrared Space Observatory (ISO) observed the universe at infrared wavelengths from 2.5 to 240 μm with four different instruments: ISOCAM, an infrared camera (2.5 - 17 μm), ISOPHOT, an imaging photopolarimeter (2.5 - 240 μm), ISO-LWS, a long wavelength spectrometer (43 - 196.7 μm), and ISO-SWS, a short wavelength spectrometer (2.38 to 45.2 μm). Scientific operations on ISO lasted from February 1996 to April 1998. We present results obtained using ISO data in Chapter 3 and compare them to COBE data. Lastly, in Chapter 6, ground-based observations of candidate planetary debris disks using the Heinrich Hertz Telescope (HHT) of the Sub-millimeter Telescope Observatory (SMTO) in the 870 and 1300 μm wave bands are presented.

1.2 Dynamical Models of Circumstellar Dust Disks

In the most general case, models are based on the theory of dust particle capture into mean motion resonances in the presence of drag forces (Weidenschilling and Jackson 1993) and the theory of secular perturbations, the classical method used to study the long term orbital evolution of both planets and minor planets in planetary systems. The dynamical evolution of the particles is followed from source to sink with Poynting Robertson light drag (PR drag), solar wind drag, radiation pressure, and the effects of planetary gravitational perturbations included. Based on these effects, a set of orbits is generated for the particles in the disk. The models are built by distributing the orbits of the particles through a three dimensional array of cells. A Line of Sight Integrator allows a model to be viewed as it would appear to an Earth-based observer in a given wave band at a specified distance. The brightness along the line of sight is calculated assuming the particles are spheres of a given diameter which are composed of a specified material (such as astronomical silicate). The model can be convolved with a beam size or pixel size to simulate how an observation would appear to a specific telescope or space craft.

We create models of warped disks and discuss our results in Chapter 3 and models of a resonant ring in the Kuiper disk are presented in Chapter 4. Chapter 5 focuses on the subtraction of dynamical models of the dust bands and Earth's resonant ring, developed by Grogan et al. (2001) and Jayaraman (1995), respectively, from the COBE data to search for the resonant signature of the Kuiper disk. We also develop some trial background zodiacal cloud models in this chapter, but we find that further development of a background zodiacal cloud model is needed.

1.3 Numerical Integrations

We use the numerical integrator RADAU (Everhart 1989) to study the evolution of particles in resonance. RADAU is a very accurate integration code which

employs the Runge-Kutta method with Gauss-Radau spacings. RADAU is also very flexible, allowing the introduction of additional forces. Most of our runs have 249 particles, giving an accuracy in the estimate of the number of particles in resonance of $\sim \sqrt{N_r}/N_r$, where N_r is the number of particles in resonance. In order to decrease the error, we increase the total number of particles to 1017 for a small number of runs. Our integrations are run for 250,000 years and the orbital elements of the particles are output every 100 years. The integrator includes Poynting-Robertson drag, solar wind drag, radiation pressure, and the effects of the gravitational perturbations of seven planets (Mercury and Pluto are excluded). In addition, we also consider the effect of the Lorentz force and the effect of neutral interstellar gas drag in certain runs. The numerical simulations and their analytical interpretation are discussed in Chapter 4.

1.4 Objective of this Dissertation

The objective of this dissertation is to study the connection between structure in circumstellar disks and the presence of planets, focusing on asymmetries in the zodiacal cloud and the Kuiper disk. Chapter 2 will cover introductory material, namely a brief overview of secular perturbation theory, mean motion resonances, and a discussion of the forces on a dust particle. Structure in the zodiacal cloud, namely the warp and offset of the cloud, are linked to the presence of planets in this dissertation using secular perturbation theory. COBE observations of the warp and COBE and ISO observations of the offset and are discussed in Chapter 3.

Resonant structure in the hypothetical Kuiper disk is discussed at length in Chapters 4 and 5. In Chapter 4, we present the results of one of the first detailed studies of the resonant structure in the Kuiper disk. In the other prominent trapping study by Liou and Zook (1999), particles were initially located outside the 3:2 resonance and allowed to evolve in to the resonance by means of Poynting-Robertson

drag. In contrast, in this dissertation the particles are generated by bodies already inhabiting the 3:2 mean motion resonance, which is a more likely scenario. The dynamical evolution of the particles in the disk is followed from source to sink with Poynting-Robertson light drag, solar wind drag, radiation pressure, the Lorentz force, neutral interstellar gas drag, and the effects of planetary gravitational perturbations included. None of the published studies to date have included both the Lorentz force and the effect of neutral interstellar gas drag, which are important for the region of the Kuiper belt. From our numerical integrations, we determine what percentage of particles remain in the 3:2 resonance for a variety of particle and source body sizes.

In Chapter 5, we conduct a search in the COBE data for far-infrared emission from the postulated Kuiper dust disk, which is predicted to be, at most, a few percent of the brightness of the zodiacal cloud from COBE upper limits (Dermott et al. 1999, Backman et al. 1995). An accurate model of the warm background zodiacal component must be subtracted from the COBE data, possibly leaving residuals due to the cold Kuiper disk which could be viewed at wavelengths $\geq 60\mu m$. Kelsall et al. (1998) claim to have such a model of the total zodiacal cloud which includes the dust bands, the background zodiacal cloud, and the resonant ring. However, all of these models have fatal flaws, making the objective of obtaining accurate residuals which may contain the signature of the Kuiper disk presently unattainable. Our conclusion is that all of the Kelsall et al. (1998) zodiacal cloud models must be replaced with dynamical models. We are able to use two dynamical models: the dust band model (Grogan et al. 2001) and the resonant ring model (Jayaraman et al. 1995). However, the most important model, the background zodiacal cloud model, is still incomplete, mainly because an accurate background zodiacal cloud model necessitates the inclusion of large particles (100 - 500 μm), the dynamics of which are relatively unknown and in need of further study. We conclude that

a dynamical two-component (both inner and outer) zodiacal cloud model must be created to complete the search for the resonant signature of the Kuiper disk.

In an effort to connect our work on the zodiacal cloud and the Kuiper belt with dust disks around other potential exo-solar systems, we undertake a survey of nearby Sun-like stars in the sub-millimeter regime and present our results in Chapter 6. We obtain upper limits on the flux around ten Vega-type stars using the Sub-millimeter Telescope Observatory in the 870 μm and 1300 μm wave bands, which will be used to determine the most promising candidates for future observations. Finally, the conclusions of this dissertation and recommended future work are discussed in Chapter 7.

CHAPTER 2
DYNAMICS OF DUST IN CIRCUMSTELLAR DISKS

A body, such as an asteroid or dust particle, orbiting a star possessing a planetary system is subject to three types of gravitational perturbations due to planets in the system: long-period or secular perturbations, resonant perturbations, and gravitational scattering by the planets. In addition, for dust particles $\leq$ 500-1000 μm in diameter, non-gravitational forces must also be considered. This chapter addresses secular perturbations and resonant perturbations as well as several non-gravitational forces: radiation pressure, Poynting-Robertson light drag, solar wind drag, the Lorentz force, and neutral interstellar gas drag. Different combinations of these forces are included in the dynamical models and numerical integrations throughout this thesis. The Yarkovsky force and the effect of collisions are also briefly discussed but are not included in the models.

2.1 Forces on a Dust Particle

The orbit of a particle or a planet can be described by a set of six osculating elements: the semi-major axis (a), eccentricity (e), inclination of the orbit to a reference plane (I), longitude of ascending node (Ω), longitude of pericenter ($\tilde{\omega}$), and the mean longitude (λ). The forces below are calculated for the case of the solar system, but it is trivial to derive expressions for an exo-solar system case. In general, forces on a dust particle can be separated into two categories: gravitational and non-gravitational forces. The gravitational forces will be discussed in more detail in subsequent sections on secular perturbation theory and mean motion resonances.

2.1.1 Gravity

The force of gravity, F_{grav}, can be written as

$$F_{grav} = -\frac{GMm}{r^2}\hat{r} \tag{2.1}$$

where G = 6.67 x 10^{-11} N m^2/kg^2 is the gravitational constant, M is the mass of the Sun ($M_\odot$ = 1.99 x 10^{30} kg) or, in general, the central star, r is the heliocentric distance and m is the mass of an individual dust particle. For a spherical particle with radius s and density ρ in cgs units, the force of gravity can be written as

$$F_{grav} = \frac{4\pi s^3 \rho\, GM}{3\, r^2}\hat{r}. \tag{2.2}$$

In addition, there are several non-gravitational forces on particles that must be taken into account: radiation pressure, Poynting Robertson light drag, solar wind corpuscular drag, the Lorentz force, and the effects of neutral interstellar gas drag. Another drag force, the Yarkovsky effect, typically only affects large bodies on the order of a meter in diameter. Since our studies only encompass small micron sized particles, we can omit the Yarkovsky effect from the following discussion.

2.1.2 Radiation Pressure

Particles are affected by photons streaming out from the Sun. These photons act on the particles, producing a repulsive force known as the radiation pressure force, F_{rad}.

$$F_{rad} = \frac{S_o A Q_{pr}}{r^2 c}\hat{r} \tag{2.3}$$

where S_o = 1.36 x 10^6 ergs cm^{-2} sec^{-1} is the solar constant, A is the geometrical cross section of the particle, Q_{pr} is the efficiency factor for radiation pressure, r is radial distance from the Sun and c is the speed of light (Burns et al. 1979, Gustafson 1994). A dimensionless quantity, β, is used to describe radiation pressure. It is defined as the ratio of the radiation pressure force to the force of gravity: $\beta = F_{rad}/F_{grav}$. Using

equations 2.2 and 2.3, β can be written

$$\beta = \frac{5.7 \times 10^{-5} Q_{pr}}{\rho s} \tag{2.4}$$

where Q_{pr} is averaged over the solar spectrum (Burns et al. 1979). Assuming a constant density and a value for Q_{pr} (usually calculated from Mie theory), a value for β can be calculated for a given particle size. If we combine the forces of gravity and radiation pressure, the resulting total force on the particle is

$$F = -\frac{G(1-\beta)Mm}{r^2}\hat{r} \tag{2.5}$$

which means that when a particle is acted upon by radiation pressure, it "feels" a less massive sun by a factor of (1 - β).

2.1.3 Poynting Robertson Light Drag

When a particle absorbs incident radiation from the Sun, it re-radiates it isotropically in the particle's rest frame. However, since the particle is moving with respect to the Sun, according to special relativity the particle does not re-radiate the energy flux isotropically in the rest frame of the Sun. The particle re-radiates more energy in the direction of its velocity than in the opposite direction, causing a loss of momentum. Since the mass of the particle is constant, this loss of momentum translates into a deceleration of the particle, resulting in a net drag on the particle. The drag effect is referred to as Poynting Robertson light drag (Poynting 1903, Robertson 1937, Burns et al. 1979). The loss of momentum causes the particle to move to a lower orbit, resulting in the particle slowly spiraling into the Sun over a period of time called the Poynting Robertson drag lifetime (Burns et al. 1979). The PR drag lifetime is denoted by

$$\tau_{pr} = \frac{L_\odot}{L_\star}\left[\frac{s\,\rho\,a^2}{3 \times 10^{-4} < Q_{pr} >}\right] \tag{2.6}$$

where $L_\odot$ and $L_\star$ are the luminosities of the Sun and the star which the particle is orbiting, respectively, τ_{pr} is given in years, the particle radius, s, is in microns, the

particle density, ρ, is in g/cm^3 and the particle semi-major axis, a, is in AU (Roques et al. 1994). In the geometrical optics case, $< Q_{pr} >$, the radiation pressure efficiency factor can be set equal to one for particles with radii ≥ 1 μm (Burns et al. 1979). To the first order in v/c, the total radiation force (radiation pressure force combined with Poynting Robertson light drag) acting on a spherical particle is

$$|F_{grav}|\beta \left[1\hat{r} - (2\dot{r}/c)\hat{r} - (r\dot{\theta}/c)\hat{\theta}\right] \tag{2.7}$$

where the unit vector $\hat{\theta}$ is normal to $\hat{r}$ in the orbital plane (Burns et al. 1979, Klacka 1992, Gustafson 1994). The first term is the radiation pressure force already discussed above. The second term is due to the Doppler shift. Both the second and third terms are what is known as Poynting Robertson light drag, or PR drag. The change in orbital elements due to PR drag can be calculated. Since PR drag is a radial force, the inclination and the ascending node are not affected and the change in longitude of perihelion is negligible for small eccentricities. The equations for da/dt and de/dt, the changes in semi-major axis and eccentricity with respect to time, were originally derived by Robertson (1937), then later by Wyatt and Whipple (1950), and finally and more completely by Burns et al. (1979) using special relativity transformations. Presented here are the equations in the form given by Wyatt and Whipple (1950):

$$\frac{da}{dt} = -\frac{\alpha_{pr}\beta}{a}\frac{(2+3e^2)}{(1-e^2)^{3/2}} \tag{2.8}$$

$$\frac{de}{dt} = -\frac{5\alpha_{pr}\beta}{2a^2}\frac{e}{(1-e^2)^{1/2}} \tag{2.9}$$

$$\frac{dI}{dt} = 0 \tag{2.10}$$

where $\alpha_{pr} = GM/c$. Combining equations 2.8 and 2.9 gives the change in eccentricity corresponding to a change in semi-major axis

$$\frac{de}{da} = \frac{5e}{2a}\frac{(1-e^2)}{(2+3e^2)}. \tag{2.11}$$

2.1.4 Solar Wind Corpuscular Drag

Another non-gravitational force acting on dust particles is the force due to solar wind corpuscular drag, F_{sw}, which is caused by solar wind protons streaming out from the Sun and impacting the particles in their paths. F_{sw} is analogous to the total radiation force given in equation 2.7. We can define a β_{sw} to be equal to F_{sw}/F_{grav}. Taking v_{sw} to be the solar wind speed, we can write the solar wind force as

$$F_{sw} = |F_{grav}|\beta_{sw}\left[1\hat{r} - (2\dot{r}/v_{sw})\hat{r} - (r\dot{\theta}/v_{sw})\hat{\theta}\right] \tag{2.12}$$

which has the same form as equation 2.7 (Gustafson 1994). We can approximate the solar wind drag force as being roughly 1/3 the value of the total radiation force given in equation 2.7

2.1.5 Lorentz Force

Interplanetary dust particles are charged and as a result are coupled to the solar wind driven interplanetary magnetic field. The particles acquire a charge by a variety of methods: photo-emission of electrons from the absorption of ultraviolet (UV) solar radiation and the accretion of solar wind electrons and solar wind protons which are in the path of the dust particles. It is predicted that under normal conditions, photo-emission dominates over the accretion of solar wind particles, giving the dust particles a net positive potential, U, of ≈ 5 V (Goertz 1989, Gustafson 1994). This potential is independent of distance since solar wind density follows an approximate $1/r^2$ decrease in density (Leinert and Grün 1990), and it corresponds to a charge q=$4\pi\epsilon_o U$ s on a spherical particle where $\epsilon_o = 8.859$ x 10^{-12} C V^{-1} m^{-1}. The electromagnetic force exerted on the particle by the interplanetary magnetic field, $\vec{B}$, can be written as

$$\vec{F}_L = q\vec{v} \times \vec{B} \tag{2.13}$$

where $\vec{v}$, the velocity with respect to this field, can be broken down into components $\vec{v}_g$, the heliocentric velocity of the particle, and $\vec{v}_{sw}$, the solar wind velocity:

$$\vec{F}_L = q(\vec{v}_g \times \vec{B} - \vec{v}_{sw} \times \vec{B}) \tag{2.14}$$

This is the classical representation of the Lorentz Force. The second term in the above equation is independent of the particle's motion and can be viewed as resulting from an induced electric field. Gustafson and Misconi (1979) and more recently Grogan et al. (1996) modeled the magnetic field, utilizing the expanding solar corona model of the solar magnetic field (Parker 1958). In Parker's model, the gas flowing outward from the solar corona draws out the solar magnetic field lines as the Sun rotates, so that close to the Sun the field is approximately radial, but farther from the sun the field lines form an Archimedean spiral (Grogan et al. 1996, Gustafson 1994). In the following equations, B_o is the magnetic field strength at some reference distance, b ($B_o \sim 3$ nT), ω is the angular velocity of the Sun ($\omega \approx 2.7 \times 10^{-6}$), r is radial distance from the Sun, ϕ is the azimuth angle, and θ is the heliocentric colatitude angle. The solar wind velocity, v_{sw}, is taken to be 400 km/s.

$$B_r = \frac{B_o}{r^2} \tag{2.15}$$

$$B_\phi = \frac{-B_o \omega b^2 (r-b) sin(\theta)}{v_{sw} r^2} \tag{2.16}$$

$$B_\theta = 0 \tag{2.17}$$

The above equations are derived using the velocity of the gas flowing out from the sun, v, where $v_r = v_{sw}$, $v_\phi = \omega(r-b)sin(\theta)$, and $v_\theta = 0$ (Parker 1958).

2.1.6 Neutral Interstellar Gas Drag

This last force, while small in magnitude, acts from a specific direction and can cause noticeable effects on the orbits of dust particles over a large period of time. The solar system inhabits a "Local Bubble" in the local interstellar medium (LISM)

consisting of hot plasma (10^6 K) of very low density (5×10^{-3} cm^{-3}) that spans roughly 100 parsecs (pc). It is thought that this void was created by a supernova explosion (Gehrels and Chen 1993, Grün et al. 1994). Within the Local Bubble lies the "Local Fluff", consisting of several clouds a few pc wide having higher densities and cooler temperatures than those of the Local Bubble, and within the Local Fluff lies our solar system. The cloud in which the Sun resides has a temperature of 10^4 K and a density of 0.1 H atoms cm^{-3} (Bertin et al. 1993, Grün et al. 1994). The interaction of the solar wind with the LISM causes a cavity to form which extends out to approximately 100 AU and is termed the heliosphere. Inside the heliosphere only neutral gas atoms, primarily hydrogen, reach the planetary system since interstellar ions are removed from the solar system by the solar wind (Geiss et al. 1994, Gloeckler et al. 1993, Grün et al. 1994).

The Ulysses spacecraft has detected a stream of interstellar helium, a tracer of hydrogen, originating from an ecliptic longitude of 252° and an ecliptic latitude of +2.5° moving with a speed of 26 km/s (Witte et al. 1993, Grün et al. 1994), which is in good agreement with direction of motion of the local cloud in which the Sun is embedded with respect to the solar system (Bertin et al. 1993). These neutral gas atoms can collide with dust grains in the solar system, causing a change in the momentum of the dust particles. While the effects of one collision are negligible, over a period of time repeated collisions have the potential to alter the orbital elements of the dust particle significantly (Gustafson personal communication, Scherer 2000).

For a spherical dust grain with radius, s, mass, m, and velocity, v, the drag force, F_H, on the dust particle due to collisions with neutral interstellar hydrogen particles of mass, m_H, moving with a velocity, v_H, can be written as

$$F_H = -N\, m_H\, u\, \hat{u} \tag{2.18}$$

where $\vec{u} = \vec{v} - \vec{v_H}$, $u = |\vec{v} - \vec{v_H}|$, $\hat{u}$ is the unit vector in the u direction, and N, the average number of collisions of hydrogen atoms on a dust particle of collisional cross

sectional area, σ, per unit time is defined as

$$N = n_H \, \sigma \, u \, C_D \tag{2.19}$$

where n_H is the number density of hydrogen atoms, $\sigma = \pi s^2$ where s is the radius of the dust particle, and C_D is the free molecular drag coefficient due to hydrogen atoms in a Maxwellian velocity distribution of temperature T_H impacting a spherical dust particle (Gustafson personal communication, Scherer 2000), where $T_H \sim 8000K$. Substituting equation 2.19 into equation 2.18 gives

$$F_H = -n_H \, \pi \, s^2 \, m_H \, |\vec{v} - \vec{v_H}|^2 \, C_D \, \hat{u} \tag{2.20}$$

where the numerical values of the constants are as follows: n_H = 0.1 H atoms/cm^3, s is a range of sizes which will be discussed in Chapter 4, m_H = 1.675 x 10^{-24} g, the particle velocity, v, is calculated at each time step in numerical integrations, v_H is 26 km/s, and C_D, which is a unitless constant defined below, is $\sim$ 1-2 (Gustafson personal communication). C_D can be written

$$C_D = \frac{2S^2+1}{\sqrt{\pi}S^3} e^{-S^2} + \frac{4S^4+4S^2-1}{2S^4} \, erf(S) \tag{2.21}$$

$$+ \frac{2(1-\varepsilon)\sqrt{\pi}}{3S} \left(\frac{T_d}{T_H}\right)^{1/2} \left(1 + Y_H \frac{m}{m_H}\right) \tag{2.22}$$

where the Mach number $S = u/c_H$ ($10 \lesssim S \lesssim 15$) and the sound speed $c_H = \sqrt{2kT_H/m_H}$. T_H is the temperature of the hydrogen atoms, T_d is the temperature of the dust grains, k is Boltzmann's constant, and $erf(S)$ is the error function which can be assumed to equal 1 (Gustafson 1994, Scherer 2000). The third term in equation 2.22 takes into account the specular reflection of the hydrogen atoms (ε is the fraction of the atoms which are specularly reflected) and sputtering, the process by which a dust grain is eroded by hydrogen atoms striking its surface. If Y_p, the sputtering yield, is equal to zero (i.e., in the no sputtering case) and $T_d \ll T_H$, then the third term can be neglected (Gustafson 1994), which is the case considered in

this dissertation. Then, equation 2.22 can be written in such a way as to include an adsorption or sticking factor ξ ($1 \leq \xi \leq 2$) which describes the type of collision considered:

$$C_D = \frac{\xi}{2}\left[\frac{2S^2+1}{\sqrt{\pi}S^3}e^{-S^2} + \frac{4S^4+4S^2-1}{2S^4}\,erf(S)\right] \tag{2.23}$$

A ξ of 1 corresponds to either specular or diffuse collisions and $1 < \xi \leq 2$ corresponds to adsorption (Scherer 2000). When ξ is 2, equation 2.23, is equivalent to the first two terms of equation 2.22. The value of C_D varies with the type of collision which is assumed to occur, so in this dissertation a range of values will be used: $C_D = 1$ and $C_D = 2$. Detailed analysis and the results of numerical integrations of dust particles will be presented in Chapter 4.

2.1.7 Other Processes: The Yarkovsky Effect and Collisions

The Yarkovsky Force

The Yarkovsky effect is due to the non-uniform heating of a rotating dust grain. The warm evening side of the grain radiates more thermal energy than the cool morning side of the grain. In the large particle approximation (Burns et al. 1979), which applies to particles with diameters larger than $\sim 3.4\ \mu m$, the Yarkovsky force, F_Y, on a particle with heat capacity, C, density, ρ, and thermal conductivity, K, is expressed as the ratio of the Yarkovsky force to the force due to PR drag, F_{pr}:

$$\frac{F_Y}{F_{pr}} = \frac{W\sqrt{P}\sin\xi}{r\sqrt{K\,\rho\,C}} \tag{2.24}$$

where W is a constant given by Burns et al. (1979): $W = 1.31 \times 10^7\ ergs\ \text{AU}\ sec^{-1}\ K^{-1}\ cm^{-2}$. The spin period of the particle is P and it is assumed that the particle spins about an axis that makes an angle ξ to the solar direction (Gustafson 1994). According to Gustafson (1994), for a 20 μm diameter dust grain at r AU, $\frac{F_Y}{F_{pr}} \sim$ r 10^{-2} AU. It is not until we reach particles of $\sim 2\ cm$ in diameter that $\frac{F_Y}{F_{pr}} \sim 1$ for an r of 1 AU. For the small particles considered in this thesis ($\lesssim 100\ \mu m$), we can neglect the Yarkovsky force.

Collisions

Collisions between dust particles will also affect some dust particles. For small particles ($\lesssim$ 100 μm) in the asteroid belt, collisions are not important since their collisional lifetimes are much longer than their PR drag lifetimes. Leinert and Grün (1990) estimate the average impact speed between two dust particles as

$$< v(r) >= v_0 \left(\frac{r}{r_0} \right)^{-0.5} \tag{2.25}$$

where $v_0 = 20\ km/s$ at $r_0 = 1$ AU. The rate $C(m,r)$ of catastrophic collisions, collisions which result in the fragmentation of both particles, is given by

$$C(m,r) = \int_{m/\gamma(v(r))}^{\infty} \sigma\, n(m_p,r)\ < v(r) >\ dm_p \tag{2.26}$$

where σ is the the cross sectional area inside the circle where the two particles touch, m_p is the mass of the projectile, $n(m_p,r)$ is the number density of particles of mass m at heliocentric distance r, and $\gamma(v(r))$ is defined by

$$m_p \geq \frac{1}{\gamma(v(r))}\, M_t \tag{2.27}$$

where M_t is the mass of the target particle (Leinert and Grün 1990). The collisional lifetime of a particle is defined as

$$\tau_c = \frac{1}{C(m,r)} \tag{2.28}$$

the reciprocal of the rate of catastrophic collisions (Leinert and Grün 1990). So, roughly speaking, $n(m_p,r) \sim r^{-3}$, $< v(r) > \sim r^{-0.5}$, so $C(m,r) \sim r^{-3.5}$ making $\tau_c \sim r^{3.5}$. The PR drag lifetime only goes as $\tau_{pr} \sim a^2 \sim r^2$. Since the collisional lifetime at heliocentric distance r is a steeper function of r than the PR drag lifetime, we can make the assumption that the collisional lifetime of particles at r is longer than their PR drag lifetime. We can assume that collisions can be neglected for small particles at a distance r from the Sun. However, we know that collisions do become important for particles larger than $\sim$ 100 μm in diameter (Gustafson et al. 1992) and will need to be considered in future work.

2.2 Secular Perturbation Theory

Whether we are modeling the zodiacal cloud, the Kuiper belt, or planetary debris disks around other stars, secular perturbation theory is a powerful tool for interpreting asymmetries in dust disks. In this chapter we briefly introduce the theory of secular perturbations which is the classical method used to study the long-term orbital evolution of both planets and minor planets or dust particles in planetary systems. In Chapter 3, we discuss the applications of low-order secular perturbation theory to a simple three-body system, analogous to a system composed of a central star and two perturbers having a non-zero mutual inclination, I_{mutual}.

The orbit of a particle or a planet can be described by a set of six osculating, or instantaneous, elements: the semi-major axis (a), eccentricity (e), inclination (I), longitude of ascending node (Ω), longitude of pericenter ($\tilde{\omega}$), and the mean longitude (λ). Secular perturbation theory is the classical way to study the long-term rates of change of orbital elements of small bodies in planetary systems, provided there are no mean motion resonances, orbits do not overlap, and the eccentricities and inclinations of all the objects in the system are small (Brouwer and Clemence 1961 and Murray and Dermott 1999). The long-term variations of e, $\tilde{\omega}$, I, and Ω of a small body are largely determined by the terms in its disturbing function which are independent of the mean longitudes of any of the objects involved. These terms are called the secular terms. We can use secular perturbation theory to study a system of n planetary perturbers and a dust particle (or point mass minor planet, such as an asteroid or Kuiper Belt object) orbiting a central star. Let us assume that the test particle has unsubscripted osculating elements ($a, e, I, \tilde{\omega}, \Omega, \lambda$) and mean motion, n, and the j^{th} planet has osculating elements ($a_j, e_j, I_j, \tilde{\omega}_j, \Omega_j, \lambda_j$) and mass, m_j. Assuming e and I are small, the disturbing function to second order in e and I

describing the perturbations on the orbit of the dust particle can be written

$$R = na^2\left[\frac{1}{2}Ae^2+\sum_{j=1}^{n}A_j e e_j\cos(\tilde{\omega}-\tilde{\omega}_j)+\right. \tag{2.29}$$

$$\left.\frac{1}{2}BI^2+\sum_{j=1}^{n}B_j I I_j\cos(\Omega-\Omega_j)\right]$$

where

$$A = +n\frac{1}{4}\sum_{j=1}^{n}\frac{m_j}{m_\star}\alpha_j\bar{\alpha}_j b_{3/2}^{(1)}(\alpha_j) \tag{2.30}$$

$$A_j = -n\frac{1}{4}\frac{m_j}{m_\star}\alpha_j\bar{\alpha}_j b_{3/2}^{(2)}(\alpha_j)$$

$$B = -n\frac{1}{4}\sum_{j=1}^{n}\frac{m_j}{m_\star}\alpha_j\bar{\alpha}_j b_{3/2}^{(1)}(\alpha_j)$$

$$B_j = +n\frac{1}{4}\frac{m_j}{m_\star}\alpha_j\bar{\alpha}_j b_{3/2}^{(1)}(\alpha_j)$$

where $\alpha_j = a_j/a$ if $a_j < a$ and $\alpha_j = a/a_j$ if $a_j > a$ and, similarly, $\bar{\alpha}_j = 1$ if $a_j < a$ and $\bar{\alpha}_j = a/a_j$ if $a_j > a$. The mass of the central star is $m_\star$ and we are assuming the dust particle is sufficiently large so that radiation pressure can be neglected in this discussion (i.e., $\beta = F_{rad}/F_{grav} = 0$). The Laplace coefficients, $b_{3/2}^{(1)}$ and $b_{3/2}^{(2)}$, are defined as

$$b_{(i+1/2)}^{(j)}(\alpha_j) = \frac{1}{\pi}\int_0^{2\pi}\frac{\cos(j\psi)\,d\psi}{(1-2\,\alpha\,\cos(\psi)+\alpha^2)^{(i+1/2)}}. \tag{2.31}$$

for the general case. The evolution of a planetary system can be studied using Lagrange's planetary equations which describe the rates of change of the osculating elements. Defining G, m and R to be the universal gravitational constant, the mass of a given dust particle, and the disturbing function where

$$n^2a^3 = G(m_\star+m) \tag{2.32}$$

$$\lambda \equiv \epsilon+\int n dt$$

we can write the Lagrange's planetary equations as

$$\frac{da}{dt} = \frac{2}{na}\frac{\partial R}{\partial \lambda} \tag{2.33}$$

$$\frac{de}{dt} = -\frac{\sqrt{1-e^2}}{na^2 e}\left(\left(1-\sqrt{1-e^2}\right)\frac{\partial R}{\partial \lambda} - \frac{\partial R}{\partial \tilde{\omega}}\right) \tag{2.34}$$

$$\frac{dI}{dt} = \frac{-\tan(I/2)}{na^2\sqrt{1-e^2}}\left(\frac{\partial R}{\partial \lambda} + \frac{\partial R}{\partial \tilde{\omega}}\right) - \frac{1}{na^2\sqrt{1-e^2}\,\sin I}\frac{\partial R}{\partial \Omega} \tag{2.35}$$

$$\frac{d\Omega}{dt} = \frac{1}{na^2\sqrt{1-e^2}\,\sin I}\frac{\partial R}{\partial I} \tag{2.36}$$

$$\frac{d\tilde{\omega}}{dt} = \frac{\sqrt{1-e^2}}{na^2 e}\frac{\partial R}{\partial e} + \frac{\tan(I/2)}{na^2\sqrt{1-e^2}}\frac{\partial R}{\partial I} \tag{2.37}$$

$$\frac{d\epsilon}{dt} = \frac{-2}{na}\frac{\partial R}{\partial a} + \frac{\sqrt{1-e^2}\,(1-\sqrt{1-e^2})}{na^2 e}\frac{\partial R}{\partial e} + \frac{\tan(I/2)}{na^2\sqrt{1-e^2}}\frac{\partial R}{\partial I} \tag{2.38}$$

In order to avoid singularities that arise in Lagrange's planetary equations for small eccentricities and inclinations, we define four variables h, k, p, and q to replace e, $\tilde{\omega}$, I, and Ω.

$$h = e\sin\tilde{\omega} \qquad k = e\cos\tilde{\omega}$$

$$p = I\sin\Omega \qquad q = I\cos\Omega$$

Likewise, we define a similar set of four variables h_j, k_j, p_j, and q_j (j = 1,n) for each perturbing body and the disturbing function becomes

$$R = na^2\left[\frac{1}{2}A(h^2+k^2) + \sum_{j=1}^{n} A_j(h_j h + k_j k)\right. \tag{2.39}$$

$$\left. + \frac{1}{2}B(p^2+q^2) + \sum_{j=1}^{n} B_j(p_j p + q_j q)\right]$$

To simplify the presentation, from here onward only the p and q equations are discussed. The equations in h and k follow a similar derivation. The Lagrangian equation of motion for p and q is

$$\dot{p} = +\frac{1}{na^2}\frac{\partial R}{\partial q} \qquad \dot{q} = -\frac{1}{na^2}\frac{\partial R}{\partial p} \tag{2.40}$$

Substituting for R from Equation (2.39) we can rewrite the above equation as

$$\dot{p} = +Bq + \sum_{j=1}^{n} B_j q_j \qquad \dot{q} = -Bp - \sum_{j=1}^{n} B_j p_j$$

Substituting for q_j and p_j defined below from a similar derivation

$$p_j = \sum_{i=1}^{n} I_{ji} \sin(f_i t + \gamma_i) \qquad q_j = \sum_{i=1}^{n} I_{ji} \cos(f_i t + \gamma_i) \tag{2.41}$$

$$\dot{p} = +Bq + \sum_{j=1}^{n} B_j \sum_{i=1}^{n} I_{ji} \cos(f_i t + \gamma_i) \tag{2.42}$$

$$\dot{q} = -Bp - \sum_{j=1}^{n} B_j \sum_{i=1}^{n} I_{ji} \sin(f_i t + \gamma_i)$$

Taking a second time derivative of Equation (2.42) and then making appropriate substitutions from (2.42) we have

$$\ddot{p} = -B^2 p - \sum_{i=1}^{n} \mu_i (B + f_i) \sin(f_i t + \gamma_i) \tag{2.43}$$

$$\ddot{q} = -B^2 q - \sum_{i=1}^{n} \mu_i (B + f_i) \cos(f_i t + \gamma_i)$$

$$\mu_i = \sum_{j=1}^{n} B_j I_{ji}$$

The solutions to the uncoupled differential equations in (2.43) are

$$p = I_{proper} \sin(Bt + \gamma) + p_0(t) \qquad q = I_{proper} \cos(Bt + \gamma) + q_0(t) \tag{2.44}$$

where I_{proper} and γ are constants determined from the boundary conditions and, more importantly,

$$p_0(t) = -\sum_{i=1}^{n} \frac{\mu_i}{(B - f_i)} \sin(f_i t + \gamma_i) \tag{2.45}$$

$$q_0(t) = -\sum_{i=1}^{n} \frac{\mu_i}{(B - f_i)} \cos(f_i t + \gamma_i)$$

Similar equations follow for $h_0(t)$ and $k_0(t)$ (Murray and Dermott 1999). If we define the quantities

$$e_{forced} = \sqrt{h_0^2 + k_0^2} \qquad I_{forced} = \sqrt{p_0^2 + q_0^2} \tag{2.46}$$

the solutions given in Equation 2.44 have a simple geometric interpretation which is illustrated in Figure 2-1. The osculating, or instantaneous, inclination traces out a circle in the $p - q$ plane that can be thought of as having a center (q_0, p_0) and radius, I_{proper} in the $p - q$ plane. The center of the circle is governed by the forced elements while the proper elements precess about the center in the clockwise direction (counter-clockwise for eccentricity and argument of pericenter) at a rate B, which is equal to $\dot{\Omega}_{proper}$. Note that in the case of a system with only one perturber, the forced elements of the particle would be constant with time (Murray and Dermott 1999).

As demonstrated above, low-order secular perturbation theory allows the osculating elements, eccentricity (e), inclination (I), longitude of ascending node (Ω), and longitude of pericenter ($\tilde{\omega}$), to be decomposed into proper and forced elements. The assumptions for the low-order theory are that (1) no mean motion resonances are involved, (2) there is no overlap of orbits, and (3) the eccentricities and inclinations of the objects in the system are small enough so that a second-order expansion of the disturbing function is sufficient to describe the system.

The proper elements, which represent the stable long-term averages after the effects of planetary perturbations have been removed, are dependent on initial conditions and denote fundamental orbital parameters of the particle. These parameters

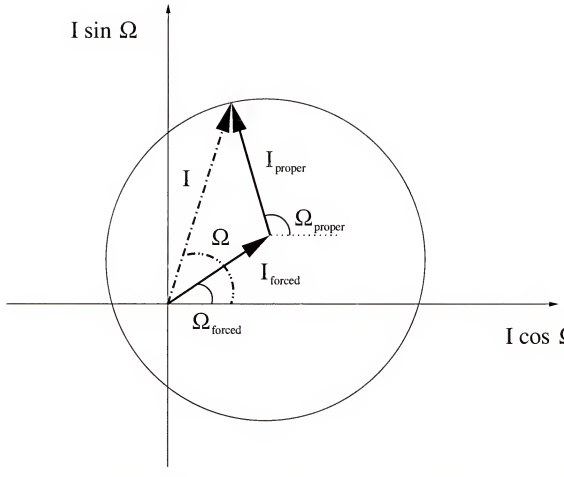

Figure 2-1: Decomposition of osculating elements into forced and proper elements.

can link the particle to an asteroid family. Lastly, it is important to note that the perturbations on a particle's orbit serve to precess both the longitude of ascending node (Ω) and longitude of pericenter ($\tilde{\omega}$) so that on secular time scales the distributions of these proper elements become effectively random.

Conversely, the forced elements are imposed on the particle's orbit by the gravitational perturbations of the planets. These perturbations can be characterized as (1) secular (i.e, long period), (2) transient, and (3) resonant (i.e., short period). The forced elements depend solely on the secular solution of the perturbers in the system and on the particle's semi-major axis, a, which changes due to drag forces in the system (Murray and Dermott 1999). As discussed in the previous section, the

principal drag forces are radiation pressure, Poynting-Robertson light drag, and solar wind or corpuscular drag.

2.3 Mean Motion Resonances

2.3.1 Physics of Resonance

We briefly summarize the discussion of Murray and Dermott (1999) on the physics of objects in resonance. We consider two objects orbiting a central star, in the case where the object of negligible mass is on an external, eccentric orbit and the inner object is on a circular orbit in the same plane as the particle. We consider that the objects are in a mean motion resonance such that conjunctions always occur at the same latitude. If the conjunctions always occur at pericenter or apocenter, then the tangential force that the particle experiences immediately before conjunction is equal and opposite to the tangential force the particle experiences immediately after conjunction, resulting in a zero net tangential force. Only a tangential force can change the angular momentum of a particle in orbit. If conjunctions occur at either apocenter or pericenter then a tangential force is required to change the particle's semi-major axis. Thus, if a particle having a conjunction at pericenter or apocenter experiences a zero net tangential force, the particle's semi-major axis stays constant and the particle is in resonance. For an external resonance, the case discussed here, conjunctions at the particle's apocenter give the stable configuration. If, however, the conjunction of the particle occurs at some other point on the orbit, the tangential force experienced by the particle causes subsequent conjunctions to occur closer to apocenter, until the particle's conjunction occurs at apocenter and the particle is in resonance (Peale 1976, Greenberg 1977, Peal 1986, Murray and Dermott 1999).

2.3.2 Dynamics of Resonance

Consider two objects moving around a large, central mass in circular, coplanar orbits. The outer object (primed) is said to move in resonance with the inner object,

if their mean motions, n' and n, respectively, can be related as

$$\frac{n}{n'} = \frac{p+q}{p} \tag{2.47}$$

where p and q are integers, q denoting the order of the resonance. Since the mean motion can be related to the semi-major axis by $\mu_\odot = GM_\odot = n^2a^3$, the following relation can be written

$$a' = a\left(\frac{p+q}{p}\right)^{2/3}. \tag{2.48}$$

Following the derivations given in Dermott et al. (1988), Weidenschilling and Jackson (1993), Jayaraman (1995), and Murray and Dermott (1999), if we consider only the resonant terms, the perturbing force on a particle due to a planet can be written as a series expansion in the orbital elements of the planet (a, e, I Ω, $\tilde{\omega}$, λ) and the particle (a', e', I', Ω', $\tilde{\omega}'$, λ'):

$$R'_{res} = \mu \sum S'(a, e, I, a', e', I') \cos\varphi \tag{2.49}$$

where $\mu = GM$, G is the gravitational constant, and M is the mass of the planet. The strength of the resonance, S', the strength of an individual term in the series, can be written $S' = S'(\alpha, \sin I, \sin I', e, e')$ where $\alpha = (a/a')$. The general form of the resonant argument, φ, can be written

$$\varphi = j_1\lambda' + j_2\lambda + j_3\tilde{\omega}' + j_4\tilde{\omega} + j_5\Omega' + j_6\Omega \tag{2.50}$$

where $j_1 = (p+q)$, $j_2 = -q$, and the primed quantities denote those orbital elements of the exterior orbiting body and the unprimed quantities denote those of the interior body. Physically, the resonant argument can be thought of as the angular distance between the particle's perihelion and the longitude of conjunction of the particle with the planet. We will retain the primes in the subsequent discussion so that the orbital elements of the planet, in this case Neptune, will be denoted as (a_n, e_n, I_n Ω_n, $\tilde{\omega}_n$, λ_n) and those of the Plutinos and dust particles associated with the Plutinos as (a',

e', I', Ω', $\tilde{\omega}'$, λ'). This distinction is important to make since the disturbing functions are different for internal and external resonances, and so the derivation of libration width depends on whether the resonance is an interior or an exterior one. Also note that if $p = 1$, an extra term must be included in the disturbing function. However, since we are dealing with the 3:2 resonance, a $p = 2$ resonance, we need not include that term in our derivation.

2.3.3 First Order External Resonances

For exact first order external resonances $|j_3| = 1 = q$, and j_4, j_5, and j_6 are zero, giving

$$\varphi = (p+1)\lambda' - p\lambda_n - \tilde{\omega}' \tag{2.51}$$

if we take j_3 to be -1. More generally, we can write

$$\varphi = j_1\lambda' + j_2\lambda_n + j_3\tilde{\omega}' \tag{2.52}$$

Now we write the general term in the averaged expansion of the disturbing function, with both secular and resonant terms included. The first term on the right hand side is the secular term which depends on $f_{s,1}(\alpha)$. The second term is the resonant term and it is a function of $f_d(\alpha)$. Both $f_{s,1}(\alpha)$ and $f_d(\alpha)$ are functions of Laplace coefficients. The term containing $f_{s,1}(\alpha)$ will be eventually neglected, and accordingly, $f_{s,1}(\alpha)$ will not be defined here. For the 3:2 external mean motion with Neptune, the resonant argument is

$$\varphi = 3\lambda' - 2\lambda_n - \tilde{\omega}' \tag{2.53}$$

and the general expression for $f_d(\alpha)$ can be written as

$$f_d(\alpha) = \frac{1}{2}(-1 + 2j_1 + \alpha D)\, b_{1/2}^{(j_1-1)} \tag{2.54}$$

where, from Murray and Dermott (1999), D $\equiv$ d/dα is defined as

$$D b_s^{(j)} = s\left(b_{s+1}^{(j-1)} - 2\,\alpha\, b_{s+1}^{(j)} + b_{s+1}^{(j+1)}\right). \tag{2.55}$$

Values for $f_d(\alpha)$ for different resonances with Neptune are given in Tables 2-1 and 2-2. The sign of $f_d(\alpha)$ indicates the value at which φ is stable. If $f_d(\alpha) < 0$, the motion will be stable about $\varphi = 0$. If $f_d(\alpha) > 0$, the motion will be stable about $\varphi = \pi$. As can be seen from Tables 2-1 and 2-2, the latter case holds for first order exterior mean motion resonances and the stable point is about $\varphi = \pi$.

Table 2-1: Laplace coefficients for the β=0 no drag case for several important first order resonances in the Kuiper belt.

MMR (q)	j_1	j_2	j_3	j_4	j_5	j_6	$f_d(\alpha)$	$\alpha = (a_n/a')$	Laplace Coefficients $b_i^{(j)}(\alpha)$
3:2	3	-2	-1	0	0	0	$\frac{1}{2}[5+\alpha D]\, b_{1/2}^{(2)}$	0.7631428	$b_{1/2}^{(2)}$=0.6174491
(1)							=		$b_{3/2}^{(1)}$=12.084771
									$b_{3/2}^{(2)}$=10.485689
									$b_{3/2}^{(3)}$=8.8484109
2:1	2	-1	-1	0	0	0	$\frac{1}{2}[3+\alpha D]\, b_{1/2}^{(1)}$	0.6299605	$b_{1/2}^{(1)}$= 0.7568403843
(1)							=1.688310811		$b_{3/2}^{(0)}$= 6.058253849
									$b_{3/2}^{(1)}$=4.922561382
									$b_{3/2}^{(2)}$= 3.655435400

Laplace coefficients for the β=0 no drag case for several important first order resonances in the Kuiper belt. We calculate the Laplace coefficients as defined in Murray and Dermott (1999).

Now, we can write Equation 2.49 as

$$< R'_{res} >= \frac{GM_n}{a_n}\, \alpha \left(f_{s,1}(\alpha) e'^2 + f_d(\alpha) e'^{|j_3|} \cos(\varphi) \right) \tag{2.56}$$

where φ for the 3:2 resonance given by Equation 2.53. In most cases, the secular contribution is small so the contribution from the first term on the right hand side of

Table 2-2: Laplace coefficients for the β=0 no drag case for several important second order resonances in the Kuiper belt.

MMR (q)	j_1	j_2	j_3	j_4	j_5	j_6	$f_d(\alpha)$	$\alpha = (a_n/a')$	Laplace Coefficients $b_i^{(j)}(\alpha)$
6:4	6	-4	-2	0	0	0	$\frac{1}{8}[104 + 22\alpha D$	0.7631428	$b_{1/2}^{(4)}$= 0.2704376377
(2)							$+\alpha^2 D^2] b_{1/2}^{(4)}$		$b_{3/2}^{(3)}$= 8.830059041
							= 8.2452174		$b_{3/2}^{(4)}$= 7.319852836
									$b_{3/2}^{(5)}$= 5.994332420
									$b_{5/2}^{(2)}$=144.0722604
									$b_{5/2}^{(3)}$=133.3735430
									$b_{5/2}^{(4)}$=120.9249333
									$b_{5/2}^{(5)}$= 107.7889609
									$b_{5/2}^{(6)}$= 94.73545715
5:3	5	-3	-2	0	0	0	$\frac{1}{8}[67 + 18\alpha D$	0.7113787	$b_{1/2}^{(3)}$= 0.190599485
(2)							$+\alpha^2 D^2] b_{1/2}^{(3)}$		$b_{3/2}^{(2)}$= 6.698016985
							=4.7443175		$b_{3/2}^{(3)}$= 5.320969552
									$b_{3/2}^{(4)}$= 4.140804309
									$b_{5/2}^{(1)}$= 70.84706201
									$b_{5/2}^{(2)}$= 65.44595179
									$b_{5/2}^{(3)}$= 58.29300353
									$b_{5/2}^{(4)}$= 50.48635337
									$b_{5/2}^{(5)}$= 42.77082747

Laplace coefficients for the β=0 no drag case for several important second order resonances in the Kuiper belt. We calculate the Laplace coefficients as defined in Murray and Dermott (1999).

Equation 2.56 can be neglected, but we will retain the secular term in this derivation for completeness.

In Section 2.2, we stated Lagrange's equations which describe the variation of the orbital elements for a given perturbing potential. If we then substitute R'_{res} from Equation 2.56 into Lagrange's equations, the equations of motion become

$$\dot{n'} = 3\, j_1\, C'_r\, \alpha\, n'\, e'^{|j_3|} \sin(\varphi) \tag{2.57}$$

$$\dot{e'} = -j_3\, C'_r\, \alpha\, e'^{|j_3|-1} \sin(\varphi) \tag{2.58}$$

$$\dot{\tilde{\omega}'} = 2\, C'_s\, \alpha + |j_3|\, C'_r\, \alpha\, e'^{|j_3|-2} \cos(\varphi) \tag{2.59}$$

where the constants arising from the resonant (C'_r) and secular (C'_s) parts of the disturbing function are given by

$$C'_r = \left(\frac{GM_n}{a'^2 a_n n'}\right) f_d(\alpha) \tag{2.60}$$

$$C'_s = \left(\frac{GM_n}{a'^2 a_n n'}\right) f_{s,1}(\alpha) \tag{2.61}$$

where M_n is the mass of Neptune and G is the solar gravitational constant. The C_s' term in Equation 2.59 will be neglected later, but the C_r term is important for first order resonances.

Pendulum Model

If we assume Neptune's mean motion is constant with time ($\dot{n}_n = 0$), we can view our resonance model in terms of a simple pendulum. We take two time derivatives of Equation 2.52 which gives

$$\ddot{\varphi} = (p+q)\,(\dot{n'} + \ddot{e'}) - \ddot{\tilde{\omega}'} \tag{2.62}$$

or, more generally,

$$\ddot{\varphi} = j_1 \dot{n'} + j_1 \ddot{e'} + j_3 \ddot{\tilde{\omega}'}. \tag{2.63}$$

Assuming we can neglect $\ddot{\omega}'$ (which is a good assumption except for the case of first Order resonances) and $\ddot{\epsilon}'$ and using $\dot{n}'$ from Equation 2.57 we can write

$$\ddot{\varphi} = -w_o^2 \sin(\varphi) \tag{2.64}$$

where $w_o^2 = -3j_1^2 C_r' \alpha n' e'^{|j_3|}$. In the case of an odd order external mean motion resonance, the stable value of the resonant argument is π. Therefore, we must substitute $\varphi' = \varphi + \pi$ into Equation 2.64, yielding $\ddot{\varphi}' = -w_o^2 \sin(\varphi')$, which is of the same form as Equation 2.64. Hereafter, we will drop the prime on φ' and continue with the derivation. We can write the energy of the system, E, as

$$E = \frac{1}{2}\dot{\varphi}^2 + 2w_o^2 \sin^2\left(\frac{1}{2}\varphi\right) \tag{2.65}$$

Libration Width

The maximum energy for libration, E_{max}, with ($\varphi = \pm\pi$ and $\dot{\varphi} = 0$) is 2 w_o^2 or

$$E_{max} = -6\, j_1^2\, C_r'\, \alpha\, n'\, e'^{|j_3|} \tag{2.66}$$

We now set the value of E in Equation 2.65 to E_{max} which gives a variation in φ of

$$\dot{\varphi} = \pm\, j_1 \left(12\,|C_r'|\,\alpha\, n'\, e'^{|j_3|}\right)^{1/2} \cos\left(\frac{1}{2}\varphi\right) \tag{2.67}$$

Using Equation 2.57, we can derive a relationship for dn' which can then be integrated to yield

$$n' = n_o' \pm \left(12\,|C_r'|\,\alpha\, n'\, e'^{|j_3|}\right)^{1/2} \cos\left(\frac{1}{2}\varphi\right) \tag{2.68}$$

So, the maximum change in the mean motion, which occurs at $\varphi = 0$ is

$$\delta n'_{max} = \pm \left(12\,|C_r'|\,\alpha\, n'\, e'^{|j_3|}\right)^{1/2} \tag{2.69}$$

Using the relationship given by Kepler's Third Law that $n'^2 a'^3 = \mu_\odot = GM_\odot$, and subsequently $\delta a' = -(2a')/(3n')\,\delta n'$, we can write Equation 2.69 in terms of semi-major axis, thus deriving the libration width:

$$\delta a'_{max} = \pm \left(\frac{16\,|C_r'|\,\alpha}{3\,n'}\, e'^{|j_3|}\right)^{1/2} a' \tag{2.70}$$

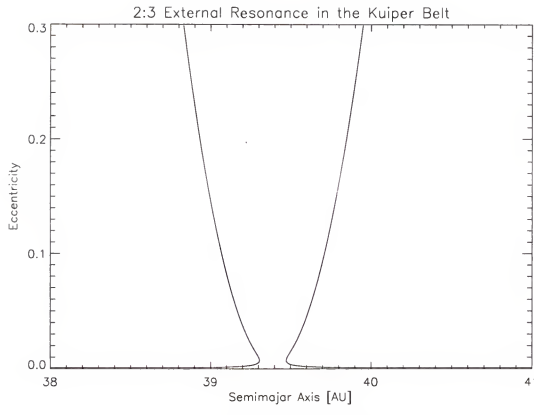

Figure 2-2: The maximum libration widths in a-e space for the 3:2 external mean motion resonance with Neptune.

However, the above equation is inappropriate for first order resonances, since the $\ddot{\omega}$ term in $\ddot{\varphi}$ (Equation 2.62) is not negligible. For first order external resonances, j_3 = -1 and the relationship for libration width is the following

$$\delta a'_{max} = \pm \left[\sqrt{\left(\frac{16\,|C'_r|\,\alpha}{3\,n'}\, e' \right) \left(1 + \frac{1}{27\,j_1^2\, e'^3} \frac{|C'_r|\,\alpha}{n'} \right)} - \frac{2}{9\,j_1\, e'} \frac{|C'_r|\,\alpha}{n'} \right] a'. \qquad (2.71)$$

Figure 2-2 shows the maximum libration widths, calculated using Equation 2.71, in a-e space for the 3:2 external mean motion resonance with Neptune.

Libration Period

Ordinarily, for low eccentricities and small libration amplitudes, the libration period, T_{lib}, can be calculated by integrating over the resonant argument, φ, to the

libration amplitude, φ_0

$$T_{lib} = 4 \int_0^{\varphi_0} \frac{d\varphi}{\dot{\varphi}} \tag{2.72}$$

assuming $\dot{\varphi} = 0$ and $\varphi = \varphi_0$. Substituting from Equation 2.65, $E = 2w_o^2 \sin^2 \varphi_0/2$, Equation 2.72 becomes

$$T_{lib} = \frac{1}{w_0} \int_0^{2\pi} \frac{d\theta}{\sqrt{1 - \frac{E}{2w_o^2} \sin^2 \theta}} \tag{2.73}$$

where $\sin \varphi/2 = \sin \varphi_0/2 \sin \theta$ (Murray and Dermott 1999). Equation 2.73 gives an accurate value for the libration period in the case of small eccentricities and small libration amplitudes, such as in the case of external mean motion resonances with the Earth. However, Malhotra et al. (1996) cautions against using the pendulum model for the calculation of libration periods for objects in mean motion resonances in the Kuiper belt. Here the eccentricities of the objects involved are high and the libration amplitudes are large. In the case of the 3:2 Neptune-Pluto resonance, the eccentricity of Pluto is 0.25 while the libration amplitude is 76° (Murray and Dermott 1999). The libration period which is computed using Equation 2.73 is 9447 years, while the measured libration period from Murray and Dermott (1999) is 19,670 years, which is a significant difference.

CHAPTER 3
WARPED DISKS AND THE OFFSET OF THE ZODIACAL CLOUD

Our studies to date show that at least three different types of asymmetries can serve to indicate bodies orbiting a star in a disk, one of which is a warp in the plane of symmetry of the disk due to the variation of the forced inclinations, I_{forced}, with respect to the astrocentric distances of the dust particles (Dermott et al. 1996b). We identify the warp in the zodiacal cloud from the analysis of COBE (The Cosmic Background Explorer satellite) observations in the 4, 12, 25, and 60 μm wave bands and present the results in Section 3.1. In Section 3.2, we discuss the applications of low-order secular perturbation theory to a simple three body system, analogous to a system composed of a central star and two perturbers having a non-zero mutual inclination, I_{mutual}. In this case, we use the HR 4796 system as our example, since it is a planetary debris disk that has been observed to show an definite offset asymmetry, which may be an indirect indication of the presence of at least one planet in the system (Telesco et al. 2000). The observations also show a slight warp, but it is not known whether this is a real effect or an artifact of incomplete point spread function (PSF) subtraction. We take the parameters obtained from modeling the offset (Wyatt et al. 1999) and demonstrate to what extent a planet could produce a warp in the system. Using low-order secular perturbation theory, where M_i and $a_i (i = 1, 2)$ are the mass and semi-major axis of the i^{th} perturber (where i=1 is HR 4796B and i=2 is the planet), and where I_{mutual} is the mutual inclination of these two perturbers, we can show how varying certain parameters (M_2/M_1, a_2/a_1, and I_{mutual}) can affect the degree of warp of the system. Lastly, we can determine how effective a particular satellite or telescope would be for detecting warps in exo-solar

system debris disks. The magnitude of a possible warp in the plane of symmetry of a circumstellar dust disk can be determined by dynamical modeling and it is possible to determine whether the Space InfraRed Telescope Facility (SIRTF) will be able to detect a warp in a debris disk. In Section 3.3, we find that SIRTF will only be able to detect a very extreme warp and that SIRTF will not be able to detect a small warp, similar to that seen in our solar system's zodiacal cloud.

Another asymmetry which can be diagnostic of the presence of planets in a system is an offset in the center of symmetry of the disk with respect to the central star due to the forced eccentricities of the dust particles. We observe the offset in the 12 and 25 μm COBE DIRBE wave bands and present the results in Section 3.4. We find that a purely asteroidal model that does not include collisions between dust particles does not account for the observed offset. Either there must be a significant loss of asteroidal particles due to collisions or the zodiacal cloud must have a non-negligible cometary component that must be included in future models (Holmes et al. 1998).

Since COBE only operated for 10 months (from December 11, 1989 to September 21, 1990), we were unable to get a complete 12-month sinusoidal variation of the data. To supplement the COBE data, we took photometric data from the Infrared Space Observatory (ISO) in the 25 μm from December 8, 1997 through January 27, 1998. Although the ISO data, shown in Section 3.5, roughly confirm the COBE observations, we must derive a scale factor to the ISO data to match the observed COBE brightness. This scale factor can be used by the ISO team to calibrate their data.

3.1 COBE Observations of the Warp in the Zodiacal Cloud

The warp in the plane of symmetry of the zodiacal cloud is caused by the variation of the forced inclinations of the dust particles with respect to their heliocentric

distances. A dust particle orbiting in the asteroid belt has a forced inclination which is determined by the perturbing effects of the major planets. When a particle leaves the asteroid belt to spiral in towards the Sun due to Poynting-Robertson light drag, its semi-major axis, a_{dust}, changes with time. The change in semi-major axis causes the gravitational perturbations on the particle to change, since the semi-major axes of the planets are constant. Using low-order secular perturbation theory, for small inclinations and eccentricities, I_{forced} is a function of only semi-major axis, a_{dust}, and particle size. A cloud with particles having a range of semi-major axes will have a range of force inclinations, which will produce a warp in the cloud.

The Diffuse Infrared Background Experiment (DIRBE) on the Cosmic Background Explorer (COBE) spacecraft operated for 10 months from December 11, 1989 to September 21, 1990 in 10 photometric wave bands at 1.25, 2.2, 3.5, 4.9, 12, 25, 60, 100, 140, and 240 μm. COBE DIRBE was designed to search for the cosmic infrared background (CIB), diffuse infrared radiation originating from outside of the Milky Way galaxy. However, foreground scattered light and thermal emission from interplanetary dust particles in the zodiacal cloud were significant contributors to the diffuse infrared sky brightness making COBE data an excellent tool for the study of asymmetries in the cloud. The warp in the zodiacal cloud can be identified by comparing the positions of the ascending and descending nodes as observed by COBE at the north and south (N and S) ecliptic poles (at 1 AU) with the positions of the nodes as observed near the ecliptic in the directions leading and trailing (L and T) the Earth in its orbit, that is, external to 1 AU (Dermott et al. 1996b). In the bottom plot in Figure 3-1, the brightness of the zodiacal cloud at the north and south ecliptic poles is plotted with respect to the ecliptic longitude of Earth for the 25 μm wave band. The COBE observations for the north and south ecliptic poles are each fitted with well defined sine curves. The ascending and descending nodes, Ω_A and Ω_D, are measured at the ecliptic longitudes of Earth at which the north polar brightness is

equal to the south polar brightness, or where the Earth lies in the midplane of the cloud. We find that the position of the ascending node at 1 AU is 70.7°± 0.4° (Dermott et al. 1998, Holmes et al. 1999). The zodiacal cloud is not expected to have a large vertical extent so the observed polar brightness is assumed to originate from ≈ 1 AU. Comparisons can be made to the near ecliptic brightnesses of the zodiacal cloud in the leading and trailing directions, which originates from dust external to 1 AU. From previous work, the position of the ascending node in the near ecliptic case was determined to be 58.40°± 2.33° (Dermott et al. 1996b). The top plot of Figure 3-1 shows the latitude of the peak flux of the cloud as seen by COBE in the 25 μm wave band versus the ecliptic longitude of Earth in the leading (dotted curve and open circles) and trailing (solid curve and filled circles) directions and the fits to the data. The positions of the ascending and descending nodes of the cloud are given at the ecliptic longitude of Earth at which the latitude of the trailing curve is equal and opposite to the latitude of the leading curve (Dermott et al. 1999a). If the cloud had only one plane of symmetry, the value of the ascending node observed at the ecliptic poles would be the same as that observed in the leading and trailing directions. As seen in Figure 2-1, the inclination and the node are related by the particle in a circle method, which is why the difference in node implies a difference in inclination. The difference in inclination with respect to astrocentric distance is a measure of the warp in the cloud. The statistically significant disparity - the nodes differ by more than 12° - between ascending nodes for observations at the ecliptic poles (north and south) and for observations near the ecliptic (leading and trailing) indicates that the zodiacal cloud is indeed warped. These results are presented in Table 3.1 and in addition a comparison is made to the inclinations and ascending nodes of Jupiter, Saturn, and the ten degree dust bands. The ascending node (100°± 8°) and inclination (1.16°± 0.09°) of the ten degree dust bands, determined from previous work, match well with

the ascending node (100.5°) and inclination (1.30°) of Jupiter. The forced inclinations and nodes of the dust particles in the ten degree dust bands are locked on to the inclination and node of Jupiter. However, in comparison, the inclination and node of Jupiter differ greatly from the inclination and node of the background zodiacal cloud (Dermott et al. 1998). Further theoretical evidence of the warp of the background cloud is presented in Figure 3-2 which shows the variation of the forced inclinations and forced node with respect to semi-major axis for different sized particles (4, 9, 14, and 25 μm in diameter). In the asteroid belt, at approximately 3 AU, the I_{forced} and Ω_{forced} of the particles are locked on to Jupiter's inclination and node, respectively (Dermott et al. 1996b). However, by 2 AU, the particles all have different forced elements ranging from $\sim$ 50 - 90° depending on particle size, and by 1 AU, Ω_{forced} ranges from $\sim$ 50 - 70°. Correspondingly, I_{forced} also varies as a function of particle size and semi-major axis, producing a warped background cloud.

Table 3-1: Orientation of the planes of symmetry with respect to the ecliptic.

	Inclination to the ecliptic (I)	Longitude of Ascending Node (Ω)
Jupiter	1.30°	100.5°
Saturn	2.49°	113.7°
Ten Degree Dust Bands	1.16 ± 0.09°	100 ± 8°
Zodiacal Cloud (25 μm, ecliptic)	1.49 ± 0.07°	58.40 ± 2.33°
Zodiacal Cloud (25 μm, poles)	Undetermined	70.7 ± 0.2°
Zodiacal Cloud (12 μm, poles)	Undetermined	76.4 ± 0.2°

Orientation of the planes of symmetry with respect to the ecliptic. The inclination to the ecliptic and the longitude of ascending node (Ω) of several planets for the year 1990 (Astronomical Almanac 1990). I and Ω were also determined from the 1989-1990 COBE DIRBE observations for the zodiacal cloud in the ecliptic and polar directions in the 25 μm wave band. (Dermott et al. 1998)

Figure 3-3 shows the brightness of the north and south ecliptic poles as seen by COBE versus ecliptic longitude of Earth for the 4, 12, 60, and 100 μm wave

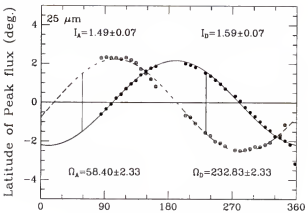

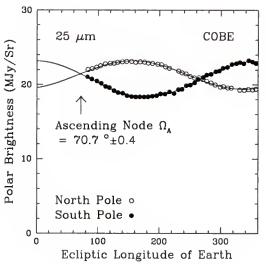

Figure 3-1: COBE DIRBE data showing the warp in the zodiacal cloud in the 25 μm wave band. (top) The latitude of the peak flux of the cloud as seen by COBE in the 25 μm wave band is plotted versus the ecliptic longitude of Earth in the leading (dotted curve and open circles) and trailing (solid curve and filled circles) directions, that is, external to 1 AU. The positions of the ascending and descending nodes of the cloud are given at the ecliptic longitude of Earth at which the latitude of the trailing curve is equal and opposite to the latitude of the leading curve. The ascending node, Ω_A, is measured to be 58.40°± 2.3 (Dermott et al. 1996b). (bottom) In comparison, COBE DIRBE data of the north and south ecliptic poles (at 1 AU) is presented. The brightness in MJy/sr of the north and south ecliptic poles is plotted versus ecliptic longitude of Earth. Ω_A at the poles is observed to be 70.7°± 0.4. The difference between these nodes (12.3°± 2.3) is significant and indicates that the background zodiacal cloud is warped (Dermott et al. 1998, Holmes et al. 1999).

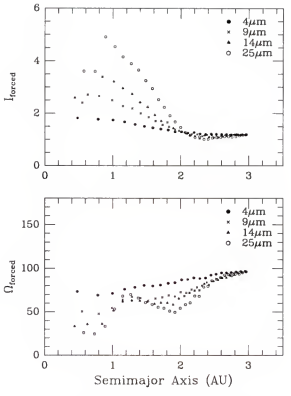

Figure 3-2: Variation of Forced Inclination and Forced Node with respect to semimajor axis for different sized particles. In the asteroid belt, I_{forced} and Ω_{forced} are locked on to Jupiter's inclination and node, respectively (Dermott et al. 1996b).

bands. We obtain the location of the ascending node for the 4 μm wave band: Ω_A = 107.7° ± 0.1°. The value of the ascending node for the 12 μm wave band (Ω_A = 76.4 ± 0.2°) agrees roughly with the value we obtained for the 25 μm wave band (Ω_A = 70.7 ± 0.2°). The sine curves for the 60 μm (Ω_A = 33.6° ± 6.3°) are not as well defined, however, possibly due to the presence of galactic emission complicating the results. Another explanation for the differences in nodes for the different wave bands is that emission at a particular wave band is a function of particle size. In general, the larger the wavelength, the larger the particles are that contribute to the emission. For example, particles (composed of astronomical silicate) which are less

than 0.1 μm in diameter do not contribute much to the thermal emission in the 12 and 25 μm because their absorption efficiency, Q_{abs}, approaches zero. For the 60 μm wave band, the cutoff particle size increases to $\sim$ 10 μm (Grogan 1997, Gustafson 1994). In turn, forced inclination is a function of particle size, so a different particle size distribution could produce a different I_{forced} and thus a different forced node. The sine curves for the fits to the north and south polar data for the 100 μm wave bands do not even cross, giving no value for the ascending node, due most probably to contamination from galactic emission, which begins to dominate the emission in the wave bands $\geq$ 60 μm.

Another confirmation of the warp in the zodiacal cloud is that if the cloud were not warped, the ascending and descending nodes would lie exactly 180° apart. In the 25 μm wave band polar case, $\Omega_A = 70.7° \pm 0.2°$ and $\Omega_D = 264.2° \pm 0.2°$. The difference between the two nodes is $193.5° \pm 0.2°$, clearly different from 180°. For the 12 μm wave band polar case, $\Omega_A = 76.4° \pm 0.2°$ and $\Omega_D = 255.3° \pm 0.2°$. The difference between the two nodes is $178.9° \pm 0.2°$. From Figure 3-3, it is clear that the differences in the ascending and descending nodes for the 4 and 60 μm wave band are also not 180°.

The warp in the plane of symmetry of the zodiacal cloud is caused by the fact that the planets do not lie in the same orbital plane. For instance, Jupiter, the most massive of the planets, is inclined to the ecliptic by 1.30° as seen in Table 3-1. The mutual inclination, I_{mutual}, of Jupiter to Saturn most likely produces the warp in the zodiacal cloud. Since I_{mutual} is small ($\sim$ 1.2°), the warp in the zodiacal cloud is small (Dermott et al. 1998). As seen in Figure 2-1, the inclination and the node are linked, which is why the difference in node implies a difference in inclination.

In a multiple planet exo-solar system, we expect that the planets would not all lie in the same orbital plane, which would produce a warp in the exo-solar system debris disk. A warp could also be produced in a binary star system that has one

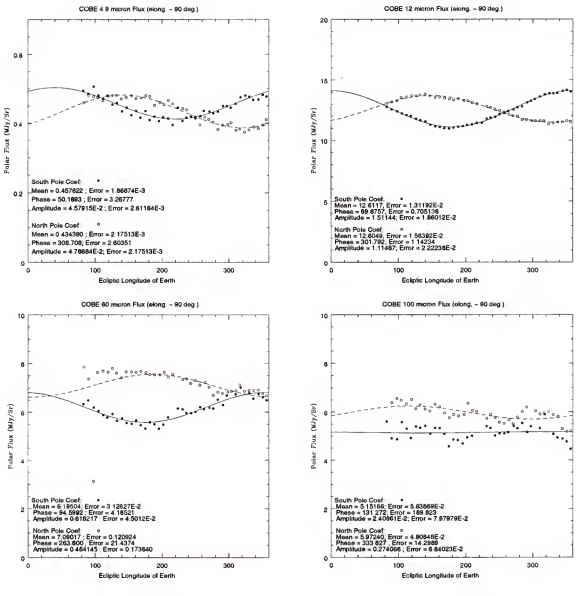
COBE 4.9 micron Flux (elong. - 90 deg.)
Polar Flux (MJy/Sr)
Ecliptic Longitude of Earth
South Pole Coef:
Mean = 0.457622 ; Error = 1.86874E-3
Phase = 50.1663 ; Error = 3.26777
Amplitude = 4.57915E-2 ; Error = 2.61164E-3
North Pole Coef:
Mean = 0.434390 ; Error = 2.17513E-3
Phase = 308.708; Error = 2.60351
Amplitude = 4.76684E-2; Error = 2.17513E-3
COBE 12 micron Flux (elong. - 90 deg.)
Polar Flux (MJy/Sr)
Ecliptic Longitude of Earth
South Pole Coef:
Mean = 12.8117; Error = 1.31192E-2
Phase = 69.8757; Error = 0.705136
Amplitude = 1.51144; Error = 1.86012E-2
North Pole Coef:
Mean = 12.6422; Error = 1.56382E-2
Phase = 301.749; Error = 1.14234
Amplitude = 1.11467; Error = 2.22258E-2
COBE 60 micron Flux (elong. - 90 deg.)
Polar Flux (MJy/Sr)
Ecliptic Longitude of Earth
South Pole Coef:
Mean = 6.19504; Error = 3.12627E-2
Phase = 94.6982; Error = 4.16521
Amplitude = 0.618217 Error = 4.5012E-2
North Pole Coef:
Mean = 7.09017; Error = 0.120924
Phase = 263.805; Error = 21.4374
Amplitude = 0.484145 ; Error = 0.173640
COBE 100 micron Flux (elong. - 90 deg.)
Polar Flux (MJy/Sr)
Ecliptic Longitude of Earth
South Pole Coef:
Mean = 5.15166; Error = 5.63686E-2
Phase = 131.272; Error = 1.66.823
Amplitude = 2.40861E-2; Error = 7.97979E-2
North Pole Coef:
Mean = 5.97340; Error = 4.90845E-2
Phase = 333.67; Error = 14.2988
Amplitude = 0.274046 ; Error = 6.84023E-2

Figure 3-3: The brightness of the north and south ecliptic poles as seen by COBE versus ecliptic longitude of Earth for the 4, 12, 60, and 100 μm wave bands. (top left) We obtain a value of Ω_A for the 4 μm data of $107.7° \pm 0.1°$. (top right) The value of Ω_A for the 12 μm data of $76.4° \pm 0.2°$ corresponds roughly to the 25 μm value. (bottom left) We find a value of Ω_A for the 60 μm of $33.6° \pm 6.3°$, but we note that the data may be contaminated by galactic emission. (bottom right) The fits to the north and south polar data for the 100 μm wave bands do not even cross, giving no value for the ascending node, due most probably to contamination from galactic emission.

planet. The extent of such a warp can be determined using secular perturbation theory.

3.2 Applications of Secular Perturbation Theory to HR 4796

Given observations of an asymmetric cloud, we can use secular perturbation theory to investigate which model parameters to vary to produce desired asymmetries. For a system of two perturbers and a test particle, the variation of I_{forced} with respect to a depends on M_2/M_1 (the masses of the two perturbers), a_2/a_1 (the semi-major axes of the two perturbers), and I_{mutual}, the mutual inclination of the perturbers. This method eliminates some of free parameters of our models.

3.2.1 Warp: Variation of Forced Inclination

A warp in the plane of symmetry of the disk is caused by the variation of the forced inclinations of the dust particles with respect to their astrocentric distances. For the "no drag" case, i.e., assuming the particle has the same proper elements as it did when it left the asteroid (which, although not physical, is adequate for an elementary demonstration of this particular technique) we can calculate the variation of the I_{forced} of the particles as a function of semi-major axis. Figure 3-4 represents the particle's forced inclination at different semi-major axes in the system. When the particle is close to a planet, it's forced inclination equals the inclination of that planet ($I_{forced} = I_{planet}$). The peak in the curve (around $\sim$ 1 AU) corresponds to a secular resonance, which occurs when the nodal precession rate of the test particle approaches an eigenfrequency of one of the planets. The most important feature to note is that the decrease in I_{forced} between I_{planet} and $I_{HR\ 4796B}$ is indicative of the warp of the cloud. Lastly, after a certain semi-major axis the curve flattens out. The value of I_{forced} at this point corresponds to the inclination of the plane of symmetry of the system due to its mean angular momentum.

The HR 4796 system is composed of two stars (A and B) of mass $M_{\star A} = 2.5 M_{Sun}$ and $M_{\star B} = 0.38 M_{Sun}$. Wyatt et al. (1999) theorizes that there may be an additional body, a planet of $0.1 M_{Jupiter} < M_{planet} < 20 M_{Jupiter}$, in the system. This

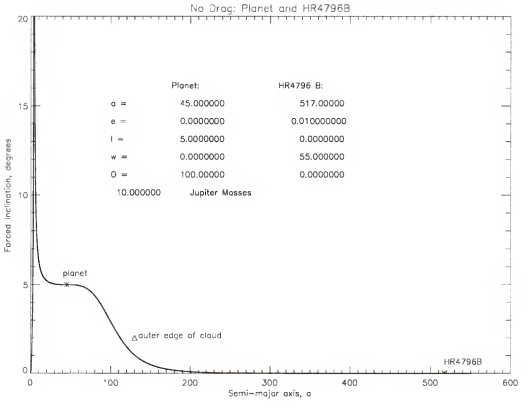

Figure 3-4: Secular perturbation theory variation of I_{forced} with respect to semi-major axis for HR 4796. A warp in the plane of symmetry of the disk is caused by the variation of the forced inclinations of the dust particles with respect to their astrocentric distances. For the "no drag" case, i.e., assuming the particle has the same proper elements as it did when it left the asteroid (which, although not physical, is adequate for an elementary demonstration of this particular technique) we can calculate the variation of the I_{forced} of the particles as a function of semi-major axis. This figure represents the particle's forced inclination at different semi-major axes in the system. When the particle is close to a planet, it's forced inclination equals the inclination of that planet ($I_{forced} = I_{planet}$). The peak in the curve (around ~ 1 AU) corresponds to a secular resonance, which occurs when the nodal precession rate of the test particle approaches an eigenfrequency of one of the planets. The most important feature to note is that the decrease in I_{forced} between I_{planet} and $I_{HR\ 4796B}$ is indicative of the warp of the cloud. Lastly, after a certain semi-major axis the curve flattens out. The value of I_{forced} at this point corresponds to the inclination of the plane of symmetry of the system due to its mean angular momentum.

Table 3-2: Osculating elements of known and hypothetical perturbers in the HR 4796 system.

Perturber	a (AU)	e	I	$\tilde{\omega}$	Ω
HR 4796B	517	0.01	0°	55°	0°
Planet	45	0	5°	0°	100°

Osculating elements of known and hypothetical perturbers in the HR 4796 system. We use these osculating elements obtained by Wyatt et al. (1999) to construct dynamical models of the warp in HR 4796.

theory is based on the observation of a brightness asymmetry between the two lobes of the disk around HR 4796A (Telesco et al. 2000). We can use the osculating elements theorized for the planet (listed in Table 3-2) and information from the observations about HR 4796B to begin to make simple predictions about how such a system will perturb a dust cloud in equilibrium around HR 4796A.

The variation of I_{forced} with respect to a depends on M_{planet}/M_{*B}, a_{planet}/a_{*B}, and I_{mutual}. The mass of the star (0.38 M_{Sun}) is fairly well defined and obviously much greater than the mass of the planet. The semi-major axis of the planet is assumed to be 45 AU based on modeling the lobe brightness asymmetry and the semi-major axis of star B is assumed to be its projected distance of 517 AU. If we define the inclination of HR 4796B as 20° and the inclination of the planet to be 0°, we can vary the mass of the planet to produce various warps (See Figure 3-6). The warp is evident in the part of the models exterior to $\sim |10|$ AU. Three different models were run for various planetary masses: 0.1 $M_{Jupiter}$ (solid line), 1 $M_{Jupiter}$ (dotted line) and 10 $M_{Jupiter}$ (dashed line) producing three different degrees of warping. Interestingly, as predicted by Wyatt et al. (1999) using secular perturbation theory diagrams similar to Figure 3-4, the degree of warping is largest for the model with the smallest planetary mass, $M_{planet} = 0.1\ M_{Jupiter}$. This is because if $M_{planet} \leq 0.1\ M_{Jupiter}$, then the symmetry plane of the system is aligned with HR 4796B, which we have

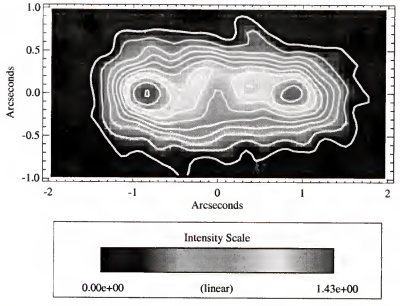

Figure 3-5: Infrared observations of HR 4796. A false color image of HR 4796 in the IHW18 (18.2 μm) wave band (Telesco et al. 2000). A slight warp of the cloud can be seen in the image, especially in the inner most contours where the brightness is represented by the color yellow. It is uncertain whether this warp is a real effect or due to incomplete PSF subtraction.

assigned an inclination of 20°. If $M_{planet} > 0.1\ M_{Jupiter}$, then the symmetry plane of the HR 4796 system is aligned with the planet, producing in the above case, a smaller warp. Thus, the warp of the system depends on I_{mutual}, but the alignment of the symmetry plane depends on the mass of the planet. Although the observations of HR 4796 only show a hint of a warp, there are other systems, such as β Pictoris which show a definite warp and will be the subject of future investigations.

3.3 Heuristic Models of Warped Disks

The magnitude of a possible warp in the plane of symmetry of a circumstellar dust disk can be determined by dynamical modeling and it is possible to determine whether a specific space craft, such as the Space InfraRed Telescope Facility (SIRTF), will be able to detect a warp in a debris disk. We find that SIRTF will only be able

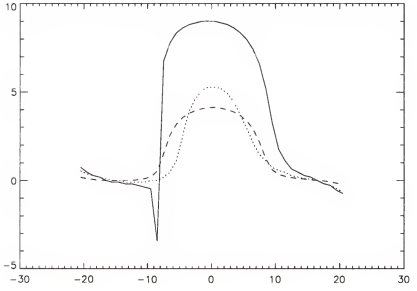

Figure 3-6: Characterizing the warp in HR 4796. The warp is evident in the part of the models exterior to $\sim$ |10| AU (the x axis is in AU). In all of the models, the semi-major axis of the planet is 45 AU, the semi-major axis of HR 4796B is 517 AU, the inclination of the planet is set to 0°, and the inclination of the star is set to 20°. The eccentricities and nodes were the same as in previous models (Wyatt et al. 1999). The mass of the star was taken to be 0.38 M_{Sun}, while the mass of the planet was varied. Three different models were run for various planetary masses: 0.1 $M_{Jupiter}$ (solid line), 1 $M_{Jupiter}$ (dotted line) and 10 $M_{Jupiter}$ (dashed line) producing three different degrees of warping. Interestingly, as predicted by Wyatt et al. (1999), the degree of warping is largest for the model with the smallest planetary mass, $M_{planet} = 0.1\ M_{Jupiter}$.

to detect a very extreme warp. SIRTF will not be able to detect a small warp, similar to that seen in our solar system's zodiacal cloud.

3.3.1 Exo-zodiacal Cloud Model

We build dynamical models of dust clouds from asteroidal particles which include radiation pressure and PR drag. The particles are $9\mu m$ in diameter and assumed to be spheres composed of astronomical silicate. The radial extent of the cloud is 7.0 AU (an arbitrary cutoff) to 300.0 AU and the particles populate the inner solar system according to a $1/r$ distribution (PR drag). The effects of forced

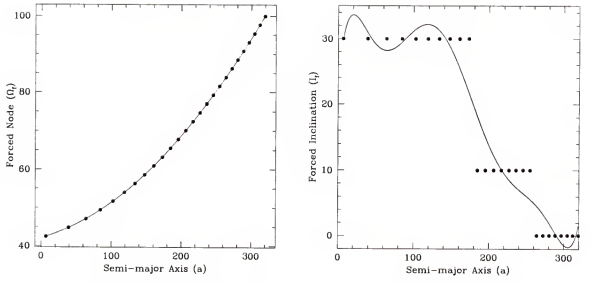

Figure 3-7: Heuristic variations of Ω_{forced} and I_{forced}. (left) The variation of Ω_{forced}, the forced longitude of ascending node and the corresponding Chebychev polynomial fit. (right) The variation of I_{forced}, the forced inclination and the corresponding Chebychev polynomial fit. There is a steep step functional decrease in forced inclination with respect to semi-major axis. The range of I_{forced} shown here is very large. These curves are heuristic variations, though they demonstrate how a warp would be generated in a real system.

elements are included in the model. Specifically, heuristic ranges of both I_{forced} and Ω_{forced} are included while e_{forced} and $\tilde{\omega}_{forced}$ are set to zero. The particles' orbits are then distributed through a 3D array of cells and a Line of Sight Integrator allows a model to be viewed as it would appear to an Earth-based observer. The face on optical depth of the cloud is $\tau \approx$ 1.2e-8. The optical depth for the zodiacal cloud is $\tau \sim$ 1e-7, so the model cloud is quite diffuse. The function for I_{forced} for the model is a steep step functional decrease in I_{forced} ranging from $\sim 30°$ to $0°$ with respect to increasing a. The range of I_{forced} shown here is very large. For comparison, in our own solar system I_{mutual} for Jupiter and Saturn is $\approx 1.19°$. A smaller difference in mutual inclination of the perturbers produces a correspondingly smaller variation in I_{forced} and hence a smaller warp. However, for demonstration purposes, we have chosen to model a disk with a large warp (Figure 3-7). An image of the model cloud

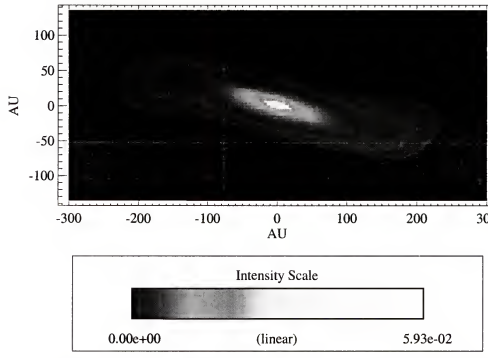

Figure 3-8: Warped model cloud viewed at 1.35 pc as it would appear in the 70 μm wave band assuming a SIRTF sensitivity limit of 610 μJy.

as viewed edge on by an external observer at 1.35 pc, assuming a SIRTF Multiband Imaging Photometer (MIPS) slow scan mapping sensitivity of 610 μJy (Rieke 1998), in the 70 μm wave band is presented in Figure 3-8).

3.3.2 Implications for SIRTF

Listed in the SIRTF Science Requirements Document are several candidate stars with possible debris disks. The closest candidates are α Cen A and α Cen B at 1.35 pc. We therefore scale the brightness of our model to the MIPS sensitivity requirements for the 70 μm wave band at this distance. We then filter the model with a Gaussian of width 7 ($\sim \lambda/D$) to simulate convolving the model with a stellar PSF. Lastly, we convert the pixels in our model to represent the 5 " pixel width of MIPS in super-resolution mode. A warp in the cloud is clearly evident (see Figure 3-9). Thus, SIRTF has the potential to detect a significant warp in large disks very close to our

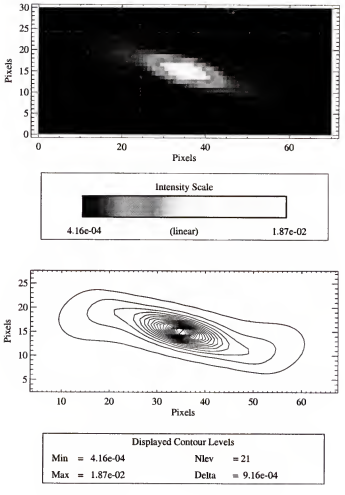

Figure 3-9: Warped model as it would appear to SIRTF. (top) The model viewed at 1.35 pc as it would appear to SIRTF in the MIPS 70 μm wave band using the sensitivity limit of 610 μJy and the super-resolution pixel size of 5 ". 1 SIRTF pixel in super-resolution model is equivalent to 3 pixels in the original model. (bottom) A contour plot of the model in (a), clearly showing the warp.

solar system. In addition, models of warped clouds were run with radii out to 3.0 AU (representing a zodiacal disk) and 40.0 AU (representing a solar system type Kuiper disk). However, the extent of these disks in SIRTF pixels were too small to determine the structure of any asymmetries when viewed at 1.35 pc. It may only be possible for SIRTF to map asymmetries in large nearby disks having significant warps, such as β Pictoris. However, if the warp in the debris disk is small, similar to the warp in

our solar system's zodiacal cloud, SIRTF MIPS will not have the resolution needed to detect the asymmetry.

3.4 COBE Observations of the Offset in the Zodiacal Cloud

Using COBE data, we determined the variation with the longitude of the Earth of the brightness of the zodiacal cloud as seen at the north and south ecliptic poles in the 12 and 25 μm wave bands. The north and south polar brightnesses, N and S, from the bottom plot in Figure 3-1 were combined to yield the mean of the north and south brightnesses, $(N + S)/2$ in the 25 μm wave band. For the 12 μm wave band, the north and south polar brightnesses from the upper right-hand plot in Figure 3-3 were combined to yield the average polar brightness (see Figure 3-10). The variation in $(N + S)/2$ with ecliptic longitude of Earth can be represented as a superposition of two sine curves: one for the variation in $(N + S)/2$ due to the Earth's eccentric orbit and the other for the variation in $(N + S)/2$ due to the forced eccentricities of dust particles in the cloud. If the cloud were symmetric about the Sun, that is, if there were no offset, the maximum and minimum brightnesses of the cloud would occur at perihelion and aphelion, respectively. As seen in Figure 3-10 the minimum of the sine curve fit to the 12 μm COBE data is located at $225.7° \pm 2.6°$ and the minimum of the sine curve fit to the 25 μm COBE data is at $223.8° \pm 3.0°$, both of which are clearly displaced from Earth's aphelion, located at 282.9°. This demonstrates that the center of symmetry of the cloud is displaced from the Sun.

The offset in the center of symmetry of the cloud with respect to the Sun is caused by the forced eccentricities, e_{forced}, of the dust particles. In the asteroid belt, a particle has a forced eccentricity which is determined by the perturbing effect of Jupiter. The forced eccentricity causes the particle to move in an elliptical orbit with the Sun at one focus instead of a circular orbit with the Sun at the center.

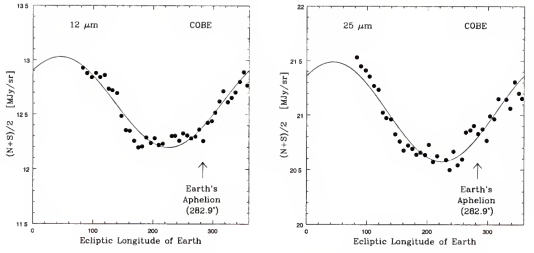

Figure 3-10: Offset of the zodiacal cloud in the 12 (left) and 25 μm (right) wave bands. If the zodiacal cloud were symmetric about the Sun (i.e., if there were no offset), the maximum and minimum (N+S)/2 brightnesses of the cloud would occur at perihelion and aphelion, respectively. However, the minimum of the COBE curves is clearly displaced from Earth's aphelion at 282.9°, showing that the center of symmetry of the cloud is displaced from the Sun. In the 12 μm wave band, the minimum of the sine curve fit to the COBE data is 225.7°± 2.6° and in the 25 μm wave band, the minimum is 223.8°± 3.0°. The error bars for the COBE data are smaller than the filled circles of the data points.

If we could take Figure 3-10 and turn off the effect of the Earth's eccentricity, we could isolate the sine curve due to e_{forced}. When we do this for a model cloud of asteroidal particles, however, we do not see a variation in $(N+S)/2$ for two reasons: 1) although the particle orbits are circularized due to Poynting-Robertson light drag (PR drag), the wedge shape of the cloud cancels out any number density variation as a function of radial distance and 2) even though we would expect the orbits of the particles to be more densely spaced at perihelion than at aphelion (provided all the particles had the same e_{forced} and $\tilde{\omega}_{forced}$), due to Kepler's Second Law the particles spend less time at perihelion than at aphelion effectively canceling out any noticeable effect on the number density. However, when we build a new model cloud governed by a constant distribution of particles ($1/r^{\gamma}$ where $\gamma = 0$) instead of a $1/r$ distribution due to PR drag, we do see a sinusoidal variation in $(N+S)/2$ with

ecliptic longitude of Earth. These results imply that the particles contributing to the observed offset do not have a PR drag distribution, that is, they are not simply asteroidal particles. Future work will determine whether cometary particles (having a theoretical $\gamma = 1.5$), collisionally evolved asteroidal particles, or a combination of both types of particles are responsible for the offset of the center of symmetry of the zodiacal cloud (Holmes et al. 1998).

3.5 ISO Observations

Launched in 1995, the Infrared Space Observatory (ISO) observed the universe at infrared wavelengths from 2.5 to 240 μm with four different instruments: ISOCAM, an infrared camera (2.5 - 17 μm), ISOPHOT, an imaging photopolarimeter (2.5 - 240 μm), ISO-LWS, a long wavelength spectrometer (43 - 196.7 μm), and ISO-SWS, a short wavelength spectrometer (2.38 to 45.2 μm). From December 8, 1997 through January 27, 1998 we took photometric data with ISOPHOT with the P03 and P05 Astronomical Observation Templates (AOTs) in the 25 μm wave band in order to confirm the offset of the center of symmetry of the disk with respect to the central star as initially observed by the COBE. P03 is a general multi-filter photometry AOT and P05 is the absolute photometry AOT. As shown in Table 3-3, we took ten measurements of the polar brightness for each pole (north and south) spanning 77° to 126° longitude of Earth with the 180 arc second aperture. Using the ISOPHOT Interactive Analysis Packet version 8.0 (PIA V8.0), we followed the standard pipeline procedures for data reduction using the Fine Calibration Source (FCS) responsivities and a color correction based on a black body model with T = 280 K, the approximate temperature of the zodiacal cloud at 1 AU (Gustafson 1994). A comparison of the ISO data to the COBE data is shown in Figure 3-11. We now show the north and south polar brightnesses separately for comparison with ISO data. The large error

Table 3-3: ISO observations of the north and south polar brightnesses of the zodiacal cloud.

Observation	Longitude of Earth	AOT
NPOLABS	107°	P05
NPOL1	107°	P03
NPOL2	110°	P03
NPOL3	118°	P03
NPOL4	77°	P03
NPOL5	78°	P03
NPOL6	82°	P03
NPOL7	88°	P03
NPOL8	95°	P03
NPOL9	123°	P03
SPOLABS	99°	P05
SPOL1	99°	P03
SPOL2	113°	P03
SPOL3	123°	P03
SPOL4	77°	P03
SPOL5	81°	P03
SPOL6	84°	P03
SPOL7	88°	P03
SPOL8	98°	P03
SPOL9	126°	P03

ISO observations of the north and south polar brightnesses of the zodiacal cloud. The ISO data where NPOL and SPOL refer to observations of the north and south polar brightnesses of the zodiacal cloud. The P05 AOT is an absolute calibration measurement while the P03 AOTs are relatively calibrated.

bars of the ISO data come from PIA version 8.0 processing assuming the default stray light error of 4 per cent.

In Figure 3-11, the separate north and south polar brightness data are plotted for the ISO data and the COBE data and a sine fit to the COBE data is also shown. From Figure 3-11, it is evident that the COBE data and the ISO data have very different brightnesses - the average ISO brightness is almost twice that of COBE. However, the ISO data seem to roughly conform to shape of the COBE curve. This

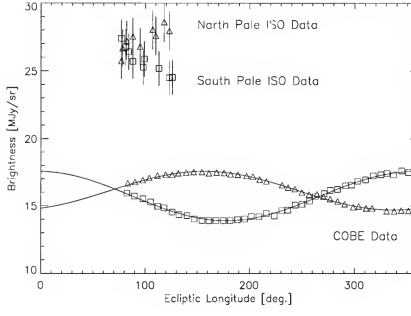

Figure 3-11: North and south polar brightness curves for the ISO data (top) and COBE data (bottom). The north polar brightnesses are represented as triangles and the south polar brightnesses are shown as squares for both the ISO and COBE data. Both data sets were color corrected in the same fashion for comparison purposes.

leads to the question of whether a scale factor or a baseline shift could best fit the ISO data to the COBE data. In Figure 3-12, we subtract a somewhat arbitrarily derived baseline of 10.4 MJy/sr from the ISO data and plot the resulted shifted data points with the north and south polar brightness sine curve fits to the COBE data. Also plotted are the values of the root mean square deviations of the baseline subtracted ISO data points from the COBE curve for both north and south poles. Most of the northern ISO points lie above the northern COBE curve, while most of the southern ISO points lie below the southern COBE curve implying that a shift in the baseline is not adequate to explain the difference in the ISO and COBE data points - a scale factor must be applied.

Figure 3-13 shows the ISO data scaled down to the COBE data. This is a better fit since now the residuals are smaller and most of the points seem to lie closer

to the COBE curve. We scaled the first data point (NPOL1 and SPOL1, respectively) to the COBE curve for the appropriate longitude of Earth, to get a north and south scale factor which we averaged together to create a final scale factor of 0.601. This scale factor was applied to the north and south polar data to scale them down to the COBE curves. Also plotted are the values of the root mean square deviations of the scaled ISO data points from the COBE curve for both north and south poles. For both the north and south poles, the rms deviations are less than for the baseline subtracted case shown in Figure 3-12. The scale factor reduces the width of the north and south data points which proves to be critical. If we did not have data for both the north and south poles we would not have been able to come to the conclusion

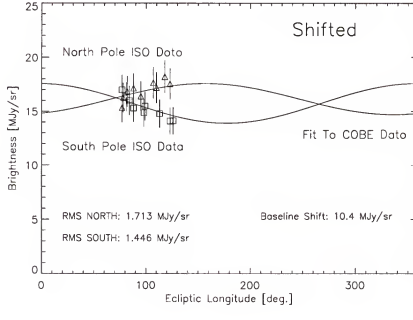

Figure 3-12: Shifted north and south polar brightness data are shown for the ISO data points (top) and COBE curve (bottom). The north polar brightnesses are represented as triangles and the south polar brightnesses are shown as squares for both the ISO and COBE data. A baseline of 10.4 MJy/sr is subtracted from the ISO data to better compare it with the COBE data. However, the north pole ISO points overestimate the COBE curve while the south pole ISO points underestimate the curve, implying that the width of the ISO data will not match the width of the COBE curve for any baseline.

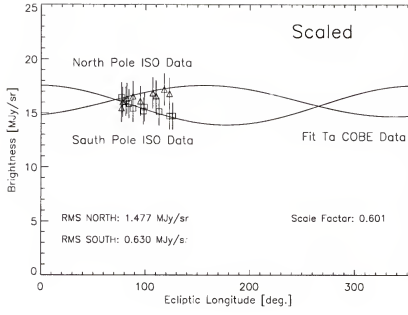

Figure 3-13: Scaled north and south polar brightness data are shown for the ISO data points (top) and COBE curves (bottom). The north polar brightnesses are represented as triangles and the south polar brightnesses are shown as squares for both the ISO and COBE data. A scale factor for the north pole is derived by comparing the NPOL1 datum to the corresponding brightness value of the COBE sine curve fit for a Longitude of Earth of 107° and a scale factor for the south pole is derived by comparing the SPOL1 datum to the corresponding value of the COBE curve for a Longitude of Earth of 99°. These scale factors are averaged to yield a final scale factor of 0.601. The residuals of the scale factor are smaller than in the baseline shifted case and thus the scale factor provides a better fit to the data.

that a scale factor was necessary rather than just a simple shift in the baseline. Thus, the two sets of data points give us a constraint on the correction factor.

COBE observations reveal an offset in the center of symmetry of the zodiacal cloud from the Sun. If the zodiacal cloud were symmetric about the Sun, the maximum and minimum average of the north (N) and south (S) polar brightnesses, $(N + S)/2$, of the cloud would occur at perihelion and aphelion, respectively. However, the minimum of the COBE curve is displaced from aphelion showing that the cloud is offset from the Sun. In the 25 μm wave band, we show the ISOPHOT data (P03 and P05) for the variation in the north and south polar brightnesses with

Ecliptic Longitude of Earth. It is evident that the COBE data and the ISO data have very different brightnesses - the average ISO brightness is almost twice that of COBE. However, the ISO data seem to roughly conform to shape of the COBE curve. A scale factor, as opposed to a baseline shift, is needed to properly scale the width of the ISO north and south brightnesses to the width of the COBE curve. When this scale factor is applied, the ISO data do confirm the COBE results.

CHAPTER 4
RESONANT STRUCTURE IN THE KUIPER DISK

A Kuiper dust disk will have a resonant structure, with two concentrations in brightness along the ecliptic longitude arising because 10-15% of the Kuiper belt objects are in the 3:2 mean motion resonance with Neptune. The estimated brightness of the Kuiper disk in the 60 μm wave band is expected to be $0.3 < I_{KB}(\nu) < 16.0$ MJy/sr, though the high value is a poorly constrained upper limit (Teplitz et al. 1999). Making simple assumptions about the size frequency distribution of bodies in the Kuiper belt, q, the diameter of the largest body that is still in collisional equilibrium, D_{max}, and the total mass of the Kuiper belt, M_{cum}, we should be able to predict the brightness of the Kuiper disk based on calculations of a cumulative area distribution. However, in Section 4.2 we find that it is not possible to make reasonable predictions for the brightness of a Kuiper disk since the parameters used to determine the cumulative area distribution, M_{cum}, D_{max}, q, and even the albedo of dust particles in the Kuiper belt are not well enough determined for the task.

In our quest to ultimately develop a dynamical model of the Kuiper disk, we run numerical integrations of particles originating from source bodies trapped in the 3:2 resonance and we determine what percentage of particles remain in the resonance for a variety of particle and source body sizes. Because the shape of the particles is not known, the variable we use to denote particle size is β, the ratio of the force of radiation pressure to the force of gravity. The dynamical evolution of the particles is followed from source to sink with Poynting-Robertson light drag, solar wind drag, radiation pressure, the Lorentz force, neutral interstellar gas drag, and the effects of planetary gravitational perturbations included. We find that the number of

particles in the 3:2 mean motion resonance increases with decreasing β (i.e., increasing particle size). Consequently, a size frequency distribution for a Plutino disk must be weighted toward larger particles (i.e., those with smaller βs). In addition, as long as the potential, U, of the particles is small ($U \approx 5V$), the Lorentz force does not seem to prevent the particles from remaining in resonance. Similarly, the addition of the effect of neutral interstellar gas drag does not significantly change the percentage of particles remaining in resonance.

4.1 Introduction

In 1943 and 1951 respectively, Edgeworth and Kuiper independently speculated that planetary material may lie in our solar system beyond the orbit of Neptune (Jewitt 1999; Edgeworth 1943; Kuiper 1951). In 1992, Jewitt and Luu discovered 1992 QB1, the first object in what came to be known as the Kuiper belt or the Edgeworth-Kuiper belt (Jewitt and Luu 1993). As of September 2001, more than 430 Kuiper belt objects, or KBOs, have been discovered (Parker 2001), which translates into an estimated 1×10^5 KBOs with diameters greater than 100 km (Jewitt 1999). The Kuiper belt, at approximately 30 to 50 AU, was formed either because planet formation at that heliocentric distance did not occur due to the low density of planetesimals and the long encounter time scales between objects and/or because planetesimals were displaced into the region due to perturbing encounters with young Uranus and Neptune (Backman and Paresce 1993). In the asteroid belt, collisions between asteroids supply dust particles to the zodiacal cloud, the Sun's inner dust disk. By comparison, it has been postulated that collisions between KBOs could initiate a collisional cascade, similar to that in the asteroid belt, which would produce a Kuiper dust disk. In fact, the Kuiper belt is the region of our solar system that is most analogous to the planetary debris disks we see around other stars such as Vega, β Pic, Fomalhaut, and ϵ Eridani (Backman and Paresce 1993). In this chapter we

discuss the properties and formation of the Kuiper belt, how it relates to planetary debris disks around other stars, and the resonant structure of the Kuiper disk.

4.1.1 Kuiper Belt

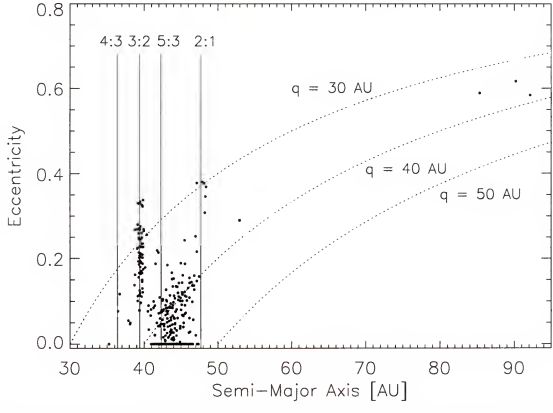

Figure 4-1: A plot of the known Kuiper belt objects with data obtained from the Minor Planet Center.

Kuiper belt objects are divided into three dynamical classes: Plutinos, Classical KBOs, and Scattered KBOs (SKBOs). The Plutinos are distinct in that they reside in the 3:2 mean motion resonance with Neptune at a = 39.4 AU. Pluto also resides in this resonance (Malhotra and Williams 1998), and like the Plutinos, avoids close encounters with Neptune by being an aphelion librator. Approximately 35% of the observed KBOs are Plutinos. However, once the current observations are debiased, Plutinos probably compose 10 to 15% of the KBO population inside 50 AU, which translates into an estimated 10,000 - 15,000 Plutinos with diameters greater

than 100 km (Jewitt et al. 1998). The eccentricities ($0.1 \leq e \leq 0.34$) and inclinations ($10 \leq I \leq 20°$) of the Plutinos bracket the values of Pluto ($e = 0.25, I = 17°$). Other resonances such as the 4:3, the 5:3, and the 2:1 resonance are also somewhat populated (see Figure 4-1).

The Classical objects, which account for approximately two thirds of the known KBOs, have semi-major axes $41 \leq a \leq 47$ AU, and seem unassociated with resonances. They have moderate eccentricities ($e \approx 0.1$) and their inclinations lay in the range $0 \leq I \leq 32°$) (Jewitt 1999). The last dynamical class of KBOs, the Scattered KBOs, has more than four members at the present time (Trujillo and Jewitt 2000). The first member to be discovered, $1996TL_{66}$ has a semi-major axis of 85 AU, an eccentricity of 0.59, and an inclination of 24° (Luu et al. 1997). As a whole, the SKBOs are characterized by large eccentricities, large semi-major axes (> 50 AU), and perihelia, q, near 35 AU. The total number of SKBOs with diameters larger than 100 km is estimated to be on the order of 30,000. The SKBOs are thought to have been scattered by Neptune into a scattered disk (Trujillo and Jewitt 2000). Lastly, it should be noted that the observational techniques are biased toward lower inclinations, so the reported range of inclinations for these dynamical classes may not coincide with the actual range in the Kuiper belt.

4.1.2 Planetary Debris Disks

Outside our solar system, the Infrared Astronomical Satellite (IRAS) detected excess far-infrared emission from more than 15% of all nearby main sequence A-K stars, indicating the presence of circumstellar dust clouds (Backman and Paresce 1993, Elachi et al. 1996). In particular, dust disks have been imaged around Vega, β Pic, Fomalhaut, ϵ Eridani, and HR 4796 A, all of which were IRAS excess stars. All of these systems show evidence of a central clearing of material (or at least drastically reduced density in the inner disk), most show signs of asymmetries, and the Poynting Robertson drag (PR drag) lifetimes of the particles in the disks are estimated to be

much shorter than the ages of the stars which they orbit (Backman and Paresce 1993) indicating that the grains are being replenished. As an example, using Equation 2.6, and assuming a particle having a radius of 5 μm, a density of 2.5 g/cm^3, and a semi-major axis of 300 AU, which is orbiting a star of luminosity equal 60 $L_\odot$ (for the case of Vega), the PR drag lifetime is 5×10^7 years, while the age of Vega is approximately 4×10^8 years (Backman and Paresce 1993).

These phenomenon point to evidence of small bodies such as asteroids, comets, KBO like objects, or planets living within the disks. These disks are thought to be most analogous in scale and temperature to the Kuiper belt (Backman and Paresce 1993). The flux, and thus the detectability, of a circumstellar dust disk is most sensitive to the area rather than its mass. If our solar system were studied with an instrument, such as SIRTF, from the approximate distance of β Pic ($\sim$ 16 pc), the only component of our planetary system likely to be detected would be the theoretical Kuiper disk (Backman and Paresce 1993, Backman et al. 1995, Aumann and Good 1990). However the vertical geometric optical depth in these disks is several orders of magnitude greater than expected in Kuiper belt models which account for a size distribution that includes micron-sized grains. This may indicate that the Kuiper belt we see today is merely a small remnant of a primordial denser circumstellar disk (Backman et al. 1997) .

4.2 Size-Frequency Distribution of the Kuiper Disk

As Kuiper belt objects continue to be found, the existence of a Kuiper dust disk having an equilibrium grain population orbiting at 30 to 50 AU has been postulated (Backman et al. 1995). As such a disk has not yet been observed, many theoretical questions remain about the size-frequency distribution of the particles in the disk, the evolution of the disk and subsequent implications for the detectability of the Kuiper disk from existing or future observations.

The size-frequency distribution of the asteroid belt (and the Kuiper belt) can be described by

$$\frac{dN}{dD} = D_o \, D^{-(p+1)} \tag{4.1}$$

where D_o is a constant, D is the diameter of the smallest particle being considered, dN is the number of particles in a bin of width dD, and p is a constant that indicates whether the particles are in collisional equilibrium, a state in which there is a balance between grain creation (by collisions) and grain removal (by radiation pressure, Poynting-Robertson light drag, mutual destructive collisions, and sublimation) from the system. The constant p can be written as

$$p \equiv 3(q - 1) \tag{4.2}$$

where q is the size-frequency index. A system in collisional equilibrium has a size-frequency index of $q = 1.83$, and correspondingly, a p equal to 2.5 (Dohnanyi 1969). The cumulative number of particles with diameters greater than D is given by

$$N_{cum}(> D) = \frac{1}{p} \left(\frac{D_o}{D} \right)^p \tag{4.3}$$

assuming that $D \ll D_{max}$, where D_{max} is the diameter of the largest body in the distribution and $p > 1$, which is the case for collisional equilibrium. The distribution of area for the system can be written as

$$dA = \left(\frac{\pi}{4} D^2 \right) dN \tag{4.4}$$

where $\pi/(4D^2)$ is the area of an individual particle of diameter D. Integrating Equation 4.4 from D_{min}, the diameter of the smallest particles in the distribution, to D_{max} and using Equation 4.1 yields

$$A_{cum} = \int_{D_{min}}^{D_{max}} \frac{\pi}{4} D_o^p \, D^{-(p-1)} dD. \tag{4.5}$$

If $p > 2$, which is the case for collisional equilibrium, using Equation 4.2, the cumulative area can be written as

$$A_{cum} = \frac{\pi D_{min}^2}{4(3q - 5)} \left(\frac{D_o}{D_{min}} \right)^{3(q-1)}. \tag{4.6}$$

In this $p > 2$ case, the area is dominated by small particles and A_{cum} is independent of D_{max}. If we assume that each particle has a mass of $m_p = \frac{4}{3}\pi\rho\frac{D^3}{8}$, where ρ is the density of a given particle, a cumulative mass, M_{cum}, can be calculated from a mass increment, dM:

$$dM = m_p\, dN \tag{4.7}$$

$$M_{cum} = \int_{D_{min}}^{D_{max}} \left(\frac{\pi\rho}{6}D^3\right) dN \tag{4.8}$$

If $p < 3$, which is true for collisional equilibrium, then the mass is dominated by large particles and the cumulative mass can be expressed as

$$M_{cum} = \frac{\pi\rho}{6}D_o^3\frac{1}{(3-p)}\frac{D_{max}}{D_o}^{(3-p)} \tag{4.9}$$

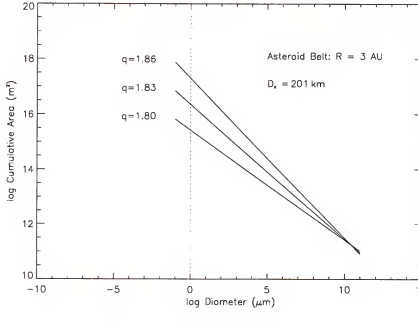

Figure 4-2: Cumulative surface area for the asteroid belt (assuming a D_o of $\approx$ 201 km, appropriate for a $D_{max} \approx 229$ km) associated with $q = 1.83$, the theoretical collisional equilibrium value of the size-frequency index (Dermott et al. 1999a).

There are two different ways to determine D_o. In the first method, we assume that the dust disk or dust band is formed from an original asteroid or Kuiper belt

object that has mass M_H and diameter D_H. If we take the diameter of the largest fragment, which has survived a dust generating impact, to be $x\ D_H$, where $x < 1$, we can write Equation 4.9 as

$$M_{cum} = M_H = \frac{\pi\rho}{6}\frac{D_o^3}{(3-p)}\left[\frac{xD_H}{D_o}\right]^{(3-p)} \tag{4.10}$$

where $x\ D_H$ has replaced D_{max} from Equation 4.9. For the calculations in this dissertation, x is assumed to be 0.5. With some manipulation and given that $M_H = \pi\rho D_H^3/6$, we can solve for D_o:

$$D_o = \left[\frac{(3-p)}{x^{(3-p)}}\right]^{1/p} D_H. \tag{4.11}$$

This approach is appropriate for a dust disk generated by one asteroid or KBO. It does not take into consideration multiple objects with the same D_{max}. Figure 4-2 shows the cumulative surface area of material associated with the distribution of particles in the asteroid belt assuming a D_o of $\sim$ 201 km for the $q = 1.83$ value for collisional equilibrium, as well as values of q that bracket the collisional equilibrium value (Dermott et al. 1999a). The geometrical area shown in Figure 4-2 increases linearly to infinity, but the effective geometrical area associated with particles composed of astronomical silicate remains at a constant value for particles $\leq 0.1\ \mu m$, since the emission efficiency of particles $< 0.1\ \mu m$ approaches zero. In addition, particles smaller than $\sim 1\ \mu m$ will tend to be ejected by radiation pressure or destroyed by collisions. Consequently, particles $< 0.1\ \mu m$ were not considered in the size distributions (Grogan 1997).

The second approach to obtaining a value for D_o is to assume an appropriate value for D_{max}, set M_{cum} equal to the total mass of the system for which the bodies have the same size-frequency index, and then solve Equation 4.9 for D_o. For the case of collisional equilibrium, D_{max} is the size of the largest body still in collisional equilibrium and M_{cum} is the total mass of the system for bodies with diameters in the range from D_{min} to D_{max}.

Both of the methods for determining D_o are appropriate for the dust bands and the background zodiacal cloud since all of the crucial parameters (q, D_{max}, and M_{cum}) are well constrained (Durda and Dermott 1997). Using data from the Palomar-Leiden Survey of faint asteroids, Durda and Dermott (1997) determined D_{max} for main belt asteroids to be 30 - 100 km, and determined q to be 1.78 ± 0.02, which is very close to the value for collisional equilibrium (i.e., $q = 1.83$). In addition, since $p < 3$, the mass is dominated by the large particles, that is, the asteroids. The mass of the asteroid belt is approximately $3 \times 10^{-4}\ M_{\oplus}$ (Cox 2000).

The size-frequency distribution of Kuiper belt objects, on the other hand, is poorly constrained. Only $\sim$ 430 KBOs have been discovered to date (Parker 2001), compared to several thousand asteroids, so the values for D_{max} and M_{cum} are less well constrained for the Kuiper belt than they are for the asteroid belt. This allows for a very wide range of D_o, on which A_{cum} and the total surface brightness of the cloud, $B_{total}(\lambda)$, depends highly. It is not known if the Kuiper belt is in collisional equilibrium, which means that the constraints on q are also poor. However, by making some reasonable choices for M_{cum}, D_{max}, and q, we attempt to calculate the surface brightness of the Kuiper disk. First, a value for M_{cum}, or the total mass of the Kuiper belt, M_{KB}, must be chosen. The total mass of the Kuiper belt is estimated to be $0.1 < M_{KB} < 0.3 M_{\oplus}$ (Backman et al. 1995, Jewitt et al. 1998). Jewitt et al. (1998) used Pluto's diameter ($D_{Pluto} \sim 2300$ km) as an initial estimate for D_{max} and through collisional modeling found no evidence of an upper limit for the diameters of Kuiper belt objects. However, a lower limit of $D_{max} > 500$ km has been established. In regard to the size frequency index, Jewitt et al. (1998) estimated that $1.83 \leq q \leq 2.17$, which is compatible with a collisional equilibrium size-frequency index. The Kuiper dust disk is predicted to be, at most, a few percent of the brightness of the zodiacal cloud (Dermott et al. 1999, Backman et al. 1995, Teplitz et al. 1999) from COBE upper limits. For the 60 μm wave band, Teplitz

et al. (1999) reports four different upper limits for the signal from the Kuiper belt, $I_{KB}(\nu)$. The estimated brightness is expected to be $0.3 < I_{KB}(\nu) < 16.0$ MJy/sr, though the high value is a poorly constrained upper limit.

By assuming a radial distance, R, an emissivity, $\epsilon(\nu)$, and an albedo, we can calculate the surface brightness, $B_{total}(\nu)$, of the dust at R. For the asteroid belt we assume a radial distance of 3 AU, an albedo of 0.06, and $\epsilon = 0.9$. For the Kuiper belt, we assume a radial distance of 40 AU, an emissivity of 0.9, and an albedo of 0.04. The expression for the brightness in terms of the cumulative area is given as

$$B_{total}(\nu) = A_{cum} \frac{1}{R} \frac{\epsilon(\nu) B_\nu}{\pi \sin(\theta)} \tag{4.12}$$

where B_ν is the black body Planck function given by

$$B_\nu = \frac{2h\nu^3}{c^2} \frac{1}{e^{h\nu/kT} - 1} \tag{4.13}$$

and θ denotes the latitude range over which we expect the dust torus to extend. For both the asteroid belt and the Kuiper belt, we assume $\theta \sim 10°$, which corresponds to the average inclination of a typical body in either disk. The mean inclination for a large main belt asteroid is roughly 10° and as mentioned previously the inclinations of the Plutinos ($10 \leq I \leq 20°$) bracket the value for Pluto ($I = 17°$), and 10° is therefore a conservative estimate for the extent of the Kuiper disk torus.

From Equation 4.12, the surface brightness of the dust torus that would be included in a line of sight (LOS) integration of, for instance a SIMUL model (See Appendix A), can be calculated. The beam size of the LOS integrator is dependent on three parameters: (1) *rstep*, the step size in radial direction, (2) *tstep*, the step size in ecliptic longitude, and (3) *pstep*: the step size in ecliptic latitude. *Rstep* is assumed to be zero since the dust particles for this first order estimate are all taken to lie at the same distance from the Sun, R. The smallest *tstep* for the integrator is 3°. (For comparison, each COBE pixel is roughly $0.32° \times 0.32°$ (Hauser et al. 1998).) The particles are assumed to have a maximum inclination, I, of 10°, making the

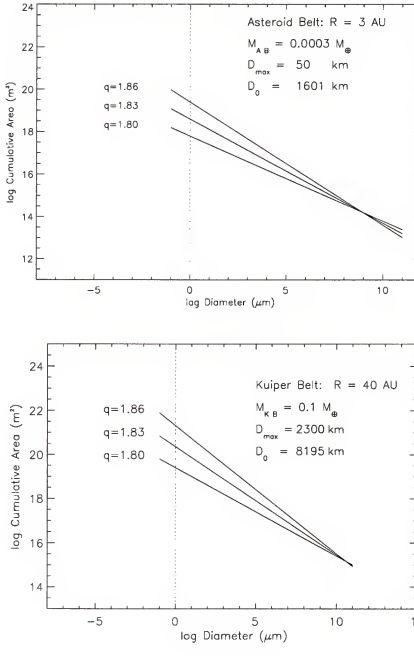

Figure 4-3: Cumulative surface area for the asteroid belt (top) assuming a $D_{max} = 50$ km and $M_{cum} = 0.0003 M_{\oplus}$ for size-frequency indices $q = 1.80, 1.83$, and 1.86. (bottom) The cumulative surface area for the Kuiper belt assuming a $D_{max} = 2300$ km, the diameter of Pluto, and $M_{cum} = 0.1 M_{\oplus}$ for size-frequency indices $q = 1.80, 1.83$, and 1.86.

height of the dust ring $2R\tan 10°$. In order to compare the total brightness to those obtained by the LOS integrator, we take a slice of the dust torus, which is defined by the step size of our LOS integrator in longitude (3°). The fractional slice, S_f is given by $3°/360° \approx 0.0083$, making the LOS brightness, $B_{LOS}(\nu)$ 0.83% of the total brightness, $B_{total}(\nu)$.

$$B_{LOS}(\nu) = S_f B_{total}(\nu). \tag{4.14}$$

The brightness values we calculate for the Kuiper disk in Figures 4-4 to 4-6 are much higher than all of the upper limits quoted by Teplitz et al. (1999). Although the upper limit of 16 MJy/sr does not seem too different from the results presented here, that limit is the weakest one since it is merely the full COBE DIRBE infrared signal given in Backman et al. (1995). The other limits of 0.3, 1.50, and 0.75 MJy/sr were obtained in the following fashion. The 1.50 MJy/sr limit is a 2 σ limit found by Hauser et al. (1999), while the 0.75 MJy/sr value was a standard deviation given by Hauser et al. (1999). The smallest limit for the 60 μm wave band, $I_{KB} = 0.3$ MJy/sr, was obtained by the subtraction of the component of the COBE data due to asteroidal emission using the Reach et al. (1998) zodiacal cloud model. In Chapter 5, we aim to further explore the subtraction of the zodiacal cloud component from the COBE data using a more sophisticated model than was available to Reach et al. (1998). In conclusion, at the present time, it is not possible to make reasonable predictions for the brightness of a Kuiper disk since the parameters used to determine the cumulative area distribution, M_{cum}, D_{max}, q, and even the albedo of dust particles in the Kuiper belt are not well enough determined for the task.

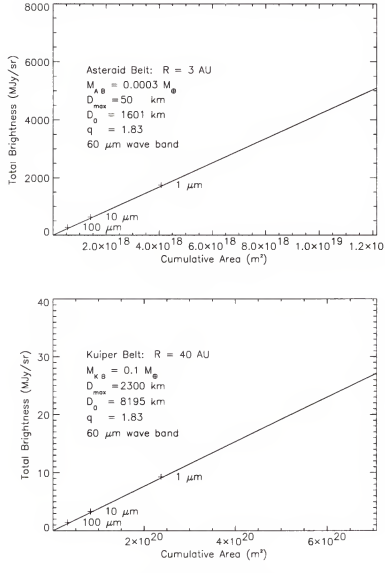

Figure 4-4: The total brightness in MJy/sr versus cumulative area for the asteroid belt (top) and Kuiper belt (bottom) assuming a cumulative mass of the Kuiper belt of $M_{cum} = 0.1M_\oplus$. The calculated brightness for the Kuiper belt is significantly higher than the upper limits given by Teplitz et al. (1999). The total brightness for the asteroid belt (top) is calculated for this dissertation assuming a density of $\rho = 2500$ kg/m^3, an albedo of 0.06, a constant emissivity of 0.9, $R = 3$ AU, $D_{maz} = 50$ km, and $M_{cum} = 0.0003M_\oplus$ for size-frequency indices $q = 1.80, 1.83$, and 1.86. (bottom) The total brightness for the Kuiper belt is calculated assuming an albedo of 0.04, a constant emissivity of 0.9, $R = 40$ AU, $D_{maz} = 2300$ km, $M_{cum} = 0.1M_\oplus$, and a density of 2030 kg/m^3 for size-frequency indices $q = 1.80, 1.83$, and 1.86. The predicted brightnesses are a function of particle diameter, and as such, the brightnesses corresponding to particles of 1, 10, and 100 μm are labeled with crosses.

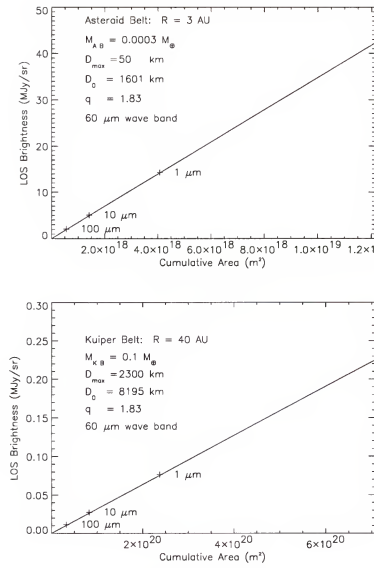

Figure 4-5: Line of sight (LOS) brightness in MJy/sr versus cumulative area for the asteroid belt (top) and Kuiper belt (bottom) assuming a cumulative mass of the Kuiper belt of $M_{cum} = 0.1M_\oplus$. The calculated brightness for the Kuiper belt is significantly higher than the upper limits given by Teplitz et al. (1999). The LOS brightness for the asteroid belt (top) is calculated assuming a density of $\rho = 2500$ kg/m^3, an albedo of 0.06, a constant emissivity of 0.9, $R = 3$ AU, $D_{max} = 50$ km, and $M_{cum} = 0.0003M_\oplus$ for size-frequency indices $q = 1.80, 1.83$, and 1.86. (bottom) We calculate the LOS brightness for the Kuiper belt assuming an albedo of 0.04, a constant emissivity of 0.9, $R = 40$ AU, $D_{max} = 2300$ km, $M_{cum} = 0.1M_\oplus$, and a density of 2030 kg/m^3 for size-frequency indices $q = 1.80, 1.83$, and 1.86. The predicted brightnesses are a function of particle diameter, and as such, the brightnesses corresponding to particles of 1, 10, and 100 μm are labeled with crosses.

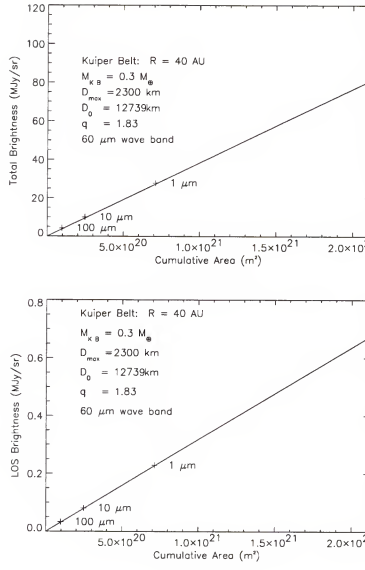

Figure 4-6: Total brightness (top) and LOS brightness (bottom) for the Kuiper belt with the same parameters in Figures 4-4 and 4-5 except that $M_{cum} = 0.3M_\oplus$. The brightness we calculate for the Kuiper belt is significantly higher than the upper limits given by Teplitz et al. (1999).

4.3 Resonant Structure: Mean Motion Resonances

If a Kuiper disk exists, it would most likely have a resonant structure, with two concentrations in brightness along the ecliptic longitude (see Figure 4-7). The structure arises from dust particles originating from the Plutinos, the Kuiper belt objects trapped in the 3:2 mean motion resonance with Neptune, meaning the particles orbit the Sun twice for every three times Neptune completes an orbit (See Figure 4-8). We build a simple model of a Plutino disk which is shown in Figure 4-7. The particles in the model are all one size: they are assumed to be large with a $\beta = F_{rad}/F_{grav} \approx 0$. The particles' orbits are distributed through a three dimensional array of cells and a Line of Sight Integrator allows the model to be viewed as it would appear in the 70 μm wave band in a coordinate frame that co-rotates with Neptune. Note the presence of the two lobes. A disk of particles trapped in a $p+1:p$ external mean motion resonance will have p lobes, which are located at the particle's pericenters. In the rotating frame, the lobes are caused by the fact that the angular velocity of the particles at pericenter becomes comparable to that of the velocity of the rotating frame (Murray and Dermott 1999). The circle in the middle represents the Sun and is not part of the model. The position of Neptune would lie 90° from the two lobes, since the Plutinos are aphelion librators. Essentially, Figure 4-7 represents a snapshot of how the resonant cloud would appear, since the lobes co-rotate with Neptune; the positions of the lobes will change with time with respect to a non-Neptunian reference point. For example, in January of 2001 Neptune's geocentric ecliptic longitude is $\sim 126°$ (U. S. Naval Observatory and Royal Greenwich Observatory 2001) and the geocentric ecliptic longitudes of the lobes would be 36° and 216°. In December of 2001 Neptune's geocentric ecliptic longitude is $\sim 128°$ and, correspondingly, the geocentric ecliptic longitudes of the lobes would be 38° and 218°, demonstrating that this signal is time varying. Since the Plutinos populate the densest and closest resonance to the inner edge of the Kuiper belt (see Figure 4-1), dust from these bodies would generate

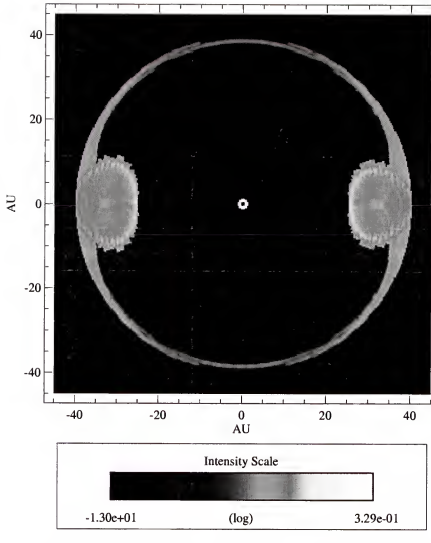

Figure 4-7: Model of a Plutino disk. The particles in the model are assumed to be large ($\approx 300\ \mu m$ in diameter) with a $\beta = F_{rad}/F_{grav} \approx$ zero. The particles' orbits are distributed through a three dimensional array of cells and a Line of Sight Integrator allows the model to be viewed as it would appear in the 70 μm wave band in a coordinate frame that co-rotates with Neptune. Note the presence of the two lobes. A disk of particles trapped in a $p+1 : p$ external mean motion resonance will have p lobes, which are located at the particle's pericenters. In the rotating frame, the lobes are caused by the fact that the angular velocity of the particles at pericenter becomes comparable to that of the velocity of the rotating frame (Murray and Dermott 1999). The circle in the middle represents the Sun and is not part of the model. The position of Neptune would lie 90° from the two lobes, since the Plutinos are aphelion librators.

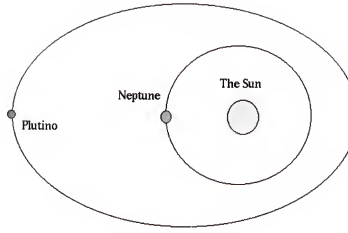

Figure 4-8: A Plutino in the 3:2 mean motion resonance with Neptune. The Plutino will orbit the Sun twice for every three times that Neptune completes an orbit.

the brightest emission. This Plutino resonant ring is similar in nature to the resonant ring of dust particles co-rotating with the Earth (Dermott et al. 1994b, Jayaraman 1995, Jayaraman et al. 2001). Ultimately, the resonant structure in the Kuiper disk may be detectable using data from COBE or SIRTF. The main impediment to detecting the Plutino ring is that, since it is located at approximately 39.4 AU, it will be very faint. Many brighter layers of emission will need to be subtracted from the data before the faint residuals can be studied for traces of the Plutino resonant structure. A search for the resonant structure in the Kuiper disk in the COBE DIRBE weekly skymap data set is detailed in Chapter 5. Shown in Figure 4-9 is a similar model to that shown in Figure 4-7 but with a non-zero libration width. Note how the lobes are still visible, but have a smoothed appearance.

The goal of the following subsections is to calculate, first analytically and then numerically, the percentage of particles that stay in or become trapped in the 3:2 mean motion resonance for a given set of initial conditions.

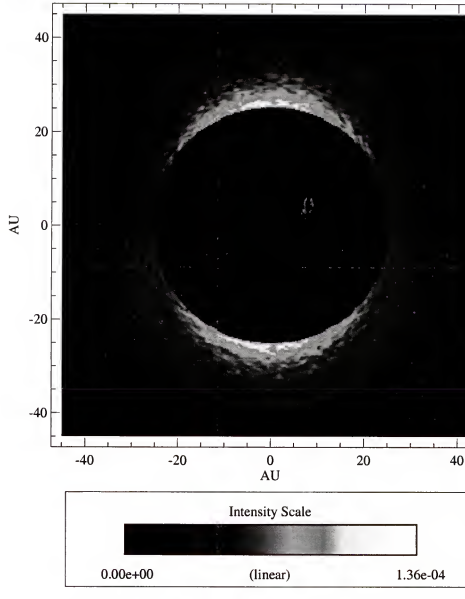

Figure 4-9: A model of a Kuiper disk from asteroidal particles (with a distribution of eccentricities and inclinations) in the 3:2 mean motion resonance with Neptune with a non zero libration amplitude. This model is similar to that in Figure 4-7 but with a non-zero libration width, which is represented by a Gaussian distribution of width $\sim$ 30°. The two lobes are still visible but have a smoothed appearance.

4.3.1 Source Bodies

Particles are generated in the Kuiper belt by the breakup of Kuiper belt objects. If a parent body has orbital elements (a_s, e_s, I_s Ω_s, $\tilde{\omega}_s$), then the collisional

by products of that parent body have a range of orbital elements (Δa, Δe, ΔI, $\Delta\Omega$, $\Delta\tilde{\omega}$). We can determine if particles will stay in a given resonance by comparing Δa with the libration width, $\delta a'_{max}$, for that particular resonance. If

$$\Delta a < \delta a'_{max} \tag{4.15}$$

then particles will stay in the resonance, at least initially. We can calculate Δa by making the following assumptions. The escape velocity a particle needs to leave its parent body is

$$v_{esc} = \sqrt{\frac{2GM_s}{R_s}} \tag{4.16}$$

where G = 6.67 x 10^{-8} cm^3 g^{-1} s^{-2} is the solar gravitational constant and M_s and R_s are the mass and radius of the parent body, respectively. Gauss's equations of motion (Brouwer and Clemence 1961; Zappalà et al. 1984) can be used to relate changes in orbital elements of the particle with changes in velocity. By assuming a certain velocity dispersion, we can deduce a maximum dispersion in semi-major axis which can be compared to the libration width. Gauss's equations are

$$\Delta a = \frac{2}{n'\sqrt{1-e'^2}}\left[(1+e'\cos f')\,\Delta v_t + e'\sin f'\,\Delta v_r\right] \tag{4.17}$$

$$\Delta e = \frac{\sqrt{1-e'^2}}{n'a'}\left[\frac{(e'+2\cos f'+e'\cos^2 f')}{1+e'\cos f'}\,\Delta v_t + \sin f'\,\Delta v_r\right] \tag{4.18}$$

$$\Delta I = \frac{\sqrt{1-e'^2}}{n'a'}\left[\frac{\cos(\omega'+f')}{1+e'\cos f'}\right]\Delta v_\perp \tag{4.19}$$

where Δv_t, Δv_r, and $\Delta v_\perp$ are the dispersions in the tangential, radial, and perpendicular components of the particles' velocities, respectively. Zappalà et al. (1984) estimate the average components of the velocity dispersion are equal to each other ($\Delta v_t \cong \Delta v_r \cong \Delta v_\perp$) and the sum of the squares of each component roughly equals the average escape velocity of the particles. Thus, if we assume the collisions disperse particles isotropically, we can derive an estimate of the dispersion in tangential

velocity from the escape velocity:

$$\Delta v_t \cong \Delta v_r \cong \Delta v_\perp \cong \frac{v_{esc}}{\sqrt{3}} \tag{4.20}$$

The mean motion of the particle, n, can be calculated assuming it depends on the semi-major axis of the resonance. In the case of the 3:2 External resonance with Neptune, $a' = 39.4$ AU and $n' = 2\pi/a'^{3/2} = 2.54 \times 10^{-2}\ yr^{-1}$. So, Δa can now be written as

$$\Delta a \cong R_s \left(\frac{2}{3} a'^{3/2} \sqrt{\frac{2G\rho_s}{\pi}} \right) \tag{4.21}$$

where ρ_s is the density of the parent body ($\rho_s \cong 2\ \mathrm{g}/cm^3$ for the Plutinos). From

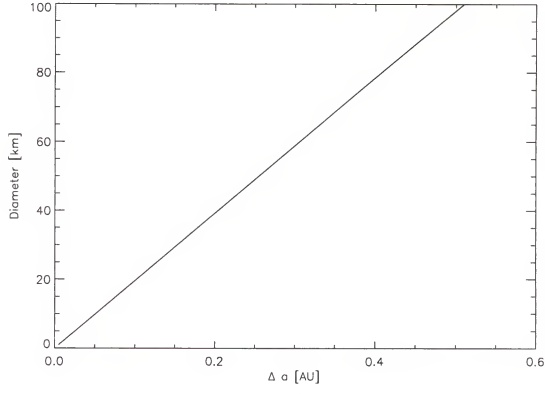

Figure 4-10: Δa, in AU, as a function of the diameter, in km, of the parent Plutino from which the the dust particles escape. Note that Δa is a linear function of diameter. The parent Plutino is assumed to have a semi-major axis of 39.4 AU and to lie in the 3:2 mean motion resonance with Neptune.

Equation 4.21, we can see that Δa is a function of R_s and the semi-major axis at

which the resonance is located. Figure 4-10 shows the variation in Δa for different sized source bodies. Collisions between particles are not considered for the sake of simplicity. However, in future work, a collisional model such at that described in Gustafson et al. (1992) could be applied to the breakup of KBO source bodies.

4.3.2 Analytical Predictions for Trapping

Micron sized dust particles can be generated in the Kuiper belt by the breakup of Kuiper belt objects. The sizes of the source bodies and the sizes of the particles themselves determine whether the particles will become trapped in a particular resonance. For instance, particles generated from a parent body larger than $\sim$ 60 km in diameter will not all become trapped in the resonance, since the dispersion in initial semi-major axis of dust particles that escape from a 60 km diameter source body will be greater than the libration width.

Trapping is also a function of the size of the particle. For particles less than $\sim$ 500 μm, radiation pressure plays a significant role. The location of the resonance is a function of β, where β is equal to the ratio of radiation pressure force to the force of gravity (see Equation 2.4). As β increases, the location of the resonance, a', moves further inward (see Table 4-1).

$$a' = a'_{\beta=0}\,(1-\beta)^{1/3}$$

$$= a_n \left(\frac{p+q}{p}\right)^{2/3} (1-\beta)^{1/3} \tag{4.22}$$

$$n' = \sqrt{\frac{GM_\odot\,(1-\beta)}{a'^3}} \tag{4.23}$$

Particles with a high enough value of β will get "blown out" of the maximum libration width and will not remain in resonance, at least initially. Due to Poynting-Robertson light drag, they could eventually spiral into orbits with smaller and smaller semi-major axes until they become trapped in the resonance, or they could become trapped

Table 4-1: Location of the 3:2 external mean motion resonance as a function of $\beta = F_{rad}/F_{grav}$

Sphere Diameter (μm)	β	a'_{β} (AU)
4	0.12928	37.61
7	0.07104	38.43
10	0.04868	38.74
13	0.03688	38.90
20	0.02343	39.08
50	0.00905	39.27
100	0.00446	39.33
–	0	39.39

Location of the 3:2 external mean motion resonance as a function of $\beta = F_{rad}/F_{grav}$. The particle diameters are obtained by assuming the particles are spheres composed of astronomical silicate. However, the calculations in this dissertation are performed as a function of β, which allows for a wider assumption of particle sizes and shapes. β is highly dependent on particle mass, but less dependent on particle shape or structure (Gustafson et al. 2001).

in the other resonances that populate the inner Kuiper belt, such as the 2:1 or the 5:3 mean motion resonances. It is necessary to run numerical integrations to understand this complicated behavior; however we can make some analytical predictions about it.

Neglecting all forces except PR drag, radiation pressure, and gravity, we can calculate the minimum value of the eccentricity a particle needs to have to become trapped in the 3:2 resonance, as well as the smallest size particle, corresponding to a maximum value of β, that can be trapped (Dermott et al. 1988, Weidenschilling and Jackson 1993, Jayaraman 1995).

To find the minimum eccentricity a particle must have to become trapped in an external mean motion resonance, we must equate the magnitude of the change in semi-major axis with time due to resonant trapping, $\frac{da'}{dt}|_{res}$, with the change in semi-major axis with time due to PR drag, $\frac{da'}{dt}|_{PR}$. Using Equation 2.62, we can take

$\dot{n}' = 0$ and, assuming the eccentricities of the particles are $\gtrsim 0.01$, we can neglect $\ddot{\omega}'$. From Equations 2.33, 2.38, and 2.32 of Lagrange's equations, we can write

$$\frac{da'}{dt}|_{res} = \frac{2}{n'a'}\frac{\partial R'_{res}}{\partial \lambda'} \tag{4.24}$$

$$= -\frac{2\,(p+q)\,M_n\,f_d(\alpha)\,e'\sin\varphi}{M_\odot\,n'\,a'^2}$$

$$= -2\,n'\,a'\,(M_n/M_\odot)\,(p+q)\,f_d(\alpha)\,e'\sin\varphi. \tag{4.25}$$

Rewriting Equation 2.8, in terms of the primed quantities:

$$\frac{da'}{dt}|_{PR} = -\frac{GM_\odot\,\beta}{a'c}\frac{(2+3e'^2)}{(1-e'^2)^{3/2}} \tag{4.26}$$

where c is the speed of light. When a particle is trapped in resonance, $\frac{da'}{dt}|_{res}$ almost exactly balances $\frac{da'}{dt}|_{PR}$ and we can write

$$\frac{da'}{dt}|_{res} + \frac{da'}{dt}|_{PR} \approx 0 \tag{4.27}$$

which can be solved for $\sin\varphi$, using Equations 4.26, 4.24, 4.22, and 4.23 to yield

$$\sin\varphi = -\frac{(GM_\odot)^{1/2}}{2\,f_d(\alpha)\,\mu_n\,c}\frac{p^{1/3}}{(p+q)^{4/3}}\frac{\beta}{a_n^{1/2}\,(1-\beta)^{2/3}}\frac{(2+3e'^2)}{e'\,(1-e'^2)^{3/2}} \tag{4.28}$$

where $\mu_n = GM_n$. Due to the momentum loss PR drag induces, $\frac{da'}{dt}|_{PR}$ is a negative quantity, which implies that $\frac{da'}{dt}|_{res}$ is positive and therefore that $\sin\varphi$ is negative. The maximum negative value of $\sin\varphi$, which of course is -1, will provide the largest resonant torque (Weidenschilling and Jackson 1993). By setting $\sin\varphi = -1$ in Equation 4.27 and solving for e', we can find the minimum value of eccentricity a particle needs to have in order to become trapped in a given resonance, e'_{min}, since $\frac{da'}{dt}|_{res}$ is a maximum. Neglecting terms of order e'^2 and higher and solving for e' yields

$$e'_{min} \gtrsim \frac{(GM_\odot)^{1/2}}{f_d(\alpha)\,\mu_n\,c}\frac{p^{1/3}}{(p+q)^{4/3}}\frac{\beta}{a_n^{1/2}\,(1-\beta)^{2/3}}. \tag{4.29}$$

We can then solve Equation 4.29 for β in order to determine β_{max}, the maximum value of β a particle can have and still remain trapped in a given resonance. Since

β is a function of particle size, β_{max} gives a limit on the smallest particles that can be trapped in resonance. Unfortunately, Equation 4.29 can not be easily solved for β_{max} since it is not a simple function of β and since $f_d(\alpha)$ and a', which is really a'_β, are functions of β. Nevertheless, an approximate expression for β_{max} can be written as

$$\frac{\beta_{max}}{(1-\beta_{max})^{2/3}} \lesssim \frac{e'\, a_n^{1/2}\, f_d(\alpha)\, \mu_n\, c}{(GM_\odot)^{1/2}}\, \frac{(p+q)^{4/3}}{p^{1/3}} \tag{4.30}$$

For $e' = 0.05$, $0.13 \lesssim \beta_{max} \lesssim 0.64$, which corresponds to a particle diameter, d, of roughly $1\mu m \lesssim d \lesssim 4\mu m$ assuming a spherical particle composed of astronomical silicate. β_{max} is somewhat challenging to calculate since the right side of Equation 4.30 is also a function of β_{max}, since α and $f_d(\alpha)$ are functions of β. Another value of interest is the maximum value of eccentricity, e'_{max} a particle can have in a given resonance. As derived in Weidenschilling and Jackson (1993), this maximum value is given as

$$e'_{max} = \sqrt{\frac{2}{5(p+q)}} \tag{4.31}$$

neglecting terms higher than order e'^2. The derivation is based on analysis of the evolution of the eccentricity as a function of time, but will not be discussed in this dissertation. Values for e'_{min} and e'_{max} are given in Table 4-2 as a function of p, q, and β. Two other important quantities remain to be discussed, the critical value of the eccentricity, e'_{crit}, and the capture probability, $P_{capture}$. For a first order resonance ($q = 1$), the critical value of eccentricity is given as

$$e'_{crit} = \left[\frac{2\sqrt{6}\,(M_n/M_\odot)\,\alpha^3\, f_d(\alpha)}{p^2}\right]^{1/3} \tag{4.32}$$

where we have assumed that the mass of the dust particle is zero (Dermott, Malhotra, and Murray 1988). The probability of capture into a first order resonance, $P_{capture}$, can be determined from e'_{crit}. From Dermott, Malhotra, and Murray (1988):

$$P_{capture} = \begin{cases} 1 & \text{for } e' < e'_{crit} \\ \dfrac{2}{\pi 3^{3/4}} \left(\dfrac{e'_{crit}}{e'}\right)^{3/2} & \text{for } e' \gg e'_{crit}. \end{cases} \tag{4.33}$$

It should be noted that the equations for e'_{crit} and $P_{capture}$ are applicable only under

Table 4-2: Critical parameters on 10 and 100 μm diameter dust particles for $e' = 0.05$ and $e' = 0.25$.

						Sphere Diameter 10 μm ($\beta = 0.04868$)			
		Resonance							
p	q	(p+q):p	e'	α	$f_d(\alpha)$	e'_{min}	e'_{max}	e'_{crit}	$P_{capture}$
2	1	3:2	0.050	0.776	2.641	0.00196	0.365	0.0426	21.985 %
2	1	3:2	0.250	0.776	2.641	0.00196	0.365	0.0426	1.966 %
1	1	2:1	0.050	0.641	1.740	0.0135	0.447	0.0325	14.649 %
1	1	2:1	0.250	0.641	1.740	0.0135	0.447	0.0325	1.310 %
						Sphere Diameter 100 μm ($\beta = 0.00446$)			
		Resonance							
p	q	(p+q):p	e'	α	$f_d(\alpha)$	e'_{min}	e'_{max}	e'_{crit}	$P_{capture}$
2	1	3:2	0.050	0.764	2.497	0.000184	0.365	0.0412	20.898 %
2	1	3:2	0.250	0.764	2.497	0.000184	0.365	0.0412	1.869 %
1	1	2:1	0.050	0.631	1.693	0.00144	0.447	0.0302	13.107 %
1	1	2:1	0.250	0.631	1.693	0.00144	0.447	0.0302	1.172 %

Critical parameters on 10 and 100 μm diameter dust particles for $e' = 0.05$ and $e' = 0.25$. Note, that for the 2:1 resonance, the indirect term of the disturbing function must be taken into account, $f_i(\alpha) = -0.5/\alpha$ (Murray and Dermott 1999). The semi-major axis of Neptune, a_n, is taken to be 30.06 AU, making $\alpha = 30.06/a'$.

the adiabatic criterion, which states that the change in semi-major axis due to drag (in this case, PR drag) in one libration period should be much less than the $\delta a'_{max}$, the resonant libration width:

$$\frac{da'}{dt}|_{PR}\, T_{lib} \ll \delta a'_{max} \tag{4.34}$$

As discussed in Dermott, Malhotra, and Murray (1988), the adiabatic criterion is valid only for well separated resonances. To determine whether the Kuiper disk is in the adiabatic region, we chose $T_{lib} = 19{,}670$ yr, the libration period of Pluto, since the pendulum model does not provide accurate values for the libration period for the 3:2 resonance with Neptune. Using Equations 2.71 and 4.26, for an eccentricity $e' = 0.25$ and $\beta = 0.04868$ (for a $10\mu m$ diameter spherical particle), $\frac{da'}{dt}|_{PR} = 1.89 \times 10^{-6}$

AU/yr, and $\delta a'_{max} \approx 0.52$ AU, so that $\frac{da'}{dt}|_{PR}\, T_{lib} = 0.037$ AU, which is, indeed, much less than the libration width of 0.52 AU, and therefore dust particles in the 3:2 mean motion resonance with Neptune are in the adiabatic regime.

4.3.3 Other Resonances

Table 4-2 also lists some parameters for the 2:1 resonance. The 2:1 resonance is a special case of an external resonance since when $p = 1$, the indirect term of the expansion of the disturbing function, $f_i(\alpha)$, must be taken into account. Taking into account the extra factor of α in front of $f_d(\alpha)$ for external resonances in Equation 2.56, Equation 2.60 can now be written

$$C'_r = \left(\frac{GM_n}{a'^2\, a_n\, n'}\right)\left[f_d(\alpha) + \frac{f_i(\alpha)}{\alpha}\right] \tag{4.35}$$

where $f_i(\alpha) = -1/(2\alpha)$. This in turn can be used to calculate the libration width for the 2:1 resonance. By following Murray and Dermott (1999), we calculate the libration widths for the 5:3 and the 6:4 resonances. Since they are second order resonances, the shape of their libration widths are different than those of the 2:1 and 3:2 resonances.

4.3.4 Additional Forces

In the preceding discussion, we have neglected all forces except radiation pressure, gravity, and PR drag. However, other forces such as the Lorentz force and the effect of neutral interstellar gas drag are important to Kuiper dust grains. For instance, Lorentz forces become important for small particles at large heliocentric distances since the Lorentz force varies as $1/r$ while gravity and radiation pressure vary as $1/r^2$ (Gustafson 1994). These additional forces are not incorporated in the theory, so instead they must be included in numerical simulations.

We calculate the magnitude of various forces (in Newtons) on dust particles of different βs (assuming the particles are spheres with diameter $= d$) and present them in Table 4-3, assuming a given particle has a density of $\rho = 2.5$ g/cm^3, a mass

of m_{dust}, a semi-major axis, a where $a = r = 39.4$ AU, and an eccentricity $e = 0$. In this case, the heliocentric velocity of the particle is given by $v = \sqrt{GM_{\odot}/a} = 4.7454$ km/s. Recall that 1 N = 1 kg m /s^2, and that G = 6.67 x 10^{-11} N m^2/kg^2. The mass of the Sun, $M_{\odot}$, is taken to be 1.99×10^{30} kg. The solar wind velocity is taken to be 400 km/s, and B_o is $\sim$ 3 nano Tesla = 3×10^{-9} N s m^{-1} C^{-1}. The charge, q, on the dust particle is $q = 4\pi\epsilon_o Ud/2$, where $\epsilon_o = 8.86 \times 10^{-12}$ C V^{-1}m^{-1} is the permeability of a vacuum. The force of gravity, F_{grav}, is defined in Equation 2.1. The force due to radiation pressure, F_{rad}, is given by Equation 2.3. The force due to Poynting-Robertson Light Drag, F_{PR}, is represented by the second and third terms in Equation 2.7. The Lorentz Force, F_L, is defined in Equation 2.14 and for the above calculations, we chose the azimuth angle, ϕ, to be 0° and the heliocentric colatitude angle, θ, to be 45°. Lastly, F_H, the force due to neutral interstellar gas particles impacting the dust grains, is given by Equation 2.20. Additional constants and assumptions are given in Chapter 2.

The ratios of the forces in Table 4-3 are shown in Table 4-4. In the case of the 10 μm diameter Kuiper disk particle, we see that the ratio of the radiation pressure force to the force of gravity ($|F_{rad}/F_{grav}| = 4.9 \times 10^{-2}$) is the same order of magnitude as the ratio of the Lorentz force to the force of gravity ($|F_L/F_{grav}| = 1.2 \times 10^{-2}$ for $U = 5$ V). However, for the 100 μm particle, the ratio of the radiation pressure force to the force of gravity ($|F_{rad}/F_{grav}| = 4.5 \times 10^{-3}$) is an order of magnitude greater than the ratio of the Lorentz force to the force of gravity ($|F_L/F_{grav}| = 1.2 \times 10^{-4}$ for $U = 5$ V), making the Lorentz force much less important for larger particles. For both the 10 and 100 μm size particles, the magnitude of the ratio of the PR drag force to the force of gravity is the same order of magnitude as the magnitude of the ratio of the neutral interstellar gas drag force to the force of gravity, and in both cases the ratio is four orders of magnitude less than $|F_{rad}/F_{grav}|$.

Table 4-3: Magnitude of various forces on 10 μm (β = 0.04868) and 100 μm (β = 0.00446) diameter spheroidal dust particles.

	Sphere Diameter	
	10 μm	100 μm
$\beta = F_{rad}/\|F_{grav}\|$	0.04868	0.00446
$a = r$	39.4 AU	39.4 AU
m_{dust}	1.3 x 10^{-12} kg	1.3 x 10^{-9} kg
$\|F_{grav}\|$	5.0 x 10^{-18} N	5.0 x 10^{-15} N
$\|F_{rad}\|$	2.4 x 10^{-19} N	2.2 x 10^{-17} N
$\|F_{PR}\|$	9.5 x 10^{-24} N	8.7 x 10^{-22} N
$\|F_L\|$ ($U = 5V$)	6.1 x 10^{-20} N	6.1 x 10^{-19} N
$\|F_L\|$ ($U = 20V$)	2.4 x 10^{-19} N	2.4 x 10^{-18} N
$\|F_H\|$ ($C_D = 1$)	1.2 x 10^{-23} N	1.2 x 10^{-21} N

Magnitude of various forces (in Newtons) on 10 μm ($\beta = 0.04868$) and 100 μm ($\beta = 0.00446$) diameter spheroidal dust particles. A given particle has a density of ρ = 2.5 g/cm^3, a mass of m_{dust}, a semi-major axis, a where a = r = 39.4 au, assuming the eccentricity of the dust particle is zero. In this case, the heliocentric velocity of the particle is given by v = $\sqrt{GM_\odot/a}$ = 4.7454 km/s. Recall that 1 N = 1 kg m /s^2, and that G = 6.67 x 10^{-11} N m^2/kg^2. The mass of the Sun, $M_\odot$, is taken to be 1.99 x 10^{30} kg. The solar wind velocity is taken to be 400 km/s, and B_o is $\sim$ 3 nano Tesla = 3 x 10^{-9} N s m^{-1} C^{-1}. The charge, q, on the dust particle is q = $4\pi\epsilon_o Ud/2$, where ϵ_o = 8.86 x 10^{-12} C V^{-1}m^{-1} is the permeability of a vacuum. F_{grav}, the force of gravity, is defined in Equation 2.1. F_{rad}, the force due to radiation pressure, is given by Equation 2.3. F_{PR}, the force due to Poynting-Robertson Light Drag, is represented by the second and third terms in Equation 2.7. The Lorentz Force, F_L, is defined in Equation 2.14 and for the above calculations, we chose the azimuth angle, ϕ, to be 0° and the heliocentric colatitude angle, θ, to be 45°. Lastly, F_H, the force due to neutral interstellar gas particles impacting the dust grains, is given by Equation 2.20. Additional constants and assumptions are given in Chapter 2.

4.3.5 Numerical Integrations

We use the numerical integrator RADAU (Everhart 1989) to find the percentages of particles in resonance for a variety of initial conditions. RADAU is a very accurate integration code which employs the Runge-Kutta method with Gauss-Radau spacings. We chose a precision factor of 10^{-10} for high accuracy. RADAU is very flexible, allowing the introduction of additional forces. Most of our runs have

Table 4-4: Ratios of the magnitude of the forces on a 10 μm ($\beta = 0.04868$) and 100 μm ($\beta = 0.00446$) dust particle.

	Sphere Diameter	
	10 μm	100 μm
$\lvert F_{rad}/F_{grav}\rvert = \beta$	4.9 x 10^{-2}	4.5 x 10^{-3}
$\lvert F_{PR}/F_{grav}\rvert$	1.9 x 10^{-6}	1.7 x 10^{-7}
$\lvert F_L/F_{grav}\rvert$ ($U = 5\ V$)	1.2 x 10^{-2}	1.2 x 10^{-4}
$\lvert F_L/F_{grav}\rvert$ ($U = 20\ V$)	4.8 x 10^{-2}	4.8 x 10^{-4}
$\lvert F_H/F_{grav}\rvert$ ($C_D = 1$)	2.4 x 10^{-6}	2.4 x 10^{-7}

Ratios of the magnitude of the forces on a 10 μm ($\beta = 0.04868$) and 100 μm ($\beta = 0.00446$) dust particle. See Table 4-3.

249 particles, giving an accuracy in the estimate of the number of particles in resonance of $\sim \sqrt{N_r}/N_r$, where N_r is the number of particles in resonance. When N_r was zero, the error was estimated to be approximately zero. In order to decrease the error, we increase the total number of particles to 1017 for a small number of runs The integrations were run for 250,000 years and the orbital elements of the particles were output every 100 years so we could obtain an accurate variation of the resonant argument. The integrator considers Poynting-Robertson drag, solar wind drag, radiation pressure, and the effects of the gravitational perturbations of seven planets (Mercury and Pluto are excluded from consideration since their masses are very low). In addition, in some of the runs, we have considered the effect of the Lorentz force on the particles as well as the effect of neutral interstellar gas drag. Runs have been completed for particles ejected from source bodies of 0 km, 10 km, and 100 km with a variety of sizes: 4, 10, 20, 50, 100 μm diameter spherical astronomical silicate particles (corresponding to $\beta = 0.12928$, 0.04868, 0.02343, 0.00905, and 0.00446) and the $\beta = 0$, or no drag case. We also run several cases for particles having a $\beta =$ 0.07104 and 0.03688, corresponding to 7 and 13 μm spherical particles composed of

astronomical silicate. We find that as β increases, the percentage of particles in the 3:2 mean motion resonance decreases.

Shown in Figures 4-11 and 4-12 is an example of a particle (particle 1 from RADAU run plu_0km_nodrag_250) which is in the 3:2 mean motion resonance with Neptune for the entire length of the integration. The eccentricity versus semi-major axis for particle 1 is plotted in Figure 4-11. The run (plu_0km_nodrag_250) consists of 249 particles integrated for 250,000 years and includes the effects of the gravitational perturbations of seven planets. The particles, having a β equal to zero, were released from a 0 km source body in a Pluto-like orbit. Each diamond represents the particle's orbital elements at 100 year intervals. The 3:2, 5:3, and 2:1 maximum libration widths are shown as solid lines while the 6:4 maximum libration width is shown as a dashed line. The exact location for each resonance is plotted as a dotted line. It is clear that particle 1 is trapped in the 3:2 mean motion resonance with Neptune since for the majority of the time, the particle stays within the 3:2 libration width. In Figure 4-12, it becomes apparent that particle 1 is indeed trapped in the 3:2 resonance for the entire 250,000 years.

Figure 4-12 shows the variation of semi-major axis, resonant argument, and eccentricity with time for particle 1 in the plu_0km_nodrag_250 RADAU run. The exact location for 3:2 resonance for the $\beta = 0$ case is plotted as a dotted line. The semi-major axis of particle 1 is clearly librating around the exact location of the 3:2 resonance. The resonant argument, φ, is very clearly librating showing that the particle is trapped in the 3:2 resonance for the entire integration time of 250,000 years. Also plotted is the variation of the eccentricity with time. The dashed line is the value of e_{max}, the maximum value of eccentricity a particle trapped in the 3:2 resonance can reach. As expected, the particle's eccentricity never reaches e_{max} for the no drag case.

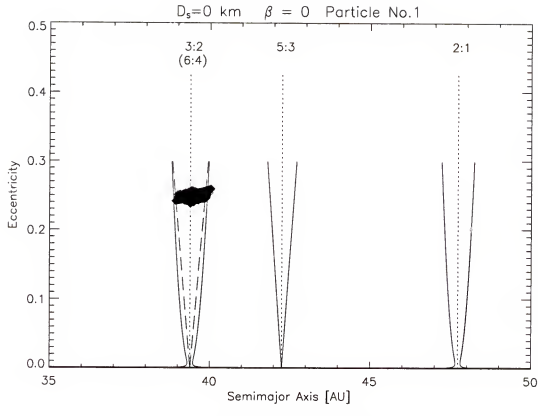

Figure 4-11: Eccentricity versus semi-major axis for particle 1 in a RADAU run for the no drag case ($\beta = 0$) including the effects of the gravitational perturbations of seven planets. Mercury and Pluto are excluded. The run (plu_0km_nodrag_250), consist of 249 particles integrated for 250,000 years. The particles, having a β equal to zero, were released from a 0 km source body in a Pluto-like orbit. Each diamond represents the particle's orbital elements at 100 year intervals. The 3:2, 5:3, and 2:1 libration widths are shown as solid lines while the 6:4 libration width is shown as a dashed line. The exact location for each resonance is plotted as a dotted line. It is clear that particle 1 is trapped in the 3:2 mean motion resonance with Neptune since for the majority of the time, the particle stays within the 3:2 libration width. In Figure 4-12, it becomes apparent that particle 1 is indeed trapped in the 3:2 resonance for the entire 250,000 years. None of the particles in this run were excluded from the system.

Not all particles that are captured spend the whole time trapped in resonance. Shown in Figures 4-13 and 4-16 is a particle which is initially trapped in the 3:2 resonance. Particle 10 remains in the 3:2 resonance for approximately 160,000 years, but then escapes the resonance. Its semi-major axis and eccentricity both increase

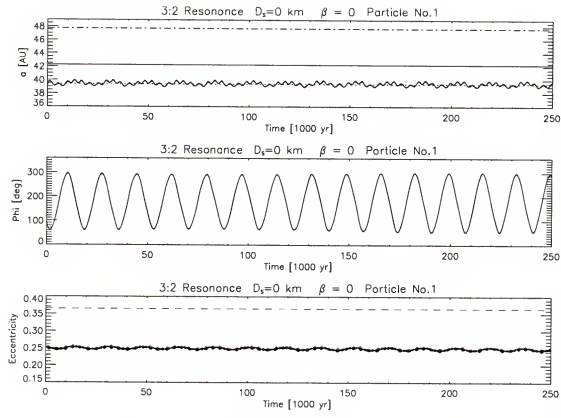
3:2 Resonance D=0 km β = 0 Particle No.1
a [AU]
Time [1000 yr]
3:2 Resonance D=0 km β = 0 Particle No.1
Phi [deg]
Time [1000 yr]
3:2 Resonance D=0 km β = 0 Particle No.1
Eccentricity
Time [1000 yr]

Figure 4-12: Variation of semi-major axis, resonant argument, and eccentricity with time for particle 1 in a RADAU run for the no drag case ($\beta = 0$) including the gravitational effects of seven planets. Mercury and Pluto are excluded. The run (plu_0km_nodrag_250), consists of 249 particles integrated for 250,000 years. The particles, having a β equal to zero, were released from a 0 km source body in a Pluto-like orbit. (Top) The variation of semi-major axis, a, with time. The exact location for 3:2 resonance for the $\beta = 0$ case is plotted as a dotted line. The exact locations of the 5:3 and 2:1 resonances are plotted as a solid line and as a dash-dot line, respectively. The semi-major axis of particle 1 is clearly librating around the exact location of the 3:2 resonance. (Middle) The variation of the resonant argument for the 3:2 resonance (where $j_1 = 3$, $j_2 = -2$, $j_3 = -1$, $j_4 = 0$, $j_5 = 0$, and $j_6 = 0$) with time. The resonant argument is librating the entire time showing that the particle is trapped in the 3:2 resonance for the entire integration time of 250,000 years. (Bottom) The variation of the eccentricity with time for particle 1. The dashed line is the value of e_{max}, the maximum value of eccentricity a particle trapped in the 3:2 resonance can reach. As expected, the particle's eccentricity never reaches e_{max} in this no drag case.

until it is very briefly trapped in the 5:3 resonance (for 8,600 years). A separate plot, which is not shown, of the resonant argument for the 5:3 resonance (where $j_1 = 5$,

$j_2 = -3$, $j_3 = -2$, $j_4 = 0$, $j_5 = 0$, and $j_6 = 0$) confirms that the resonant argument is librating for a short time.

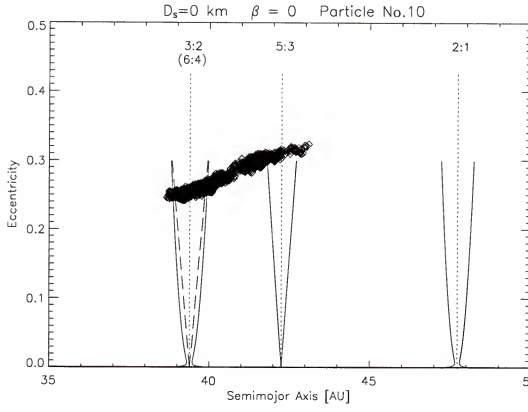

Figure 4-13: Eccentricity versus semi-major axis for particle 10 in a RADAU run for the no drag case ($\beta = 0$) including the gravitational effects of seven planets. The run (plu_0km_nodrag_250), consist of 249 particles integrated for 250,000 years. The particles, having a β equal to zero, were released from a 0 km source body in a Pluto-like orbit. Each diamond represents the particle's orbital elements at 100 year intervals. The 3:2, 5:3, and 2:1 libration widths are shown as solid lines while the 6:4 libration width is shown as a dashed line. The exact location for each resonance is plotted as a dotted line. Initially, particle 10 is trapped in the 3:2 resonance, but after about 160,000 years, the particle escapes from the 3:2 resonance and eventually becomes briefly trapped in the 5:3 resonance.

Not all particles that appear to be trapped in a resonance are actually in resonance. Although Figure 4-15 is similar in appearance to Figure 4-13, particle 10 for RADAU run lorplu_0km_nodrag_250 is not trapped in the 5:3 resonance for any

length of time. Particle 10 in the run lorplu_0km_nodrag_250 had the same initial conditions as particle 10 in the run plu_0km_nodrag_250.

Shown in Figure 4-17 is the eccentricity versus semi-major axis for particle 10 in RADAU run ismplu_0km_nodrag_250. The run consists of 249 particles integrated for 250,000 years, and includes the effects of gravity, the Lorentz force ($U = 5\ V$) and the effects of neutral interstellar gas drag ($C_D = 1$). The run (ismplu_0km_nodrag_-250), consists of 249 particles integrated for 250,000 years. The particles, having a β equal to zero, were released from a 0 km source body in a Pluto-like orbit. The top panel of Figure 4-18 shows the variation of semi-major axis, a, with time. The semi-major axis of particle 10 is clearly librating around the exact location of the 3:2 resonance for the first 105,000 years. The semi-major axis increases upon escape from the resonance, but then after around 25,000 years, the semi-major axis decreases until it reaches approximately 31 AU. This particle had the same initial conditions as particle 10 in the plu_0km_nodrag_250 and lorplu_0km_nodrag_250 runs. It is interesting to see how the addition of different forces affects the orbit of the particle. Yet, in all three cases, the particle is trapped in the 3:2 mean motion resonance for at least 100,000 years. In this case, the particle is trapped for less time, but on the whole, the trapping time of the particles is not significantly reduced by the inclusion of additional forces. The middle panel shows the variation of the resonant argument, φ, for the 3:2 resonance (where $j_1 = 3$, $j_2 = -2$, $j_3 = -1$, $j_4 = 0$, $j_5 = 0$, and $j_6 = 0$) with time. The resonant argument is librating for the first 105,000 years showing that the particle is trapped in the 3:2 resonance. Eventually, particle 10 escapes from the resonance. The bottom panel shows that, as expected for the $\beta = 0$ case, the particle's eccentricity never reaches e_{max}, represented by the horizontal dashed line, but its eccentricity and semi-major axis increase when the particle leaves the 3:2 resonance. Then, at about 140,000 years, the eccentricity suddenly drops and then slowly increases until the end of the integration.

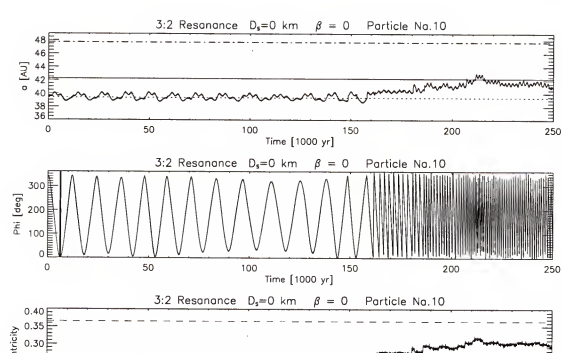
3:2 Resonance D$_s$=0 km β = 0 Particle No.10
a [AU]
Time [1000 yr]
3:2 Resonance D$_s$=0 km β = 0 Particle No.10
Phi [deg]
Time [1000 yr]
3:2 Resonance D$_s$=0 km β = 0 Particle No.10
Eccentricity
Time [1000 yr]

Figure 4-14: Variation of semi-major axis, resonant argument, and eccentricity with time for particle 10 in a RADAU run for the no drag case ($\beta = 0$) including the gravitational effects of seven planets. The run (plu_0km_nodrag_250) consists of 249 particles integrated for 250,000 years and includes the effects of the gravitational perturbations of Venus, Earth, Mars, Jupiter, Saturn, Uranus, and Neptune. The particles, having a β equal to zero, were released from a 0 km source body in a Pluto-like orbit. (Top) Shown in the top panel is the variation of semi-major axis, a, with time. The exact location for 3:2 resonance for the $\beta = 0$ case is plotted as a dotted line. The exact locations of the 5:3 and 2:1 resonances are plotted as a solid line and as a dash-dot line, respectively. The semi-major axis of particle 10 is clearly librating around the exact location of the 3:2 resonance for approximately 160,000 years. Eventually, particle 10 escapes from the resonance and eventually the particle becomes very briefly trapped in the 5:3 resonance. (Middle) We show the variation of the resonant argument for the 3:2 resonance (where $j_1 = 3$, $j_2 = -2$, $j_3 = -1$, $j_4 = 0$, $j_5 = 0$, and $j_6 = 0$) with time in the middle panel. The resonant argument, φ, is librating the for approximately 160,000 years showing that the particle is trapped in the 3:2 resonance. After 160,000 years, φ is seen to be circulating and the particle is no longer trapped. (Bottom) The variation of the eccentricity with time for particle 10 is shown in the bottom panel. The dashed line is the value of e_{max}, the maximum value of eccentricity a particle trapped in the 3:2 resonance can reach. As expected for the no drag case, the particle's eccentricity never reaches e_{max}, but its eccentricity and semi-major axis increase when the particle leaves the 3:2 resonance.

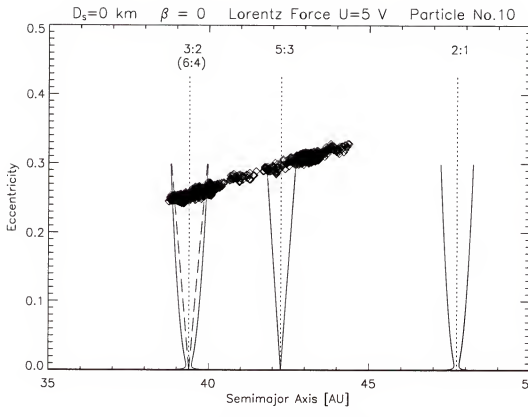

Figure 4-15: Eccentricity versus semi-major axis for particle 10 in a RADAU run for the $\beta = 0$ case including gravity and the Lorentz force ($U = 5\ V$). The run (lorplu_-0km_nodrag_250), consist of 249 particles integrated for 250,000 years, includes the effects of gravity and the Lorentz force assuming the particles have a potential, U, equal to 5 V. The particles, having a β equal to zero, were released from a 0 km source body in a Pluto-like orbit. Each diamond represents the particle's orbital elements at 100 year intervals. The 3:2, 5:3, and 2:1 libration widths are shown as solid lines while the 6:4 libration width is shown as a dashed line. The exact location for each resonance is plotted as a dotted line.

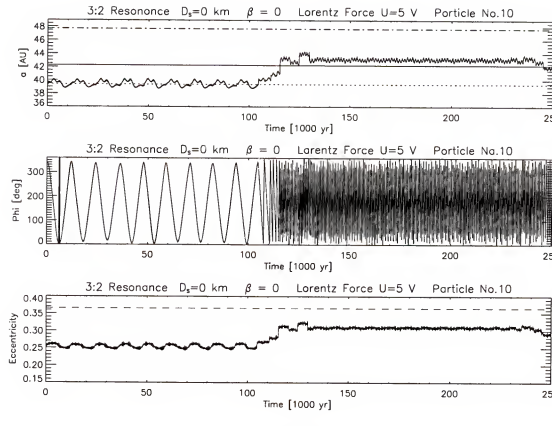
3:2 Resonance D=0 km β = 0 Lorentz Force U=5 V Particle No.10
a [AU]
Time [1000 yr]
3:2 Resonance D=0 km β = 0 Lorentz Force U=5 V Particle No.10
Phi [deg]
Time [1000 yr]
3:2 Resonance D=0 km β = 0 Lorentz Force U=5 V Particle No.10
Eccentricity
Time [1000 yr]

Figure 4-16: Variation of semi-major axis, resonant argument, and eccentricity with time for particle 10 in a RADAU run for the $\beta = 0$ case including gravity and the Lorentz force ($U = 5\ V$). The run (lorplu_0km_nodrag_250), consists of 249 particles integrated for 250,000 years, and includes the effects of gravity and the Lorentz force assuming the particles have a potential, U, equal to 5 V. The particles, having a β equal to zero, were released from a 0 km source body in a Pluto-like orbit. (Top) The variation of semi-major axis, a, with time. The exact location for 3:2 resonance for the $\beta = 0$ case is plotted as a dotted line. The exact locations of the 5:3 and 2:1 resonances are plotted as a solid line and as a dash-dot line, respectively. The semi-major axis of particle 10 is clearly librating around the exact location of the 3:2 resonance for the first 120,000 years. (Middle) The variation of the resonant argument for the 3:2 resonance (where $j_1 = 3$, $j_2 = -2$, $j_3 = -1$, $j_4 = 0$, $j_5 = 0$, and $j_6 = 0$) with time. The resonant argument is librating for the first 120,000 years showing that the particle is trapped in the 3:2 resonance. Eventually, particle 10 escapes from the resonance. (Bottom) As expected for the no drag case, the particle's eccentricity never reaches e_{max}, represented by the horizontal dashed line, but its eccentricity and semi-major axis increase when the particle leaves the 3:2 resonance.

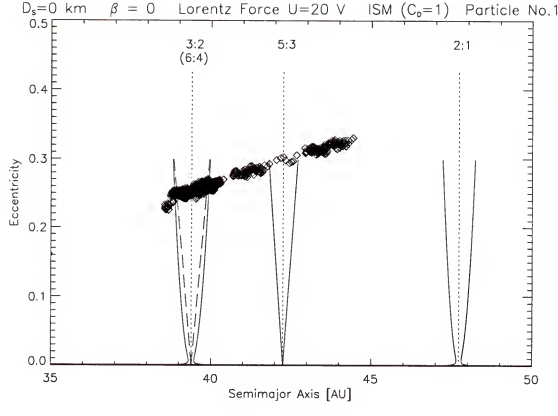

Figure 4-17: Eccentricity versus semi-major axis for particle 10 in a RADAU run for the $\beta = 0$ case including gravity, the Lorentz force ($U = 5\ V$), and the effects of neutral interstellar gas drag ($C_D = 1$). The run (ismplu_0km_nodrag_250) consist of 249 particles integrated for 250,000 years. The particles, having a β equal to zero, were released from a 0 km source body in a Pluto-like orbit. Each diamond represents the particle's orbital elements at 100 year intervals. The 3:2, 5:3, and 2:1 libration widths are shown as solid lines while the 6:4 libration width is shown as a dashed line. The exact location for each resonance is plotted as a dotted line.

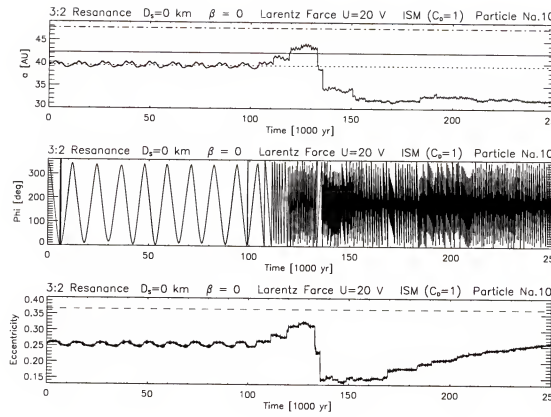
3:2 Resonance D_s=0 km β = 0 Lorentz Force U=20 V ISM (C_D=1) Particle No.10
a [AU]
Time [1000 yr]
3:2 Resonance D_s=0 km β = 0 Lorentz Force U=20 V ISM (C_D=1) Particle No.10
Phi [deg]
Time [1000 yr]
3:2 Resonance D_s=0 km β = 0 Lorentz Force U=20 V ISM (C_D=1) Particle No.10
Eccentricity
Time [1000 yr]

Figure 4-18: Variation of semi-major axis, resonant argument, and eccentricity with time for particle 10 in a RADAU run for the $\beta = 0$ case including gravity, the Lorentz force ($U = 5\ V$), and the effects of neutral interstellar gas drag ($C_D = 1$). The run (ismplu_0km_nodrag_250), consists of 249 particles integrated for 250,000 years. The particles, having a β equal to zero, were released from a 0 km source body in a Pluto-like orbit. (Top) The variation of semi-major axis, a, with time. The exact location for 3:2 resonance for the $\beta = 0$ case is plotted as a dotted line. The exact locations of the 5:3 and 2:1 resonances are plotted as a solid line and as a dash-dot line, respectively. The semi-major axis of particle 10 is clearly librating around the exact location of the 3:2 resonance for the first 105,000 years. It increases upon escape from the resonance, but then after around 25,000 years, the semi-major axis decreases until it reaches approximately 31 AU. This particle had the same initial conditions as particle 10 in the plu_0km_nodrag_250 and lorplu_0km_nodrag_250 runs. (Middle) The variation of the resonant argument for the 3:2 resonance (where $j_1 = 3$, $j_2 = -2$, $j_3 = -1$, $j_4 = 0$, $j_5 = 0$, and $j_6 = 0$) with time. The resonant argument is librating for the first 105,000 years showing that the particle is trapped in the 3:2 resonance. Eventually, particle 10 escapes from the resonance. (Bottom) The particle's eccentricity never reaches e_{max}, represented by the horizontal dashed line, as expected for the $\beta = 0$ case, but its eccentricity and semi-major axis increase when the particle leaves the 3:2 resonance. Then, at about 140,000 years, the eccentricity suddenly drops and then slowly increases until the end of the integration.

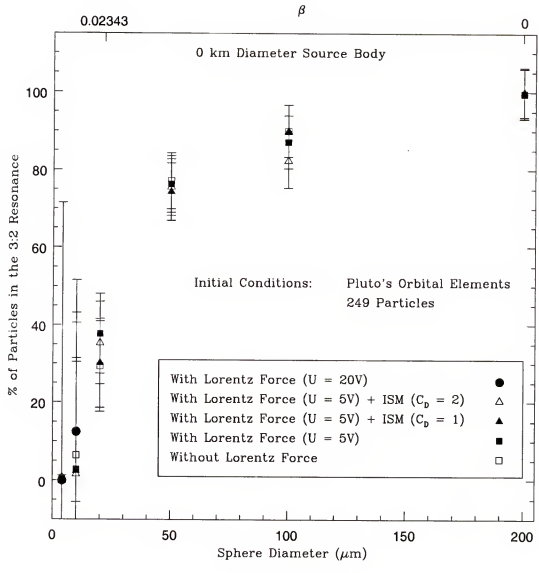

Figure 4-19: Percentage of particles in the 3:2 mean motion resonance with Neptune assuming particles were generated from source body of 0 km in diameter in the 3:2 resonance. The particles were integrated for 250,000 years. The open squares correspond to RADAU runs including the "standard forces", that is, the effects of gravity, PR drag, solar wind corpuscular drag, and radiation pressure. The filled squares and filled circles correspond to RADAU runs which include, in addition to the standard forces, the Lorentz force with a potential, U, equal to 5 Volts and 20 Volts, respectively. The filled triangles correspond to RADAU runs which include the standard forces, the Lorentz force with $U = 5\ V$, and the effects of neutral interstellar gas drag assuming C_D is equal to 1. The open triangles correspond to RADAU runs which include the standard forces, the Lorentz force with $U = 5\ V$ and the effects of neutral interstellar gas drag assuming $C_D = 2$. Each numerical run is composed of 249 particles, giving an error in the estimate of the number of particles in resonance of $\sim \sqrt{N_r}/N_r$, where N_r is the number of particles in resonance.

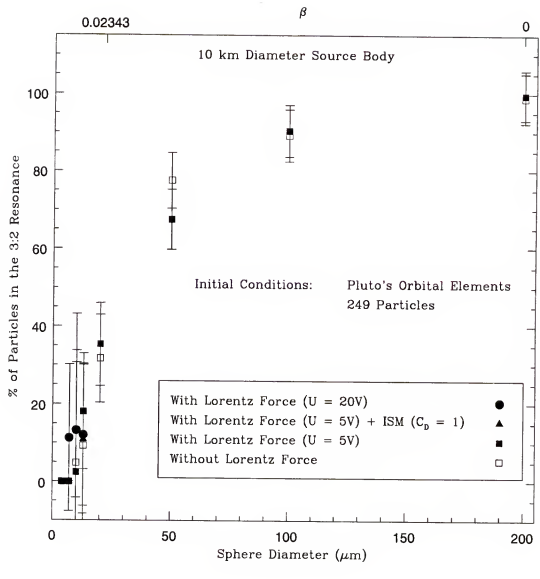

Figure 4-20: Percentage of particles in the 3:2 mean motion resonance with Neptune assuming particles were generated from source body of 10 km in diameter in the 3:2 resonance. The open squares correspond to RADAU runs including the "standard forces", that is, the effects of gravity, PR drag, solar wind corpuscular drag, and radiation pressure. The filled squares and filled circles correspond to RADAU runs which include, in addition to the standard forces, the Lorentz force with a potential, U, equal to 5 Volts and 20 Volts, respectively. The filled triangles correspond to RADAU runs which include the standard forces, the Lorentz force with $U = 5\ V$, and the effects of neutral interstellar gas drag assuming $C_D = 1$. Each numerical run is composed of 249 particles, giving an error in the estimate of the number of particles in resonance of $\sim \sqrt{N_r}/N_r$, where N_r is the number of particles in resonance. The particles were released from 10 km diameter source bodies in Pluto-like orbits and were integrated for 250,000 years.

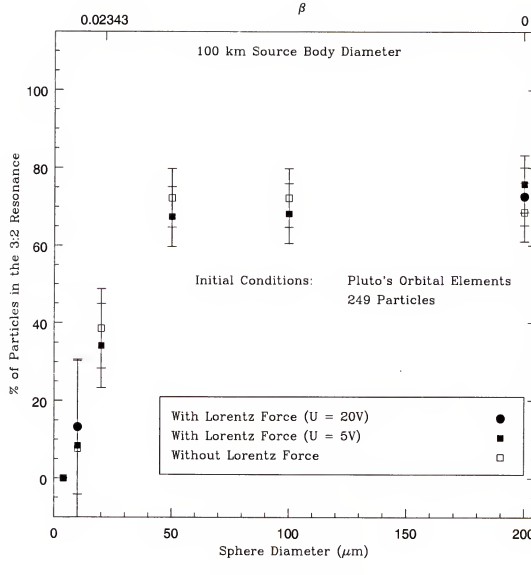

Figure 4-21: [Percentage of particles in the 3:2 mean motion resonance with Neptune assuming particles were generated from source body of 100 km in diameter in the 3:2 resonance. The open squares correspond to RADAU runs including the "standard forces", that is, the effects of gravity, PR drag, solar wind corpuscular drag, and radiation pressure. The filled squares and filled circles correspond to RADAU runs which include, in addition to the standard forces, the Lorentz force with a potential, U, equal to 5 Volts and 20 Volts, respectively. Each numerical run is composed of 249 particles, giving an error in the estimate of the number of particles in resonance of $\sim \sqrt{N_r}/N_r$, where N_r is the number of particles in resonance. When N_r was zero, the error was estimated to be near zero. The particles were released from 100 km diameter source bodies in Pluto-like orbits and were integrated for 250,000 years.

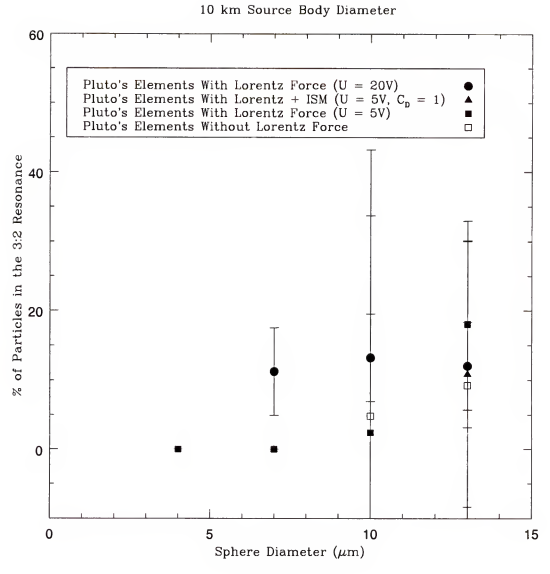

Figure 4-22: Close up of the plot of the percentage of particles in the 3:2 mean motion resonance with Neptune assuming particles were generated from source body of 10 km in diameter in the 3:2 resonance. The open squares correspond to RADAU runs including the "standard forces", that is, the effects of gravity, PR drag, solar wind corpuscular drag, and radiation pressure. The filled squares and filled circles correspond to RADAU runs which include, in addition to the standard forces, the Lorentz force with a potential, U, equal to 5 Volts and 20 Volts, respectively. The filled triangles correspond to RADAU runs which include the standard forces, the Lorentz force with $U = 5\ V$, and the effects of neutral interstellar gas drag assuming $C_D = 1$. Each numerical run is composed of 249 particles, giving an error in the estimate of the number of particles in resonance of $\sim \sqrt{N_r}/N_r$, where N_r is the number of particles in resonance. When N_r was zero, the error was estimated to be near zero. The particles were released from 10 km diameter source bodies in Pluto-like orbits and were integrated for 250,000 years.

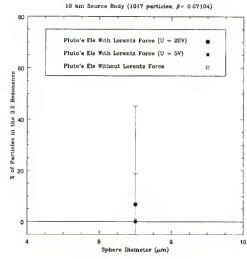
10 km Source Body (1017 particles, β= 0.07104)
Pluto's Ele With Lorentz Force (U = 20V)
Pluto's Ele With Lorentz Force (U = 5V)
Pluto's Ele Without Lorentz Force
% of Particles in the 3:2 Resonance
Sphere Diameter (μm)

a) 3:2 Resonance

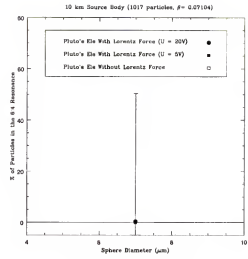
10 km Source Body (1017 particles, β= 0.07104)
Pluto's Ele With Lorentz Force (U = 20V)
Pluto's Ele With Lorentz Force (U = 5V)
Pluto's Ele Without Lorentz Force
% of Particles in the 6:4 Resonance
Sphere Diameter (μm)

b) 6:4 Resonance

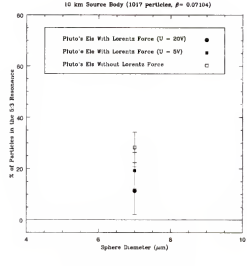
10 km Source Body (1017 particles, β= 0.07104)
Pluto's Ele With Lorentz Force (U = 20V)
Pluto's Ele With Lorentz Force (U = 5V)
Pluto's Ele Without Lorentz Force
% of Particles in the 5:3 Resonance
Sphere Diameter (μm)

c) 5:3 Resonance

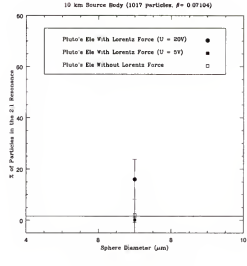
10 km Source Body (1017 particles, β= 0.07104)
Pluto's Ele With Lorentz Force (U = 20V)
Pluto's Ele With Lorentz Force (U = 5V)
Pluto's Ele Without Lorentz Force
% of Particles in the 2:1 Resonance
Sphere Diameter (μm)

d) 2:1 Resonance

Figure 4-23: Percentage of particles (with $\beta = 0.07104$) in the 3:2, 6:4, 5:3, and 2:1 resonances assuming the particles were generated from a source body of 10 km in diameter in the 3:2 resonance. In (a) more particles are in the 3:2 resonance from the run which includes the Lorentz force with $U = 20\ V$ than in the run which includes the Lorentz force with $U = 5\ V$ or the runs which only include the "standard forces," although the error bars are rather large. Initially this is puzzling since we would not expect that the addition of an extra force would increase the likelihood that a particle would remain in resonance. However, the phenomenon we see in (a) is simply a consequence of the fact that many of the particles in the "standard forces" run are trapped instead in the 5:3 resonance, due of the high β value of the particles. Each run consists of 1017 particles.

The Lorentz Force

We wish to test the impact of the Lorentz force on particles in the Kuiper belt. Two sets of runs have been made - one set which does not include the Lorentz force in the calculations and one which does include it. As discussed in Chapter 2, interplanetary dust particles are charged. A typical particle is expected to have a net positive potential, U, of ≈ 5 V (Goertz 1989, Gustafson 1994). However, this quantity is uncertain and could be as high as 100 V (Leinert and Grün 1990). An increase in U corresponds to an increase in the charge to mass ratio. As seen in Figures 4-19, 4-20, and 4-21, the Lorentz force does not have much of an effect on whether the particles remain in the 3:2 resonance on the whole. However, as shown in Figures 4-22 and 4-23, for small particles, ~ 10 μm in diameter, the Lorentz force can have an appreciable effect, especially if the potential, U, is increased to 20 V. This potential is probably too high for grains in the Kuiper belt, but it does serve as an interesting test case for the effects of the Lorentz force. Figure 4-23 shows the trapping results for four different mean motion resonances with Neptune (the 3:2, the 6:4, the 5:3, and the 2:1) with the initial conditions that the particles escape from a source body 10 km in diameter. The results appear to be counterintuitive in that more particles are trapped into the 3:2 resonance in the $U = 20$ V Lorentz force case than in the case without the Lorentz force included. In the case of increased drag, one would expect that less particles would be trapped. However, this increase in trapping occurs because the particles in the non-Lorentz force case are getting trapped in the 5:3 resonance before their orbits can evolve down to a semi-major axis where they can become trapped in the 3:2 resonance. Radiation pressure exerts a strong influence on small particles and as a result, many of them start out some distance away from 39.4 AU, allowing them to become initially trapped in other resonances. Another illustration of this point is in Figures 4-24 and 4-25 where it can be clearly seen that the particle starts out being trapped in the 5:3 resonance,

reaches a maximum eccentricity, e_{max}, and then evolves out of the 5:3 resonance and eventually becomes trapped in the 3:2 resonance. In (d) of Figure 4-23, we see that significantly more particles are trapped in the 2:1 resonance in the $U = 20\ V$ Lorentz force case than in the case without the Lorentz force included. Many of the $U = 20\ V$ Lorentz force case particles eventually are excluded from the numerical integrations due to the particles obtaining a high eccentricity and/or large semi-major axis. In fact, 57% of the particles in the $U = 20\ V$ Lorentz force 249 particle run with 7 μm diameter particles originating from 10 km diameter source bodies were eventually excluded from the integrations, while none of the particles in any of the other runs were excluded (see Table 4-5). In the plu_10km_7mu_250 run, most of the particles become trapped in the 5:3 resonance. However, the addition of the Lorentz force with a high enough grain potential ($U = 20\ V$) seems to scatter some particles out to large semi-major axes where they can become trapped in the 2:1 resonance, or small semi-major axes where they can become trapped in the 3:2 resonance. In the case of the other runs (lorplu_10km_7mu_250 and ismplu_10km_7mu_250) slightly less particles are trapped in the 5:3 and 2:1 resonances than in the plu_10km_7mu_250 run, which is to be expected for additional drag forces. In the case of the 6:4 and 5:3 resonance we are only considering one of the eccentricity resonances. That is, in the case of the 6:4 external resonance, we consider the case where: $j_1 = 6$, $j_2 = -4$, $j_3 = -2$, and $j_4 = j_5 = j_6 = 0$, and in the case of the 5:3 external resonance, we only consider the case where $j_1 = 5$, $j_2 = -3$, $j_3 = -2$, and $j_4 = j_5 = j_6 = 0$.

For the 7 μm diameter particle run ($\beta = 0.07104$), originating from 10 km diameter source bodies and including only the effects of gravity, PR drag, solar wind corpuscular drag, and radiation pressure, we did check for trapping for all of the 5:3 external mean motion resonances. We did not find any particles trapped in the other eccentricity resonances. However, we did find particles trapped in the inclination resonances. The percentages of particles trapped in all of the external

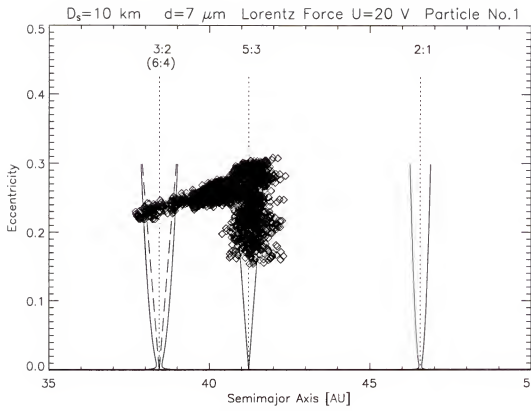

Figure 4-24: Eccentricity versus semi-major axis for particle 1 in a RADAU run including the Lorentz force where $U = 20\ V$. The $\beta = 0.07104$ (7 μm diameter) particles in this RADAU run were released from a 10 km source body. The 3:2, 5:3, and 2:1 libration widths are shown as solid lines while the 6:4 libration width is shown as a dashed line. The exact location for each resonance is plotted as a dotted line. Each diamond represents the particle's orbital elements at 100 year intervals. Note that for the majority of the time, particle 1 appears to be within the 5:3 libration width, but for a short period of time, the particle is also within both the 3:2 and the 5:4 resonant widths. As can be seen in the next figure, the particle is in fact trapped in both the 5:3 and the 3:2 resonances.

5:3 mean motion resonances for this particular run are listed in Table ??. The criteria for trapping is based on whether the resonant argument, φ, is librating. Recalling Equation 2.50 which gives $\varphi = j_1\lambda' + j_2\lambda_n + j_3\tilde{\omega}' + j_4\tilde{\omega}_n + j_5\Omega' + j_6\Omega_n$ where the primed osculating elements are those of the dust particles and the unprimed elements subscripted with an "n" are Neptune's. As can be seen from Table 4-6, the assumption that the $\tilde{\omega}'$ eccentricity resonance was most important was correct as no

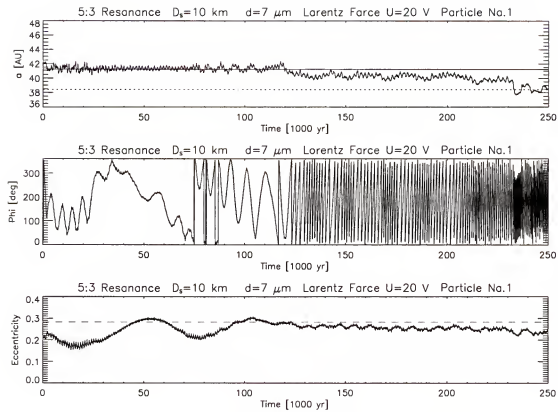
5:3 Resonance D$_s$=10 km d=7 μm Lorentz Force U=20 V Particle No.1
a [AU]
Time [1000 yr]
5:3 Resonance D$_s$=10 km d=7 μm Lorentz Force U=20 V Particle No.1
Phi [deg]
Time [1000 yr]
5:3 Resonance D$_s$=10 km d=7 μm Lorentz Force U=20 V Particle No.1
Eccentricity
Time [1000 yr]

Figure 4-25: Variation of semi-major axis, resonant argument, and eccentricity with time for particle 1 in a RADAU run including the Lorentz force where $U = 20\ V$. The $\beta = 0.07104$ (7 μm diameter) particles in this RADAU run were released from a 10 km source body. (Top) The variation of semi-major axis, a, with time. The exact location for the 5:3 resonance is plotted as a solid line, while the exact location of the 3:2 resonance is plotted as a dotted line. (Middle) The variation of the resonant argument for the 5:3 resonance (where $j_1 = 5$, $j_2 = -3$, $j_3 = -2$, $j_4 = 0$, $j_5 = 0$, and $j_6 = 0$) with time. For approximately the first 120,000 years, the resonant argument is librating and therefore the particle is trapped in the 5:3 resonance. After 120,000 years, φ is circulating and the particle is no longer trapped in the 5:3 resonance. It does eventually become trapped in the 3:2 resonance, however. (Bottom) The variation of the eccentricity with time for particle 1. The dashed line is the value of e_{max}, the maximum value of eccentricity a particle trapped in the 5:3 resonance can reach. Note, however, that the particle's eccentricity becomes slightly higher than e_{max} while the particle is clearly still trapped in resonance. The theory to calculate e_{max} is only valid for low eccentricities since it is only to second order in e, so it is not surprising that the theory and the results do not agree completely.

particles are trapped in any of the other eccentricity resonances. This is expected as the eccentricities of the Plutino dust particles ($e' \approx 0.25$) are much greater than the

Table 4-5: A comparison of results for numerical runs for 7 μm diameter particles (β = 0.07104) originating from 10 km diameter source bodies.

Numerical Run (Designation)	Percentage of Particles Trapped in Resonance				Percentage of Particles Excluded from System
	3:2	6:4	5:3	2:1	
Standard forces (plu_10km_7m_250)	0.0%	0.0%	34.1%	2.4%	0.0%
Standard forces and Lorentz force ($U = 5V$) (lorplu_10km_7mu_250)	0.0%	0.0%	21.7%	0.4%	0.0%
Standard forces and Lorentz force ($U = 5V$) and ISM ($C_D = 1$) (ismplu_10km_7mu_250)	0.0%	0.0%	29.3%	0.4%	0.0%
Standard forces and Lorentz force ($U = 20V$) (u20lplu_10km_7mu_250)	11.2%	0.4%	9.6%	12.9%	57.4%

A comparison of results for numerical runs for 7 μm diameter particles (β = 0.07104) originating from 10 km diameter source bodies. The source bodies had orbital elements identical to those of Pluto's. The runs contained 249 particles. The errors are assumed to be $\sim \sqrt{N_r}/N_r$, where N_r is the number of particles in resonance. The entry "standard forces" refers to a numerical run with the effects of gravity, PR drag, solar wind corpuscular drag, and radiation pressure included. Lorentz force (U = 5 V) refers to the inclusion of the Lorentz force in the run, assuming a potential equal to 5 Volts. ISM ($C_D = 1$) refers to the inclusion of the effect due to neutral interstellar gas drag assuming that C_D, the free molecular drag coefficient defined in Chapter 2, is equal to 1. These results are confirmed by a separate set of runs having 1017 particles each. In the case of the 6:4 and 5:3 resonance we are only considering one of the eccentricity resonances. That is, in the case of the 6:4 external resonance, we consider the case where j_1 = 6, j_2 = -4, j_3 = -2, and $j_4 = j_5 = j_6$ = 0, and in the case of the 5:3 external resonance, we only consider the case where j_1 = 5, j_2 = -3, j_3 = -2, and $j_4 = j_5 = j_6 = 0$.

eccentricity of Neptune ($e_n \approx 0.009$) and the strength of the resonance is a function of the eccentricity. Consequently, the particle is preferentially trapped in the strongest resonance, or the resonance associated with the largest coefficient, in this case the (j_1 = 5, j_2 = -3, j_3 = -2, and $j_4 = j_5 = j_6 = 0$) resonance. (Murray and Dermott 1999).

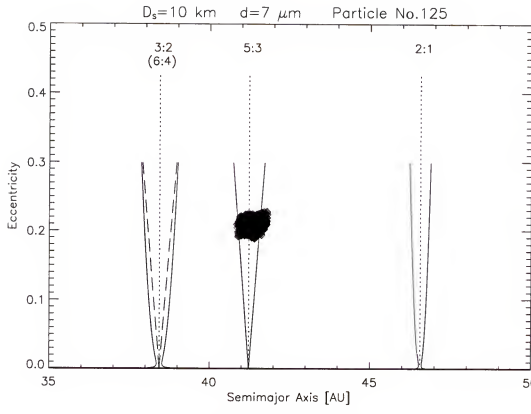

Figure 4-26: Eccentricity versus semi-major axis for a particle trapped in the 5:3 mean motion resonance with Neptune. Particle 125 is from a RADAU run for the case of 7 μm diameter particles ($\beta = 0.07104$) that are released from a 10 km diameter source body. The run (plu_10km_7mu_250) consists of 249 particles integrated for 250,000 years and includes the effects of gravity, PR drag, solar wind corpuscular drag, and radiation pressure. Each diamond represents the particle's orbital elements at 100 year intervals. The 3:2, 5:3, and 2:1 libration widths are shown as solid lines while the 6:4 libration width is shown as a dashed line. The exact location for each resonance is plotted as a dotted line.

In the 5:3 resonance for the case discussed above, a sizeable percentage of particles are trapped in the inclination resonances (some particles may be trapped in multiple resonances). An example of such a particle (trapped in the 5:3 resonance where $j_1 = 5$, $j_2 = -3$, $j_3 = 0$, $j_4 = 0$, $j_5 = -2$, and $j_6 = 0$) is shown in Figure 4-32. The inclination resonances are a topic for future study.

Lastly, it is important to note that the Lorentz force could also create a structure similar in appearance to a dust band. The interplanetary solar magnetic

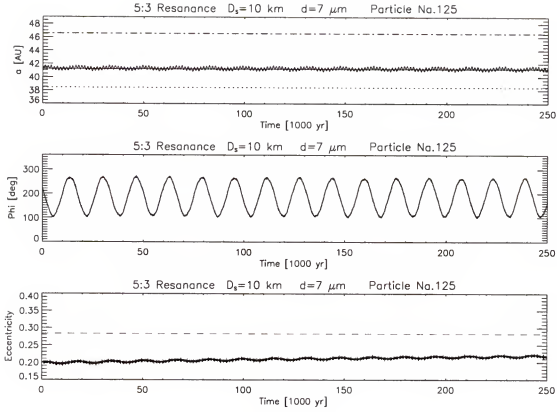
5:3 Resonance D$_s$=10 km d=7 μm Particle No.125
a [AU]
Time [1000 yr]
5:3 Resonance D$_s$=10 km d=7 μm Particle No.125
Phi [deg]
Time [1000 yr]
5:3 Resonance D$_s$=10 km d=7 μm Particle No.125
Eccentricity
Time [1000 yr]

Figure 4-27: Variation of semi-major axis, resonant argument, and eccentricity with time for particle 125 in a RADAU run (for 7 μm diameter particles released from a 10 km source body) including the standard forces. The run (plu_10km_7mu_250) consists of 249 particles integrated for 250,000 years and includes the effects of gravity, PR drag, solar wind corpuscular drag, and radiation pressure. (Top) The variation of semi-major axis, a, with time. The exact location for 3:2 resonance for the $\beta = 0$ case is plotted as a dotted line. The exact locations of the 5:3 and 2:1 resonances are plotted as a solid line and as a dash-dot line, respectively. The semi-major axis of particle 125 is clearly librating around the exact location of the 5:3 resonance for the entire time. (Middle) The variation of the resonant argument for the 5:3 resonance (where $j_1 = 5$, $j_2 = -3$, $j_3 = -2$, $j_4 = 0$, $j_5 = 0$, and $j_6 = 0$) with time. The resonant argument, φ, is clearly librating. (Bottom) The variation of the eccentricity with time for particle 125. The dashed line is the value of e_{max}, the maximum value of eccentricity a particle trapped in the 3:2 resonance can reach. The particle's eccentricity never reaches e_{max}, nor does it appear to be approaching e_{max}, implying that the particle may be trapped in the 3:2 for much longer than 250,000 years.

field is composed of different sectors which alternate in polarity. The Lorentz force increases particle inclinations due to particles in low inclination orbits experiencing a random walk in inclination due to both stochastic variations in solar magnetic

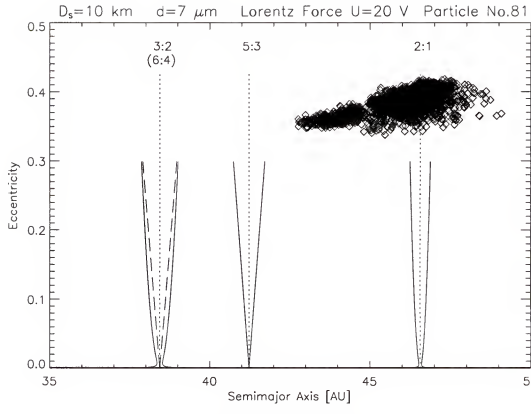

Figure 4-28: Eccentricity versus semi-major axis for particle 81 in a RADAU run including the standard forces and the Lorentz force where $U = 20\ V$. The run (u20lplu_10km_7mu_250), consist of 249 particles integrated for 250,000 years, includes the effects of gravity, PR drag, solar wind corpuscular drag, radiation pressure, and the Lorentz force assuming the particles have a potential, U, equal to 20 V. The 7 μm diameter particles ($\beta = 0.07104$) were released from a source body 10 km in diameter in a Pluto-like orbit. Each diamond represents the particle's orbital elements at 100 year intervals. The 3:2, 5:3, and 2:1 libration widths are shown as solid lines while the 6:4 libration width is shown as a dashed line. The exact location for each resonance is plotted as a dotted line.

field sector length and the alternating polarity of the sectors. As a result of this random walk, the inclination of a particle can increase over time due to the Lorentz force. Over all, this effect produces a dispersion in particle inclinations (Leinert and Grün 1990). The Lorentz force also causes a precession of nodes about the solar equator. Coupled with the dispersion in inclination, the structure will resemble a puffed up ring of material (Gustafson 2000). However, this circumsolar ring is

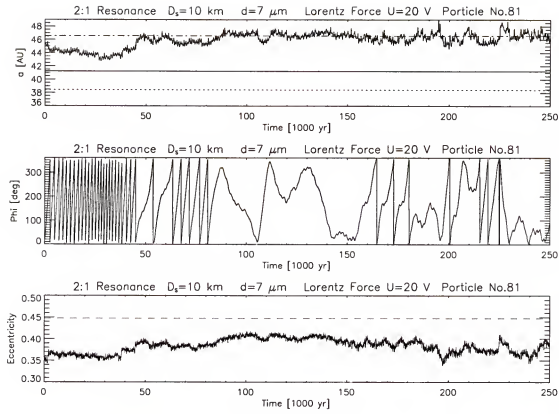
2:1 Resonance D=10 km d=7 μm Lorentz Force U=20 V Particle No.81
a [AU]
Time [1000 yr]
2:1 Resonance D=10 km d=7 μm Lorentz Force U=20 V Particle No.81
Phi [deg]
Time [1000 yr]
2:1 Resonance D=10 km d=7 μm Lorentz Force U=20 V Particle No.81
Eccentricity
Time [1000 yr]

Figure 4-29: Variation of semi-major axis, resonant argument, and eccentricity with time for particle 81 in a RADAU run including the standard forces and the Lorentz force where $U = 20\ V$. The run (u20lplu_10km_7mu_250), consist of 249 particles integrated for 250,000 years, includes the effects of gravity, PR drag, solar wind corpuscular drag, radiation pressure, and the Lorentz force assuming the particles have a potential, U, equal to $20\ V$. The 7 μm diameter particles ($\beta = 0.07104$) were released from a source body 10 km in diameter in a Pluto-like orbit. (Top) The variation of semi-major axis, a, with time. The exact location for 3:2 resonance for the $\beta = 0$ case is plotted as a dotted line. The exact locations of the 5:3 and 2:1 resonances are plotted as a solid line and as a dash-dot line, respectively. The semi-major axis of particle 81 is clearly librating around the exact location of the 2:1 resonance. (Middle) The variation of the resonant argument for the 2:1 resonance (where $j_1 = 2$, $j_2 = -1$, $j_3 = -1$, $j_4 = 0$, $j_5 = 0$, and $j_6 = 0$) with time. The resonant argument, φ, is librating for approximately 200,000 years, though for part of that time, φ seems to be circulating. (Bottom) The particle's eccentricity never reaches e_{max}.

completely independent of the presence of planets in the system unlike the resonant rings we have been discussing in this chapter.

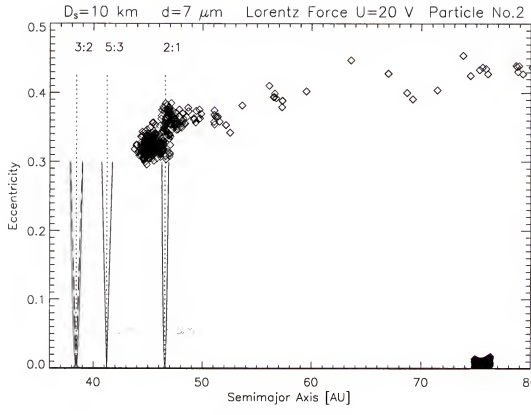

Figure 4-30: Eccentricity versus semi-major axis for particle 2 in a RADAU run including the standard forces and the Lorentz force where $U = 20\ V$. The run (u20lplu_10km_7mu_250) consist of 249 particles integrated for 250,000 years, includes the effects of gravity, PR drag, solar wind corpuscular drag, radiation pressure, and the Lorentz force assuming the particles have a potential, U, equal to $20\ V$. The 7 μm diameter particles ($\beta = 0.07104$) were released from a source body 10 km in diameter in a Pluto-like orbit. Each diamond represents the particle's orbital elements at 100 year intervals. The 3:2, 5:3, and 2:1 libration widths are shown as solid lines while the 6:4 libration width is shown as a dashed line. The particle is initially trapped in the 2:1 resonance, but eventually achieves a parabolic or hyperbolic orbit so RADAU "excludes" it from the system, assigning it a semi-major axis of 75 AU and an eccentricity of 0.

Neutral Interstellar Gas Drag

Note that Scherer (2000) does not take the Lorentz force into consideration, and furthermore predicts that trapping of particles into mean motion resonances in the presence of neutral interstellar gas drag is very unlikely. In Figure 4-19, a full set of runs (for 4, 10, 20, 50, and 100 μm diameter particles as well as the $\beta = 0$ case)

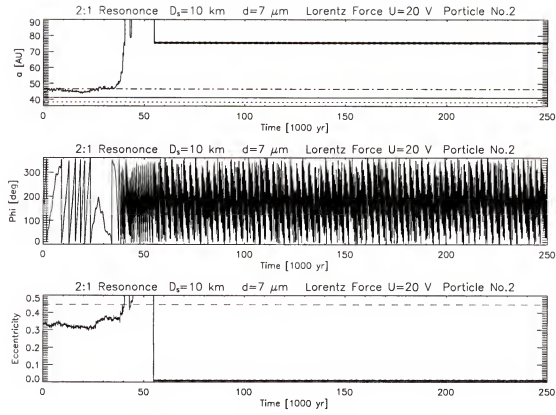
2:1 Resonance D=10 km d=7 μm Lorentz Force U=20 V Particle No.2
a [AU]
Time [1000 yr]
2:1 Resonance D=10 km d=7 μm Lorentz Force U=20 V Particle No.2
Phi [deg]
Time [1000 yr]
2:1 Resonance D=10 km d=7 μm Lorentz Force U=20 V Particle No.2
Eccentricity
Time [1000 yr]

Figure 4-31: Variation of semi-major axis, resonant argument, and eccentricity with time for particle 2 in a RADAU run including the standard forces and the Lorentz force where $U = 20\ V$. The run (u20lplu_10km_7mu_250) consist of 249 particles integrated for 250,000 years, includes the effects of gravity, PR drag, solar wind corpuscular drag, radiation pressure, and the Lorentz force assuming the particles have a potential, U, equal to 20 V. The 7 μm diameter particles ($\beta = 0.07104$) were released from a source body 10 km in diameter in a Pluto-like orbit. (Top) The variation of semi-major axis, a, with time. The exact location for 3:2 resonance for the $\beta = 0$ case is plotted as a dotted line. The exact locations of the 5:3 and 2:1 resonances are plotted as a solid line and as a dash-dot line, respectively. Particle 2 is initially trapped in the 2:1 resonance. Eventually, however, the particle achieves a parabolic or hyperbolic orbit and RADAU "excludes" it from the system by assigning it $a = 75$ AU and $e = 0$. (Middle) The variation of the resonant argument for the 2:1 resonance (where $j_1 = 3$, $j_2 = -2$, $j_3 = -1$, $j_4 = 0$, $j_5 = 0$, and $j_6 = 0$) with time. The resonant argument is alternating between librating and circulating for the first 30,000 to 40,000 years, before the particle becomes excluded from the system. (Bottom) The particle's eccentricity appears to reach e_{max} shortly before the particle achieves a parabolic or hyperbolic orbit and is excluded from the system by RADAU.

Table 4-6: Percentage of particles in the 5:3 resonances for the plu_10km_7mu_250 numerical run.

j_1 λ'	j_2 λ_n	j_3 $\tilde{\omega}'$	j_4 $\tilde{\omega}_n$	j_5 Ω'	j_6 Ω_n	Percentage Trapped
5	-3	-2	0	0	0	34.1%
5	-3	-1	-1	0	0	0.0%
5	-3	0	-2	0	0	0.0%
5	-3	0	0	-2	0	30.5%
5	-3	0	0	-1	-1	28.9%
5	-3	0	0	0	-2	25.7%

Percentage of particles in the 5:3 resonances for the plu_10km_7mu_250 numerical run. The run consists of 7 μm diameter particles ($\beta = 0.07104$) originating from 10 km diameter source bodies with the effects of gravity, PR drag, solar wind corpuscular drag, and radiation pressure included. The source bodies had orbital elements identical to those of Pluto's. The run contains 249 particles and the error bars are $\sim \sqrt{N_r}/N_r$, where N_r is the number of particles in resonance. A more thorough study of trapping in inclination resonances is left for future work.

with the Lorentz force ($U = 5\ V$) and the neutral interstellar gas drag ($C_D = 1$) are shown. Also shown is a full set of runs including the Lorentz force ($U = 5\ V$) and the neutral interstellar gas drag where $C_D = 2$. The results are not statistically different than the basic case which does not include the Lorentz force or neutral gas drag, in contrast to the predictions of Scherer (2000). As far as the percentage of particles trapped in the 3:2 resonance, neutral gas drag does not appear to have an appreciable effect. However, if plots of the projection of the orbits of the particles onto the X and Y axis are studied for the ism plus Lorentz force case, the "standard forces" case, and both Lorentz force cases, the orbits look slightly different, with the neutral ism case exhibiting a different shaped distribution in X-Y space. As seen in Figure 4-33, the torus of dust for the ism case (ismplu_10km_7mu_250) seems "squashed" compared to the standard forces case (plu_10km_7mu_250) and the $U = 5\ V$ Lorentz force case (lorplu_10km_7mu_250 cases). In the case of the $U = 20\ V$ Lorentz force case (u20lplu_10km_7mu_250), the orbits are scattered out to much larger ranges of

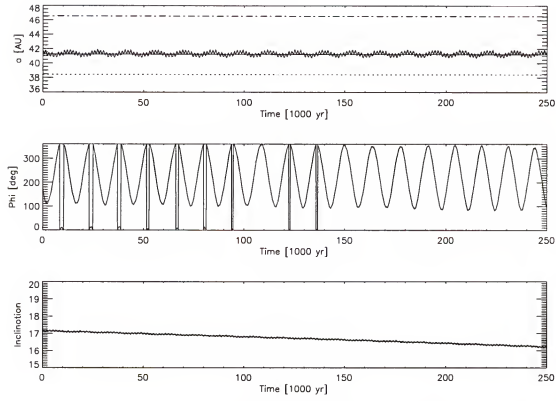

Figure 4-32: The variation of semi-major axis, resonant argument, and inclination with time for particle 8 in a 5:3 inclination resonance. The RADAU run (plu_10km_-7mu_250) includes the effects of gravity, PR drag, solar wind corpuscular drag, and radiation pressure. The 7 μm diameter particles ($\beta = 0.07104$) in this RADAU run were released from a 10 km source body. (Top) The variation of semi-major axis, a, with time. The exact location for the 5:3 resonance is plotted as a solid line, the exact location of the 3:2 resonance is a dotted line, and the exact location of the 2:1 resonance is a dash-dot line. (Middle) The variation of the resonant argument for the 5:3 resonance (where $j_1 = 5$, $j_2 = -3$, $j_3 = 0$, $j_4 = 0$, $j_5 = -2$, and $j_6 = 0$) with time. The resonant argument is clearly librating. (Bottom) The variation of the inclination of particle 8 with time.

than the other runs. This reflects the fact that many of the u20lplu_10km_7mu_250 particles eventually become excluded from the system.

4.4 Discussion

From Figures 4-19, 4-20, and 4-21, it is clear that the probability that the particles remain in (or are later recaptured into) the 3:2 mean motion resonance increases

with decreasing β (i.e., increasing particle size). Consequently, a size distribution for a Plutino disk must be weighted toward the larger size particles. In addition, as long as the potential, U, of the particles is small ($U \approx 5V$), the Lorentz force does not seem to inhibit trapping. The same is true for the effect of neutral interstellar gas drag. Also interesting is the fact that for the 10 μm diameter particles for the standard forces case, the percentage of particles trapped in the 3:2 resonance for different sized source bodies (6.4%, 4.8%, and 7.6% for 0 km, 10 km, and 100 km source bodies, respectively) fall within the predicted values of $P_{capture}$ listed in Table 4-2: $1.966\% < P_{capture} < 21.985\%$. However in the case of the 100 μm diameter particles, significantly more particles are trapped than are predicted by $P_{capture}$ (90.0%, 89.2%, and 72.3% for 0 km, 10 km, and 100 km source bodies, respectively) compared to $1.869\% < P_{capture} < 20.898\%$. Our capture probabilities are larger than predicted values for the 100 μm diameter particles because our particles started out within the libration width and were not required to evolve into the resonance, making capture into resonance for large particles much easier. Overall, Figures 4-19, 4-20, and 4-21 indicate that larger particles are much more likely to remain in the 3:2 resonance. Few particles smaller than 10 μm in diameter will remain in resonance in a Plutino disk.

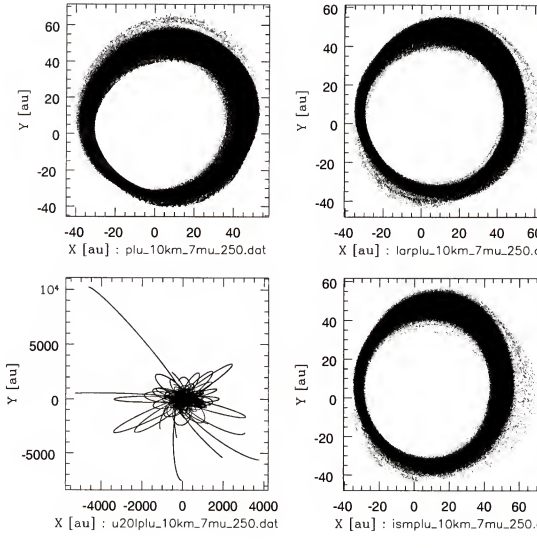

Figure 4-33: The X-Y distribution of orbits for the standard forces case, both Lorentz force cases, and the neutral interstellar gas drag case. The runs are for the case of 7 μm diameter particles originating from 10 km diameter source bodies: (top left) plu_10km_7mu_250, the standard forces case, (top right) lorplu_10km_7mu_250, the standard forces with the addition of the Lorentz force with a $U = 5\ V$, (bottom left) u20lplu_10km_7mu_250, the standard forces with the addition of the Lorentz force with a $U = 20\ V$ (bottom right) ismplu_10km_7mu_250, the standard forces with the addition of the Lorentz force with a $U = 5\ V$ and the effects of neutral interstellar gas drag with $C_D = 1$.

CHAPTER 5
SEARCHING THE COBE DATA FOR THE PLUTINO DISK

The Diffuse Infrared Background Experiment (DIRBE) on the Cosmic Background Explorer (COBE) spacecraft operated for 10 months from December 11, 1989 to September 21, 1990 in 10 photometric wave bands at 1.25, 2.2, 3.5, 4.9, 12, 25, 60, 100, 140, and 240 μm with a $0.7° \times 0.7°$ field of view.. COBE DIRBE was designed to search for the cosmic infrared background (CIB), diffuse infrared radiation originating from outside of the Milky Way galaxy. However, foreground scattered light and thermal emission from interplanetary dust particles in the zodiacal cloud and foreground emission from galactic sources were significant contributors to the diffuse infrared sky brightness and needed to be removed from the data. An empirical, parameterized model for emission from the zodiacal cloud was developed by Kelsall et al. (1998) in order to allow for the removal of the zodiacal emission from the COBE data. The model consists of a combination of models for the zodiacal background cloud, three asteroidal dust bands, and Earth's resonant ring. Since it was also necessary to remove diffuse and point source contributions due to galactic emission from the COBE data, Arendt et al. (1998) created a model for the diffuse contribution from the galaxy in addition to detailing the blanking out procedure for bright discreet sources due to the galaxy. In this way, both the zodiacal and galactic emission can be removed from the COBE DIRBE data in the hunt for the isotropic signal of the cosmic infrared background.

The goal of this chapter is two-fold: to refine and place constraints on Kelsall's empirical model for the zodiacal cloud and to search for the signature of the Kuiper belt in the COBE data, either detecting the signature or placing upper limits

on such a signal. Our search for the Kuiper disk follows the same basic approach as the search for the cosmic infrared background: it is imperative to subtract both a complete zodiacal cloud model and a galactic model from the COBE data, as structures associated with these two components lying in the ecliptic plane might mask the Kuiper disk signature. A complete model of the zodiacal cloud would consist of three distinct components: (1) the **background zodiacal cloud**, (2) the asteroidal **dust bands**, and (3) the **resonant ring**, a ring of circumsolar material trapped in first order exterior mean motion resonances with the Earth. Understanding the origin of these components is crucial because they exhibit prominent asymmetries. One of the most important asymmetries to this dissertation is that of Earth's resonant ring. The resonant ring exhibits a trailing/leading asymmetry seen by IRAS and COBE (Dermott et al. 1994, Jayaraman 1995, Jayaraman et al. 1996). In the COBE data, the brightness trailing the Earth in its orbit is consistently greater than the brightness leading the Earth in its orbit in the 4.9, 12, 25, and 60 μm wave bands. Shown in Figure 5-1, are plots of the peak flux in MJy/sr versus ecliptic longitude of Earth for the 4.9, 12, 25, 60, and 100 μm DIRBE wave bands. The filled circles represent data obtained in the trailing direction, and open circles represent data taken in the direction leading the Earth in its orbit. Curves are fit to the data and for the 4.9, 12, 25, and 60 μm data, the trailing curve is always brighter than the leading curve, which is an indication that the circumsolar resonant ring has a density enhancement that trails the Earth in its orbit. The effect is not seen in the case of the 100 μm data; however this wave band is strongly affected by galactic emission (Jayaraman 1995). The dynamical explanation of the trailing/leading asymmetry will be explained in a later section. Unlike the uniform cosmic infrared background radiation (CIB) signature, the emission from the Kuiper disk is asymmetric, time variable, and located primarily in the ecliptic plane, and because of this last factor in particular, it is of the utmost importance to subtract the best models for structure in the ecliptic, namely

the best models for the dust bands and Earth's resonant ring. At first, we attempt to use the empirical models of Kelsall et al. (1998). However, the short-comings of these empirical models become apparent and we are led to choose dynamical models instead. These dynamical models incorporate the physics behind the asymmetric nature of the zodiacal cloud and are therefore preferable to the non-physically based empirical models.

To begin with, we give a brief overview of the COBE DIRBE data set. Then, we discuss the strengths and weaknesses of both the empirical Kelsall models and the dynamical models (for the dust bands and Earth's resonant ring) which have been developed at the University of Florida. We also briefly discuss the methods used by Arendt et al. (1998) to remove the foreground galactic component of the emission. Finally, we subtract each of the models (background zodiacal cloud, dust bands, resonant ring, and galactic) and discuss the residuals, first pausing after the subtraction of the background zodiacal cloud and the dust band models to study the residuals which, in the ecliptic, are dominated by Earth's resonant ring. By removing emission due to the background zodiacal cloud and the dust bands, we expect to see the trailing/leading signature of Earth's resonant ring. However, when subtracted from the data, we find that none of the empirical background zodiacal cloud models give the residuals predicted by theory. We conclude that a dynamical two-component (both inner and outer) zodiacal cloud model must be created to complete our search.

5.1 COBE Observations

The COBE DIRBE data is organized into Weekly Sky Maps which provided average intensities for each pixel for a specific week, corresponding to a particular longitude of Earth, $\lambda_{\oplus}$. There are 41 weekly sky maps covering all of the DIRBE wave bands: 1.25, 2.2, 3.5, 4.9, 12, 25, 60, 100, 140, and 240 μm. Each map covers approximately half of the sky (Hauser et al. 1998). Each COBE DIRBE pixel is

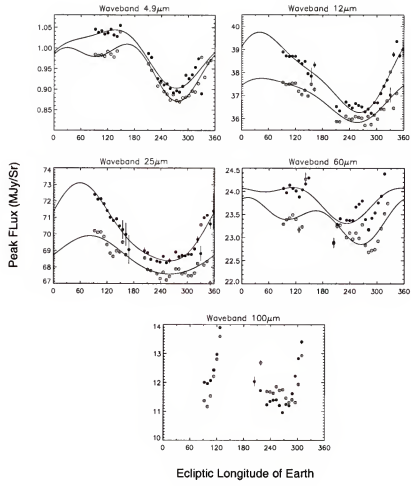

Figure 5-1: Trailing/leading asymmetry as seen in the COBE data. Plots of the peak flux at a solar elongation angle of 90° versus ecliptic longitude of Earth for the 4.9, 12, 25, 60, and 100 μm DIRBE wave bands. The filled circles represent data obtained in the trailing direction, and open circles represent data taken in the direction leading the Earth in its orbit. Curves are fit to the data and for the 4.9, 12, 25, and 60 μm data, the trailing curve is always brighter than the leading curve, which is an indication that the circumsolar resonant ring has a density enhancement that trails the Earth in its orbit. The effect is not seen in the case of the 100 μm data; however this wave band is strongly affected by galactic emission (Jayaraman et al. 1996).

roughly $0.32° \times 0.32°$. The Sky Maps are composed of two separate scans, one scan taken with the satellite pointing in the direction **leading** the Earth in its orbit and the other scan **trailing** the Earth. Shown in Figure 5-2 is the weekly sky map for

the 33rd week, corresponding to a longitude of Earth of 287°, in the 60 μm wave band. For Week 33, the leading scan is the right half of Figure 5-2, while the left half of the figure is the trailing scan. The S-shaped feature is due to galactic emission. The oval-shaped feature is primarily due to emission from the zodiacal cloud, but could mask the signature of the Kuiper disk. The brightness is given in MJy/sr. One

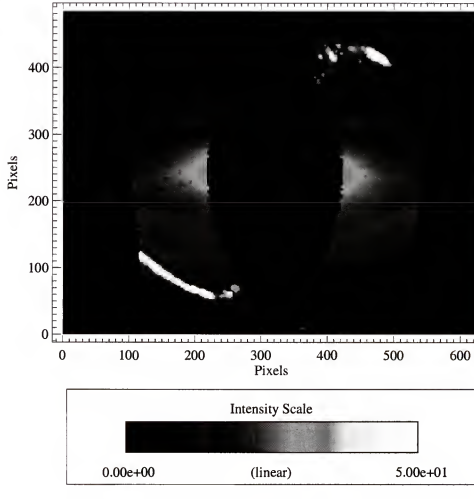

Figure 5-2: COBE DIRBE Weekly Sky Map data in the 60 μm wave band for Week 33 (corresponding to $\lambda_{\oplus} = 287°$). The left side of the image corresponds to lines of sight trailing the Earth in its orbit, while the right side corresponds to leading lines of sight. The S-shaped feature is due to galactic emission. The oval-shaped feature is primarily due to emission from the zodiacal cloud, but could mask the signature of the Kuiper disk.

advantage of using COBE data is that DIRBE continuously scanned the sky at solar

elongations from 64° to 124° over a 10 month interval in order to produce the weekly sky maps, which offer previously unparalleled coverage of the infrared sky. Another advantage of using COBE data is that DIRBE is an absolutely calibrated photometer. By chopping between the sky signal and a zero-flux internal surface, DIRBE made very reliable absolute photometric measurements (Boggess et al. 1992, Hauser et al. 1998, Kelsall et al. 1998). In contrast, the calibration of the photometric zero-point of IRAS was relatively uncertain.

5.2 Kelsall Zodiacal Cloud Model

We present below a description of the Kelsall model following Kelsall et al. (1998.) The Kelsall model for the zodiacal cloud is for an integrated brightness based on a wavelength, λ, and a distance dependent temperature, $T(R) = T_o R^{-\delta}$ where T_o = 286 K is the temperature of the dust at 1 AU and the parameter δ =0.467 is very close to the theoretical value of 0.5 for large gray grains in radiative equilibrium. The brightness integral for the entire model can be written as

$$Z_\lambda = \sum_{c=1}^{3} \int n_c(X,Y,Z) \left[A_{c,\lambda} F_\lambda^\odot \Phi_\lambda(\Theta) + (1 - A_{c,\lambda}) E_{c,\lambda} B_\lambda(T) K_\lambda(T) \right] ds \qquad (5.1)$$

where the sum is over the different components (i.e., the dust bands, the resonant ring, and the background cloud), $n_c(X,Y,Z)$ is the density distribution for component c (dust bands, resonant ring, or background cloud) with regards to heliocentric ecliptic coordinates (X,Y,Z), $A_{c,\lambda}$ is the albedo for component c at wavelength λ, $F_\lambda^\odot$ is the solar flux, $\Phi_\lambda(\Theta)$ is the phase function for scattering at an angle Θ, and $E_{c,\lambda}$ is the emissivity factor that corrects for deviations from $B_\lambda(T)$, the blackbody thermal emission. Finally, $K_\lambda(T)$ is the color correction factor, the use of which is equivalent to convolving the source function with the DIRBE spectral response (Kelsall et al. 1998, Hauser et al. 1998). For the mid and far infrared wave bands we are considering

($\lambda \geq 12\ \mu m$), the albedos are zero, so equation 5.1 reduces to

$$Z_\lambda = \sum_{c=1}^{3} \int n_c(X,Y,Z) E_{c,\lambda} B_\lambda(T) K_\lambda(T) ds \tag{5.2}$$

The parameters for the zodiacal cloud models were determined by using the Levenberg-Marquardt nonlinear least-squares optimization algorithm (Kelsall et al. 1998, Bevinton 1969) and the relevant parameters, taken from Kelsall et al. (1998), for the 25 and 60 μm wave band are listed in Table 5-1. Since the CIB was assumed to be isotropic, the rational of Kelsall et al. (1998) was to fit parameters of the zodiacal cloud relying on the assumption that the zodiacal cloud brightness would be time varying. Due to the fact that the CIB was expected to be faint compared to the foreground components, the Kelsall zodiacal cloud model was hoped to reproduce the zodiacal cloud brightness to within a few percent (Kelsall et al. 1998). All that remains is defining the density distributions for the different components.

5.2.1 Kelsall Background Zodiacal Cloud Model

The background zodiacal cloud is offset from the sun. Kelsall et al. (1998) account for this by allowing the model to be offset from the Sun by (X_o, Y_o, Z_o) so that the coordinates of the cloud became X', Y', and Z', where $X' = X - X_o$. Y' and Z' are similarly defined. As we will later see, the values for X_o, Y_o, and Z_o appear to be incorrect since the given model offset does not match the offset seen in the COBE data. The height above the mid-plane of the cloud, Z_c, is written as $Z_c = X' \sin(\Omega) \sin(i) - Y' \cos(\Omega) \sin(i) + Z' \cos(i)$ where i and Ω are the inclination and ascending node of the background cloud mid-plane. We can define a function, $f(\zeta)$, which represents a fan-like vertical distribution as $f(\zeta) = e^{-\beta_v g^\gamma}$ where $\zeta = |Z_c/R_c|$ and β_v and γ are model parameters representing a vertical shape parameter and a vertical power law exponent, respectively. The variable g is defined as

$$g = \begin{cases} \zeta^2/2\mu & \text{for } \zeta < \mu \\ \zeta - \mu/2 & \text{for } \zeta \geq \mu \end{cases} \tag{5.3}$$

Table 5-1: Relevant parameters for Kelsall zodiacal cloud model.

Parameter Name	Description	Value	68 % Joint Confidence Uncertainty
n_o	Density at 1 AU	1.13×10^{-7} AU^{-1}	6.4×10^{-10} AU^{-1}
α	Radial power-law exponent	1.34	0.022
β_v	Vertical shape parameter	4.14	0.067
γ	Vertical power-law exponent	0.942	0.025
μ	Widening parameter	0.189	0.014
i	Inclination of cloud	2.03°	0.017°
Ω	Ascending node of cloud	77.7°	0.6°
X_o	x offset from Sun	0.0119 AU	0.0011 AU
Y_o	y offset from Sun	0.00548 AU	0.00077 AU
Z_o	z offset from Sun	-0.00215 AU	0.00043 AU
T_o	Temperature at 1 AU	286 K	–
E_6	Emissivity factor for background cloud at 25 μm	1.00	–
E_7	Emissivity factor for background cloud at 60 μm	0.733	0.0055

Relevant parameters are listed for the Kelsall zodiacal cloud model. These parameters for the background cloud in the 25 and 60 μm wave bands are taken from Table 1 of Kelsall et al. (1998).

and we can then write the density distribution for the background zodiacal cloud as

$$n_c(X, Y, Z) = n_o R_c^{-\alpha} f(\zeta) \tag{5.4}$$

where n_o is the density at 1 AU and α is the radial power law exponent. As can be seen, there are many different parameters in one single density distribution. The strengths and weaknesses of the model are discussed in subsequent sections.

5.2.2 Kelsall Dust Band Model

The density distribution for the i^{th} dust band can be written as

$$n_{Bi}(X, Y, Z) = e^{-C_i}\left(1 - e^{-D_i}\right)\left(\frac{3n_{3Bi}}{R}\right)\left[v_{Bi} + \left(\frac{\zeta_{Bi}}{\delta_{\zeta Bi}}\right)^{pBi}\right] \tag{5.5}$$

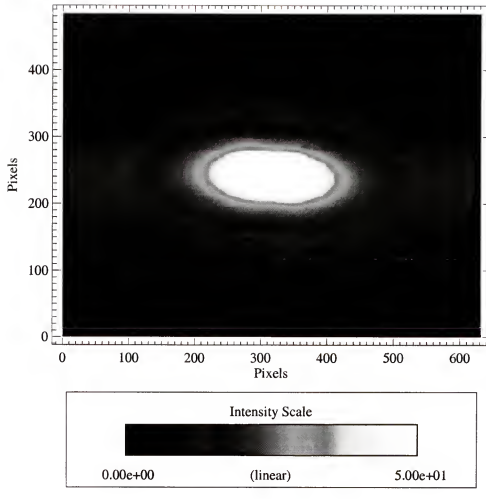

Figure 5-3: Kelsall background zodiacal cloud model. The model is viewed in the 60 μm wave band for Week 33 (corresponding to $\lambda_{\oplus} = 287°$).

where

$$Ci = \left(\frac{\zeta_{Bi}}{\delta_{\zeta Bi}} \right)^{6} \tag{5.6}$$

and

$$Di = \left(\frac{R}{\delta_{RBi}} \right)^{20} \tag{5.7}$$

n_{3Bi} is the density of the i^{th} dust band at 3 AU, $\delta_{\zeta Bi}$, υ_{Bi}, and p_{Bi} are shape parameters, and δ_{RBi} is a parameter which determines how far the i^{th} dust band has migrated in toward the Sun. $\zeta_{Bi} = |z_{Bi}/R_b|$ is the ratio of the height of the i^{th} dust

band above the mid-plane to its radial location. The weaknesses of this model and why we choose not to use it are discussed in subsequent sections.

5.2.3 Kelsall Circumsolar Ring Model

Kelsall et al. (1998) choose to model the resonant ring and trailing/leading asymmetry as an empirical parameterized model. The density distribution for the ring, $n_R(X, Y, Z)$, is composed of two distinct parts, one component due to the circumsolar ring, n_{ring}, and a second component n_{blob}, due to a "trailing blob," the trailing/leading asymmetry seen by IRAS and COBE (Dermott et al. 1994):

$$n_R(X, Y, Z) = n_{ring} + n_{blob} \tag{5.8}$$

where

$$n_{ring} = n_{SR} \times exp\left[-\frac{(R - R_{SR})^2}{2\sigma_{rSR}^2} - \frac{|Z_R|}{\sigma_{zSR}}\right] \tag{5.9}$$

and

$$n_{blob} = n_{TB} \times exp\left[-\frac{(R - R_{TB})^2}{2\sigma_{rTB}^2} - \frac{|Z_R|}{\sigma_{zTB}} - \frac{(\theta - \theta_{TB})^2}{2\sigma_{\theta TB}^2}\right] \tag{5.10}$$

In the above equations, the subscript SR stands for the circumsolar ring component while TB stands for the trailing density enhancement component. The n parameters refer to peak number density at location R, and the σ parameters are free parameters for the scale lengths in the corresponding R, Z_R, and θ coordinates. θ is the heliocentric ecliptic longitude relative to the mean longitude relative to the mean longitude of Earth. The fact that this ring model divides the ring into two components is non-physical and will be discussed in subsequent sections. Ultimately, we choose not to use this model in favor of a dynamical ring model.

5.2.4 Discussion of Kelsall Models

As an initial step to searching for the Kuiper disk, we attempt to recreate the three components of the empirical zodiacal cloud model, following the description of each component as provided by Kelsall et al. (1998). However, we are only

able to successfully reconstruct the empirical background zodiacal cloud model to $\sim 1\%$. Our attempts to reconstruct the dust band model, for instance, produce a model that appears similar in form to the results of Kelsall et al. (1998). However, upon comparison with the actual model brightnesses for two different positions at two different times (DIRBE Pixel 162811 ($\lambda = 122°$, $\beta = 0°$) Week 22 and DIRBE Pixel 64552 ($\lambda = 137°$, $\beta = 46°$ Week 25), our model brightnesses differed from the published values by 16 to 19% for the 25 μm wave band, and 15 to 21% for the 60 μm wave band. The fact that our results do not differ by a simple scale factor is worrisome, and implies the parameters of the Kelsall model have not been published accurately. Furthermore, we are unable to reproduce the Kelsall ring model with any degree of reliability and simply do not believe that their method of dividing the ring model into a ring and a separate blob is physically meaningful. As a result, we are not using our reproductions of either the Kelsall dust band model or the Kelsall circumsolar ring model for the analysis in this dissertation. Instead, we replace the empirical dust band and ring models with a dynamical dust band model from Grogan et al. (2001) and a dynamical ring model from Jayaraman (1995) and Jayaraman et al. (2001).

5.3 Dynamical Zodiacal Cloud Models

The University of Florida dynamical models are based on the theory of dust particle capture into mean motion resonances in the presence of drag forces (Weidenschilling and Jackson 1993, Liou and Zook 1997) and the theory of secular perturbations, the classical method used to study the long term orbital evolution of both planets and minor planets in planetary systems. The dynamical evolution of the particles is followed from source to sink with Poynting Robertson light drag (PR drag), solar wind drag, radiation pressure, and the effects of planetary gravitational perturbations included. Based on these effects, a set of orbits is generated for the particles

in the disk. The orbits of the particles are distributed through a three-dimensional array of cells, generating a three-dimensional numerical SIMUL model, the basic assumptions of which are outlined in Appendix A. A Line of Sight (LOS) Integrator allows a model to be viewed as it would appear to an Earth-based observer in a given wave band at a specified distance. The brightness along the line of sight is calculated assuming the particles are spheres of a given diameter which are composed of a given material (such as astronomical silicate), and the optical properties of these particles are obtained using an advanced Mie theory (Gustafson 1994). The model can even be convolved with a beam size or pixel size to simulate how an observation would appear to a specific telescope or space observatory, such as as COBE. Models of this kind have been successfully used to study asymmetries in the zodiacal cloud (Dermott et al. 1998; Holmes et al. 1998), planetary debris disks (Wyatt et al. 1999), the Kuiper disk (Liou et al. 1999), and exo-zodiacal clouds (Holmes et al. 1999).

5.3.1 Background Zodiacal Cloud

As of yet, there is no complete dynamical model of the background zodiacal cloud, which is why it is necessary to utilize an empirical model like that of Kelsall (1998). Dynamical models of both the dust bands (Grogan et al. 2001) and Earth's resonant ring (Jayaraman 1995) have been produced, however. These models are preferable to the empirical Kelsall models because they provide physical insights into the processes which form and maintain these structures. Discrete features like the dust bands and resonant ring are relatively simple to model compared to the background zodiacal cloud, which is a very complicated system. Many unresolved questions remain about the background cloud, such as what is the dominant source of particles, what is the size frequency distribution of the dust, and how can dynamical models be constructed to account for the warp and offset of the background cloud.

The dominant source of the cloud is still not known. Clearly, both asteroidal and cometary particles contribute to the cloud, but their percentage contributions

have not yet been definitively determined, though the current view is that asteroidal particles dominate (Dermott et al. 2000). The dynamical modeling techniques use low-order secular perturbation theory which applies only to low eccentricity orbits. Typically, comets and cometary particles have highly eccentric orbits, while asteroids and asteroidal particles have low eccentricities. As a result, the dynamical models have focused on low eccentricity asteroidal dust particles. Recently, it has been shown that mean motion resonances can transform asteroidal orbits into cometary orbits. Likewise, scattering and secular resonances can also transform asteroidal orbits into cometary orbits (Dermott et al. 2000). In addition, dust particles from the Kuiper belt (Liou et al. 1996) as well as interstellar dust particles (Grogan et al. 1996) may contribute a small percentage of the brightness of the background cloud.

In the past, a collisional size frequency distribution corresponding to collisional equilibrium was assumed, with a size frequency index q=1.83 (Dohnanyi 1969). A record of the actual size frequency distribution of the dust particles at 1 AU exists in the cratering record on the LDEF satellite (Love and Brownlee 1993). This record shows that the surface area is dominated by large particles, peaking at approximately 100 μm diameter particles, rather than smaller particles as assumed by collisional equilibrium. The linear portion of the curve between 10 and 100 μm gives a $q_{LDEF} \approx$ 1.2. This result, is a measure of q at 1 AU and may be complicated by the presence of Earth's resonant ring and the fact that Earth preferentially accretes asteroidal particles. Consequently, q_{LDEF} may differ from the true q for the background cloud. (Dermott et al. 1999a).

As discussed in previous Chapter 3, the background zodiacal cloud is warped and the center of symmetry of the background cloud is displaced from the Sun. These asymmetries are caused by the presence of planets in the solar system. The warp in the plane of symmetry of the zodiacal cloud is caused by the variation of the forced inclinations of the dust particles with respect to their heliocentric distances. The

warp is due to the fact that the planets do not have a common orbital plane (Holmes et al. 1997, Dermott et al. 1998). The offset is due to the fact that the planets have eccentric orbits (Holmes et al. 1998, Dermott et al. 1998). Models of heuristic warped clouds have been constructed (Holmes et al. 1998) as well as models of an offset disk around another star, HR 4796A (Wyatt et al. 1999). However, a complete model of the background zodiacal cloud which accounts for both its warp and offset has not yet been developed.

Due to these unresolved questions, it is necessary to utilize the Kelsall et al. (1998) model for the background zodiacal cloud, but with a modification to the original model X_o, Y_o, and Z_o offsets, requiring that the model offset fits the offset seen in the COBE data. As seen in Figure 5-4, the maximum of the (N+S)/2 variation is located at $43.8° \pm 3.0$ for the COBE data and at $90.7° \pm 0.1$ for the Kelsall model, a difference of 46.9°. The residuals from the subtraction of both the original Kelsall model and modified Kelsall models will be discussed in subsequent sections.

5.3.2 Dynamical Dust Band Model

Discovered by IRAS (Low et al. 1984), the dust bands have been attributed to the break up of three Hirayama asteroid families: Eos, Themis, and Koronis (Dermott et al. 1984). Components due to each of these families are included in the dynamical dust band model developed by Grogan et al. (2001) which we use in this dissertation. Specifically, models for the Eos dust bands are combined with models for the Themis and Koronis dust bands to produce a total dust band model. Each of the dust band models are three dimensional models constructed from a given set of initial orbital elements.

In constructing a model, the dynamical evolution of a set of dust particles of various sizes is followed from source to sink using the RADAU numerical integrator with Poynting Robertson light drag (PR drag), solar wind drag, radiation pressure,

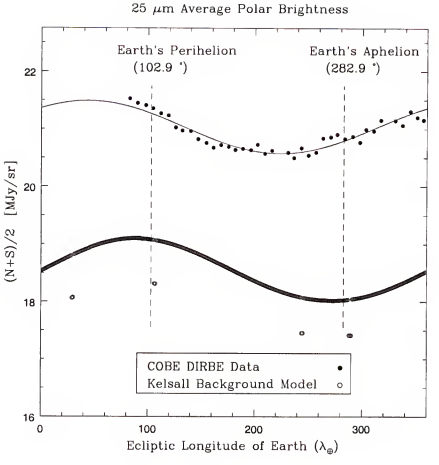

Figure 5-4: Average polar brightness for the 25 μm COBE DIRBE vs. the Kelsall background cloud model. The peak of the COBE data is clearly different than the peak of the Kelsall model, implying the offset of the COBE data is different than the offset of the Kelsall model. The maximum of the (N+S)/2 variation is located at $43.8° \pm 3.0$ for the COBE data and at $90.7° \pm 0.1$ for the Kelsall model, a difference of 46.9°.

and the effects of planetary gravitational perturbations included. The orbital elements of these dust particles are decomposed into forced elements and proper elements, in accordance with low-order secular perturbation theory. The inclination and eccentricity of asteroidal orbits are typically low, and therefore the forced elements are independent of the proper elements and are functions of only the semi-major axis and the particle size. The proper elements are determined from the initial conditions on the dust particles. Since the particles in each family dust band are believed to

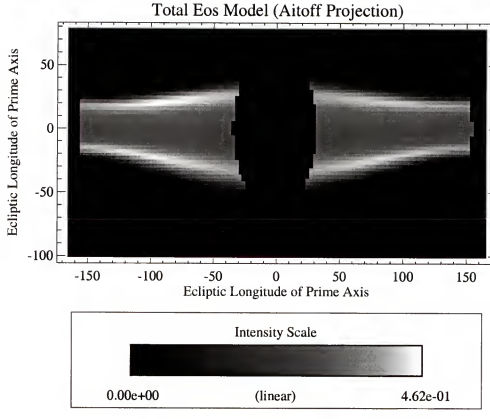

Figure 5-5: For this dissertation, we construct an Aitoff projection of the total Eos dust band model in the 25 μm wave band. This is now the model would appear to an exo-solar observer. I_{proper} is approximately 9.4°. This model was originally developed by Grogan et al. (2001).

have originated from the corresponding asteroid family, an initial guess for the proper inclination is that of the mean inclination of the asteroid family. This initial value for I_{proper} is refined experimentally, by fitting a succession of dust band models to IRAS data until the best fit is determined (Grogan et al. 2001). The forced and proper elements are then added vectorially to find the osculating elements, in accordance with the particle in a circle method described in Chapter 2 (See Figure 2-1).

Based on the set of osculating elements generated by the numerical integrations, a SIMUL model is constructed (See Appendix A). The models are built by generating a set of orbits for the particles in the model disk and then distributing the orbits through a three dimensional array of cells. A Line of Sight (LOS) Integrator

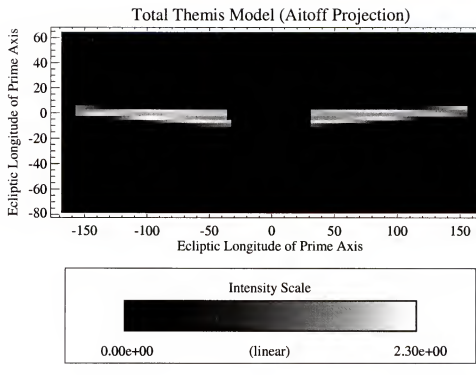

Figure 5-6: An Aitoff projection of the total Themis dust band model in the 25 μm wave band. I_{proper} is approximately 1.4° (Grogan et al. 2001).

allows a model to be viewed as it would appear to an Earth-based observer in a given wave band at a specified distance. The brightness along the line of sight is calculated assuming the particles are spheres of a given diameter which are composed of astronomical silicate, and the optical properties of these particles are obtained using an advanced Mie theory (Gustafson 1994). Using the LOS Integrator, the model can be viewed as if it were an exo-solar dust band or it can be converted to the weekly sky map format so it can be compared to the COBE DIRBE data. Three different models are constructed (an Eos model, a Themis model, and a Koronis model) and then combined into a total dust band model.

The Eos dust band model has a proper inclination, I_{proper}, equal to 9.35° with a mean semi-major axis of 3.015 AU. The Themis dust band model is located at approximately 3.148 AU with an I_{proper} of 1.43°. Lastly, the Koronis dust band

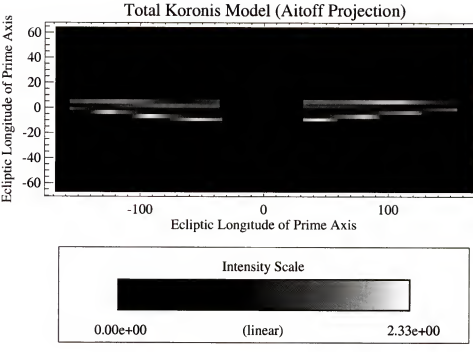

Figure 5-7: An Aitoff projection of the total Koronis dust band model in the 25 μm wave band. I_{proper} is approximately 2.1° (Grogan et al. 2001).

model has an $I_{proper} = 2.11°$ with a mean semi-major axis of 2.876 AU (Grogan et al. 2001). Each model is composed of several different models based on single size particles. Models for particles with diameters of 4, 9, 14, 25, and 100 μm are included. These individual models are weighted according to a size frequency distribution with index q = 1.43 and are show in Figure 5-5, Figure 5-6, and Figure 5-7. In turn, the Eos, Themis, and Koronis models are combined to form a total dust band model by weighting each model according to its respective contribution to the dust band:

$$Total\ Dust\ Band\ Model\ =\ 4.0\ Eos + 0.35\ Themis + 0.35\ Koronis \qquad (5.11)$$

The total dynamical dust band model is shown in an exo-zodiacal view for the 25 μm wave band in Figure 5-8 and as a COBE Weekly Skymap for Week 33, which corresponds to a longitude of Earth, $\lambda_{\oplus} = 287°$, in Figure 5-9. The total area of dust in the dynamical dust band model is 4.7×10^9 km^2.

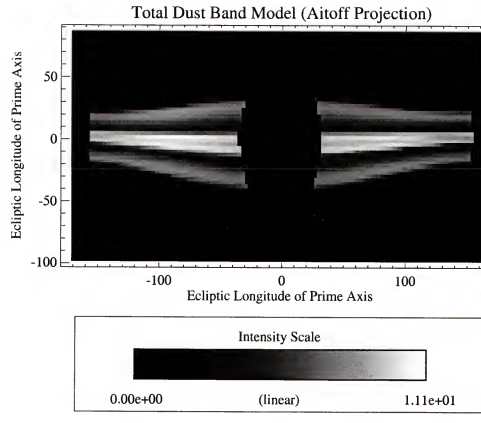

Figure 5-8: An Aitoff projection of the total dust band model in the 25 μm wave band. (Grogan et al. 2001).

It should be noted that the dust bands have two distinct components: a low frequency component that blends into the background cloud and a high frequency component that is easily identifiable and has been associated with three Hirayama asteroid families (Eos, Themis, and Koronis). Due to the existence of the low frequency component, an iterative process (Dermott et al. 1994a, Grogan et al. 1997, Grogan et al. 2001) must be used to to separate the low frequency dust band component from the background cloud signal. First, the dust band model is added to the background zodiacal cloud. Either an observation or a model of the background cloud can be used, and in this case the Kelsall background zodiacal cloud model is used. The combination of the dynamical dust band model and the Kelsall background cloud model is then Fourier filtered. The resultant high frequency component (RHC) is simply

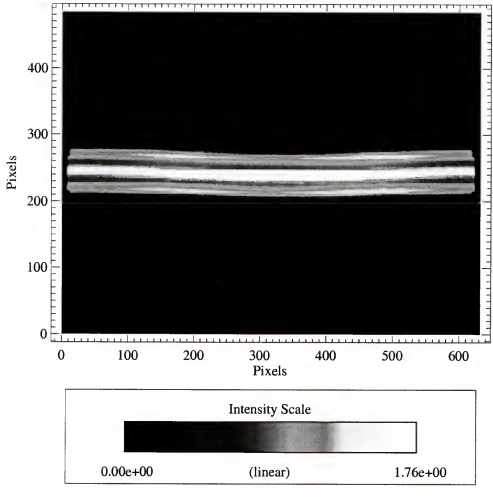

Figure 5-9: A COBE Weekly Skymap type projection of the total dust band model in the 60 μm wave band for Week 33 (corresponding to $\lambda_{\oplus} = 287°$). This model was originally developed by Grogan et al. (2001).

the high frequency component of the dust band model. The resultant low frequency component (RLC) has three distinct members: (1) the background zodiacal cloud, or the "true background cloud," (2) the low frequency component of the dust band model, and (3) the low frequency component of the dust bands that had previously blended into the background cloud. Assuming that (2) and (3) are approximately equal, the true background cloud can be determined by subtracting the low frequency component, RLC, from twice the original background cloud (Grogan et al. 2001),

which contains both the low frequency component of the dust band model (Low) and the true zodiacal background cloud (True Zody). Denoting (1) as "True Zody" and (2) and (3) as "Low," we can write

$$\begin{aligned} True\ Zody &= 2 \times (Kelsall\ Background) - RLC && (5.12) \\ &= 2 \times (Low + True\ Zody) - RLC && (5.13) \\ &\cong 2 \times (Low + True\ Zody) - (True\ Zody + Low + Low) \\ &\cong True\ Zody \end{aligned}$$

where True Zody is the true zodiacal background cloud, that is, the background cloud without the extra low frequency dust band component. In this dissertation, when we subtract the background cloud from the COBE data to study the residuals, we will be subtracting the true zodiacal background cloud.

5.3.3 Dynamical Circumsolar Ring Model

The dynamical circumsolar ring model was produced by Jayaraman et al. 1995 in the following manner. First, numerical integrations of particles of a set diameter were run to determine the capture rates of these particles into various first order external mean motion resonances with the Earth. The percentage of particles trapped in the $p : p + 1$ external resonances, where p ranged from 3 to 17, was determined experimentally as was the average trapping time for the particles. For $12\mu m$ diameter particles, on average approximately 20% of the particles were trapped. An approach to modeling that was numerical in nature was considered, but later rejected. To build a numerical model by means of numerical integrations requires large numbers of particles to obtain the desired model resolution, especially since such a large number of resonances had to be considered. At the time, it was considered that due to the low percentage of trapped particles, it would be an inefficient use of computer

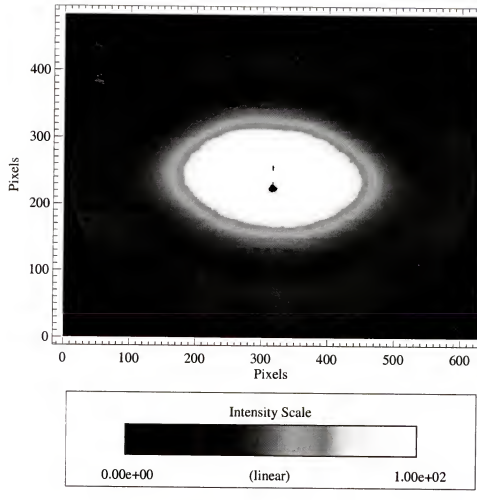

Figure 5-10: True background zodiacal cloud model in the 25 μm wave band for the original Kelsall background zodiacal cloud model and the dynamical dust band model. The brightness levels at the center of the model have a very sharp peak (22516.8 MJy/sr), due to the fact that this model and the Kelsall model are centered on the Sun. The maximum displayed brightness is set to 100 MJy/sr in order to be able to see the dimmer parts of the model farther out from the Sun. In addition, there is also a trough in brightness near the center and near the poles, there are some areas of very low brightness. These are both functions of the Fourier fitting routines, but are not troublesome since the problematic regions near the Sun are neatly encompassed by the Sun-avoidance region in the COBE data and our search for the Kuiper disk is centered in the ecliptic and not near the poles. The Kelsall et al. (1998) background zodiacal cloud model used is shown in Figure 5-3 and the dynamical dust band model used is shown in Figure 5-9, but for the 60 μm wave band. The shape and basic attributes of the models are similar from wave band to wave band, but the flux levels are different.

time to generate enough orbits to build a model numerically. Instead, a different approach was taken which consisted of selecting a "typical" orbit for each resonance. The criteria for choosing these typical orbits were a large libration amplitude and a long trapping lifetime. Each typical orbit was integrated for its experimentally determined trapping lifetime and then weighted by its numerically obtained capture probability. The orbits were combined to produce the initial orbital model. A three dimensional model was then constructed in much the same way the dynamical dust band SIMUL models were created. The orbits in the model were distributed through a toroidal, three dimensional array of cells around the Earth's orbit. A Line of Sight (LOS) Integrator allows a model to be viewed as it would appear to an Earth-based observer in a given wave band at a specified distance (Jayaraman et al. 1995, Jayaraman et al. 2001). Shown in Figure 5-11 is an exo-solar system view of a model of Earth's resonant ring. The model is composed solely of 12 μm diameter particles and is viewed in the 12 μm wave band. The white dot in the center of the torus represents the Sun, while the dot that is above the Sun represents the Earth. The concentration of material to the right of the Earth is the trailing density enhancement discussed earlier. Since the toroidal dust ring co-rotates with the Earth, it is easy to see why the trailing scans would always be brighter than the leading scans. There are several important points to note about the dynamics of the resonant ring model, the first of which is that, in a frame which co-rotates with the Earth, the orbit of a particle in a $p+1:p$ resonance has p lobes, which appear as regions of particle density enhancement (Murray and Dermott 1999) in a multiple particle system. For example, in a 3:2 external mean motion resonance, the particle orbits the Sun twice for every three times the Earth completes an orbit. Hence, the resonant ring will have 2 lobes, which co-rotate with the planet. Over many cycles with multiple particles, the particle density distribution will appear to be a toroidal ring with two lobes of enhanced brightness, as discussed in Chapter 4 for the case of the 3:2 mean motion

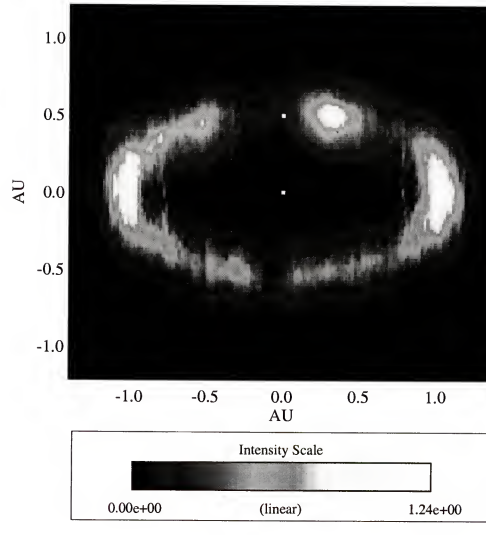

Figure 5-11: Exo-solar system view of a dynamical model of Earth's resonant ring composed of 12 micron diameter particles as viewed in the 12 μm wave band. The white dot in the center of the torus represents the Sun, while the dot that is above the Sun represents the Earth. The dots are not to scale. The concentration of material to the right of the Earth is the trailing density enhancement discussed earlier. Since the toroidal dust ring co-rotates with the Earth, it is easy to see why the trailing scans would always be brighter than the leading scans in the 12 μm wave band. The intensity scale is in MJy/sr (Jayaraman et al. 1995, Dermott et al. 1998, Jayaraman et al. 2001).

resonance with Neptune. In the case of the Earth's resonant ring, there are many different external mean motion resonances in which particles become trapped, so the ring is a supper-position of many lobes. In the case where there are no drag forces on

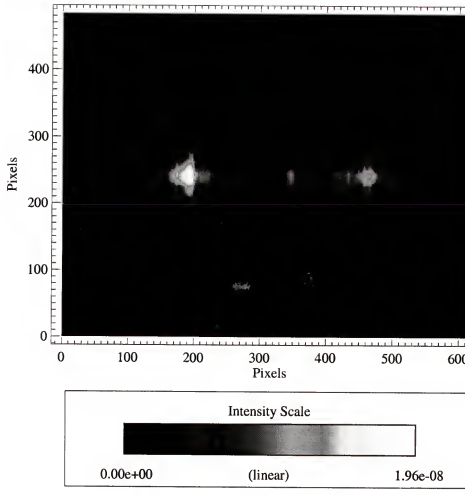

Figure 5-12: COBE Weekly Skymap type projection of the resonant ring model, constructed with 15 μm diameter particles in the 60 μm wave band for Week 33 (corresponding to $\lambda_{\oplus} = 287°$). The left side of the image corresponds to lines of sight trailing the Earth in its orbit, while the right side corresponds to leading lines of sight. The concentration of material on the left (or trailing) side is clearly brighter than that on the right (or leading) side of the image, illustrating the trailing/leading asymmetry. The intensity is in MJy/sr.

the particle, that is if $\beta = 0$, then the ring's lobes would be symmetric with respect to the Earth-Sun line, with the Earth residing between the lobes for the case of stable aphelion librators, corresponding to a resonant argument, ϕ, of 180°. However, since the resonant argument depends on the drag rate, when drag is introduced into the system ($\beta > 0$), the resonant argument takes on a value that maximizes $< \sin\phi >$ in

order to compensate for the drag force. This results in $\phi > \pi$ which means that the conjunction of the particle with the Earth occurs after the particle's aphelion and which makes the lobes in the orbit asymmetric with respect to the Earth-Sun line. Since the Earth's resonant ring involves many different resonances, in the presence of substantial drag forces (i.e., for small particles), the lobes of the particles bunch together behind the Earth in its orbit causing the brightness trailing the Earth in its orbit to always be brighter than the brightness leading the Earth in its orbit. This effect can be seen in the model (Figure) and in the COBE data (Dermott et al. 1994b, Dermott et al. 1999a, Jayaraman et al. 1995, Malhotra 1996, Jayaraman and Dermott 2001).

5.4 Arendt ISM Models

In addition to the zodiacal cloud, there is another component which needs to be subtracted from the COBE DIRBE data to complete our search for the Kuiper disk: the component of the infrared sky brightness that is due to galactic emission. Following the derivation outlined in Arendt et al. (1998), we can break the infrared sky brightness, $I_{obs}(l, b, \lambda, t)$, into components:

$$I_{obs}(l, b, \lambda, t) = Z(l, b, \lambda, t) + G_S(l, b, \lambda) + G_I(l, b, \lambda) + I_0(l, b, \lambda) \tag{5.14}$$

where l and b are Galactic longitude and latitude, λ is the wave band in microns, t is time, $Z(l, b, \lambda, t)$ is the emission due to all three components of the zodiacal cloud, and $G_S(l, b, \lambda)$ is the galactic emission due to resolved and unresolved stars. $G_S(l, b, \lambda)$ can be broken down further into emission due to bright sources and emission due to faint sources. The bright sources are simply blanked out. The faint sources are modeled using a Faint Source Model (Arendt et al. 1998, Wainscoat et al. 1992) which is physically based on a statistical model for galactic brightness. The Faint Source Model only pertains to wave bands $\leq 25\mu m$, so is not needed for our analysis of the $60\mu m$ COBE data. $G_I(l, b, \lambda)$ is the galactic emission due to the interstellar

medium (ISM). $I_0(l, b, \lambda)$ represents the residual brightness obtained by subtracting the components of the infrared sky brightness due to the zodiacal cloud, the bright and faint galactic sources, and the ISM from the observed infrared sky brightness. $I_0(l, b, \lambda)$ should contain both emission from the Kuiper disk, if it is detectable with COBE, and emission from the isotropic cosmic infrared background (CIB), which is produced by pregalactic sources, protogalaxies, evolving galaxies, and exotic processes uncommon in the local universe (Arendt et al. 1998; Bond, Carr and Hogan 1986). The CIB should not hinder our search for the Kuiper disk component, since we expect the CIB to be isotropic while the Kuiper component should have an asymmetry due to particles in mean motion resonance with Neptune.

5.4.1 Bright Source Blanking and the Faint Source Model (G_S)

Bright galactic sources were not removed individually. Instead, cutoff values for the DIRBE brightnesses were determined. These cutoffs were 85 and 100 Jy for the 12 and 25 μm wave bands, respectively, and 4.5 MJy/sr for the 60, 100, 140, and 240 μm wave bands. In the Arendt et al. (1998) analysis, pixels with brightnesses that were greater than the locally determined background brightness by more than the cutoff values were set to zero brightness. In this analysis, we use Zodi-Subtracted Mission Average (ZSMA) maps, for the determination of the 100 μm template, and do not set any pixels to zero brightness, since we assume that the brightest pixels will be averaged out.

The Faint Source Model (FSM) was based on the SKY model developed by Wainscoat et al. (1992) and is a statistical model for calculating the line of sight brightness due to the various stellar components of the galaxy. It applies to wave bands $\leq 25\mu m$. For the 60, 100, 140, and 240 μm, the brightness contribution from faint galactic stellar sources is assumed to be negligible.

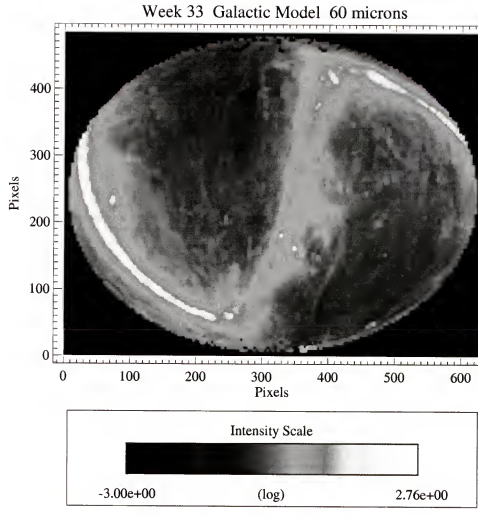

Figure 5-13: The ISM model in the 60 μm wave band for Week 33 (corresponding to $\lambda_{\oplus} = 287°$).

5.4.2 ISM Model (G_I)

Arendt et al. (1998) constructs a model for the brightness contribution of the galactic interstellar medium to the infrared sky brightness seen in the COBE data. The model is based on the correlation of H I column densities with I_{ZG}, the 100 μm zodiacal light subtracted, bright source blanked DIRBE data, which is defined as

$$I_{ZG} = I_{obs}(l, b, \lambda) - Z(l, b, \lambda) - G_S(l, b, \lambda) \tag{5.15}$$

Note that equation 5.15 is not time dependent and therefore we can use the Zodi-Subtracted Mission Average (ZSMA) DIRBE maps, which list $I_{obs}(l,b,\lambda) - Z(l,b,\lambda)$. The 100 μm wave band is chosen because it provides full coverage of the sky, it has better sensitivity than the data at longer wavelengths, and it is less affected than the shorter wave bands by the errors associated with the removal of the three-component Kelsall et al. (1998) total zodiacal cloud model. In addition, as a middle wavelength, it will not bias the ISM model towards structures only seen at shorter or longer wavelengths (Arendt et al. 1998).

Two regions of the sky, the north ecliptic pole and the region of minimum H I column density (the Lockman Hole), are chosen to calculate the correlation of the H I data to $I_{ZG}(100\mu m)$, based on the low column densities, the existence of good H I data, and the ability to estimate contributions from the other (molecular and ionized) ISM components in these regions. The intercept of the correlation, νI_0, is the mean intensity which is unassociated with the H I component of the interstellar medium, and is found to be $19.8 \times 10^{-9} W m^{-2} sr^{-1}$ by averaging the intercepts for the two regions (Arendt et al. 1998). This translates into $I_0 = 6.6 \times 10^5$ Jy/sr for the 100 μm wave band. We can use this value to derive $G_I(l,b,100\mu m)$ and then to derive $G_I(l,b,\lambda)$ in general. $G_I(l,b,100\mu m) = I_{ZG} - I_0(100\mu m)$ where $I_0(100\mu m) = 6.6 \times 10^5$ Jy/sr. Using equation 5.15, we derive the 100μm ISM template as outlined in Arendt et al. (1998):

$$G_I(l,b,100\mu m) = I_{obs}(l,b,100\mu m) - Z(l,b,100\mu m) - G_S(l,b,100\mu m) - I_0(100\mu m) \tag{5.16}$$

Then, using $R(\lambda) = I_\nu(\lambda)/I_\nu(100\mu m)$, we can write an expression for $G_I(l,b,\lambda)$

$$G_I(l,b,\lambda) = R(\lambda) G_I(l,b,100\mu m) \tag{5.17}$$

where the values for $R(\lambda)$ for the 12 to 240 μm wave bands as reported in Arendt et al. (1998) are listed in Table 5-2.

Table 5-2: Values for $R(\lambda)$ for the ISM model.

Wave Band (μm)	$R(\lambda)$ $= I_\nu(\lambda)/I_\nu(100\mu m)$
12	0.0462 ± 0.0001
25	0.0480 ± 0.0002
60	0.171 ± 0.0003
100	1.0
140	1.696 ± 0.008
240	1.297 ± 0.005

Values for $R(\lambda)$ for the ISM model. The values for $R(\lambda)$ for the 12 to 240 μm wave bands are taken from Table 4 of Arendt et al. (1998).

5.5 Residuals

The search for the signature of the Kuiper disk is carried out in a systematic manner. First, we subtract the Kelsall background zodiacal cloud model and then the dynamical dust band model from the COBE DIRBE data. This removal should yield initial residuals which are dominated by galactic emission and, in the crucial ecliptic, Earth's resonant ring, which is distinguishable by its unique trailing/leading asymmetry. The ring brightness trailing the Earth in its orbit is always greater in magnitude than in the leading direction for the wave bands we are considering. Each weekly skymap is separated into a trailing scan and a leading scan, making the orientation within a scan easily determined. As a test, when the background cloud and the dust bands are successfully removed from the COBE data, the residuals in the ecliptic should have a brightness enhancement in the trailing direction for any given week.

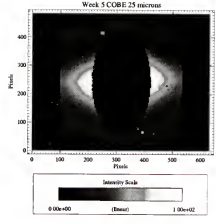

a) Week 5 ($\lambda_\oplus = 91°$)

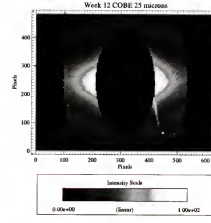

b) Week 12 ($\lambda_\oplus = 140°$)

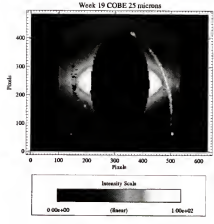

c) Week 19 ($\lambda_\oplus = 189°$)

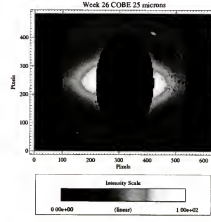

d) Week 26 ($\lambda_\oplus = 238°$)

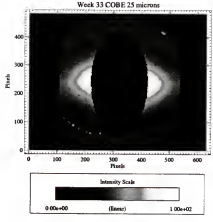

e) Week 33 ($\lambda_\oplus = 287°$)

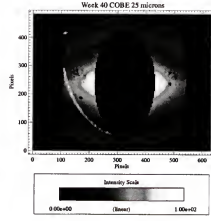

f) Week 40 ($\lambda_\oplus = 336°$)

Figure 5-14: 25 μm COBE DIRBE data in weekly skymap format. The images presented here have a fixed maximum of 100 MJy/sr for easy comparison with each other. The oval-shaped structure is emission from the zodiacal cloud.

We use Week 33 (which corresponds to a longitude of Earth: $\lambda_{\oplus} = 287°$) as a primary example, but we also study five other weeks which, together with Week 33, are separated by 49° in longitude of Earth: Week 5, Week 12, Week 19, Week 26, and Week 40. We first work with the 25 μm wave band because as shown in Figure 5-1, the trailing/leading asymmetry is most easily seen in the 25 μm wave band. Later, in order to search for the Kuiper disk, we utilize data from the 60 μm wave band. Figures 5-14 and 5-15 show the COBE DIRBE data for these weeks in the 25 and 60 μm wave bands, respectively. Figure 5-16 shows only the trailing scans for the 60 μm COBE data. The orientation is the same for the 12 and 25 μm wave bands. These scans will serve as a reference point for locating the trailing/leading asymmetry of the resonant ring. The oval-shaped structure seen in each weekly skymap is due to emission from the zodiacal cloud, which possibly masks emission from the Kuiper disk. The thin, S-shaped structure which cuts across the scans is due to galactic emission.

The images of the data presented here in the 25 μm wave band (Figure 5-14) have a fixed maximum of 100 MJy/sr for easy comparison with each other. The maximum values of the data are 303.360, 177.933, 357.429, 113.780, 133.088, and 164.960 MJy/sr for Week 5, 12, 19, 26, 33, and 40, respectively. The images of the data presented here in the 60 μm wave band (Figure 5-15) have a fixed maximum of 50 MJy/sr for easy comparison with each other. The maximum values of the data are 513.694, 863.171, 1327.73, 397.551, 729.333, 845.550 MJy/sr for Week 5, 12, 19, 26, 33, and 40, respectively. The S-shaped structure is due to galactic emission and is the brightest feature.

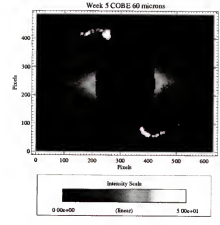

a) Week 5 ($\lambda_\oplus = 91°$)

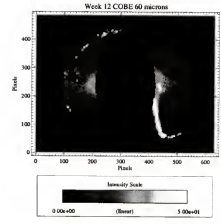

b) Week 12 ($\lambda_\oplus = 140°$)

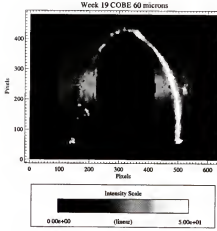

c) Week 19 ($\lambda_\oplus = 189°$)

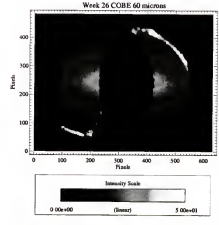

d) Week 26 ($\lambda_\oplus = 238°$)

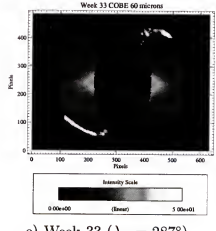

e) Week 33 ($\lambda_\oplus = 287°$)

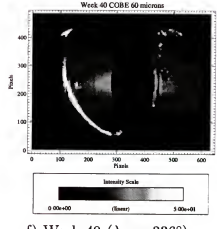

f) Week 40 ($\lambda_\oplus = 336°$)

Figure 5-15: 60 μm COBE DIRBE data in weekly skymap format. The images presented here have a fixed maximum of 50 MJy/sr for easy comparison with each other. The oval-shaped structure is emission from the zodiacal cloud.

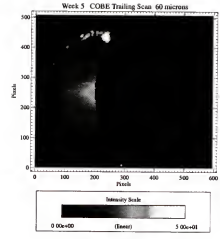

a) Week 5 ($\lambda_\oplus = 91°$)

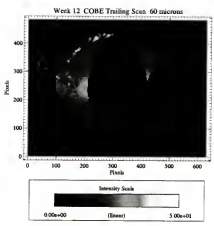

b) Week 12 ($\lambda_\oplus = 140°$)

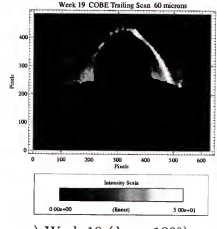

c) Week 19 ($\lambda_\oplus = 189°$)

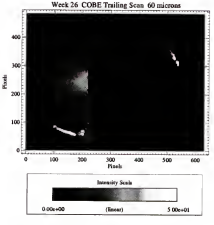

d) Week 26 ($\lambda_\oplus = 238°$)

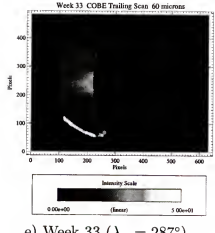

e) Week 33 ($\lambda_\oplus = 287°$)

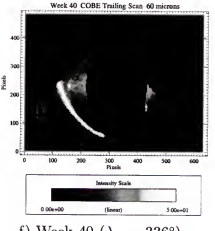

f) Week 40 ($\lambda_\oplus = 336°$)

Figure 5-16: Trailing scans for the 60 μm COBE DIRBE data. A fixed maximum of 50 MJy/sr has been imposed on the data for easy comparison between scans.

5.5.1 Subtracting the Kelsall Model

As detailed in Section 5.3.2, before subtracting the background cloud model the low frequency component of the dust bands needs to be removed. This is accomplished by Fourier Filtering a combination of the Kelsall background cloud model and the Grogan et al. (2001) dust band model as discussed previously. The technique yields a true background model, an example of which is shown in Figure 5-10 for Week 33 in the 25 μm wave band.

For the next stages of analysis, we choose to focus on three of the weeks: Week 5, Week 26, and Week 33. These weeks are chosen because the ecliptic is relatively free from galactic emission and the trailing scans are all in a favorable position for studying residuals due to Earth's resonant ring. In some of the other weeks, the galactic emission cuts across the ecliptic, possibly creating confusing residuals if it is not removed correctly. The residuals obtained by subtracting the Kelsall et al. (1998) background zodiacal cloud model from the COBE DIRBE data in the 25 μm wave band are shown in Figure 5-17. The bulk of the emission due to the lenticular background cloud appears to have been removed. The galactic component can be clearly seen as well as some dust band like residuals lying in the ecliptic. However, the leading halves of the scans appear brighter than the trailing halves, which is the opposite of what is expected. Due to the trailing/leading asymmetry of the resonant ring, the trailing side of the observations should always be brighter than the leading side. The effect should be particularly evident in the 25 μm wave band since, from Figure 5-1, the trailing/leading asymmetry is most obvious at this wavelength.

The removal of the dust band model brings the ring residuals into clearer view as shown in Figure 5-18. The residuals exhibit a leading asymmetry rather than a trailing asymmetry. Figure 5-19 shows the residuals obtained by subtracting both the dust band model (Grogan et al. 2001) and the filtered Kelsall background model from the COBE data in the 60μm wave band for Week 33. The left side

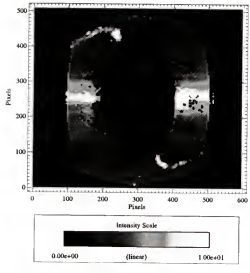

a) Week 5 ($\lambda_{\oplus} = 91°$)

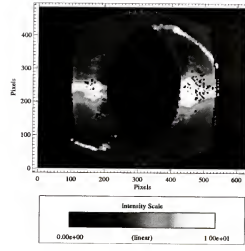

b) Week 26 ($\lambda_{\oplus} = 238°$)

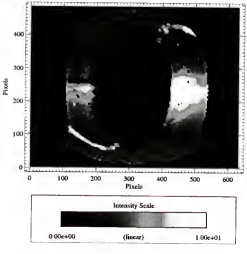

c) Week 33 ($\lambda_{\oplus} = 287°$)

Figure 5-17: Residuals obtained in the 25 μm wave band by subtracting the Kelsall background cloud model from the COBE data. Now that the bulk of the emission from the lenticular background cloud appears to have been removed, the galactic component and some dust band like residuals lying in the ecliptic can be seen. However, the leading (right) halves of the scans appear brighter than the trailing (left) halves, which is the opposite of what is expected. Due to the trailing/leading asymmetry of the resonant ring, the trailing side of the observations should always be brighter than the leading side.

of the image corresponds to lines of sight trailing the Earth in its orbit, while the right side corresponds to leading lines of sight. The brightest feature, aside from

the S-shaped galactic emission, should be due to Earth's resonant ring (since it is the closest structure that has not been removed) and in fact, there is a brightness enhancement in the ecliptic, with the leading side of the enhancement brighter than the trailing side. However, both COBE observations (Dermott et al. 1995) and a dynamical resonant ring model, in the 60 μm wave band for 15 μm diameter particles (Figure 5.3.3), exhibit an enhancement in brightness *trailing* the Earth in its orbit.

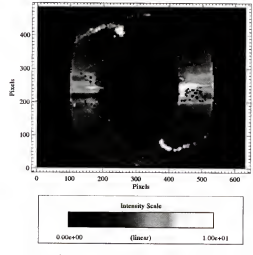

a) Week 5 ($\lambda_\oplus = 91°$)

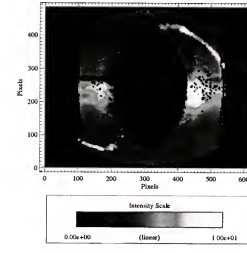

b) Week 26 ($\lambda_\oplus = 238°$)

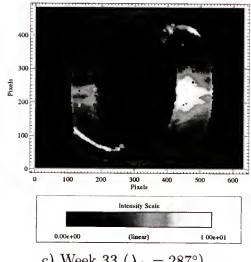

c) Week 33 ($\lambda_\oplus = 287°$)

Figure 5-18: Residuals obtained in the 25 μm wave band by subtracting the Kelsall background cloud model and the dynamical dust band model from the COBE data.

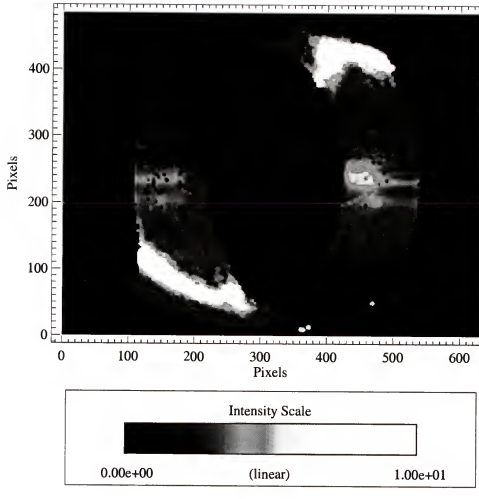

Figure 5-19: Residuals obtained in the 60 μm wave band for Week 33 by subtracting the Kelsall background cloud model and the dynamical dust band model from the COBE data initial residuals. These residuals were obtained by subtracting both the dynamical dust band model and the true Kelsall et al. (1998) background zodiacal cloud model from the COBE data in the 60 μm wave band for Week 33 (corresponding to $\lambda_{\oplus} = 287°$). The left side of the image corresponds to lines of sight trailing the Earth in its orbit, while the right side corresponds to leading lines of sight. The brightest feature, aside from the S-shaped galactic emission, should be due to Earth's resonant ring, since it is the closest structure that has not been removed. In fact, there is a brightness enhancement in the ecliptic, with the leading side of the enhancement brighter than the trailing side. However, both COBE observations (Dermott et al. 1995) and the dynamical resonant ring model, in the 60 μm wave band for 15 μm diameter particles, exhibit an enhancement in brightness trailing the Earth in its orbit.

Clearly, there is a problem with one of the models we have subtracted from the COBE data, since we are not achieving the predicted results in either the 25 or the 60 μm wave bands. The dynamical dust band model total brightness is a small fraction of the COBE DIRBE maximum brightness ($\approx$ 1.7% and 0.2% for the 25 and 60 μm wave bands, respectively). Additionally, the dynamical dust model is physically based and has been well fit to IRAS data (Grogan et al. 2001). Moreover, even before the dust band model is subtracted, the residuals shown in Figure 5-17 exhibit a brightness enhancement in the leading direction. Therefore, we conclude that the problem lies with the background zodiacal cloud model. Although the Kelsall et al. (1998) background model succeeds in matching the overall lenticular shape of the zodiacal cloud (most of the emission due to the background cloud was removed from the data in Figures 5-17 and 5-17), the Kelsall background model is inadequate for describing residuals in the inner solar system and needs to be modified before it can be used toward probing the existence of a Kuiper disk. The main question becomes how to modify the Kelsall model in order to produce the correct trailing/leading asymmetry while still retaining the model's desirable features. As mentioned earlier, the offset of the Kelsall model does not match the offset as seen in the COBE DIRBE data, as shown in Figure 5-4. Sine curves are fit to both the COBE data and the data generated from the Kelsall model. The sine curves don't agree in phase, amplitude, or mean. The maximum of the (N+S)/2 variation is located at $43.839° \pm 2.982$ for the COBE data and at $90.687° \pm 0.0840$ for the Kelsall model, a difference of almost 47°.

5.5.2 Subtracting the Kelsall Model With a Modified Offset

We can modify the offset in the Kelsall model so that the maximum of the (N+S)/2 variation is in agreement with the COBE data, which is shown in Figure 5-20. The fit to the modified Kelsall model is shown in open dots which completely overlap the Kelsall background model points. The filled dots are the COBE DIRBE

Table 5-3: Parameters for sine curve fits to the 25 μm average polar COBE data and Kelsall background cloud model.

Sine Fit Parameter	Average Polar COBE DIRBE Data	Average Polar Kelsall Background Cloud Model
Amplitude (MJy/sr)	0.457 ± 0.0238	0.539 ± 0.000791
Mean or Baseline (MJy/sr)	21.032 ± 0.0170	18.550 ± 0.000558
Phase (ϕ)	46.161° ± 2.982°	359.313° ± 0.0840°
Maximum (90° - ϕ)	43.839° ± 2.982°	90.687° ± 0.0840°

Parameters for sine curve fits to the 25 μm average polar COBE data and Kelsall background cloud model. The difference in phase between the COBE data and the Kelsall zodiacal background cloud is approximately 47°.

data. The Kelsall model exhibits a change in phase that matches within errors of the COBE data. The maximum of the COBE data is 43.84 ± 2.98° and the maximum of the modified Kelsall model is 43.93 ± 0.24°. However, the model does not have the same amplitude or mean as the COBE sine curve. The amplitude and mean were both scaled to match the amplitude and mean of the COBE data for the purposes of comparison. The residuals resulting from the subtraction of both the filtered, modified Kelsall model and the dynamical dust band model from the COBE data are shown in Figure 5-21. These residuals exhibit a *trailing* brightness enhancement that is in agreement with Jayaraman et al. (2000), Dermott et al. (1996b), and Reach et al. (1995), at least for Week 33. However, when the other weeks are viewed, the results are not so favorable.

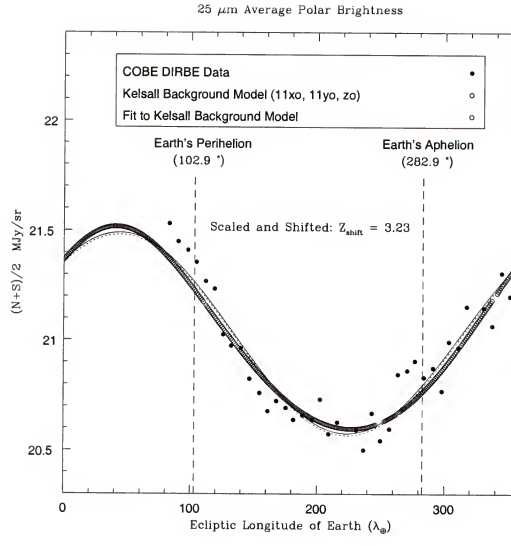

Figure 5-20: Kelsall background cloud model with modified offset. The fit to the modified Kelsall model is shown in open dots which completely overlap the Kelsall background model points. The filled dots are the COBE DIRBE data. The Kelsall model exhibits a change in phase that matches within errors of the COBE data. The maximum of the COBE data is $43.84 \pm 2.98°$ and the maximum of the modified Kelsall model is $43.93 \pm 0.24°$. However, the model does not have the same amplitude or mean as the COBE sine curve. The amplitude and mean were both scaled to match the amplitude and mean of the COBE data for the purposes of comparison.

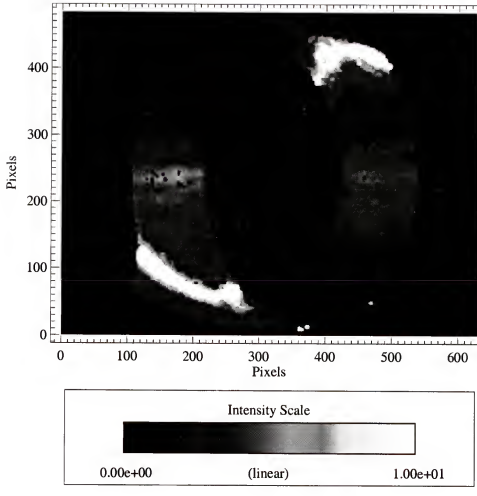

Figure 5-21: Residuals from the subtraction of a Kelsall model with a modified offset and the dynamical dust band model for Week 33 in the 60 μm wave band. These residuals were obtained by subtracting both the dynamical dust band model and the true Kelsall et al. (1998) background zodiacal cloud model with a modified offset from the COBE data in the 60 μm wave band for Week 33 (corresponding to $\lambda_{\oplus} = 287°$). The S-shaped structure is due to galactic emission while the structure at the ecliptic is primarily due to Earth's resonant ring, but could also have a small component resulting from Kuiper disk emission. The residuals exhibit a trailing brightness enhancement that is in agreement with Jayaraman et al. (2000), Dermott et al. (1996b), and Reach et al. (1995), at least for Week 33.

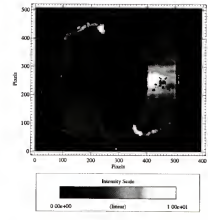

a) 25 μm Week 5

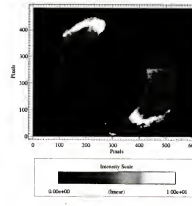

b) 60 μm Week 5

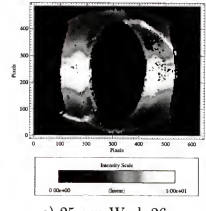

c) 25 μm Week 26

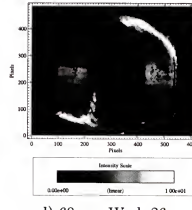

d) 60 μm Week 26

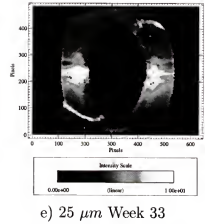

e) 25 μm Week 33

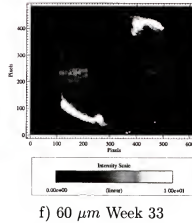

f) 60 μm Week 33

Figure 5-22: Residuals from subtracting the dynamical dust band model and a Kelsall background model with an offset modified to match that of the COBE data in the 25 (left) and 60 (right) μm wave bands. The right hand side of the scans is the trailing side. The residuals are given a fixed maximum of 10 MJy/sr to facilitate comparisons.

As can be seen from Figure 5-22, the trailing/leading asymmetry is not as evident for the rest of the weeks as it is for Week 33, casting doubt on the new modified model. It may still be possible to modify the model in some other way, remembering that neither the mean nor the amplitude of the background cloud model matched that of the COBE data. Investigations into modifying the amplitude produce a background cloud that is too thin at the edges. When we subtract this model from the COBE data, the resulting residuals still show the signature lenticular shaped emission from the background cloud, which, when subtracted from the COBE data, does not fully remove the lenticular background cloud resulting in a failure to subtract the background cloud from the data. Combining a cloud with a modified amplitude and modified baseline produce equally fruitless results.

5.5.3 Subtracting the Reach Model

Another avenue to pursue involves using a simpler background cloud model, which involves a less complicated density distribution and fewer parameters. A simple model which served as a precursor to the Kelsall et al. (1998) model was developed by Reach et al. (1995). The density distribution, $n(r, z)$, is simply

$$n(r, z) = n_0' \, r_{xy}^{-\alpha'} \, exp(-\beta_v' |z/r_{xy}|^{\gamma'}) \tag{5.18}$$

where r_{xy} is the density from the cloud center to the cloud mid-plane, z is the vertical distance from the mid-plane, $\alpha' = 1.39 \pm 0.03$, $\beta_v' = 3.26 \pm 0.04$, and $\gamma' = 1.02 \pm 0.01$. The density at 1 AU, n_0', is assumed to be 7.6×10^{-19} cm^{-1}. Reach et al. (1995) do not list the offsets used or the value for the ascending node of the mid-plane. We use the Kelsall et al. (1998) value for the ascending node of the mid-plane and use various values for the offsets. Reach et al. (1995) claim that for Week 33 in the 12 μm wave band, the Reach background cloud model is subtracted from the COBE DIRBE data and the signature of the Earth's resonant ring appears in the residuals. In Figure 2b

of Reach et al. (1995), the signature of the resonant ring is clearly evident, showing a trailing density enhancement predicted by theory.

An example of the Reach et al. (1995) model for Week 33 in the 25 μm wave band is shown in Figure 5-23. This model is a simpler model than the Kelsall model and we test it using a variety of offsets. We first test a Reach model that is not offset from the Sun ($X_o = Y_o = Z_o = 0$). The residuals we obtained by subtracting the Reach background cloud model and the dynamical dust band model from the COBE data are shown in Figure 5-24. For all of the weeks, the trailing scan is on the left. Week 5 does not exhibit a notable trailing/leading asymmetry. Week 26 and Week 33 seem brighter on the leading side. Clearly, this model does not produce the desired result.

Next, we try a Reach model that has the same offset from the Sun as the Kelsall model ($X_o = Y_o = Z_o = 1$). The residuals obtained by subtracting this version of the Reach background cloud model and the dynamical dust band model from the COBE data are shown in Figure 5-25. For all of the weeks, the trailing scan is on the left. The results are very similar to those for the Reach model with no offset from the Sun. Week 5 does not exhibit a notable trailing/leading asymmetry and Week 26 and Week 33 appear brighter on the leading side.

Finally, we try a Reach model that is has an offset designed to match the offset seen in the COBE data ($X_o = Y_o = 11, Z_o = 1$). The residuals obtained by subtracting this version of the Reach background cloud model and the dynamical dust band model from the COBE data are shown in Figure 5-26. There appears to be some improvement with this model. Week 26 and Week 33 appear to be brighter on the trailing side, but Week 5 is much brighter on the leading side than the trailing side. In fact, a portion of the ecliptic on the trailing side of Week 5, seems to be completely removed from the scan, implying that the corresponding portion of one of our models is too bright.

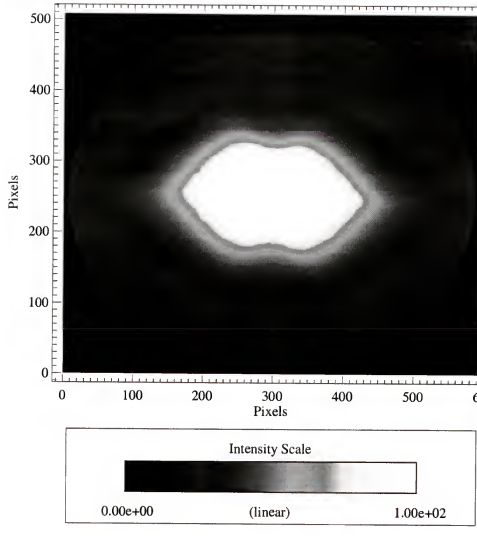

Figure 5-23: The Reach background zodiacal cloud model for Week 33 in the 25 μm wave band. The offsets used in this model are the same as those used in the original Kelsall model. The maximum value of the model has been set to 100 MJy/sr has been so that the contrast between the inner and outer parts of the cloud is low enough for the outer part of the cloud to be visible.

5.5.4 Discussion of Inadequacies of Empirical Models

Due to our lack of success with either the Kelsall et al. (1998) or the Reach et al. (1995) background zodiacal cloud models, we are forced to conclude that neither model is adequate for the task of removing the zodiacal cloud to the level of a few percent that is necessary for our search. The residuals for the models with offsets

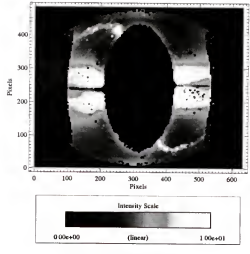

a) Week 5 ($\lambda_{\oplus} = 91°$)

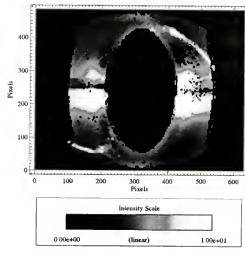

b) Week 26 ($\lambda_{\oplus} = 238°$)

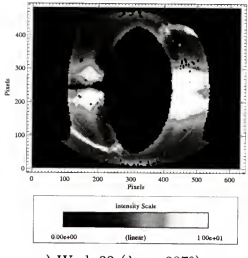

c) Week 33 ($\lambda_{\oplus} = 287°$)

Figure 5-24: Residuals we obtained in the 25 μm wave band by subtracting the Reach background cloud model, with the offsets set to zero, and the dynamical dust band model from the COBE data. The background cloud model is not offset from the Sun ($X_o = Y_o = Z_o = 0$). For all of the weeks, the trailing scan is on the left. Week 5 does not exhibit any notable asymmetries. Week 26 and Week 33 seem brighter on the leading side.

modified to match the offset of the COBE data look most promising, but there still are some inconsistencies that must be addressed. Shown in Figure 5-27, is the Kelsall model with an offset that matches the offset in the data. The shape of the modified model is much different than that of the original model (see Figure 5-3). The original

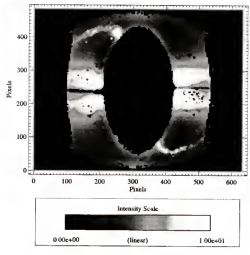

a) Week 5 ($\lambda_\oplus = 91°$)

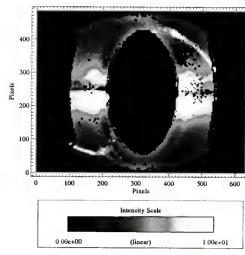

b) Week 26 ($\lambda_\oplus = 238°$)

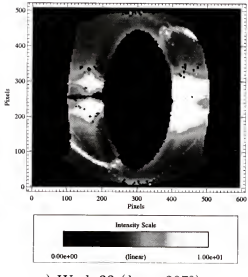

c) Week 33 ($\lambda_\oplus = 287°$)

Figure 5-25: Residuals obtained in the 25 μm wave band by subtracting the Reach background cloud model, with the offsets set to those used in the Kelsall model, and the dynamical dust band model from the COBE data. The background cloud model is offset from the Sun ($X_o = Y_o = Z_o = 1$). For all of the weeks, the trailing scan is on the left. Week 5 does not exhibit any notable asymmetries. Week 26 and Week 33 are brighter on the leading side.

Kelsall model is fairly symmetrical. In contrast, the central part of the Kelsall model with the modified offset exhibits a large asymmetric bulge on the trailing (left) side. One question that needs to be addressed is does the different shape of the modified

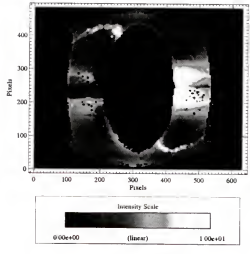

a) Week 5 ($\lambda_\oplus = 91°$)

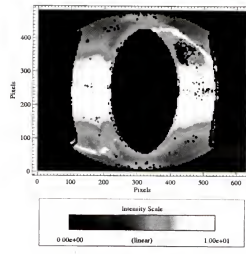

b) Week 26 ($\lambda_\oplus = 238°$)

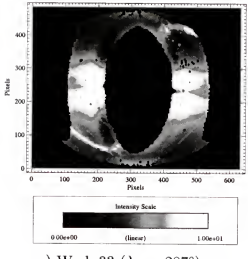

c) Week 33 ($\lambda_\oplus = 287°$)

Figure 5-26: Residuals obtained in the 25 μm wave band by subtracting the Reach background cloud model, with offsets which match the COBE data, and the dynamical dust band model from the COBE data. The background cloud model is offset from the Sun ($X_o = Y_o = 11$, $Z_o = 1$). For all of the weeks, the trailing scan is on the left. Week 26 and Week 33 appear to be brighter on the trailing side, but Week 5 is much brighter on the leading side than the trailing side.

model make the model inadequate? Is there a way to retain the correct offset without modifying the shape of the model? In an empirical, parameterized model, it is difficult to understand how the modification of a parameter corresponds to a physical process. This is a major justification for the development of a complete dynamical model of

the background zodiacal cloud. With the creation of such a model, we could be certain that the offset matched that seen in the data. We could understand fully what the model parameters corresponded to in a physical sense. And we would have a much better chance at subtracting off a zodiacal cloud to see residuals at a 10% level or lower.

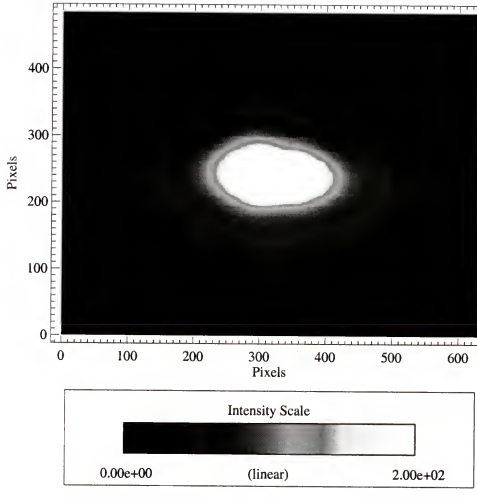

Figure 5-27: The Kelsall background zodiacal cloud model for Week 33 in the 25 μm wave band with an offset that matches that seen in the data. The offset ($X_o = Y_o = 11$, $Z_o = 1$) corresponds to a high value of forced eccentricity. The shape of the modified model is much different than that of the original model. The maximum value of the model has been set to 200 MJy/sr has been so that the contrast between the inner and outer parts of the cloud is low enough for the outer part of the cloud to be visible.

Another question is what exactly does an offset of $11X_o$, $11Y_o$, and $1Z_o$ correspond to in terms of forced eccentricity. In this case, $R_o = \sqrt{(11\,X_o)^2 + (11\,Y_o)^2 + Z_o^2}$ = 0.144 AU where R_o is the distance from the center of the cloud to the Sun. That distance is equal to ae_f where a is the semi-major axis and e_f is the forced eccentricity (Dermott et al. 1985, Wyatt et al. 1999). If a = 1 AU, then e_f = 0.144. Figure 5-28 shows plots for the forced eccentricities with respect to semi-major axis of particles of different sizes. At 1 AU, the 100 μm diameter particles have a high forced eccentricity ($e_f \sim 0.22$), but both the 10 μm and 200 μm particles have forced eccentricities that are near zero. Even though the forced eccentricity is high, it is not unreasonable depending on what particle size is considered.

5.5.5 Dynamical Background Zodiacal Cloud Model

Although we do not yet have a complete dynamical background cloud model for reasons discussed in Section 5.3.1, we can use current asteroidal dynamical models to make some key points. The background zodiacal cloud models so far have assumed that the cloud will have one offset. This is not necessarily the case since the zodiacal cloud can be thought of as consisting of two components: an outer zodiacal cloud at 2 - 3 AU, and an inner cloud inside 2 AU. The outer and inner clouds may have different offsets. The forced elements of asteroidal dust particles in the outer cloud may be locked onto Jupiter's elements(the eccentricity of Jupiter is 0.048), causing relatively high forced eccentricities and therefore a large offset. In the inner cloud, which is what the average polar scans are probing (see Figure 5-4), the offset might be quite different. The inner cloud dominates the brightness of the background zodiacal cloud since it is closer to the Sun. The dynamics of the inner cloud are dominated by large particles, 100 - 500 μm in diameter (Dermott et al. 2001, Love and Brownlee 1993). In considering the dynamics of the inner cloud, we ultimately need to include collisions between particles, resonances (in particular, the secular resonance at $\sim$ 2 AU), and gravitational scattering by the inner planets.

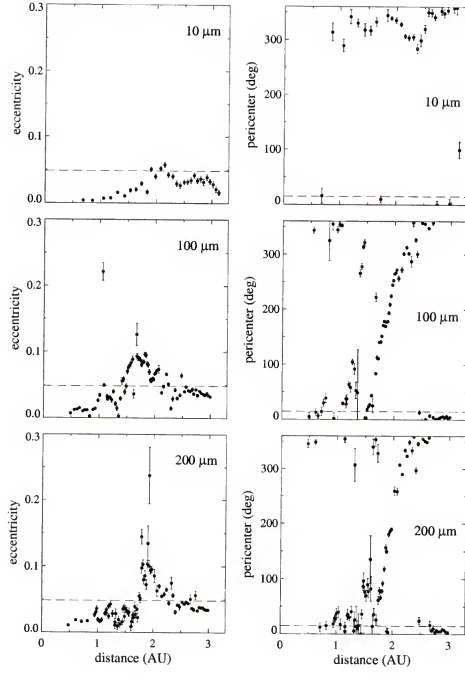

Figure 5-28: Values for forced eccentricity for various size particles near the Earth (Dermott et al. 2001).

We can begin the arduous task of creating a complete background zodiacal cloud model by building a initial trial model for the outer zodiacal cloud. The dust bands contribute roughly one third of the thermal emission of the zodiacal cloud

as a whole, if emission from the dust bands in the inner solar system is included (Grogan et al. 2001). If we take the Grogan et al. (2001) dynamical dust band model, which is confined to the region exterior to 2 AU, and build a similar model having three times the emission, we will have a basic model for the outer background zodiacal cloud. The outer cloud model has an inclination and node distribution appropriate for a background zodiacal cloud, but has forced and proper eccentricities and pericenters which are similar to those used in the Grogan et al. (2001) dynamical dust band model. The outer cloud SIMUL model includes the forced eccentricity at 2 AU for 100 μm diameter particles ($e_f = 0.07$), the highest proper eccentricity of the component dust bands, due to Themis ($e_p = 0.155$), and the forced longitude of pericenter at 2 AU for 100 μm diameter particles ($\tilde{\omega} = 200°$).

The true background cloud model for the outer background zodiacal cloud model for Week 33 in the 25 μm wave band is shown in Figure 5-29. Note that in this purely asteroidal model, the dust is basically confined to the ecliptic. There is no emission at the poles, which might be expected from a model which contained cometary dust particles or the dynamics of larger particles, which can have higher forced inclinations than small particles (Grogan et al. 2001). The shape of the outer zodiacal cloud model is markedly different from that of the Kelsall or Reach models. Residuals obtained for Week 33 in the 25 μm wave band by subtracting the outer zodiacal background cloud model and the dynamical dust band model from the COBE data are shown in Figure 5-30. It is clear, due to the oval shaped residuals dominating the ecliptic, that the bulk of the zodiacal cloud emission has not been successfully removed. An additional inner zodiacal cloud model is needed to build a complete background cloud model.

One problem with the aforementioned outer zodiacal cloud model is that the peak brightness of the model is far too low compared to the peak brightness of the COBE data for the corresponding week. We can take a background zodiacal cloud

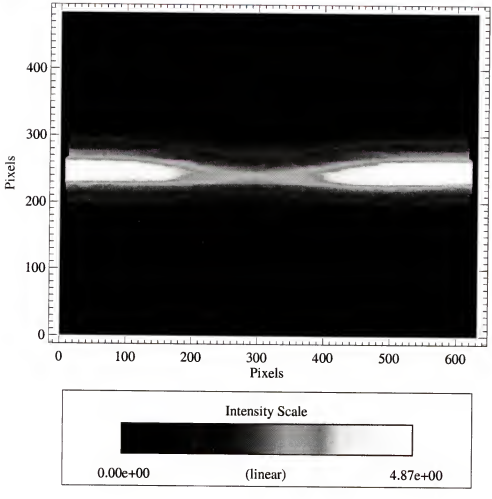

Figure 5-29: True background cloud model for the outer background zodiacal cloud model once the low frequency component of the dust band model has been removed for Week 33 in the 25 μm wave band. Note that this purely asteroidal model, the dust is basically confined to the ecliptic. There is no emission at the poles, which might be expected from a model which contained cometary dust particles. The shape of the outer zodiacal cloud model is markedly different from that of the Kelsall or Reach models.

model and scale its peak brightness so that it is comparable to that of the COBE data, and then subtract the model from the data. We choose a background zodiacal cloud model that includes the dynamics of small (9 μm diameter) particles and ranges from 0.5 to 3.2 AU which is shown in Figure 5-31. A model for small particles is used because we have yet to develop a comprehensive model that includes larger particles.

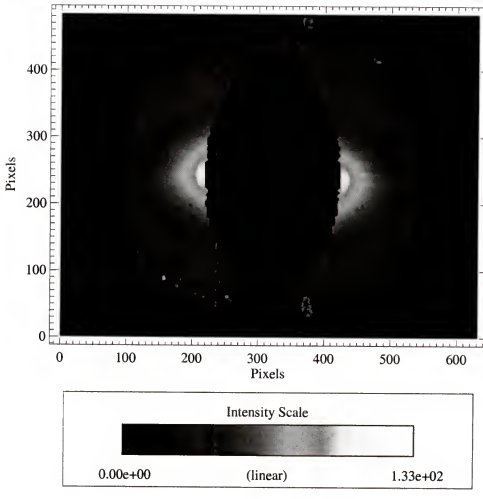

Figure 5-30: Residuals obtained for Week 33 in the 25 μm wave band by subtracting the outer zodiacal background cloud model and the dynamical dust band model from the COBE data. It is clear, due to the oval shaped residuals dominating the ecliptic, that the bulk of the zodiacal cloud emission has not been successfully subtracted. An additional inner zodiacal cloud model is needed to build a complete background cloud model.

Small particles have shorter Poynting-Robertson drag lifetimes than large particles and consequently the study of their dynamics involves numerical integration runs that are less time consuming. The accessibility of inexpensive, high-speed processors has only recently made the dynamical study of large particles possible. Shown in Figure 5-32, are the residuals obtained by subtracting the scaled background cloud model and the dynamical dust band model from the COBE data for Week 33 in the

25 μm wave band. It is clear, due to the butterfly shaped residuals dominating the regions above and below the ecliptic, that the bulk of the zodiacal cloud emission has not been successfully removed. However, the level of removal is better than that obtained by using the outer zodiacal cloud model. The poor subtraction is certainly due in part to the fact that the new total zodiacal cloud model is essentially confined to the ecliptic. Therefore it is not possible to remove structure above and below the ecliptic with this model. A horizontal line cut through the residuals in the ecliptic (at Pixel 250 on the y-axis) is shown in Figure 5-33. The leading (right) side of the residuals are clearly brighter than the trailing (left) side, which is the opposite from what is predicted by theory.

None of our current background zodiacal cloud models are sophisticated enough to allow us to obtain the residuals we expect to see. We are justified in expecting to see residuals from a resonant ring with a trailing/leading asymmetry because we see the trailing/leading asymmetry in the COBE data (see Figure 5-1). Both Reach et al. (1995) and Kelsall et al. (1998) claim to see the correct trailing/leading asymmetry when they subtract their background zodiacal cloud models from the COBE data. However, we are unable to produce their results by using their models or their models with certain modifications. We do not believe the results of Reach et al. (1995) and Kelsall et al. (1998) since they do not appear to be reproducible. Furthermore, the offset of the Kelsall model does not match the offset seen in the COBE data (see Figure 5-4). Having said this, however, we acknowledge that the Kelsall et al. (1998) model is, indeed, the most complete background zodiacal cloud model to date and that the shape of the model does match the shape of the zodiacal cloud fairly well. The detection of the Kuiper disk, however, hinges on developing a model of the zodiacal cloud that does more than simply possess the correct overall lenticular shape. Once such a model is developed, we can then subtract the Arendt et al. (1998) model for galactic emission and the model for Earth's resonant ring

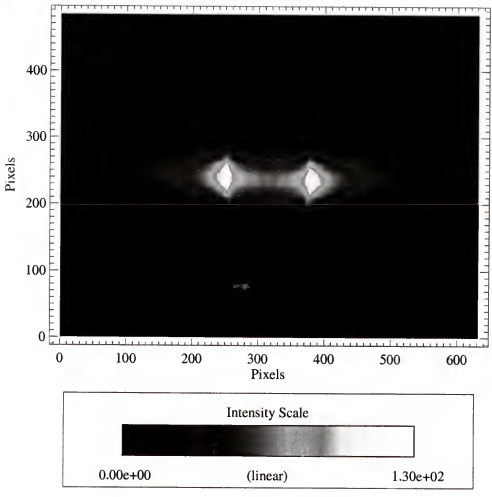

Figure 5-31: Total background zodiacal cloud model for particles 9 μm in diameter in the 25 μm wave band for Week 33. The maximum of the model has been scaled to approximately match the maximum of the COBE data (133 MJy/sr).

(Jayaraman 1995) from the COBE data. As an aside, a set of residuals in which the galactic model is removed is shown in Figure 5-34. The Arendt et al. (1998) model does remove some of the galactic emission, but not all, and may need to be scaled slightly before using to study residuals further. The S-shaped structure for the Arendt et al. (1998) model does match that seen in the data for the corresponding week.

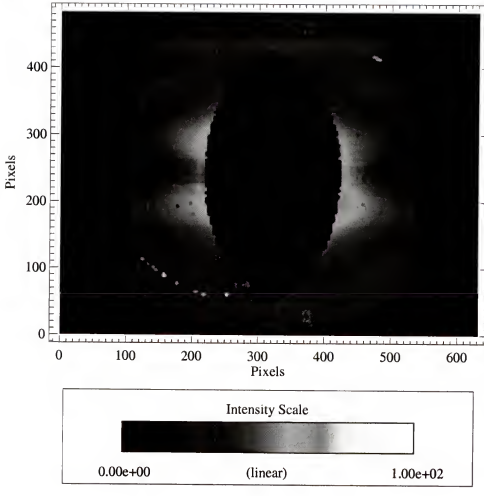

Figure 5-32: Residuals obtained for Week 33 in the 25 μm wave band by subtracting the scaled total zodiacal background cloud model and the dynamical dust band model from the COBE data. It is clear, due to the butterfly shaped residuals dominating the ecliptic, that the bulk of the zodiacal cloud emission has not been successfully subtracted.

For the 60μm wave band, Teplitz et al. (1999) reports four different upper limits for the signal from the Kuiper disk, $I_{KB}(\nu)$. The estimated brightness is expected to be $0.3 < I_{KB}(\nu) < 16.0$ MJy/sr, though the high value is a poorly constrained upper limit. The 16 MJy/sr limit is the weakest limit since it is merely the full COBE DIRBE infrared signal given in Backman et al. (1995). The other limits of 0.3, 1.50, and 0.75 MJy/sr were obtained in the following fashion. The 1.50

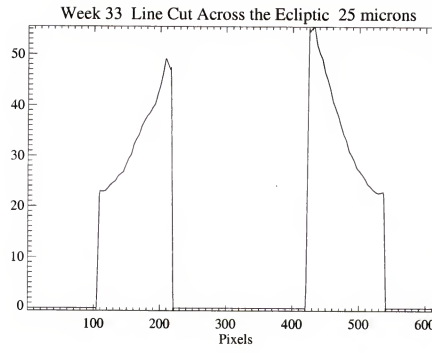

Figure 5-33: Horizontal line cut through the ecliptic of the residuals shown in Figure 5-32. The line cut is made at Pixel 250 on the y-axis. The leading (right) side of the residuals are clearly brighter than the trailing (left) side.

MJy/sr limit is a 2 σ limit found by Hauser et al. (1999), while the 0.75 MJy/sr value was a standard deviation given by Hauser et al. (1999). The smallest limit, $I_{KB}(\nu) =$ 0.3 MJy/sr, was obtained by the subtraction of the component of the COBE data due to asteroidal emission using the Reach et al. (1998) zodiacal cloud model.

In Figure 5-19, the residuals in the ecliptic obtained from subtracting the original Kelsall model and the dynamical dust band model, exhibit a maximum brightness of approximately 5.7 MJy/sr. The bulk of this brightness is presumed to be due to emission from the Earth's resonant ring, and correspondingly any emission due to the Kuiper disk must be much lower. It is difficult to assess the smaller upper limits since they are based on the removal of the Kelsall or Reach models of the background

zodiacal cloud. As it is seen from this dissertation, modifying the background cloud model can produce drastically different results. In comparing Figure 5-19 to Figure 5-21, we note that the maximum brightness of the residuals on the trailing side ranges from 4.8 to 5.8 MJy/sr and the maximum brightness of the residuals on the leading side range from to 4.6 to 5.7 MJy/sr for Week 33 in the 60 μm the wave band, depending on which model is used. It is imperative to develop a background zodiacal cloud model we are confident in so that we can remove the zodiacal cloud to the 1% level or better. Only then will we be able to conduct a thorough search for the Kuiper disk in the COBE DIRBE data.

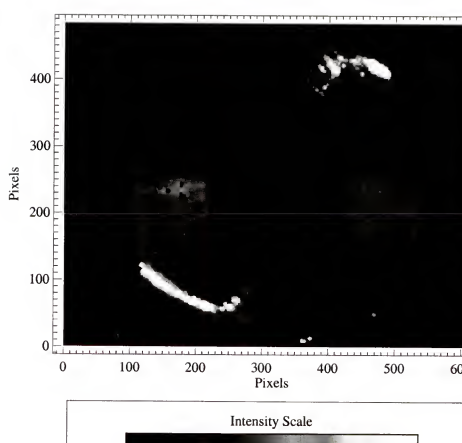

Figure 5-34: Residuals from the subtraction of a Kelsall model with a modified offset, the dynamical dust band model, and a model for galactic emission for Week 33 in the 60 μm wave band. These residuals were obtained by subtracting the dynamical dust band model (Grogan et al. 2001), the true Kelsall et al. (1998) background zodiacal cloud model with a modified offset ($11\ X_o, 11\ Y_o,\ 1Z_o$), and the galactic emission model (Arendt et al. 1998) from the COBE data in the 60 μm wave band for Week 33 (corresponding to $\lambda_\oplus = 287°$). The S-shaped structure is due to galactic emission while the structure at the ecliptic is primarily due to Earth's resonant ring, but could also have a small component resulting from Kuiper disk emission. The residuals exhibit a trailing brightness enhancement that is in agreement with Jayaraman et al. (2000), Dermott et al. (1996b), and Reach et al. (1995), at least for Week 33. The residuals are set to have a fixed maximum at 10 MJy/sr. Some of the S-shaped structure due to galactic emission has been removed but clearly a large residual component of the galactic emission is retained. Once a more complete zodiacal cloud model has been created, attention will have to be tuned to refining the ISM model to allow for more complete subtraction of the galactic component.

CHAPTER 6
SURVEY OF NEARBY STARS FOR SUB-MILLIMETER EMISSION

6.1 Introduction

The Infrared Astronomical Satellite (IRAS) detected excess far-infrared emission, at wavelengths of 60 and 100 μm, from more than 15% of all nearby main sequence A-K stars, indicating the presence of circumstellar material (Backman and Paresce 1993, Elachi et al. 1996). It is our ultimate goal to extend the infrared models into the sub-millimeter regime ($300 \lesssim \lambda \lesssim 1000$ μm) where a significant fraction of the dust emission occurs. The cool dust (T $\sim$ 50 K) detected in the sub-millimeter regime lies far (30 - 100s of AUs) from the central star. This location is most analogous to the Kuiper Belt in our solar system (Backman and Paresce 1993). The Kuiper Belt is home to an estimated $\sim 10^5$ Kuiper Belt Objects (KBOs) with a diameter $\geq$ 100 km located within 30 to 50 AU (Jewitt, Luu and Trujillo 1998). In the asteroid belt, collisions between asteroids supply dust particles to the zodiacal cloud, the Sun's inner dust disk, which is visible at infrared wavelengths. By comparison, it has been postulated that collisions between KBOs could initiate a collisional cascade, similar to that in the asteroid belt, which would produce a Kuiper dust disk (see Chapters 4 and 5). Therefore, from a modeling perspective, far-infrared and sub-millimeter observations are very interesting because they can be compared to models of a Kuiper disk.

Sub-millimeter observational maps of planetary debris disks have been limited to a small number of systems: β Pictoris, Vega, Fomalhaut (Holland et al. 1998), and ϵ Eridani (Greaves et al. 1998). IRAS detected very strong far-infrared excesses from all of these nearby main-sequence stars (Gillet 1986; Backman and Paresce 1993) and

also resolved them spatially (Backman and Paresce 1993; Aumann 1991). As a result, these four stars have been studied extensively at a number of different wavelengths. Obviously, from a statistical standpoint, we need more detections and where possible, maps, to claim a broad knowledge of debris disks as a whole and to study potential disk asymmetries, especially considering that upwards of 15% of all main-sequence A-K stars have detectable infrared excesses.

Therefore, as a first step, we embark on a sub-millimeter survey of debris disk candidates - a small selection of nearby ($\leq$ 50 pc), main-sequence stars. From our survey, we obtain upper limits on the flux around ten Vega-type stars and one Herbig Ae star with the Four Color Bolometer and the 19 Channel Bolometer Array at the Sub-millimeter Telescope Observatory using the Heinrich-Hertz Telescope (SMTO) in the 870 μm and 1300 μm wave bands, respectively. All of our sources were undetected at 870 μm. In the case of HD 131156, we technically have a 3σ detection at 1300 μm in the center channel of the 19-Channel bolometer and so we report a flux of 6.25 $\pm$ 1.88 mJy and we derive a dust mass of 1.10 $\pm$ 0.33 lunar masses for the system. However, in viewing the surrounding channels, we see that it is very unlikely that the 3σ detection is real. We retain the section on calculating a flux and dust mass for HD 131156 as an illustrative example.

6.2 Observations

We observed a total of eleven stars at the 10 meter Heinrich Hertz Telescope (HHT) of the Sub-millimeter Telescope Observatory (SMTO) located on Mt. Graham in Arizona. We searched for sub-millimeter flux around our candidate stars with the Four Color Bolometer on 1999 March 19-24 and 1999 December 9-13 at 1300 μm. We completed our survey on 2000 December 14-16 using the 19 Channel Bolometer Array at 870 μm.

In 1999 March 19-24 and December 9-13, we used the Four Color Bolometer facility instrument with central wavelengths at 1.30 mm, 0.87 mm, 0.45 mm, and 0.35 mm, and an approximately 50 GHz bandwidth. The half power beam width (HPBW) at 1300 μm is approximately 35", which is not diffraction limited. We made approximately 10 pointing observations per night, to achieve an absolute pointing accuracy of 2-3 arc seconds. Continuum on/off measurements of each source were made with a beam throw of $\pm$ 100 " in azimuth during the March observing run and a beam throw of $\pm$ 60 " in December 1999. Each continuum scan was comprised of 10 subs-cans, having on and off source scans of 30 seconds each. Total on source integration times are listed in Table $6-3$. The scans were calibrated using continuum on/off measurements on Venus, Mars, Saturn, and Uranus as well as known secondary sub-millimeter calibrators: K3-50, W3(OH), NGC 7538IRS1, G45.1, and CRL 618 (Sandell et al. 1994). Observations of standards during the spring of 1997 found the 1300 μm noise equivalent flux density (NEFD) equal to 0.6 - 0.8 Jy/sec$^{1/2}$. We observed nine Vega-type stars and one Herbig Ae star, HD 37357 (see Tables 6-1 and $6-3$).

On 2000 December 14-16, we used the newly installed 19-channel bolometer array, developed at the Max-Planck-Institut für Radioastronomie Bonn to observe eight Vega-type stars and one Herbig Ae star (see Table $6-3$). The array consists of 19 individual broadband continuum receivers, each with a central wavelength of 0.87mm (345 GHz). Eighteen of the channels form two concentric hexagons around the central channel. The NEFD level for the array is approximately 0.6 Jy/sec$^{1/2}$. Continuum on/off measurements of each sources were made with a beam throw of $\pm$ 50 " in azimuth. Each continuum scan was comprised of 20 sub-scans, having on and off source scans of 10 seconds each. Total on source integration times are listed in Table 6-3. The scans were calibrated using continuum on/off measurements

on Venus, Mars, and Saturn as well as known secondary sub-millimeter calibrators: K3-50, W3(OH), W75N, and G45.1 (Sandell et al. 1994).

6.2.1 Selection Criteria

One of the stars in our source list, β Leo, had been observed previously in the sub-millimeter: β Leo (Weintraub and Stern 1994). Of the ten previously unsurveyed stars, five were listed in the Space Infrared Telescope Facility (SIRTF) Science Requirements Document as candidate stars for possessing planetary debris disks: HD 10700 (τ Cet), HD 165341 (DM+023482 A), HD 185144 (σ Dra), HD 4614 (η Cas A), and HD 131156 (ξ *Boo A*). These stars are all main sequence solar analogs located within 6.8 pc (Simmons and Werner 1997). Specifically, they are five of the closest stars with spectral types between G0V and K0V and luminosities similar to solar ($0.37L_{\odot} < L < 1.24L_{\odot}$). Aumann and Good (1990) predict that the typical G star in the solar neighborhood is surrounded by a disk of cool dust. In addition, studying nearby stars (d $\leq$ 10pc) is advantageous since it increases the probability of a sub-millimeter detection for systems possessing a small amount of dust. It also allows lower limits on dust mass to be placed on any non detections, since the dust mass is proportional to the square of the frequently uncertain distance.

The remaining candidate stars, HD 192425 (ρ Aql), HD 82189 (22 UMa), HD 32932 (104 Tau), HD 37357, and HD 39415 were acquired from a list of SAO stars having infrared excess in the IRAS Point Source Catalogue (Oudmaijer et al. 1992). The color criteria for determining that a star had an infrared excess were [12]-[25] > 0.4 or [25]-[60] > 0.3 (Oudmaijer et al. 1992). We selected our sources from Oudmaijer et al. (1992) using the criteria that the stars were of spectral types A-K and on the main-sequence. Out of the 462 stars in the Oudmaijer et al. (1992) list, approximately 12 per cent met our criterion. Out of those stars, we ultimately observed only five due to time constraints, observability of the sources, and the elimination of sources which had already been studied extensively in the sub-millimeter (e.g. Vega and

Fomalhaut) as well as any sources showing evidence of emission lines (e.g., Herbig Ae/Be stars). Although not listed in Oudmaijer et al. (1992 as a Herbig Ae/Be star, HD 37357 has been identified as a Herbig Ae star with spectral type A0 Ve (Thé et al. 1994). Nonetheless, we have retained it in our source list for comparison purposes. We applied Oudmaijer's color magnitude criterion to our other sources and found that HD 10700 also possesses an infrared excess. Table 6-1 provides a listing of all of the sources we observed with the SMTO and Table 6-2 shows the IRAS fluxes or upper limits obtained for each source. For our non-detections, we calculated 3σ upper limits for the flux which we present in Table 6-3. These limits will help constrain future observations. In the case of HD 131156, we technically have a 3σ detection at 1300 μm in the center channel of the 19-Channel bolometer and so we calculate a flux and a dust mass for the system. However, in viewing the surrounding channels (see Figure 6-1), we see that it is very unlikely that the 3σ detection is real. We retain the section on reporting a flux and calculating a dust mass for HD 131156 as an illustrative example.

6.3 Color Correcting the IRAS Flux Densities

The raw IRAS flux densities (at 12, 25, 60, and 100 μm) must be color corrected in a process that separates the color corrected photospheric component of the flux density from the color corrected dust component. The basic idea behind color corrections is that a satellite, such as IRAS, measures a non color corrected flux density, F_ν^{obs}, which is dependent on both the responsivity of the detector as a function of wavelength and the shape of the intrinsic energy distribution of the observed astronomical source. A color correction factor, $K(\nu)$, can be found by assuming a specific function for the energy distribution of the source, where ν is the frequency corresponding to the nominal wavelength of the IRAS band pass (i.e., 12, 25, 60, or

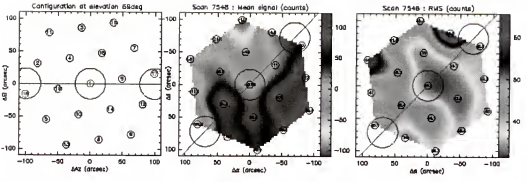

Figure 6-1: Scan 7548 of HD 131156 at 1300 μm. (left) The configuration of the 19-Channel bolometer array elements is shown at an elevation of 69°. (middle) The mean signal in counts for all of the array elements for scan 7548 is shown for the case where the mean of the 18 outer array channels are subtracted. If the 3σ detection were real, we would expect to see the signal stand out in the center channel (channel 1) against the background, and it does not. (right) The rms signal in counts for scan 7548 is shown for the case where the mean of the 18 outer array channels are subtracted.

100 μm). The color corrected flux density, F_ν^{cor}, becomes

$$F_\nu^{cor} = \frac{F_\nu^{obs}}{K(\nu)}. \tag{6.1}$$

Listed in Table Supplement VI.C.6 of the IRAS Explanatory Supplement are tables of color correction factors for different source functions. In the case of a star, this function is the Planck function for a black body at a temperature, $T_\star$, corresponding to the spectral type of the star, usually on the order of 10,000 Kelvin. For a given temperature, T, the Planck function, $B_\nu(T)$, is defined as

$$B_\nu(T) = \frac{2h\nu^3}{c^2} \frac{1}{e^{(h\nu/kT)} - 1} \tag{6.2}$$

where T is the temperature of the source, c is the speed of light (c = 2.9979 $\times 10^8$ m/s), h is Planck's constant (h = 6.626 $\times 10^{-34}$ J s), and k is the Boltzmann constant (k = 1.381 $\times 10^{-23}$ J/K). For a particular, ν, the process of color correcting a simple stellar flux density would involve using the spectral type of the star to determine the photospheric temperature, finding the corresponding value of $K(\nu)$ from the IRAS

Explanatory Supplement, and applying equation 6.1, i.e., dividing the measured flux density by $K(\nu)$ to obtain the color corrected flux density.

However, color correcting the flux density for a star with an infrared excess, due to dust grains orbiting the star, is a multiple step process. It is not adequate to simply apply a color correction factor suitable for a 10,000 K black body, since the cool dust component must also be taken into account. It is first necessary to find a scale factor, Ω_*, which will scale the black body flux, $B_\nu(T_*)$, to the flux density due to the star, F_ν. This scale factor relates to the stellar radius and distance from Earth, but can also be expressed as the ratio of the flux corresponding to the visual magnitude of the star, F_V, and the black body flux at that wavelength ($\lambda = 5556$ Angstroms)

$$\Omega_* = \frac{F_V}{B_V(T_*)}. \tag{6.3}$$

F_V is defined by

$$\log F_V = -0.400V - 22.438 \ [W/(m^2Hz)]. \tag{6.4}$$

where V is the visual magnitude of the star. Thus, we can derive a predicted flux for the star, F_ν. This predicted flux is in fact the color corrected stellar flux, $F^{cor}_{\nu*}$, which can be related to the observed stellar flux, $F^{obs}_{\nu*}$ by means of an appropriate color correction factor, $K_{\nu*}$ in the following manner

$$F^{obs}_{\nu*} = F^{cor}_{\nu*} K_{\nu*}. \tag{6.5}$$

The total observed flux, $F^{obs}_{\nu*}$, can be expressed as the sum of the observed stellar flux and the observed dust flux, $F^{obs}_{\nu\ dust}$, and it follows that the observed dust flux can be determined using the total observed flux and the stellar flux, which was calculated using equation 6.3:

$$F^{obs}_{\nu\ dust} = F^{obs}_{\nu} - F^{obs}_{\nu*} \tag{6.6}$$

which can be related to the color corrected dust flux, $F^{cor}_{\nu dust}$, by means of an equation very similar to equation . Solving for the color corrected dust flux, we have

$$F^{cor}_{\nu\ dust} = \frac{F^{obs}_{\nu\ dust}}{K_{\nu\ dust}}. \tag{6.7}$$

The next step is to obtain the appropriate color correction factor for the dust component, $K_{\nu\ dust}$, which is dependent on the dust temperature, T_dust, which is unknown. The flux due to dust emission can be written as

$$F_{\nu\ dust} = \Omega_{dust}(1 - e^{\tau_\nu})B_\nu(T_{dust}) \tag{6.8}$$

where τ_ν is the optical depth of the dust and Ω_{dust} is a scale factor similar in nature to Ω_*. Since emission from Vega-type disks is optically thin, we need only consider the optically thin case of equation 6.8:

$$F_{\nu\ dust} = (\Omega_{dust}\ \tau_\nu)B_\nu(T_{dust}) \tag{6.9}$$

Equation 6.9 has three unknowns: Ω_{dust}, τ_ν, and T_{dust}. By considering the ratio of $F_{\nu dust}$ for two different frequencies, one of these unknowns, Ω_{dust}, can be eliminated since it is independent of ν. The remaining variables can be solved for iteratively. As an example, we will consider the ratio of the fluxes for the 12 and 25 micron wave bands. $F^{obs}_{12\ dust}$ and F^{obs}_{25dust} will correspond to the observed values of $F_{\nu\ dust}$ for the 12 and 25 micron wave bands, respectively:

$$\frac{F^{obs}_{12\ dust}}{F^{obs}_{25\ dust}} = \frac{\Omega_{dust}\ \tau_{12}\ B_{12}(T_{dust})}{\Omega_{dust}\ \tau_{25}\ B_{25}(T_{dust})}. \tag{6.10}$$

As can be easily seen from the above equation, Ω_{dust} can be eliminated. The ratio of τ_{12} to τ_{25} can then be determined by writing each τ as an expression of a third common τ and then determining the determining the second τ ratio from an extinction curve. For instance,

$$\tau_{12} = \frac{\tau_{12}}{\tau_{9.7}}\ \tau_{9.7} = R_{12/9.7}\ \tau_{9.7} \tag{6.11}$$

where $\tau_{9.7}$ is the value of the optical depth of the dust emission at $\lambda = 9.7\ \mu m$. $R_{12/9.7}$ is a constant that can be obtained by using the extinction curve from Mathis (1990) shown in Figure 6-2. From the curve, $R_{12/9.7} = 0.04$ and $R_{25/9.7} = 0.0125$. Using the previous equations and solving for the ratio of the black body fluxes, equation 6.10 reduces to

$$\frac{B_{12}(T_{dust})}{B_{25}(T_{dust})} = \frac{0.04}{0.0125} \frac{F^{obs}_{12\ dust}}{F^{obs}_{25\ dust}}. \tag{6.12}$$

An iterated solution to equation 6.12 can be found. Once T_{dust} has been determined, it can be used to obtain both $(\Omega_{dust}\ \tau_\nu)$ and $K_{\nu\ dust}$, which can be used to obtain an initial value for $F^{cor}_{\nu\ dust}$, the color corrected dust flux. This new dust flux can be used to obtain a new observed dust flux, which in turn can be inserted into equation 6.12 to obtain a new T_{dust} and $K_{\nu\ dust}$. The procedure can be repeated until the solution converges.

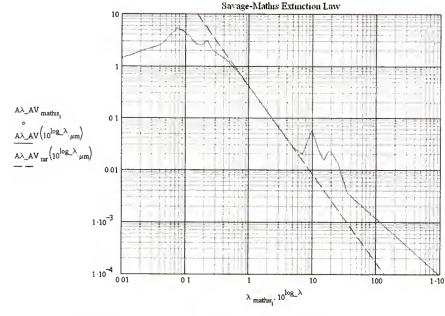

Figure 6-2: The extinction curve and overlay near-IR power law fit (Mathis 1990). Figure courtesy of Robert S. Fisher.

6.4 Results

Blackbody and graybody fits to the spectral energy distribution (SED) for each candidate star are shown in Figures 6-3, 6-4, 6-5, and 6-6. A graybody is defined as a modified blackbody where emissivity, ϵ, is a function of wavelength: $\epsilon \sim \lambda^{-\beta}$ (where $\beta = 1,2$). In Figures 6-3 and 6-4, the solid curve corresponds to a blackbody appropriate for the star's spectral type, scaled to the expected stellar flux for its observed V magnitude (plotted as an open diamond). The IRAS flux densities (at 12, 25, 60, and 100 μm) are color corrected in a process that separates the color corrected photospheric component of the flux density from the color corrected dust component, as discussed in the previous section. These components are plotted separately in Figures 6-3 and 6-4. The total color corrected IRAS fluxes are represented by an X, the color corrected stellar fluxes are plotted as open squares, and the color corrected dust component of the IRAS fluxes are plotted as filled circles. Blackbodies ($\beta = 0$, corresponding to large grains) and graybodies ($\beta = 1,2$, appropriate for small grains) are fit to the remaining dust components. Ideally, the best fit would include all of the IRAS flux densities, but that is not always possible since most sources only possess upper limits in the 60 and 100 μm wave bands. In some of these cases, there is no discernible 12 μm excess and a fit must be made using just the 25 μm flux density and one or both of the 60 or 100 μm upper limits. It is important to recognize the quality of the fit to the dust component of the IRAS fluxes in assessing the significance of the SMTO upper limits. It is also possible that, like the solar system, the star has two dust components - a warm component analogous to the zodiacal cloud and a colder component similar to the Kuiper Belt, which would require three different blackbody curves to explain the SED. For each source, the 3σ upper limits obtained from SMTO are plotted on their respective SEDs as open triangles. Depending on how well the blackbody is fit to the dust component of the IRAS data and depending on where

the upper limits from the SMTO data lie on the SED, the likelihood of the presence of dust in the system can be assessed.

6.5 Discussion

The blackbody and graybody curves for HD 10700, HD 32923, HD 39415, HD 37357, and β Leo display a good fit to the IRAS data points, clearly showing the existence of an infrared excess. The IRAS 60 and 100 μm dust component fluxes or upper limits are on or clearly above the $\beta = 0$ SED and the 3σ SMTO upper limits are also clearly above the $\beta = 0$ SED. The implication is that there is a significant probability of dust in the system and that the presence of dust detectable at sub-millimeter wavelengths can not be ruled out. These stars would be excellent candidates for more sensitive instruments such as SIRTF and the Sub-millimeter Array (SMA). We also compare our 3σ upper limit at 1300 μm for β Leo with the 3σ upper limit obtained by Weintraub and Stern (1994), which is represented in Figure 6-5 as an asterisk. We find that our upper limit is more than a factor of two lower than that obtained by Weintraub and Stern (1994). The two remaining IRAS infrared excess sources, HD 192425 and HD 82189, have no discernible 12 μm excess and small 25 μm excesses which were used to fit the blackbody curves. However, in both cases, the 60 μm upper limits were below all of the blackbody fits for dust emission, implying that either there is no emission from dust at longer wavelengths or that these sources have both a warm dust component and a colder dust component. The SMTO 3σ upper limits were above the $\beta = 1$ curves and far above the photospheric blackbody curve. HD 192425 has a very small 25 μm excess, so it is very possible that there is little or no dust in this system. However, HD 82189 has a larger excess at 25 μm, but the error bar on the measurement is quite large.

The remaining four sources (HD 165341, HD 185144, HD 4614, and HD 131156) are not listed in Oudmaijer et al. 1992 as IRAS excess sources, although

from our color correcting process, it does seem that both HD 165341 and HD 131156 may have a small 25 μm excess. The fits to the IRAS data for all of these sources are poor. In the cases of HD 165341 and HD 4614, the IRAS 60 μm flux density is only marginally above the blackbody curve for the stellar photosphere. The SMTO 3σ upper limit for HD 165341 is low making this source a poor candidate for possessing a large cold dust component. The SED of HD 4614, a spectroscopic binary, gives little evidence of a dust component in the system. The 12 and 25 μm fluxes as well as the 60 μm upper limit are nearly coincide with the blackbody curve for the stellar photosphere, though the relatively high 3σ upper limits from SMTO do not rule out a cold dust component. The fits to the dust component of the IRAS flux densities for HD 185144 is much better, though it could merely be due to a spuriously high 100 μm upper limit because there does not seem to be any excess from the measured 12 or 25 μm flux densities. Again, even though the SMTO upper limits are quite low, they can not completely rule out the existence of some cold dust surrounding the star. However, since the 1300 μm upper limit is only marginally above the $\beta = 2$ graybody curve (for the limit of small grains), a cold dust component seems unlikely.

HD 131156 (ξ Boo A and B or HR 5544) is a binary star composed of stars with types G8 V and K4 V (Abt 1981) and masses of 0.85 and 0.72 $M_{\odot}$. They are separated by approximately 7" and have a period of 151 years (Strand 1943, Wielen 1962, Harris et al. 1963., Gray 1992). Their small angular separation is much less than the SMTO beam size for both wavelengths. The star exhibits a small 25 μm excess, however the 60 μm IRAS upper limit, although above the stellar photospheres, is below the $\beta = 0$ blackbody curve. Both the 3σ upper limit at 870 μm and the tentative 3σ detection at 1300 μm lie on the $\beta = 0$ blackbody curve, leaving open the possibility of dust in this system.

6.5.1 Dust Mass

The envelopes or disks surrounding many young stars contain gas and dust, both of which contribute to the measured mass. However, in the case of the more evolved planetary debris disks, most of the gas has been cleared away as evidenced by the null results from searches for gas around Vega-type stars. The gas to dust ratio in these debris disks is reported to be at least 10 to 1000 times lower than in the interstellar medium (Dent et al. 1995; Freudling et al. 1995). For this paper, we adopt a gas to dust ratio that is 100 times less than that found in the interstellar medium (ISM), which translates into adopting a mass absorption coefficient, K_{abs}, for our systems which is 100 times greater than for a system which assumed a gas to dust ratio appropriate for the ISM. We calculated a dust mass for HD 131156 (as an example only since we do not believe we have a detection) using equation 6.13 from Zuckerman et al. (1993)

$$M_{dust} = \frac{F_\nu d^2}{B(\nu, T_{dust}) K_{abs}} \tag{6.13}$$

where M_{dust} is the estimated mass of dust or the 3σ lower limit on dust mass in the system in grams. F_ν is the flux or the 3σ rms flux (Jy), d is the distance to the star in meters, and K_{abs} is the mass absorption coefficient in units of m^2/g. $B(\nu, T_{dust})$, the blackbody intensity, is measured in Janskies and T_{dust} is the temperature of the dust grains in Kelvins. T_{dust} was derived from a blackbody ($\beta = 0$) fit to the color corrected dust component of the IRAS fluxes.

In the low temperature sub-millimeter regime, $B(\nu, T_{dust})$ can be approximated by $2kT_{dust}/\lambda^2$ in the Rayleigh-Jeans limit (Zuckerman et al. 1993, Hildebrand 1983), which is advantageous since in this approximation M_{dust} depends only inversely on the uncertain dust temperature. However, the Rayleigh-Jeans limit is inappropriate for dust temperatures less than or equal to 50 K (Weintraub and Stern 1994). We calculated 3σ upper limits for the dust mass around the candidate stars using both the full blackbody expression and the Rayleigh-Jeans limit and found a 6-10 per

cent difference in the results. As a result, we decided to use the full expression for blackbody intensity.

The mass absorption coefficient is not well constrained since it depends on the undetermined sizes of the dust particles presumed to be orbiting around the star. We use a K_{abs} for 1300 μm of 0.29 cm^2/g (Pollack et al. 1994, Zuckerman and Becklin 1993). This value for the mass absorption coefficient is derived assuming that the flux comes from particles with a radius approximately equal to 300 μm, so our estimates represent a minimum dust mass for the large grain case. K_{abs} can vary by up to a factor of 4 in the wavelength regime we are considering (Pollack et al. 1994).

HD 131156

Our one 3σ detection, HD 131156, has a flux of 6.25 ± 1.88 mJy at 1300 μm and a corresponding dust mass of 1.10 ± 0.33 lunar masses. Holland et al. (1998) found dust masses for Vega, Fomalhaut, and β Pictoris of 0.7, 1.5, and 7.8 lunar masses, respectively. As another comparison, the total mass in the observable Kuiper belt is approximately 8.2 lunar masses (Jewitt, Luu and Chen 1996; Jewitt, Luu and Trujillo 1998; Luu and Jewitt 1998). The dust mass for HD 131156 fits in well with these other estimates. When the 19 Channel Bolometer array data for HD 131156 is studied, no clear source can be seen so it is unlikely that the detection is real.

3σ Limits

Our 3σ lower limits on dust mass at 870 μm are easily compared to the values obtained by Holland et al. (1998). From our list of candidates, HD 10700, HD 185144, HD 4614, HD 131156, and β Leo show limits on dust masses at 870 μm on the order of Vega ($0.11 \leq M_{dust} \leq 0.85$). The 3σ mass limit for HD 32923 at 870 μm of 2.33 lunar masses is lower than the mass of β Pictoris. The mass limits at 1300 μm are not as tight, due to the fact that the 4 Color Bolometer is not as sensitive

as the 19 Channel Bolometer. However, they still show that for seven of our sources, the lower limits and detection are on the order of previously observed debris disks ($1.05 \leq M_{dust} \leq 9.70$). The masses of HD 192425, HD 82189, and HD 37357 are poorly constrained, most likely due to their large distances, although as a Herbig Ae star, HD 37357 is expected to have a dust mass that is much larger than a typical planetary debris disk.

6.6 Conclusions and Future Work

Our one 3σ detection, HD 131156, has a flux of 6.25 ± 1.88 mJy at 1300 μm and a corresponding dust mass of 1.10 ± 0.33 lunar masses, but it is probably not real. Nonetheless, the dust mass for HD 131156 fits in well with with the Holland et al. (1998) results and with the estimated mass of the Kuiper belt ($M_{d(Vega)} < M_{d(HD131156)} < M_{d(Fomalhaut)} < M_{d(\beta Pic)} < M_{d(KB)}$).

Upper limits will be used as guidelines for choosing the most promising candidates for future sub-millimeter and possibly SIRTF observations. As mentioned before, some of our sources were candidates for SIRTF, which has an advantage of high sensitivity and thus may be able to make detections even if other ground observations fail to detect dust disks. Nonetheless, including our marginal detection, we have no evidence for massive disks surrounding seven of these sources. If disks exist, they may be similar to the tenuous disks surrounding Vega and Fomalhaut, of the order of a lunar mass of material. The mass limits on three of the sources are poorly constrained due to their large (> 45 pc) distances, though in the case of the Herbig Ae star, HD 37357 (3σ dust mass limit at 870 $\mu m \sim 18\ M_{\oplus}$), a large dust disk would not be unexpected (check).

SIRTF will have unprecedented sensitivity in the search for emission from planetary debris disks. The nearest systems will be spatially resolved and can be imaged by the Multiband Imaging Photometer (MIPS) in the 24, 70, and 160 μm wave

bands (Hanner et al. 1999). Assuming a low background noise and an integration time of 500 seconds, the 5σ sensitivities are 0.35, 1.3, and 22.5 mJy for the 24, 70, and 160 μm wave bands, respectively. These limits, particularly at 70 μm, could help to determine the extent of an infrared excess at far-infrared wavelengths, since the IRAS far-infrared data for this source are only upper limits.

Table 6-1: SMTO Source List.

Name	RA (J2000)	Dec (J2000)	Distance (pc)	Spectral type
HD 10700 (τ Cet)	01 44 09.99	-15 56 57.9	3.65	G8V
HD 165341 (DM+023482 A)	18 05 26.36	+02 30 52.9	5.09	K0V
HD 185144 (σ Dra)	19 32 15.59	+69 41 09.6	5.77	K0V
HD 4614 (η Cas A)	00 48 59.07	+57 49 23.7	5.95	G3V (and K7V)
HD 131156 (ξ Boo A)	14 51 22.73	+19 6 8.9	6.70	G8V (and K4V)
HD 32923 (104 Tau)	05 07 25.07	+18 38 41.1	15.9	G4V
HD 192425 (ρ Aql)	20 14 16.34	+15 11 48.2	47.1	A2V
HD 82189 (22 UMa)	09 34 52.70	+72 12 23.9	49.9	F7V
HD 37357	05 37 46.96	-06 42 30.2	~480	A0Ve
HD 39415	05 54 41.54	+44 30 08.0	–	F5V
HD 102647 (β Leo)	11 49 5.26	14 34 25.16	11.1	A3V

SMTO Source List. The sources were taken from the SIRTF Science Requirements Document (Simmons and Werner 1997) and from Oudmaijer et al. (1992). The distances in the table were derived from the Hipparcos Catalogue (ESA 1997) for all sources except for HD 37357. Hipparcos parallaxes have an error of about 0.8 milli-arcsec for a typical star at 20 pc. HD 37357 is a Herbig Ae star in a double or multiple system located in Lynds 1641, the nearest giant molecular cloud at a distance of 480 pc (Strom et al. 1989). Spectral types, for each source, were obtained from SIMBAD except for HD 4614 and HD 131156, where they were obtained from Fernandes et al. (1998).

Table 6-2: IRAS Fluxes and Upper Limits [Jy].

Name	12 μm	25 μm	60 μm	100 μm
HD 10700	9.562 ± 0.669	2.157 ± 0.194	0.513 ± 0.056	1.360
HD 165341	7.374 ± 0.295	1.805 ± 0.144	0.400	1.348
HD 185144	3.313 ± 0.100	0.744 ± 0.060	0.400	4.099
HD 4614	7.609 ± 0.380	1.746 ± 0.105	0.400	1.841
HD 131156	4.086 ± 0.286	0.964 ± 0.077	0.400	1.000
HD 32923	1.924 ± 0.115	0.550 ± 0.072	0.400	6.908
HD 192425	0.497 ± 0.035	0.235 ± 0.033	0.400	1.135
HD 82189	0.612 ± 0.037	0.301 ± 0.238	0.400	1.062
HD 39415	0.30 ± 0.03	0.27 ± 0.09	0.40	1.23
HD 37357	2.01 ± 0.121	2.79 ± 0.195	2.90 ± 1.537	20.29 ± 2.638
HD 102647	6.970 ± 0.349	2.107 ± 0.232	1.179 ± 0.130	1.000

IRAS Fluxes and Upper Limits [Jy]. Listed above are the source's IRAS fluxes from the IRAS Point Source Catalog v.2.1 before color correcting. If no error is listed, the flux is an upper limit.

Table 6-3: SMTO Bolometer Observations 1999-2000.

	870 μm			1300 μm		
	On Source Integration Time	S/N	3 σ Limit [mJy]	On Source Integration Time	S/N	3 σ Limit [mJy]
HD 10700	47 min	+1.94	19.8	–	–	–
HD 165341	–	–	–	1 hr 30 min	+0.94	8.85
HD 185144	47 min	+0.043	37.53	2 hr 35 min	-1.11	3.81
HD 4614	50 min	-0.0085	26.04	40 min	-2.10	23.52
HD 131156	1 hr 27 min	+0.35	17.28	3 hr	+3.33	6.25 ± 1.88
HD 32923	30 min	+1.53	38.52	30 min	-1.34	12.60
HD 192425	17 min	+1.39	33.30	1 hr 25 min	-1.38	7.95
HD 82189	–	–	–	1 hr 55 min	-0.72	8.91
HD 37357	30 min	-1.23	38.70	20 min	+0.29	26.64
HD 39415	1 hr 10 min	+0.92	18.75	55 min	+1.53	10.68
β Leo	1 hr	+0.17	20.91	1 hr 20 min	+0.30	8.85

SMTO Bolometer Observations 1999-2000. The measured flux for HD 131156 is 6.25 ± 1.88 mJy.

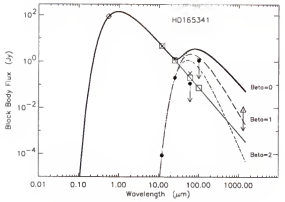

a) HD 165341

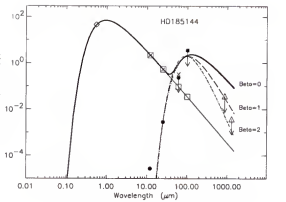

b) HD 185144 (σ Dra)

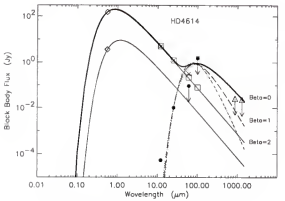

c) HD 4614 (η Cas A and B)

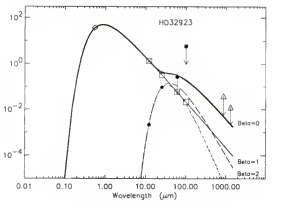

d) HD 32923

Figure 6-3: Blackbody ($\beta = 0$) and graybody ($\beta = 1$ and 2) fits to the star subtracted color corrected IRAS fluxes for (a) HD 165341, (b) HD 185144 (σ Dra), (c) HD 4614 (η Cas A and B), and (d) HD 32923. The open diamonds are fluxes derived from the V magnitudes from the Hipparcos and Tycho Catalogues (ESA 1997). The total color corrected IRAS fluxes or upper limits are represented by Xs. The stellar photospheric component of the IRAS fluxes or upper limits are denoted by open squares while the dust component of the IRAS fluxes or upper limits are shown as filled circles. Upper limits are represented by the appropriate symbol with a downward pointing arrow. Lastly, open triangles with arrows denote SMTO 3 σ upper limits from sub-millimeter observations at 870 and 1300 μm. The black body values of the stellar photosphere are plotted as a solid line. In the case of binary stars where there is information on both components (i.e., HD 4614), both photosphere curves are plotted. The black and greybody fits to the dust are also plotted. The $\beta = 0$ dust component curve is plotted as a dotted line. The $\beta = 1$ and $\beta = 2$ greybody dust component curves are plotted with dashed and dash dotted lines, respectively. The thick solid line represents the addition of the stellar photosphere curves or curves and the $\beta = 0$ blackbody fit to the dust component.

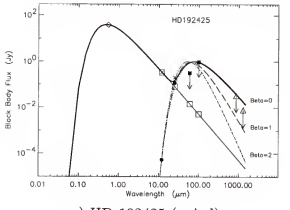

a) HD 192425 (ρ Aql)

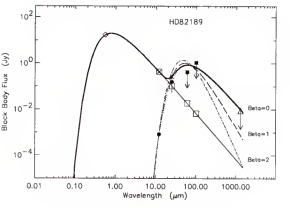

b) HD 82189 (22 UMa)

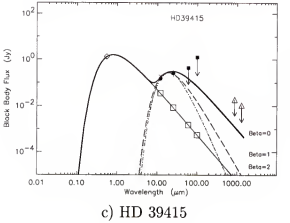

c) HD 39415

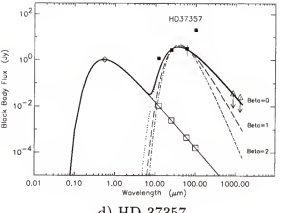

d) HD 37357

Figure 6-4: Blackbody ($\beta = 0$) and graybody ($\beta = 1$ and 2) fits to the star subtracted color corrected IRAS fluxes for (a) HD 192425 (ρ Aql), (b) HD 82189 (22 UMa), (c) HD 39415, (d) HD 37357, and (e) β Leo (HD 102647). The symbols are the same as in Figure 6-3. Open triangles with arrows denote SMTO 3 σ upper limits from sub-millimeter observations at 870 and 1300 μm. The black body values of the stellar photosphere are plotted as a solid line. The black and greybody fits to the dust are also plotted. The $\beta = 1$ curve is a dashed line and the $\beta = 2$ curve is a dotted line.The thick solid line represents the addition of the stellar photosphere curves or curves and the $\beta = 0$ blackbody fit to the dust component.

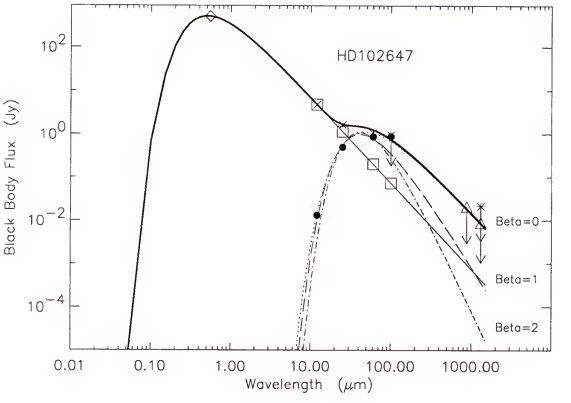

Figure 6-5: Blackbody ($\beta = 0$) and graybody ($\beta = 1$ and 2) fits to the star subtracted color corrected IRAS fluxes for β Leo. The above graph shows blackbody ($\beta = 0$) and graybody ($\beta = 1$ and 2) fits to the star subtracted color corrected IRAS fluxes for β Leo. The symbols are the same as in Figure 6-3, except that the asterisk represents the 3σ upper limit obtained by Weintraub and Stern (1994). The 3 σ upper limit at 1300 μm of 8.85 mJy found by this survey is 2.4 times smaller than the upper limit found by Weintraub and Stern (1994).

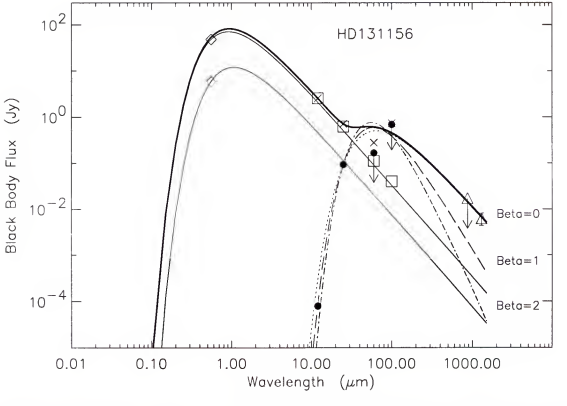

Figure 6-6: Blackbody ($\beta = 0$) and graybody ($\beta = 1$ and 2) fits to the dust component of the color corrected IRAS fluxes and upper limits for HD 131156. The symbols are the same as in Figure 6-3. Our one 3σ detection (S/N = 3.33), HD 131156, has a mean flux of 6.25 $\pm$ 1.88 mJy. If this were in fact a detection, the corresponding dust mass would be 1.10 $\pm$ 0.33 lunar masses. However, in viewing the surrounding channels of the 19-Channel bolometer, it appears unlikely that this detection is real. For comparison, the total mass in the observable Kuiper belt is of order 0.1 Earth masses, corresponding to approximately 8.2 lunar masses (Jewitt, Luu and Chen 1996; Jewitt, Luu and Trujillo 1998; Luu and Jewitt 1998).

CHAPTER 7
CONCLUSIONS

Three different types of asymmetries can serve to indicate bodies orbiting a star in a disk: 1) a warp in the plane of symmetry of the disk due to the variation of the forced inclinations of the particles with respect to their astrocentric distances (Dermott et al. 1999a, Dermott et al. 1999b), 2) an offset in the center of symmetry of the disk with respect to the central star due to forced eccentricities of the dust particles (Holmes et al. 1998), and 3) density anomalies in the plane of the disk due to resonant trapping of dust particles (Dermott et al. 1994b, Jayaraman 1995). The existence and causes of the warp and the offset in the background zodiacal cloud have been determined and knowledge about asymmetries in the zodiacal cloud has been used to make predictions about the nature of a dust disk in the Kuiper belt.

7.1 Warp and Offset

Using COBE DIRBE observations, we link structure in the zodiacal cloud, namely the warp and offset of the cloud, to the presence of planets using secular perturbation theory. We find that the position of the ascending node at 1 AU is $70.7° \pm 0.4°$ (Dermott et al. 1998, Holmes et al. 1999). From previous work, the position of the ascending node in the near ecliptic case (i.e., external to 1 AU) was determined to be $58.40° \pm 2.33°$ (Dermott et al. 1996b). The statistically significant disparity - the nodes differ by more than 12° - between ascending nodes for observations at the ecliptic poles (north and south) and for observations near the ecliptic (leading and trailing) indicates that the zodiacal cloud is indeed warped. The warp in the plane of symmetry of the zodiacal cloud is caused by the fact that the planets do not lie

in the same orbital plane. Jupiter, the most massive of the planets, is inclined to the Ecliptic by 1.30°, and Saturn is inclined to the Ecliptic by 2.49°. The mutual inclination, I_{mutual}, of Jupiter to Saturn produces the warp in the zodiacal cloud. Since I_{mutual} is small ($\sim 1.19°$), the warp in the zodiacal cloud is small. In addition, we build heuristic models of clouds with various degrees of warping and we find that SIRTF will not be capable of detecting a small warp similar to that seen in our solar system's zodiacal cloud.

Using COBE data, we determined the variation with the longitude of the Earth of the polar brightness of the zodiacal cloud, yielding knowledge about the offset of the background zodiacal cloud from the Sun. The north and south polar brightnesses, N and S, are combined to yield the mean of the north and south brightnesses, $(N+S)/2$. The variation in $(N+S)/2$ with ecliptic longitude of Earth is sinusoidal due to the variation in brightness due to Earth's eccentric orbit. If the cloud were symmetric about the Sun (i.e., if there were no offset), the maximum and minimum brightnesses of the cloud would occur at perihelion and aphelion, respectively. The minimum of the COBE curve at 244° is clearly displaced from Earth's aphelion, located at 282.9°, which demonstrates that the center of symmetry of the cloud is displaced from the Sun. The offset in the center of symmetry of the cloud with respect to the Sun is caused by the forced eccentricities of the dust particles. In addition, we obtain supplementary ISO observations and determine a scale factor for the data which we apply to calibrate the data to the observed COBE brightness.

7.2 Resonant Structure in the Kuiper Disk

Resonant structure in the hypothetical Kuiper disk is discussed at length in Chapters 4 and 5. In Chapter 4, we present the results of one of the first detailed studies of the resonant structure in the Kuiper disk. The particles are generated by bodies already inhabiting the 3:2 mean motion resonance. The dynamical evolution

of the particles in the disk is followed from source to sink with Poynting-Robertson light drag, solar wind drag, radiation pressure, the Lorentz force, neutral interstellar gas drag, and the effects of planetary gravitational perturbations included. From our numerical integrations, we determine what percentage of particles remain in the 3:2 resonance for a variety of particle and source body sizes.

From Figures 4-19, 4-20, and 4-21, it is clear that the percentage of particles in the 3:2 mean motion resonance increases with decreasing β (i.e., increasing particle size). Consequently, a size distribution for a Plutino disk must be weighted toward the larger size particles. In addition, as long as the potential, U, of the particles is small ($U \approx 5V$), the Lorentz force does not inhibit trapping to a great extent. However, if the U of the particles is increased to, for example, $20V$, the Lorentz force does significantly affect trapping for small particles. Though the value of $20V$ may be too high for particles in our solar system, this result may have important ramifications for the study of dust dynamics in exo-solar systems. We also find that the addition of the effect of neutral interstellar gas drag does not decrease the percentage of particles of a given β which remain in the 3:2 resonance by a statistically significant amount. Overall, Figures 4-19, 4-20, and 4-21 indicate that large particles are much more likely to remain in the 3:2 resonance than small particles, given our initial conditions. Few particles smaller than 10 μm in diameter will remain in a Plutino disk.

7.3 Searching the COBE Data for the Plutino Disk

By removing emission due to the background zodiacal cloud and the dust bands, we expect to see the trailing/leading signature of Earth's resonant ring. None of our current background zodiacal cloud models are sophisticated enough to allow us to obtain the residuals predicted by theory. We are additionally justified in expecting to see residuals from a resonant ring with a trailing/leading asymmetry because we see the trailing/leading asymmetry in the COBE data (see Figure 5-1). Both Reach

et al. (1995) and Kelsall et al. (1998) claim to see the correct trailing/leading asymmetry when they subtract their background zodiacal cloud models from the COBE data. However, we are unable to reproduce their results by using their models (either modified or unmodified). Furthermore, the offset of the Kelsall model does not match the offset seen in the COBE data (see Figure 5-4). Having said this, however, we acknowledge that the Kelsall et al. (1998) model is the most complete background zodiacal cloud model to date and that the shape of the model does match the shape of the zodiacal cloud fairly well. The detection of the Kuiper disk, however, hinges on developing a model of the zodiacal cloud that does more than simply possess the correct overall lenticular shape.

Our conclusion is that all of the Kelsall et al. (1998) and Reach et al. (1995) zodiacal cloud models must be replaced with dynamical models. We are able to use two dynamical models: the dust band model (Grogan et al. 2001) and the resonant ring model (Jayaraman et al. 1995). However, the most important model, the background zodiacal cloud model, is still incomplete, mainly because an accurate background zodiacal cloud model necessitates the inclusion of large particles (100 - 500 μm), the dynamics of which are relatively unknown and in need of further study. We conclude that a dynamical two-component (both inner and outer) zodiacal cloud model must be created to complete the search for the resonant signature of the Kuiper disk.

7.4 Sub-millimeter Observations

From our sub-millimeter survey of debris disk candidates, we obtain upper limits on the flux around ten Vega-type stars and one Herbig Ae star with the Four Color Bolometer and the 19 Channel Bolometer Array at the Sub-millimeter Telescope Observatory using the Heinrich-Hertz Telescope (SMTO) in the 870 μm and 1300 μm wave bands, respectively. All of our sources are undetected at 870 μm. In

the case of HD 131156, we technically have a 3σ detection at 1300 μm in the center channel of the 19-Channel bolometer and so we report a flux of 6.25 ± 1.88 mJy and we derive a dust mass of 1.10 ± 0.33 lunar masses for the system. However, in viewing the surrounding channels, we see that it is very unlikely that the 3σ detection is real. We have no evidence for massive disks surrounding these sources. If disks exist, they may be similar to the tenuous disks surrounding Vega and Fomalhaut, of the order of a lunar mass of material.

Upper limits from our sub-millimeter observations will be used as guidelines for choosing the most promising candidates for future sub-mm and possibly SIRTF observations. As mentioned before, some of our sources were candidates for SIRTF, which has an advantage of high sensitivity and thus may be able to make detections even if other ground observations fail to detect dust disks.

7.5 Future Work

7.5.1 Plutino Disk

From the percentages of particles in the 3:2 resonance we obtained from our numerical simulations, we can build a complete Plutino disk model. We can also study the effects of trapping in the inclination resonances and other resonances such as the 5:3 and the 2:1 more thoroughly. For example, in the 5:3 resonance, a sizeable percentage of particles are trapped in the inclination resonances (some particles may be trapped in multiple resonances). The inclination resonances are a topic for future study.

7.5.2 Building a Complete Background Zodiacal Cloud Model

The background zodiacal cloud is warped and the center of the cloud is offset from the Sun. A complete model of the background zodiacal cloud which accounts for both its warp and offset needs to be developed. A full two component (both inner and outer) zodiacal cloud model will be created. The outer cloud model created in

Chapter 5 will be refined and an inner cloud model will be created. The dynamics of the inner cloud are dominated by large particles, 100 - 500 μm in diameter (Dermott et al. 2001, Love and Brownlee 1993). In considering the dynamics of the inner cloud, collisions between particles, resonances (in particular, the secular resonance at approximately 2 AU), and the gravitational scattering by the inner planets must be included in future models.

7.5.3 Applications to Planetary Debris Disks

We will further develop circumstellar disk models which will probe the connection between planetary debris disks and the presence of planets. For the first time, the combination of Keck (single dish and interferometer) and SIRTF (Space Infrared Telescope Facility) data on nearby stars will allow for a complete characterization of exo-zodiacal dust disks on scales of approximately 1 to 100 AU, while the advancement in modeling techniques will allow us to build a comprehensive model of planetary debris disk dynamics. Ultimately, this research will be utilized to assess the degree to which exo-zodiacal emission will affect the Terrestrial Planet Finder mission.

We will refine and extend our modeling capabilities to incorporate collisions, a larger range of particle sizes, and gas drag. Although we have included the Lorentz force in some of our numerical integrations, we concluded that for particles in the solar system with a potential, $U \sim 5V$, the Lorentz force does not seem to hinder trapping into resonances. However, the value of the grain potentials in exo-solar systems is relatively unknown and, consequently, a larger range of potentials deserve consideration. Collisions dominate over PR drag in many debris disks, such as HR 4796 (Wyatt et al. 1999), so a size distribution of particles based on collisions must be taken into account. We have included the effects of neutral interstellar gas drag in some of our numerical integrations, but a wider range of effects due to gas drag may have to be considered. Drag due to the presence of gas in the system can

be a notable effect for dust disks around very young, pre-main sequence stars. These additions to our current capabilities will allow us to build a comprehensive model of planetary debris disk dust dynamics.

APPENDIX A
SIMUL

SIMUL models are three dimensional, numerical models of dust disks which are based on the theory of Secular Perturbations, the classical method used to study the long term orbital evolution of both planets and minor planets in planetary systems. The dynamical evolution of the particles is followed from source to sink with Poynting Robertson light drag (PR drag), solar wind drag, radiation pressure, and the effects of planetary gravitational perturbations included. Based on these effects, a set of orbits is generated for the particles in the disk. The orbits of the particles are distributed through a three-dimensional array of cells, generating a three-dimensional numerical SIMUL model. Specifically, these are the basic ideas assumption behind SIMUL:

1. A model cloud is composed of a large number (hundreds of thousands to millions) of dust particle orbits. The total cross sectional area of the model is divided equally among all of the orbits.

2. The orbital elements for the dust particles are input into SIMUL and a set of orbits are generated based on those elements. The input may be in terms of (a) total orbital elements or (b) forced and proper elements.

   Using low order Secular Perturbation Theory, the osculating elements: (eccentricity (e), inclination (I), longitude of ascending node (Ω), and longitude of pericenter ($\tilde{\omega}$), can be decomposed into proper and forced elements. The proper elements are dependent on initial conditions while the forced elements are

imposed on the particle's orbit by the gravitational perturbations of the planets. This decomposition is still applicable in the presence of drag forces. The assumptions for the low order theory are that (a) no mean motion resonances are involved, (b) and (c) the eccentricities and inclinations of the objects in the system are small enough so that a second-order expansion of the disturbing function is sufficient to describe the system (Murray and Dermott 1999).

3. The cross sectional area per orbit is spread along each orbit according to Kepler's Second Law.

4. The three dimensional model space is divided into millions of cells and SIMUL calculates the contribution of each orbit to each individual cell.

5. A three dimensional cell table is produced which contains the spatial distribution of the effective cross sectional area for the model cloud.

Then, a Line of Sight (LOS) Integrator allows a model to be viewed as it would appear to an Earth-based observer in a given wave band at a specified distance. The brightness along the line of sight is calculated assuming the particles are spheres of a given diameter which are composed of astronomical silicate, and the optical properties of these particles are obtained using an advanced Mie theory (Gustafson 1994). The model can even be convolved with a beam size or pixel size to simulate how an observation would appear to a specific telescope or space observatory, such as COBE.

APPENDIX B
OPTICAL PROPERTIES OF DUST PARTICLES

The brightesses of the particles in the dynamical dust models in this thesis are calculated using advanced Mie theory. This appendix presents the basic ideas behind light scattering as applied to circumstellar disks and follows the presentation of the topic as outlined by Gustafson (1994) and Leinert and Grun (1990).

There are two types of radiation that are important to studies of dust grains in the zodiacal cloud and other optically thin circumstellar disks: scattering and thermal emission, which is the re-radiation of absorbed stellar energy. In the case of the solar system, the equilibrium temperature of particles in a disk can be obtained by equating expressions for the absorption and emission of energy, where absorption appears on the left hand side of the following equation and emission appears on the right hand side

$$\int_0^\infty F_\odot(r,\lambda)\pi s^2 Q_{abs}(s,\lambda)d\lambda = \int_0^\infty 4\pi s^2(\pi B(T,\lambda))Q_{abs}(s,\lambda)d\lambda \qquad \text{(B.1)}$$

and $F_\odot$ is the stellar irradiance at a heliocentric distance r, λ is the wavelength, s is the particle radius, $B(T,\lambda)$ is the Planck function, and Q_{abs} is the absorption efficiency. There are several efficiency factors that need to be considered in the brightness calculations. Q_{abs} is the absorption efficiency factor. Q_{ext} is the extinction efficiency factor and Q_{sca} is the scattering efficiency factor. These Q factors are related to each other in the following manner

$$Q_{ext} = Q_{sca} + Q_{abs} \qquad \text{(B.2)}$$

and are dependent on the wavelength of radiation, the size particle under consideration, the refractive index of the grain, which is in turn dependent on the composition of the grain. When the Q factors are plotted against the quantity $x = 2\pi s/\lambda$, both Q_{abs} and Q_{sca} approach unity as x becomes large, but Q_{ext} approaches 2. (van de Hulst 1957).

REFERENCES

Cox, A. N. 2000, Allen's Astrophysical Quantities, 4th ed. Publisher: New York: AIP Press; Springer, 2000. Edited by Arthur N. Cox. ISBN: 0387987460,

Arendt, R. G., Odegard, N., Weiland, J. L., Sodroski, T. J., Hauser, M. G., Dwek, E., Kelsall, T., Moseley, S. H., Silverberg, R. F., Leisawitz, D., Mitchell, K., Reach, W. T., and Wright, E. L. (1998) The COBE diffuse infrared background experiment search for the cosmic infrared background. III. Separation of galactic emission from the infrared sky brightness. *Astrophys. J.* **508**, 74-105.

Aumann, H. H. and Good, J. C. (1990) IRAS constraints on a cold cloud around the solar system. *Astrophys. J.* **350**, 408.

Backman, D. E. and Paresce, F. (1993) Main-sequence stars with circumstellar solid material: the vega phenomenon. In *Protostars and Planets III*, (eds. E. H. Levy and J. I. Lunine), University of Arizona Press, Tucson, p.1253-1304.

Backman, D. E., Dasgupta, A. and Stencel, R. E. (1995) Model of a Kuiper belt small grain population and resulting far-infrared emission. *Astrophys. J.* **450**, L35.

Backman, D. E., Werner, G. H., and Van Cleve, J. E. (1997) Exploring planetary debris disks around solar-type stars. *From Stardust to Planetesimals,* **PASP Conference Proceedings, vol. 122,** Y.J. Pendleton and A.G.G.M Tielens, eds., Astronomical Society of the Pacific, pp. 49-66.

Bertin, P., Lallement, R., Ferlet, R., and Vidal-Madjar, A. (1993) Detection of the local interstellar cloud from high-resolution spectroscopy of nearby stars - Inferences on the heliospheric interface. *J. Geophys. Res.*, **98**, 15193-15197.

Boggess, N. W., Mather, J. C., Weiss, R., Bennett, C. L., Cheng, E. S., Dwek, E., Gulkis, S., Hauser, M. G., Janssen, M. A., Kelsall, T., Meyer, S. S., Moseley, S. H., Murdock, T. L., Shafer, R. A., Silverberg, R. F., Smoot, G. F., Wilkinson, D. T., and Wright, E. L. (1992) The COBE mission - Its design and performance two years after launch. *Astrophys. J.* **397**, 420.

Bond, J. R., Carr, B. J., and Hogan, C. J. (1986) Spectrum and anisotropy of the cosmic infrared background. *Astrophys. J.* **306**, 428.

Bowell, E. (1996) Asteroid orbital elements database (Lowel Obs.)

Brouwer, D. and clemence, G. M. (1961) Secular Perturbations. In *Methods of Celestial Mechanics*, Academic Press., p. 507-529.

Burns, J. A., Lamy, P. L., and Soter. S. (1979) Radiation forces on small particles in the solar system. *Icarus*, **40**, 1-48.

COBE/DIRBE Explanatory Supplement, Version 2.3. (1998) COBE Ref. Pub. No. 97-A. (eds. M.G. Hauser, T. Kelsall, D. Leisawitz, and J. Weiland) Greenbelt,MD: NASA/GSFC.

Dent, W. R. F., Greaves, J. S., Mannings, V., Coulson, I. M., and Walther, D. M. (1995) A search for molecular gas components in prototypal Vega-excess systems. *MNRAS*, **277**, L25-29.

Dermott, S. F., Nicholson, P. D., Burns, J. A., and Houck, J. R. (1984) Origin of the solar system dust bands discovered by IRAS. *Nature*, **312**, 505-509.

Dermott, S. F., Nicholson, P. D., Burns, J. A., and Houck, J. R. (1985) An analysis of IRAS' solar system dust bands. In *Properties and Interactions of Interplanetary Dust*, (eds. R. Giese and P. Lamy), Reidel, Dordrecht, 395-409.

Dermott, S. F., Malhotra, R., and Murray, C. D. (1988) Dynamics of the Uranian and Saturnian satellite systems: a chaotic route to melting Miranda?. *Icarus*, **76**, 295-334.

Dermott, S. F., Gomes, R. S., Durda, D. D., Gustafson, B. Å. S., Jayaraman, S., Xu, Y. L., and Nicholson P. D. (1992) Dynamics of the zodiacal cloud. In *Chaos, Resonance, and Collective Dynamical Phenomena in the Solar System* (ed. S. Ferraz-Mello) Kluwer, Dordrecht, 333-347.

Dermott, S. F., Durda, D. D., Gustafson, B. Å. S., Jayaraman, S., Liou, J. C., and Xu, Y. L. (1994a) Zodiacal dust bands. In *Asteroids, Comets, Meteors 1993*, (eds. A. Milani, M. Martini and A. Cellino) Kluwer, Dorecht, 127-142.

Dermott, S. F., Jayaraman, S., Xu, Y. L., Gustafson, B. Å. S., and Liou, J. C. (1994b) A circumsolar ring of asteroidal dust in resonant lock with the Earth. *Nature*, **369**, 719-723.

Dermott, S. F., Grogan, K., Gustafson, B. A. S., Jayaraman, S. Kortenkamp, S. and Xu, Y-L. (1996) Sources of interplanetary dust. In *Physics, Chemistry, and Dynamics of Interplanetary Dust. ASP Conference Series*, **104**, (ed. B. Å. S. Gustafson and M. S. Hanner), San Francisco, 143-153.

Dermott, S. F., Jayaraman, S., Xu, Y. L., Grogan, K., and Gustafson, B. Å. S. (1996) The origin and dynamics of the zodiacal cloud, in *Unveiling the Cosmic Infrared Background,* AIP Conference Proceedings, **348**, (ed. E. Dwek) Woodbury, New York, pp. 25-36.

Dermott, S. F., Grogan, K., Holmes, E. K., and Wyatt, M. C. (1998) Signatures of planets. in *Exozodiacal Dust Workshop Conference Proceedings* **1998-10155**(eds. D. E. Backman, L. J. Caroff, S. A. Sandford, and D. H. Wooden) p.59-63.

Dermott, S. F., Grogan, K., Holmes, E., and Kortenkamp, S. (1999a) Dynamical structure of the zodiacal cloud. In *Formulation and Evolution of Solids in Space* (eds. J. M. Greenberg and A. Li) 565-582.

Dermott, S. F., Grogan, K., Holmes, E. K., and Wyatt, M. C. (1999b) Signatures of planets in circumstellar disks. in *Modern Astrometry and Astrodynamics: Proceedings of the International Conference Honouring Heinrich Eichhorn* (eds. R. Dvorak, H. F. Haupt, and K. Wodnar), 189.

Dermott, S. F., Grogan, K., Durda, D. D., Jayaraman, S., Kehoe, T. J. J., Kortenkamp, S. J., and Wyatt, M. C. (2001) Orbital evolution of interplanetary dust. In *Interplanetary Dust*, (eds. E. Grün, B.Å.S. Gustafson, S.F. Dermott, and H. Fechtig) Springer-Verlag, Heidelberg, pp. 569–639.

Dohnanyi, J. S. (1969) Collisional models of asteroids and their debris, *J. Geophys. Res.*, **74**, 2531-2554.

Duncan, M. and Levison, H. (1998) A disk of scattered icy objects and the origin of Jupiter-family comets. *Science*, **276**, 1670-72.

Edgeworth, K. E., (1943) The evolution of our planetary system. *Journal of the British Astron. Soc.*, **53**, 181-88.

Edgeworth, K. E. (1949) The origin and evolution of the solar system. *MNRAS* , **109**, 600-609.

Elachi, C., Angel, R., Beichman, C. A., Boss, A., Brown, R., Dressler, A., Dyson, F., Fanson, J., Ftaclas, C., Goad, L., Klein, M., Leger, A., Lillie, C., Peale, S., Peterson, D., Reasenberg, B., Sandler, D., Shao, M., Simon, R., Tenerelli, D. (1996). A road map for the exploration of neighboring planetary systems (ExNPS). Technical Report, Jet Propulsion Lab96-22, (ed. C. Beichman), California Inst. of Tech. Pasadena, CA, United States.

Everhart, E., (1989) An efficient integrator that uses Gauss-Radau spacings. in *Dynamics of Comets: Their Origin and Evolution*,(eds. A. Carusi and G. B. Valeschhi), 185-202. D. Reidel Publishing Co.

ESA. (1997) The Hipparcos and Tycho catalogues. ESA SP-1200.

Fernandez, J. and Ip, W-H. (1984) Some dynamical aspects of the accretion of Uranus and Neptune, *Icarus* **58**, 109-20.

Fernandes, J., Lebreton, Y., Baglin, A. and Morel, P. (1998) Fundamental stellar parameters for nearby visual binary stars: η Cas, ξ Boo, 70 OPH and 85 Peg. Helium abundance, age and mixing length parameter for low mass stars. *Astron Astrophys.*, **338**, 455-464.

Freudling, W., Lagrange, A. M., Vidal-Madjar, A., Ferlet, R. and Forbeille, F. (1995) Gas around β Pictoris: an upper limit on the HI content. *Astron. Astrophys.* **301**, 231-235.

Gehrels, N. and Chen, W. (1993) The Geminga supernova as a possible cause of the Local Interstellar Bubble. *Nature*, **361**, 706.

Geiss, J., Gloeckler, G., and Mall, U. (1994) Origin of the O(+) pick-up ions in the heliosphere. *Astron. Astrophys.*, **289**, 933-936.

Gillet, F. (1986) in Light on dark matter, (ed. F. P. Israel), Reidel, Dordrecht, p. 61.

Gloeckler, G., Geiss, J., Balsiger, H., Fisk, L. A., Galvin, A. B., Ipavich, F. M., Ogilvie, K. W., von Steiger, R., and Wilken, B. (1993) Detection of interstellar pick-up hydrogen in the solar system. *Science*, **261**, 70.

Goertz, C. K. (1989) Dusty plasmas in the solar system. *Rev. Geophys*, **27**, 271-92.

Greaves J.S., Holland W.S., Moriarty-Schieven G., Jenness T., Dent W.R.F., Zuckerman B.,McCarthy C., Webb R., Butner H.M., Gear W. K., Walker H.J. (1998) A dust ring around epsilon Eridani: analog to the young solar system *Astrophys. J.*, **506L**, 133.

Greenberg, R. (1977) Orbit-orbit resonances among natural satellites, in *Planetary Satellites*, (ed. J. A. Burns) University of Arizona Press, Tucson, p.157-167.

Grogan, K., Dermott, S. F., and Gustafson, B. Å. S. (1996) An estimation of the interstellar contribution to the zodiacal thermal emission. *Astrophys. J.*, **472**, 812-817.

Grogan, K. (1997) Dynamical and observational constraints on the origin and evolution of the solar system dust bands. University of Florida, Ph.D. Dissertation.

Grogan, K., Dermott, S. F., and Durda, D. (2001) The size-frequency distribution of the zodiacal cloud: evidence from the solar system dust bands. *Icarus*, **152**, 251.

Grün, E., Gustafson, B. Å. S., Mann, I., Baguhl, M., Morfill, G. E., Staubach, P., Taylor, A., and Zook, H. A. (1994) Interstellar dust in the heliosphere. *Astron. Astrophys.*, **286**, 915-214.

Gustafson, B. Å. S. (1994) Physics of zodiacal dust *Annu. Rev. Earth Planet Sci.***22**, 553-95.

Gustafson, B. Å. S. (2000) Dust dynamics of transplanetary disks. *IAU JD 4E*, 11G.

Gustafson, B. Å. S. and Misconi, N. Y. (1979) Streaming of interstellar grains in the Solar System. *Nature*, **282**, 276.

Gustafson, B. Å. S., Grün, E., Dermott, S. F., and Durda, D. D. (1992) Collisional and dynamical evolution of dust from the asteroid belt. In *Asteroids, Comets, Meteors 1991*, (eds. A. W. Harris and E. Bowell), Lunar and Planetary Institute, Houston, p. 223-226.

Gustafson, B. Å. S., Greenberg, J. M., Kolokolova, L., Xu, Y. L., and Stognienko, R. (2001) Interactions with electromagnetic radiation: theory and laboratory simulations. In *Interplanetary Dust*, (eds. E. Grün, B. Å. S. Gustafson, S. F. Dermott, and H. Fechtig) Springer-Verlag, Heidelberg, pp. 509-567.

Holland W. S., Greaves J. S., Zuckerman B, Webb R., McCarthy C., Coulson I. M., Walther D., Dent W. R. F., Gear W. K., Robson, I. (1998) Submillimetre images of dusty debris around nearby stars. *Nature* **392**, 788-791.

Holmes E. K., Dermott S. F., Xu Y. L., Wyatt M. and Jayaraman, S. (1998) Modeling the effects of an offset of the center of symmetry in the zodiacal cloud. in *Exozodiacal Dust Workshop Conference Proceedings*, (eds. D. E. Backman, L. J. Caroff, S. A. Sandford, and D. H. Wooden), 272-273.

Holmes, E. K., Dermott, S. F., Grogan, K. and Wyatt, M. C. (1999) Simulations of warped dust disks. In *Astronomical Society of the Pacific Conference Series: Astrophysics with Infrared Surveys: A Prelude to SIRTF* (eds. M. D. Bicay, C. A. Beichman, R. M. Cutri, and B. F. Madore) **177**, 381-384.

Holmes, E. K. and Dermott, S. F. (2000) Comparison of ISO and COBE observations of the zodiacal cloud. In *ISO Beyond Point Sources: Studies of Extended Infrared Emission Workshop Proceedings* **SP-455** (eds. Laureijs, R. J., Leech, K., and Kessler, M. F.) 67-70.

Holmes, E. K., Dermott, S. F., and Grogan, K. (2000 submitted) Resonant structure in the Kuiper belt disk: observations and modeling. In *IAU Colloquium 181, Dust in the Solar System and Other Planetary Systems.*

ISOPHOT and PIA V8.0 manuals (1999).

Jayaraman, S. (1995) Resonance structure of the zodiacal cloud. University of Florida, Ph.D. Dissertation.

Jayaraman, S. and Dermott, S. F. (1996) COBE-DIRBE observations of the Earth's resonant ring, in *Unveiling the Cosmic Infrared Background,* AIP Conference Proceedings **348**(ed. E. Dwek) Woodbury, New York, pp. 47-50.

Jayaraman, S. and Dermott, S. F. (2001 in press) Earth's resonant ring. *Icarus.*

Jewitt, D. C. and Luu, J. X., (1993) Discovery of the candidate Kuiper belt object 1992 QB1 *Nature*, **362**, 730-732.

Jewitt, D C.., Luu, J. X., and Trujillo, C. (1998) Large Kuiper belt objects: The Manau Kea 8K CCD survey." *Astron. J.*, **115**, 2125-35.

Jewitt, D. C. (1999) Kuiper belt objects. *Annu. Rev. Earth Planet. Sci.*, **27**, 287-312.

Kelsall, T., Weiland, J. L., Franz, B. A., Reach, W. T., Arendt, R. G., Dwek, E., Freudenreich, H. T., Hauser, M. G., Moseley, S. H., Odegard, N. P., Silverberg, R. F., and Wright, E. L. (1998) The COBE diffuse infrared background experiment search for the cosmic infrared background. II. Model of the interplanetary dust cloud. *Astrophys. J* **508**, 44-73.

Klacka, J. (1992) Poynting-Robertson effect I. Equation of motion. *Earth, Moon, and Planets*, **59**, 41-59.

Koerner, D. W., Ressler, M. E., Werner, M. W., Backman, D. E. (1998) Mid-Infrared Imaging of a Circumstellar Disk around HR 4796: Mapping the Debris of Planetary Formation. *Astrophys. J.* **503**, L83.

Kortenkamp, S. (1996) Accretion of interplanetary dust particles by the Earth. University of Florida, Ph.D. Dissertation.

Kuiper, G. P. (1951) On the origin of the solar system. In *Astrophysics,* (ed. J. A. Hynek), New York, McGraw-Hill, pp. 357-424.

Lachaume, R., Dominik, C., Lanz, T., and Habing, H. J. (1999) Age determinations of main-sequence stars: combining different methods. *Astron. Astrophys.* **348**, 897-909.

U. S. Naval Observatory and Royal Greenwich Observatory (2001) *The Astronomical Almanac for the year 2001* Washington, D. C.

Leinert, C. and Grün, E. (1990) Interplanetary dust. In *IAU Colloqium 150, Physics and Chemistry in Space: Physics of the Inner Heliosphere I*, (ed. R. Schween and E. Marsch), Berlin, Springer, 207.

Liou, J.-C. (1993) Dynamical evolution of asteroidal and cometary particles and their contribution to the zodiacal cloud. University of Florida, Ph.D. Dissertation.

Liou, J.-C., Dermott, S. F., and Xu, Y.-L. (1995) The contribution of cometary dust to the zodiacal cloud. *Planet. Space Sci.*, **43**, 717-722.

Liou J.-C., Zook, H. A., Dermott, S. F. (1996) Kuiper belt dust grains as a source of interplanetary dust particles. *Icarus*, **124**, 429-40.

Liou, J.-C. and Zook, H. (1999) Signatures of the giant planets imprinted on the Edgeworth-Kuiper belt dust disk. *Astron. J. Letters*, **118**, L580.

Low, F. J., Beintema, D. A., Gautier, T. N., Gillet, F. C., Beichmann, C. A., Neugebauer, G., Young, E., Aumann, H. H., Boggess, N., Emerson, J. P., Habing, H. J., Hauser, M. G., Houch, J.R., Rowan-Robinson, M., Soifer, B. T., Walker, R. G. and Wesselius, P. R. (1984) Infrared cirrus: new components of the extended infrared emission, *Astrophys. J.*, **278**, L19-L22.

Love, S. G. and Brownlee, D. E. (1993) A direct measurement of the terrestrial mass accretion rate of cosmic dust. *Science* **262**, 550-553.

Luu, J., Marsden, B. G., Jewitt, D. Trujillo, C. A., Hergenrother, C. W., Chen, J., and Offutt, W. B. (1997) A new dynamical class in the Trans-Neptunian solar system. *Nature*, **387**, 573.

Malhotra, R. and Williams, J. G. (1998) Pluto's heliocentric orbit. In *Pluto and Charon*, (eds. S. A. Stern and D. Tholen), University of Arizona Press, Tucson, p.127-157.

Malhotra, R. (1995) The origin of Pluto's orbit: implications for the solar system beyond Neptune. *Astron. J.*, **110**, 420.

Malhotra, R. (1996) The phase space structure near Neptune resonances in the Kuiper belt. *Astronomical J.*, **111**, 504.

Marcy, G. W. and Butler, R. P. (1996) A planetary companion to 70 Virginis. *Astrophys. J. Letters*, **464**, L147.

Mayor, M. and Queloz, D. (1995) A Jupiter-mass companion to a solar-type star. *Nature*, **378**, 355.

Murray, C. D. and Dermott, S. F. (1999) *Solar System Dynamics*, Cambridge University Press, Cambridge.

Oudmaijer, R. D., van der Veen, W. E. C. J., Waters, L. B. F. M., Trams, N. R., Waelkens, C., and Engelsman, E. (1992) SAO stars with infrared excess in the IRAS Point Source Catalog. *Astron. Astrophys. Suppl. Ser.*, **96**, 625-643.

Parker. E. N. (1958) Dynamics of the interplanetary gas and magnetic fields. *Astrophys. J.*, **128**, 664.

Distant EKOs: The Kuiper Belt Electronic Newsletter, (ed. J. W. Parker), **19**, 2001.

Peale, S. J. (1976) Orbital resonances in the solar system. *Annu. Rev. Astron. Astrophys.* **14**, 215-245.

Peale, S. J. (1986) Orbital resonances, unusual configurations and exotic rotation states among planetary satellites, in *Satellites.* (ed. J. A. Burns and M. S. Mathews) University of Arizona Press, Tucson, p. 159-223.

Pollack, J. B., Holenbach, D., Beckwith, S., Simonelli, D. P., Roush, T., and Fong, W. (1994) Composition and radiative properties of grains in molecular clouds and accretion disks. *Astrophys. J.*, **421**, 615-639.

Poynting, J. H. (1903) *Phil. Trans. Roy. Soc.*, **202**, 525.

Robertson, H. P. (1937) Dynamical effects of radiation in the solar system. *Mon. Not. R. Astr. Soc.*, **97**, 423.

Roques, F., Scholl, H., Sicardy, B., and Smith, B. A. (1994) Is there a planet around β Pictorus? Perturbations of a planet on a circumstellar dust disk. *Icarus,***108**, 37-58.

Sandell, G. (1994) Secondary calibrators at submillimeter wavelengths. *Mon. Not. R. Astr. Soc.,* **271** , 75-80.

Scherer, K. (2000) Drag forces on interplanetary dust grains induced by the interstellar neutral gas. *J. Geophys. Res.*, **105**, 10329-10341.

Simmons, L. and Werner, M. (1997) The Space Infrared Telescope Facility science requirements document. 674-SN-100, Version 1.0.

Strom, K. M., Newton, G., Strom, S. E., and Seaman, R. L. (1989) A study of the stellar population in the LYNDS 1641 dark cloud. I - The IRAS catalog sources. *Astrophys. J. Suppl.*, **71**, 183-217.

Sykes, M. V., Greenberg, R. J., Dermott, S. F., Nicholson, P. D., Burns, J. A., and Gautier III, T. N. (1989) Dust bands in the asteroid belt in *Asteroids II,* (eds. R. Binzel, T. Gehrels, and M. Matthews), University of Arizona Press, Tucson, p.336-367.

Telesco, C. M., Fisher, R. S., Piña, R. K., Knacke, R. F., Dermott, S. F., Wyatt, M. C., Grogan, K., Holmes, E. K., Ghez, A. M., Prato, L., Hartmann, L. W., and Jayawardhana, R. (2000) Deep 10 and 18 μm imaging of the HR 4796A circumstellar disk: transient dust particles and tentative evidence for a brightness asymmetry. *Astrophys. J.* **530**, 329-341.

Thé, P. S., de Winter, D., Pérez, M. R. (1994) A new catalogue of members and candidate members of the Herbig Ae/Be (HAEBE) stellar group. *Astron. Astrophys. Suppl. Ser.*, **104**, 315-339.

Trujillo, C. A. and Jewitt, D. C. (2000) Population of the scattered Kuiper belt. *Astrophys. J. Letters*, **529**, L103-106.

van de Hulst, H. C. (1957) *Light Scattering by Small Particles.*New York, Wiley.

Wainscoat, R. J., Cohen, M., Volk, K., Walker, H. J., and Schwartz, D. E. (1992) A model of the 8-25 micron point source infrared sky. *Astrophys. J. Suppl.* **83**, 111.

Weidenschilling, S. J. and Jackson, A. A. (1993) Orbital resonances and Poynting-Robertson drag. *Icarus***104**, 244-254.

Weintraub, D. A. and Stern, S. A. (1994) A reinterpretation of millimeter observations of nearby IRAS excess stars. *Astron. J.*, **108** 701-710.

Witte, M., Rosenbauer, H., Banaszkiewicz, M., and Fahr, H. (1993) The ULYSSES neutral gas experiment - Determination of the velocity and temperature of the interstellar neutral helium. *Advances in Space Res.*, **13**, 121.

Wyatt, M. C., Dermott, S. F.. Telesco, C. M., Fisher, R. S., Grogan, K., Holmes, E. K., and Piña, R. K. (1999) How observations of circumstellar disk asymmetries can reveal hidden planets: Pericenter glow and its application to the HR 4796 disk. *Astrophys. J.*, **527**, 918-944.

Wyatt, S. P. and Whipple, F. L. (1950) Poynting-Robertson effect on meteor orbits. *Astrophys. J.***111**, 134-141.

Zappalà, V., Farinella, P., Knežević, and Paolicchi, P. (1984) Collisional origin of the asteroid families: Mass and velocity distributions. *Icarus*, **59**, 261-285.

Zuckerman, B., and Becklin, E. E. (1993) Submillimeter studies of main-sequence stars. *Astrophys. J.* **414**, 793-802.

BIOGRAPHICAL SKETCH

Elizabeth Katherine Holmes was born in New York, New York on June 24th, 1973. After attending Ridgewood High School in Ridgewood, New Jersey, she went on to study physics at the Massachusetts Institute of Technology. She obtained a Bachelor of Science in physics (Course 8) from MIT in June of 1995 and entered the University of Florida for her graduate work in astronomy that fall.

I certify that I have read this study and that in my opinion it conforms to acceptable standards of scholarly presentation and is fully adequate, in scope and quality, as a dissertation for the degree of Doctor of Philosophy.

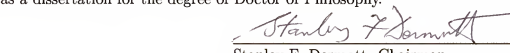

Stanley F. Dermott, Chairman
Professor of Astronomy

I certify that I have read this study and that in my opinion it conforms to acceptable standards of scholarly presentation and is fully adequate, in scope and quality, as a dissertation for the degree of Doctor of Philosophy.

Bo A. Gustafson
Professor of Astronomy

I certify that I have read this study and that in my opinion it conforms to acceptable standards of scholarly presentation and is fully adequate, in scope and quality, as a dissertation for the degree of Doctor of Philosophy.

Henry E. Kandrup
Professor of Astronomy

I certify that I have read this study and that in my opinion it conforms to acceptable standards of scholarly presentation and is fully adequate, in scope and quality, as a dissertation for the degree of Doctor of Philosophy.

Elizabeth A. Lada
Associate Professor of Astronomy

I certify that I have read this study and that in my opinion it conforms to acceptable standards of scholarly presentation and is fully adequate, in scope and quality, as a dissertation for the degree of Doctor of Philosophy.

David B. Tanner
Distinguished Professor of Physics

This dissertation was submitted to the Graduate Faculty of the Department of Astronomy in the College of Liberal Arts and Sciences and to the Graduate School and was accepted as partial fulfillment of the requirements for the degree of Doctor of Philosophy.

May 2002

Dean, Graduate School